



**FJSRL-TR-95-0004**

**FRANK J. SEILER RESEARCH LABORATORY**

**UNSTEADY AERODYNAMICS**

**WORK UNIT 2300-FF-07**

**FINAL REPORT**

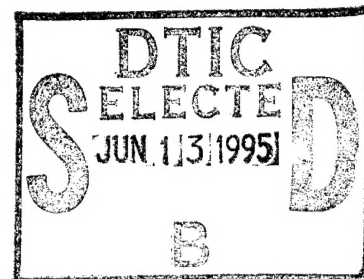
**OCTOBER 1991 - SEPTEMBER 1995**

**MAJOR ERIC J. STEPHEN  
TASK MANAGER**

**APPROVED FOR PUBLIC RELEASE;  
DISTRIBUTION UNLIMITED.**

**SEPTEMBER 1995**

**AIR FORCE MATERIEL COMMAND  
UNITED STATES AIR FORCE**



**DTIC QUALITY INSPECTED 3**

**19950612 004**




FJSRL-TR-95-0004

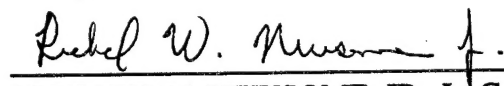
This document was prepared by the Aerospace Sciences Division, Frank J. Seiler Research Laboratory, United States Air Force Academy CO. The research was conducted under Project Work Unit Number 2300/FF/07, Unsteady Aerodynamics. Lt Col Richard W. Newsome, Jr., was the Division Chief and Major Eric J. Stephen was the Project Officer in charge of the work.

When U.S. Government drawings, specifications, or other data are used for any purpose other than a definitely related government procurement operation, the government thereby incurs no responsibility nor any obligation whatsoever, and the fact that the government may have formulated, furnished, or in any way supplied the said drawings, specifications, or other data is not to be regarded by implication or otherwise, as in any manner licensing the holder or any other person or corporation or conveying any rights or permission to manufacture, use or sell any patented invention that may in any way be related thereto.

[This report has been reviewed by the Technical Director and is releasable to the National Technical Information Service (NTIS). At NTIS it will be available to the general public, including foreign nations.]

This technical report has been reviewed and is approved for publication.

  
ERIC J. STEPHEN, Major, USAF  
Task Manager, Unsteady Aerodynamics

  
RICHARD W. NEWSOME, JR., Lt Col, USAF  
Chief, Aerospace Sciences Division

---

JOHN S. WILKES  
Technical Director

REPORT DOCUMENTATION PAGE			Form Approved OMB No. 0704-0188	
<small>Public reporting burden for this collection of information is estimated to average 1 hour per response, including the time for reviewing instructions, searching existing data sources, gathering and maintaining the data needed, and completing and reviewing the collection of information. Send comments regarding this burden estimate or any other aspect of this collection of information, including suggestions for reducing this burden, to Washington Headquarters Services, Directorate for Information Operations and Reports, 1215 Jefferson Davis Highway, Suite 1204, Arlington, VA 22202-4302, and to the Office of Management and Budget, Paperwork Reduction Project (0704-0188), Washington, DC 20503.</small>				
1. AGENCY USE ONLY (Leave blank)		2. REPORT DATE September 1995	3. REPORT TYPE AND DATES COVERED FINAL - October 1991 -- September 1995	
4. TITLE AND SUBTITLE UNSTEADY AERODYNAMICS - WORK UNIT 2300-FF-07 - FINAL REPORT			5. FUNDING NUMBERS	
6. AUTHOR(S) MAJOR ERIC J. STEPHEN				
7. PERFORMING ORGANIZATION NAME(S) AND ADDRESS(ES) FRANK J. SEILER RESEARCH LABORATORY 2354 VANDENBERG DRIVE, SUITE 6H79 USAF ACADEMY CO 80840-6272			8. PERFORMING ORGANIZATION REPORT NUMBER  FJSRL-TR-95-0004	
9. SPONSORING / MONITORING AGENCY NAME(S) AND ADDRESS(ES)			10. SPONSORING / MONITORING AGENCY REPORT NUMBER	
11. SUPPLEMENTARY NOTES				
12a. DISTRIBUTION / AVAILABILITY STATEMENT  Distribution Unlimited			12b. DISTRIBUTION CODE	
13. ABSTRACT (Maximum 200 words)				
14. SUBJECT TERMS Dynamic lift, Dynamic stall, Pitching airfoils, Pitching wings, Unsteady aerodynamics, Unsteady boundry layer			15. NUMBER OF PAGES	
			16. PRICE CODE	
17. SECURITY CLASSIFICATION OF REPORT UNCLASSIFIED	18. SECURITY CLASSIFICATION OF THIS PAGE UNCLASSIFIED	19. SECURITY CLASSIFICATION OF ABSTRACT UNCLASSIFIED	20. LIMITATION OF ABSTRACT NONE	

## GENERAL INSTRUCTIONS FOR COMPLETING SF 298

The Report Documentation Page (RDP) is used in announcing and cataloging reports. It is important that this information be consistent with the rest of the report, particularly the cover and title page. Instructions for filling in each block of the form follow. It is important to *stay within the lines* to meet *optical scanning requirements*.

### Block 1. Agency Use Only (Leave blank).

**Block 2. Report Date.** Full publication date including day, month, and year, if available (e.g. 1 Jan 88). Must cite at least the year.

**Block 3. Type of Report and Dates Covered.** State whether report is interim, final, etc. If applicable, enter inclusive report dates (e.g. 10 Jun 87 - 30 Jun 88).

**Block 4. Title and Subtitle.** A title is taken from the part of the report that provides the most meaningful and complete information. When a report is prepared in more than one volume, repeat the primary title, add volume number, and include subtitle for the specific volume. On classified documents enter the title classification in parentheses.

**Block 5. Funding Numbers.** To include contract and grant numbers; may include program element number(s), project number(s), task number(s), and work unit number(s). Use the following labels:

C - Contract	PR - Project
G - Grant	TA - Task
PE - Program Element	WU - Work Unit Accession No.

**Block 6. Author(s).** Name(s) of person(s) responsible for writing the report, performing the research, or credited with the content of the report. If editor or compiler, this should follow the name(s).

**Block 7. Performing Organization Name(s) and Address(es).** Self-explanatory.

**Block 8. Performing Organization Report Number.** Enter the unique alphanumeric report number(s) assigned by the organization performing the report.

**Block 9. Sponsoring/Monitoring Agency Name(s) and Address(es).** Self-explanatory.

**Block 10. Sponsoring/Monitoring Agency Report Number.** (If known)

**Block 11. Supplementary Notes.** Enter information not included elsewhere such as: Prepared in cooperation with...; Trans. of...; To be published in.... When a report is revised, include a statement whether the new report supersedes or supplements the older report.

**Block 12a. Distribution/Availability Statement.** Denotes public availability or limitations. Cite any availability to the public. Enter additional limitations or special markings in all capitals (e.g. NOFORN, REL, ITAR).

**DOD** - See DoDD 5230.24, "Distribution Statements on Technical Documents."

**DOE** - See authorities.

**NASA** - See Handbook NHB 2200.2.

**NTIS** - Leave blank.

### Block 12b. Distribution Code.

**DOD** - Leave blank.

**DOE** - Enter DOE distribution categories from the Standard Distribution for Unclassified Scientific and Technical Reports.

**NASA** - Leave blank.

**NTIS** - Leave blank.

**Block 13. Abstract.** Include a brief (*Maximum 200 words*) factual summary of the most significant information contained in the report.

**Block 14. Subject Terms.** Keywords or phrases identifying major subjects in the report.

**Block 15. Number of Pages.** Enter the total number of pages.

**Block 16. Price Code.** Enter appropriate price code (*NTIS only*).

**Blocks 17. - 19. Security Classifications.** Self-explanatory. Enter U.S. Security Classification in accordance with U.S. Security Regulations (i.e., UNCLASSIFIED). If form contains classified information, stamp classification on the top and bottom of the page.

**Block 20. Limitation of Abstract.** This block must be completed to assign a limitation to the abstract. Enter either UL (unlimited) or SAR (same as report). An entry in this block is necessary if the abstract is to be limited. If blank, the abstract is assumed to be unlimited.

## TABLE OF CONTENTS

INTRODUCTORY SUMMARY .....	1
UNSTEADY VORTEX DYNAMICS AND SURFACE PRESSURE TOPOLOGIES ON A FINITE PITCHING WING- S. J. SCHRECK, H. E. HELIN.....	2
NAVIER STOKES SIMULATION OF WING-TIP AND WING- JUNCTURE INTERACTIONS FOR A PITCHING WING- R. W. NEWSOME.....	12
ANALYSIS OF ROLLED DELTA WING FLOWS USING EFFECTIVE SWEEP AND ATTACK ANGLES- E. J. STEPHEN.....	33
FLOW VISUALIZATION INVESTIGATION OF THE WAKE BEHIND AN OGIVE CYLINDER- D. BUNKER, M. LUTTGES, M. ROBINSON .....	55
EXPERIMENTAL INVESTIGATION OF THE VORTEX-VERTICAL TAIL INTERACTION ON AN F-15- S. P. LEMAY, J. A. LOVATO...	68
FEEDBACK CONTROL OF THE FLOW OVER A TWO- DIMENSIONAL AIRFOIL-J. A. LOVATO, C. A. BAER .....	88
EFFECTS OF TRAILING-EDGE JET ENTRAINMENT ON DELTA WING VORTICES - H. E. HELIN, C. W. WATRY .....	95
REAL TIME-PREDICTION AND CONTROL OF 3D UNSTEADY FLOW FIELDS USING NEURAL NETWORKS - W. E. FALLER, S. J. SCHRECK, M. W. LUTTGES .....	99
PUBLICATIONS/PRESENTATIONS LIST.....	104

Accession For	
NTIS GRA&I	<input checked="" type="checkbox"/>
DTIC TAB	<input type="checkbox"/>
Unannounced	<input type="checkbox"/>
Justification	
By	
Distribution/	
Availability Codes	
Dist	Avail and/or Special
A-1	

## UNSTEADY AERODYNAMICS SUMMARY

Final report for Work Unit 2300/FF/07

This task addressed basic research to better understand unsteady, separated flows and to utilize this understanding to develop innovative concepts to control unsteady aerodynamic phenomena to enhance flight vehicle maneuverability. This effort sought to expand the flight performance boundaries by developing a capability to maneuver in the high-angle-of-attack, post-stall flight regime. Research directly supported Air Force objectives for unsteady and separated flows, as outlined in the current research Technology Area Plan for Project 2307, Fluid Mechanics.

The research was organized around two broad topical areas: (1) understanding and predicting the dynamics of unsteady, separated flows and (2) controlling unsteady, separated flows to enhance aerodynamic performance. Several types of flow fields were studied to gain an understanding of unsteady, separated flows. These included flow over rectangular wings, flow over delta wing, flow over forebodies and flow in the vicinity of the tail on a fighter type aircraft. The studies were both computational and experimental. Control efforts focused on the pulsed blowing to maintain attached flow, continuous blowing to control vortex breakdown on delta wing, and the use of neural networks to predict and control unsteady aerodynamic forces. Results for these topics are summarized in the next eight sections.

For a more detailed account of the research, see the attached Work Unit publications and presentations listing

# **Unsteady Vortex Dynamics and Surface Pressure Topologies on a Finite Pitching Wing**

S. J. Schreck and H. E. Helin

Reprinted from

## **Journal of Aircraft**

Volume 31, Number 4, Pages 899-907



*A publication of the*  
American Institute of Aeronautics and Astronautics, Inc.  
370 L'Enfant Promenade, SW  
Washington, DC 20004-6370

# Unsteady Vortex Dynamics and Surface Pressure Topologies on a Finite Pitching Wing

Scott J. Schreck\* and Hank E. Helin†  
U.S. Air Force Academy, Colorado Springs, Colorado 80840

A straight wing having an NACA 0015 cross section and rectangular planform was attached to a circular splitter plate. This configuration was pitched at a constant rate to angles exceeding the static stall angle. The unsteady, vortex-dominated flow that developed over the wing and splitter plate was characterized in detail using surface pressure measurements and flow visualization. Both types of data showed that the leading-edge vortex underwent profound three-dimensional alterations to cross section and convection over the entire wing span. These changes in leading-edge vortex structure and kinematics were correlated with prominent spanwise variations in force coefficients. When appropriately dissected, visualization results and pressure data suggested physical mechanisms to account for these three-dimensional variations in unsteady forces and surface pressures.

## Nomenclature

$C_n$	= normal force coefficient
$c$	= wing chord length, cm
$c_p$	= pressure coefficient
$LE$	= leading edge
$Re_c$	= chord Reynolds number
$s$	= wing span length, cm
$t$	= time, s
$t_{nd}$	= nondimensional time, $tU_\infty/c$
$U_\infty$	= test section velocity, m/s
$x$	= chordwise distance from leading edge
$y$	= spanwise distance from splitter plate
$\alpha$	= instantaneous angle of attack, deg
$\dot{\alpha}$	= pitch rate, rad/s
$\alpha^+$	= nondimensional pitch rate, $c\dot{\alpha}/U_\infty$

## Introduction

**T**HREE-DIMENSIONAL dynamically separated flows continue to be intensely studied. Energetic large-scale vortical structures are generated and transiently reside on wings dynamically pitched through the static stall angle of attack. These vortical structures radically alter the pressure distributions on a wing, thus producing greatly amplified aerodynamic forces and moments. If thoroughly understood and properly controlled, three-dimensional dynamically separated flows have the potential to confer dramatic performance enhancements upon future aircraft.

Flow visualization studies have documented the morphology of portions of three-dimensional unsteady flows elicited by pitching wings.<sup>1-6</sup> These studies concentrated attention on the prominent leading-edge and wingtip vortices, and successfully constructed simplistic physical models based upon vorticity conservation to explain vortex anchoring and tapering near the wingtip. Fewer investigations have employed surface pressure measurements to characterize three-dimensional unsteady flowfield development on pitching wings.<sup>7,8</sup> These studies found unsteady spanwise pressure distributions

to be augmented near the wingtip in comparison to the steady spanwise distribution.

Unsteady flows near wing-wall junctures have been shown to be as complex as those near the wingtip. Shih<sup>9</sup> examined the dynamically separated flowfield over a wing spanning a test section in which the flow speed varied sinusoidally. Velocity surveys revealed strong spanwise three-dimensionality that exhibited convective behavior suggesting the presence of separated vortical eddies. Horner and colleagues<sup>10</sup> employed flow visualization to show that the unsteady flow near the juncture between a fixed wall and a pitching wing was two dimensional immediately following leading-edge vortex initiation. However, as the vortex convected along the wing chord, the vortex arched away from the wing surface near center span, and symmetrical counter-rotating cells formed on the wing surface. Three-dimensional disruptions to the leading-edge vortex were explained with a model that relied upon mutual induction between orthogonal vortex segments.

Schreck and coworkers<sup>11</sup> and Klinge et al.<sup>12</sup> investigated the dynamically separated flow near the juncture between a wing and splitter plate undergoing constant rate and sinusoidal pitching, respectively. Both experiments measured unsteady surface pressures, enabling unambiguous characterization of leading-edge vortex convection and quantification of time-dependent normal forces. In the juncture region, the leading-edge vortex convected at a faster velocity and unsteady stall occurred earlier. Preliminary vorticity dynamics models were postulated to explain alterations to leading-edge vortex convection near the juncture.

The current investigation combines quantitative surface pressure topologies with flow visualization at identical nondimensional pitch rates and closely matched Reynolds numbers. This approach allows the presence and behavior of visualized vortex structures to be unambiguously confirmed by distinctive pressure signatures. This methodology also enables vorticity generation sites and rates to be inferred using surface pressure topologies. Thus, vorticity not aggregated into vortical structures can also be accounted for. Both flow visualization and surface pressure measurements show significant spanwise variability in the unsteady flowfield development. To account for this variability, a model is hypothesized for the three-dimensional unsteady flowfield on the wing-splitter plate configuration.

## Experimental Methods

### Surface Pressure Measurement

Surface pressure measurements were performed in the Frank J. Seiler 0.91- × 0.91-m low-speed wind tunnel located at the

Presented as Paper 93-0435 at the AIAA 31st Aerospace Sciences Meeting and Exhibit, Reno, NV, Jan. 11-14, 1993; received April 21, 1993; revision received Oct. 14, 1993; accepted for publication Oct. 30, 1993. This paper is declared a work of the U.S. Government and is not subject to copyright protection in the United States.

\*Unsteady Aerodynamics Task Manager, Frank J. Seiler Research Laboratory, 2354 Vandenberg Dr., Ste. 6H79. Member AIAA.

†Assistant Professor, Department of Aeronautics, 2410 Faculty Dr., Ste. 106. Senior Member AIAA.

U.S. Air Force Academy. A rectangular planform wing with 15.24-cm chord length was fabricated from hollow aluminum NACA 0015 airfoil stock. The basic wing was 29.10 cm long and was equipped with a fitting on the outboard end that permitted arbitrary length extensions to be added. Fifteen miniature pressure transducers were installed inside the hollow basic wing model. These transducers were close coupled to the wing surface through pressure ports located along the chord line, 3.05 cm inboard of the basic wing end. Pressure transducer signals were low-pass filtered (300 Hz cutoff) and amplified by a gain of 500. The resulting signals were then sampled and digitized by the data acquisition system.

A circular aluminum splitter plate, 30.48 cm in diam and 0.64 cm thick, was machined to a sharp edge around the plate perimeter. The splitter plate had an NACA 0015 cutout centered in it, which allowed it to slide onto the wing and be positioned at arbitrary span locations. To effectively move the pressure ports along the wing span, the splitter plate was first positioned at the desired distance from the pressure ports. Then, a tip extension of the correct length was added to the basic wing, bringing the span length to 30.48 cm and maintaining aspect ratio constant at 2.0. The chordwise row of pressure ports was successively moved to 11 span locations, effectively distributing pressure ports over the wing surface as shown in Fig. 1. All 11 tip extensions used in these experiments terminated in a square tip.

In Fig. 1, spanwise pressure port locations range from 0.0 to 0.80 span outboard of the splitter plate. Chordwise pressure port locations range from  $-0.90$  to  $0.90$  chord, with  $0.0$  chord corresponding to the wing leading edge. Positive chord values denote the wing upper surface, whereas negative chord signifies the lower surface. Unsteady surface pressures measured at these port locations were contour-plotted using a linear interpolation between adjacent grid points in both the chordwise and spanwise directions.

Model pitching was driven by a 3.5-hp synchronous stepper motor. The wing-splitter plate combination was mounted on a steel shaft 2.86 cm in diam that was connected to the stepper motor through a gear linkage having a 4:1 reduction ratio. The independent variables explored in the surface pressure experiments included nondimensional pitch rates  $0.05$ ,  $0.10$ , and  $0.20$ , as well as spanwise pressure port locations  $0.0$ ,  $0.05$ ,  $0.10$ ,  $0.15$ ,  $0.25$ ,  $0.375$ ,  $0.50$ ,  $0.625$ ,  $0.70$ ,  $0.75$ , and  $0.80$  span outboard of the splitter plate. Wing pitch axis was located at

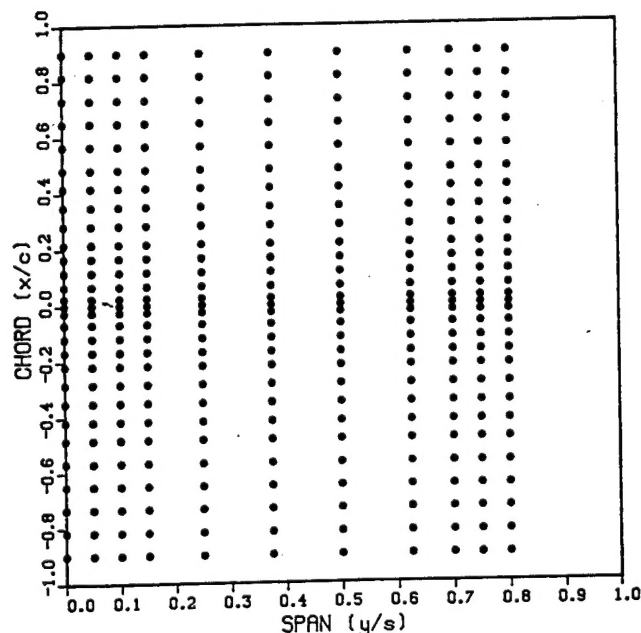


Fig. 1 Effective distribution of pressure port locations over the wing planform.

$0.25$  chord for the experimental range of nondimensional pitch rate, and at  $0.33$  chord for nondimensional pitch rate  $0.10$ . For each parameter combination, 20 consecutive wing pitch motions were sampled and ensemble-averaged. Test section velocity was held constant at  $9.14$  m/s, corresponding to a chord Reynolds number of  $6.9 \times 10^4$ .

#### Flow Visualization

Flow visualization was performed in the U.S. Air Force Academy  $0.51 \times 0.38$ -m water tunnel. Dimensions of the flow visualization wing-splitter plate model were identical to those of the surface pressure measurement model. A  $0.13$ -mm-wide slot was cut through the leading edge of the flow visualization wing along the entire wing span. This slot allowed dye to flow from the hollow wing interior to the wing exterior. Both wing and splitter plate were painted white to maximize visibility of the dark blue dye. Dye was injected directly into the boundary layer, visualizing the vorticity in the unsteady flowfield.

The wing-splitter plate model used for flow visualization was mounted on a steel shaft  $0.95$  cm in diam. The model was pitched at constant rate by a 24-V dc gear motor that was connected to the model through a gear linkage having a 5:1 reduction ratio. The visualized flowfield was illuminated by two 100-W incandescent lamps. Flow visualization images were recorded from the wing planform perspective at 30 frames/s by a VHS video camera.

Water tunnel flow visualization was performed at a test section velocity of  $0.44$  m/s and a water temperature of  $12.8^\circ\text{C}$ . This yielded a chord Reynolds number of  $5.6 \times 10^4$  that corresponded closely to that of  $6.9 \times 10^4$  for wind-tunnel surface pressure measurements. Flow was visualized for nondimensional pitch rates of  $0.05$ ,  $0.10$ , and  $0.20$ , using pitch axis locations of  $0.25$  and  $0.33$  chord. Volume coefficient of injection<sup>13</sup> out of the leading-edge slot was modest, being  $0.01$ .

#### Results

Pitching the wing-splitter plate configuration beyond static stall elicited dramatic three-dimensional modifications to leading-edge vortex structure. Visualized leading-edge vortex locations and structures correlated closely with minima in the surface pressure topologies. Three-dimensional modifications to the leading-edge vortex and correlation with surface pressure topologies persisted throughout the experimental range. Leading-edge vortex kinematics at all span locations were also well-correlated with spanwise normal force loading.

Angle-of-attack angle histories for the three measured nondimensional pitch rates of  $0.05$ ,  $0.10$ , and  $0.20$  are shown in Fig. 2. All three histories begin at  $0.0$  deg and end at  $60.0$  deg. The beginning of these histories coincides with the inception of surface pressure data acquisition. Thus, the plots in Fig. 2 can be used in conjunction with subsequent plots to convert nondimensional time to instantaneous wing angle of attack. For surface pressure measurements, the wing was pitched at a constant rate from  $0.0$  to  $60.0$  deg to collect upper

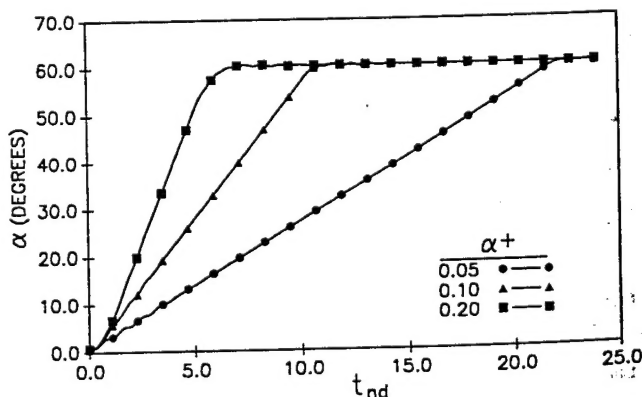


Fig. 2 Angle of attack histories for the experimental range of  $\alpha^+$ .

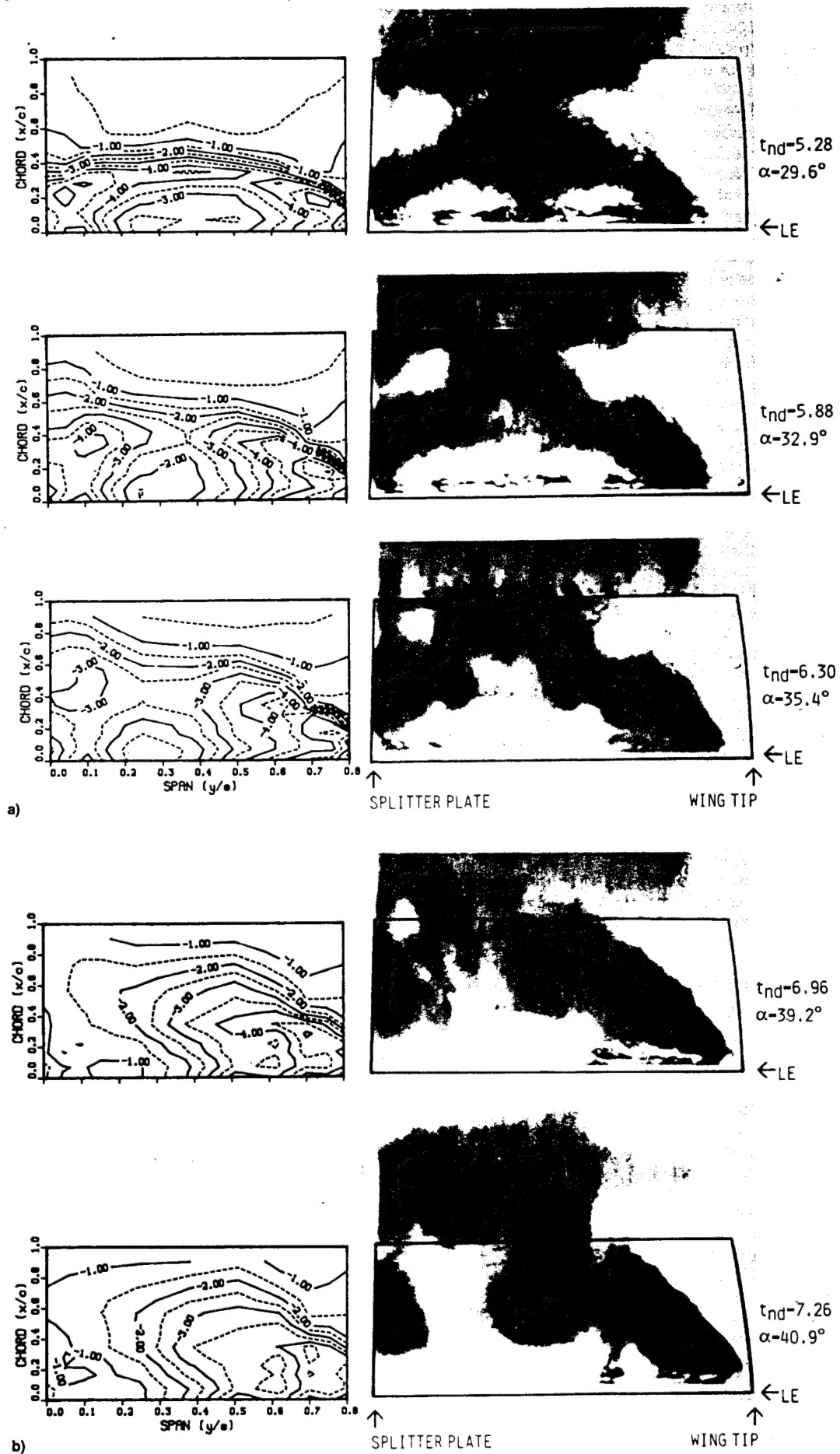


Fig. 3 Surface pressure topologies and corresponding flow visualizations for  $\alpha^+ = 0.10$  and pitch axis at  $0.33c$ , for  $t_{nd} =$  a) 5.28, 5.88, and 6.30 and b) 6.96 and 7.26.

surface data, and from 0 deg to  $-60.0$  deg to acquire lower surface data. It should be noted that none of the angle-of-attack histories exhibits prominent nonlinearity or suffers from appreciable acceleration or deceleration transients.

#### Vortex Structure and Surface Pressure Topologies

Figure 3 shows a representative series of five surface pressure coefficient topologies and corresponding dye flow visualization photographs. Nondimensional pitch rate was 0.10, and the wing was pitched about 0.33 chord. Note that surface pressure topologies extend 0.80 span from the splitter plate, whereas flow visualization shows the entire wing span. For clarity, the wing planform has been outlined in the visualization photographs. Lower surface pressure topologies were characterized by mild two-dimensional pressure gradients that underwent limited temporal evolution. Thus, lower surface data will not be presented here.

The frame 1 ( $t_{nd} = 5.28$ ) surface pressure topology in Fig. 3 is dominated by an arc-shaped suction ridge that begins near the intersection of the splitter plate and wing leading edge. The suction ridge proceeds outboard across the wing span, curves back to 0.33 chord at center span, and again approaches the leading-edge 0.80 span outboard of the splitter plate. Suction ridge position corresponds closely to the upstream boundary of the visualized leading-edge vortex. Near the splitter plate and wingtip, at 0.18 chord, prominent localized suction peaks disrupt suction ridge uniformity. Both suction peaks lie close to portions of the vortex that exhibit pronounced flexure in the visualization. Upstream of the suction ridge, two wedge-shaped contours, 0.25 and 0.50 span from the splitter plate and just behind the leading edge, denote pressure maxima that lie on either side of a low-pressure region. This low-pressure region corresponds to a chordwise dye streak that connects the wing leading edge and the vortex upstream boundary.

In frame 2 ( $t_{nd} = 5.88$ ), the suction ridge remains evident in the surface pressure topology. The inboard end of the suction ridge is still located near the intersection of the splitter plate and wing leading edge, and the outboard end still terminates near the wing leading edge. Visualization is consistent, showing the inboard and outboard ends of the vortex still located near the leading edge. Suction ridge magnitude has been substantially diminished near center span, where visualization indicates that the leading-edge vortex has arched up and away from the wing surface. Two local suction peaks are still present in the surface pressure topology. The inboard peak has moved downstream and is located at 0.36 chord, while the outboard suction peak remains at 0.18 chord. Suction peak locations lie close to portions of the visualized vortex that have undergone deformation, but remain near the wing surface.

The frame 3 ( $t_{nd} = 6.30$ ) surface pressure topology indicates the outboard end of the suction ridge still terminates near the wing leading edge. However, the inboard end of the ridge has moved downstream and is now located near midchord. Visualization shows the vortex remains at the leading edge near the wingtip, but has begun to convect downstream near the splitter plate. Two local suction peaks are still present near portions of the vortex that appear to have undergone deformation. The inboard peak has moved downstream and is located at 0.44 chord, while the outboard suction peak remains at 0.18 chord. In the ridge central portion, suction magnitude remains depressed, and the vortex arch that appeared in the previous flow visualization frame is still clearly visible. In addition, rotating cells have formed at the juncture where the legs of the vortex arch join the remainder of the vortex. At each location, cell rotation corresponds to that of the vortex, with each cell rotating in a sense opposite the other.

In frame 4 ( $t_{nd} = 6.96$ ), the surface pressure topology exhibits a suction ridge that begins near the outboard portion of the leading edge and has maximum magnitude there. Vis-

ualization is consistent, showing the vortex still anchored to the leading edge near the wingtip. The suction ridge then extends aft and inboard, decreasing in magnitude, and finally terminating near the intersection of the splitter plate and trailing edge. The outboard suction peak is still visible at 0.37 chord, whereas the inboard suction peak no longer exists. Visualization is again consistent, showing the outboard rotational cell near midchord and the inboard one centered over the trailing edge. These two cells are connected by diffuse dye streaks resembling the previously well-defined arch. Finally, a concentration of dye is visible immediately adjacent to the splitter plate. This structure remains connected to the inboard cell by a well-defined dye streak.

The frame 5 ( $t_{nd} = 7.26$ ) surface pressure topology consists principally of a broad, straight suction ridge extending from the leading edge near the wingtip to the trailing edge near the splitter plate. The outboard suction peak still persists near the wingtip and a new suction peak has formed adjacent to the splitter plate. This new suction peak has substantially lower magnitude than suction peaks observed earlier in the pitch motion, either inboard near the splitter plate or outboard near the wingtip. This is once again consistent with the visualization, which shows the outboard end of the vortex lies close to the wing leading edge. From here the vortex proceeds inboard and aft until it reaches the remaining rotational cell. From the rotational cell, the vortex extends upward and aft before flexing toward the splitter plate and extending inboard. After contacting the splitter plate, the vortex proceeds down toward the wing surface and forward toward the leading edge. It then terminates on the wing surface adjacent to the splitter plate near the new suction peak.

Figure 4 contains three flow visualization photographs showing the leading-edge vortex at chosen intermediate times in the pitch motion for the experimental range of nondimensional pitch rates. These photographs were selected to capture the initial disruptions to the leading-edge vortex gradual arc shape that were precursors to vortex arching. In the visualizations, disruptions appeared as discontinuities in the apparent upstream boundary of the leading-edge vortex. Disruptions subsequently developed into flexure points for the

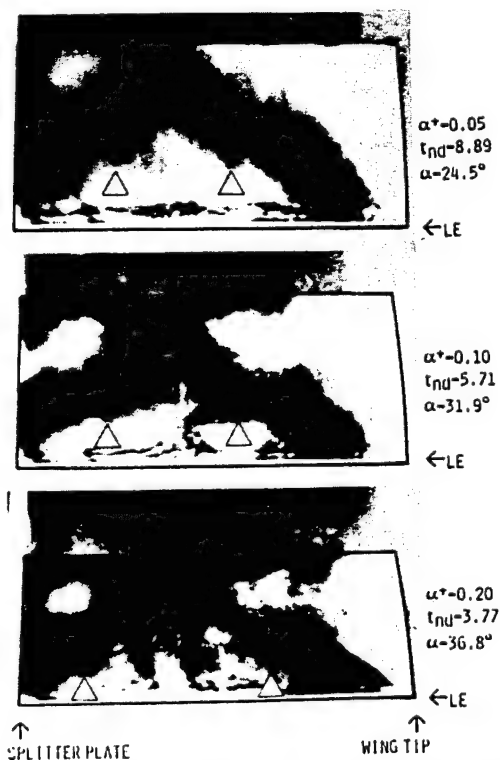


Fig. 4 Flow visualizations of leading-edge vortex at initial disruption for experimental range of  $\alpha^*$  and pitch axis at 0.33c.

vortex arch, and then rotational cells. In each photograph, spanwise location of both the inboard and outboard disruptions are marked by arrows. Spatial and temporal relationships between these initial disruptions and the wing are recorded in Table 1.

Table 1 indicates that higher nondimensional pitch rates drive the inboard initial disruption closer to the splitter plate. In addition, higher nondimensional pitch rates force the outboard initial disruption farther from the splitter plate and nearer the tip. When the initial disruptions occur, both inboard and outboard disruptions appear at the same chord location. However, increasing nondimensional pitch rate moves initial occurrence of the disruption farther forward on the wing chord, and delays it to higher angles of attack.

Figure 5 contains three surface pressure contour plots, identical in format to those presented in Fig. 3, for nondimensional pitch rates of 0.05, 0.10, and 0.20. These three contour plots correspond in orientation and scale to the three flow visualization photographs shown in Fig. 4. Thus, these topologies document surface pressure at the time when the leading-edge vortex underwent initial disruption. All three contour plots exhibit a prominent arc-shaped suction ridge that intersects the wing leading-edge inboard near the splitter plate and outboard near the wingtip. Near center span, the suction ridge curves downstream to approximately midchord. Prominent suction peaks are evident on the inboard portion of the suction ridge, located at 0.10, 0.10, and 0.05 span for nondimensional pitch rates of 0.05, 0.10, and 0.20. On the outboard part of the suction ridge, a suction peak is visible at 0.75 span for all three nondimensional pitch rates. Higher nondimensional pitch

Table 1 Spatial and temporal occurrence of initial disruptions shown by visualization in Fig. 4

$\alpha^+$	Inboard disruption span, $y/s$	Outboard disruption span, $y/s$	Both disruptions chord, $x/s$	Time of disruption occurrence, $t_{nd}$
0.05	0.25	0.56	0.32	8.89
0.10	0.23	0.57	0.25	5.71
0.20	0.16	0.65	0.18	3.77

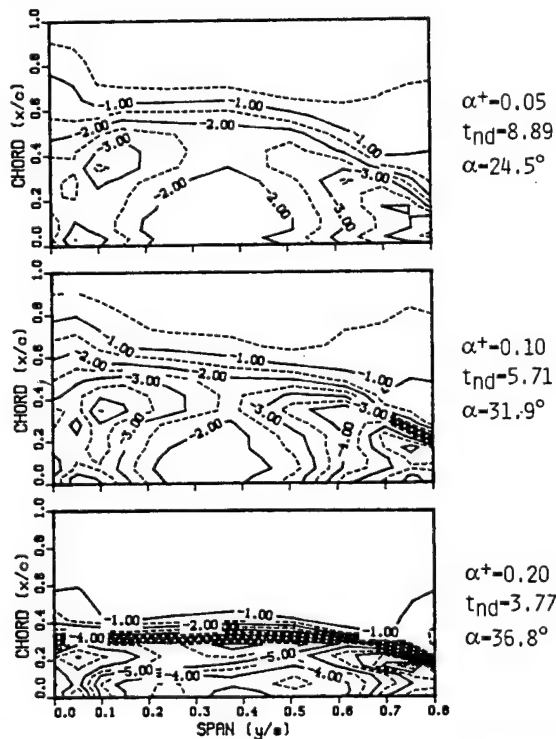


Fig. 5 Surface pressure topologies at initial vortex disruption for experimental range of  $\alpha^+$  and pitch axis at  $0.25c$ .

rates also show denser contour distributions, indicating steeper surface pressure gradients in both the chordwise and spanwise directions at higher nondimensional pitch rates.

#### Leading-Edge Surface Pressure

Figure 6 shows a representative contour plot documenting leading-edge surface pressure coefficient variation with nondimensional time and span location. This plot corresponds to a nondimensional pitch rate of 0.10 and pitch axis location of 0.33 chord. Beginning at nondimensional time 0.0, predominantly two-dimensional suction increase is indicated by the horizontal contours in the lower portion of the plot. However, gradual upward curvature at both the inboard and outboard ends of the contours indicates a lag in suction increase near the wing root and tip. After nondimensional time 4.00, leading-edge suction increase becomes radically nonuniform along the wing span, and three regions are discernible in the plot. In the central region, between 0.15–0.50 span, leading-edge suction first attains a maximum at a nondimensional time of 4.14. Suction subsequently declines at a nearly constant rate as shown by the uniform contour spacing in the vertical direction.

Inboard, between 0.0–0.15 span, the suction peak occurs 0.89 nondimensional time units later than it did in the central region. Suction reaches a local maximum at 0.05 span and nondimensional time 4.80, as indicated by the concentric contours. Following attainment of this maximum, suction decline is slow at first, and then accelerates, as shown by the closer contours after nondimensional time 6.0. Terminal rate of suction decrease is similar for the central and inboard regions of the plot, as evidenced by the comparable distances between adjacent contour lines. The outboard region is dramatically different from both the central and inboard regions. Here, leading-edge suction peaks at 0.80 span and nondimensional time 6.00, nearly 1.50 nondimensional time units after occurrence of the maxima in either the central or inboard region. After reaching this outboard peak, suction decreases at an appreciably slower rate than it did in either the central or inboard region of the plot.

Figure 7 is a summary plot that records the nondimensional time of leading-edge suction maximum at 11 span stations, for the experimental range of nondimensional pitch rate and pitch axis location. Data comprising this graph were extracted from contour plots similar to Fig. 6. Figure 7 shows that leading-edge suction reaches a maximum at earlier nondi-

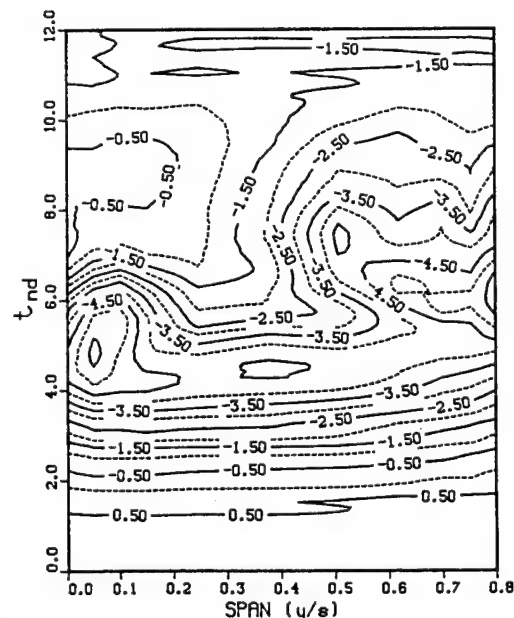


Fig. 6 Representative contour plot of leading-edge  $c_p$  vs  $t_{nd}$  and span.  $\alpha^+ = 0.10$  and pitch axis is located at  $0.33c$ .

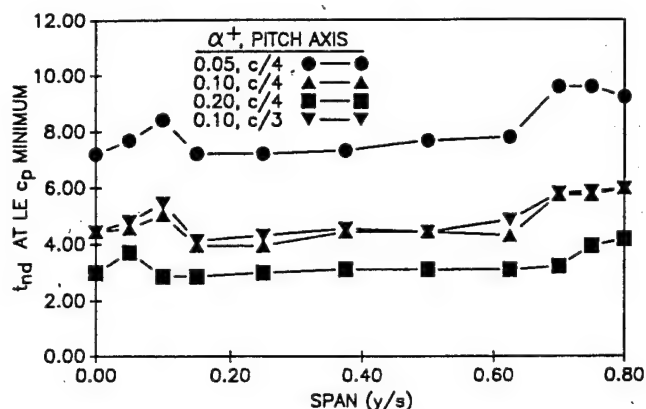


Fig. 7 Summary plot documenting  $t_{nd}$  of leading-edge suction collapse vs span for experimental range of  $\alpha^+$ .

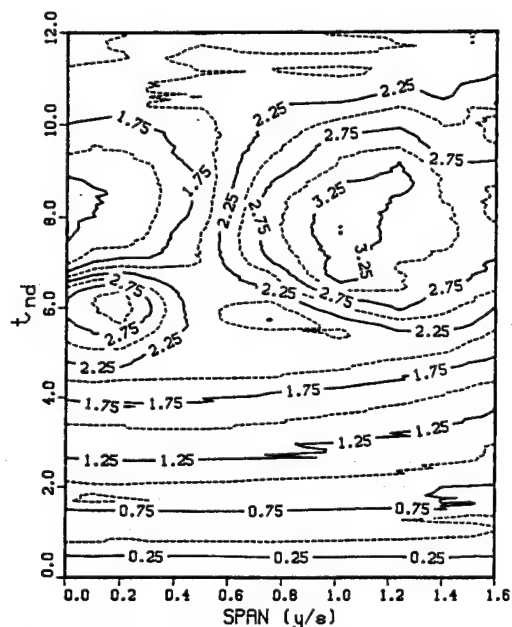


Fig. 8 Contour plot  $C_n$  vs  $t_{nd}$  and span.  $\alpha^+ = 0.10$  and pitch axis is located at  $0.33c$ .

dimensional times for higher nondimensional pitch rates, corresponding to higher instantaneous angles of attack. Moving the pitch axis from 0.25 to 0.33 chord for nondimensional pitch rate 0.10 also imposes a slight delay upon leading-edge suction peak occurrence.

All four plots in Fig. 7 are dominated by a broad, level central region. This portion of the curve shows that leading-edge suction maxima occurred first, and nearly simultaneously, over the central portion of the wing span for each nondimensional pitch rate. Inboard and outboard of these level regions, all four curves bend sharply upward. This indicates significant delays in the attainment of leading-edge suction maxima near both splitter plate and wingtip. All four plots show suction maxima occurring first in the broad central region of the wing span, followed by maxima inboard near the splitter plate and, finally, outboard near the wingtip. Higher nondimensional pitch rates generally drove the spanwise locations of suction maximum delay closer to the splitter plate and wingtip.

#### Spanwise Normal Force Loading

Figure 8 is a representative contour plot showing normal force coefficient variation with nondimensional time and span location. Normal force initially increases uniformly across the wing span with nondimensional time as shown by the horizontal contours. However, at nondimensional time 2.0, the contours at the outboard span stations begin to curve upward

and are spaced farther apart, indicating a reduced rate of normal force increase there. At nondimensional time 5.0, similar upward curvature and reduced contour density occurs at the inboard span stations, also indicating reduced rates of normal force increase near the splitter plate. Prior to nondimensional time 5.0, normal force variation remained highly uniform across the span, in spite of the minor perturbations noted above.

After nondimensional time 5.0, spanwise variation in normal force suffered severe three-dimensional disruption. Figure 8 exhibits a pronounced inboard normal force maximum of 2.95, as evidenced by the concentric contours centered at 0.1 span and nondimensional time 5.94. A similar normal force maximum of larger spatial and temporal extent, and magnitude 3.50, occurs outboard as indicated by the concentric contours centered at 0.5 span and nondimensional time 7.62. Between these two regions on the plot, from approximately 0.2 to 0.4 span, lies an area characterized by sparse contours of significantly lower magnitude. In this central region, normal force stalls at nondimensional time 5.58 and attains a maximum value of 2.16. Normal force then declines more slowly than it does either inboard near the splitter plate or outboard in the tip region.

At nondimensional time 8.0, normal force coefficient decreased to a minimum of approximately 1.25 at 0.0 span, and simultaneously increased to a maximum of 3.75 at 0.5 span. Between these two span locations, at 0.25 span, a region of nearly vertical contours indicates negligible temporal change in normal force. Subsequently, normal force increased inboard, decreased outboard, and underwent little change in the vicinity of 0.25 span. At nondimensional time 11.0, normal force became uniform across the span at a magnitude of approximately 2.0.

Figure 9 is a summary plot containing information extracted from contour plots similar to Fig. 8. Figure 9 records the nondimensional time of normal force maximum, or normal force stall, at 11 span stations for the experimental range of nondimensional pitch rate and pitch axis location. Figure 9 shows that at any given span station normal force stall occurs at earlier nondimensional times for higher nondimensional pitch rates, corresponding to higher instantaneous angles of attack. For nondimensional pitch rate 0.10, moving the pitch axis from 0.25 to 0.33 chord slightly delayed normal force stall.

All four curves in Fig. 9 show similar spanwise stall progressions. Normal force stall occurred first at 0.375 span for nondimensional pitch rate 0.20, and at 0.25 span for the remaining three conditions. Stall occurred next inboard, near the splitter plate. Here, inboard of 0.25 span, stall occurred last at 0.10 span for nondimensional pitch rate 0.05, and at 0.05 span for the other three conditions. Finally, normal force stalled outboard, near the wingtip. The spanwise location of final stall moved inboard with higher nondimensional pitch

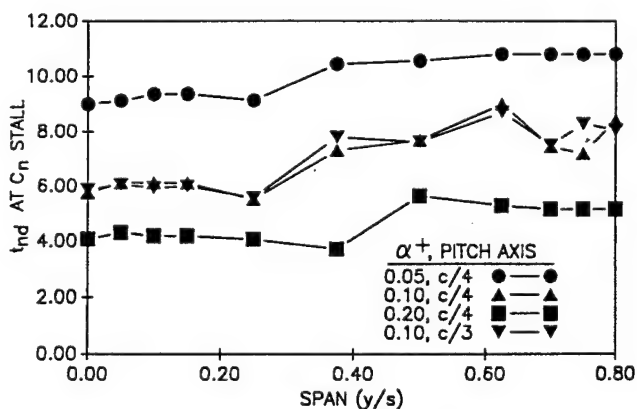


Fig. 9 Summary plot showing  $t_{nd}$  of  $C_n$  stall vs span for experimental range of  $\alpha^+$ .

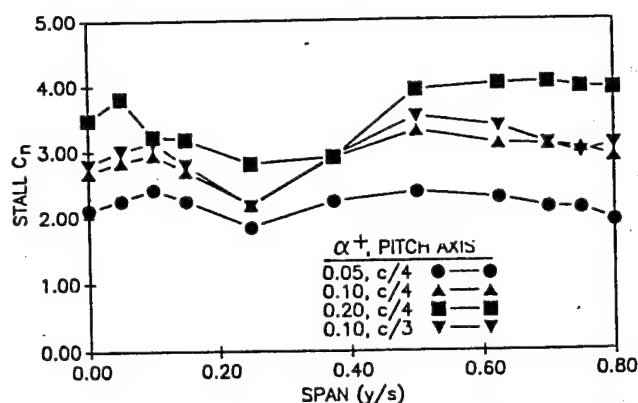


Fig. 10 Summary plot of stall  $C_n$  vs span for experimental range of  $\alpha^+$ .

rate, progressing from 0.70 to 0.625 span, and finally to 0.50 span for nondimensional pitch rates of 0.05, 0.10, and 0.20.

Figure 10 summarizes data taken from contour plots like Fig. 8, and documents stall normal force coefficient at 11 span stations for the experimental range of nondimensional pitch rate and pitch axis location. Figure 10 shows that, at any given span station, stall normal force coefficient increases with higher nondimensional pitch rate. For nondimensional pitch rate 0.10, moving the pitch axis from 0.25 to 0.33 chord generally increases stall normal force slightly.

Again, all four curves in Fig. 10 display similar trends. Stall normal force was lowest at 0.25 span for all four conditions. For each of the four curves, absolute maxima of stall normal force generally occurred outboard near the wingtip. Such absolute maxima occurred at 0.70 and 0.50 span for nondimensional pitch rates of 0.20 and 0.10. However, for nondimensional pitch rate 0.05, stall normal force reached absolute maximum at 0.10 span. In addition to the absolute maxima, local maxima also occurred at the opposite end of the span. Local maxima occurred at 0.10 span for nondimensional pitch rates 0.05 and 0.10, and at 0.05 span for nondimensional pitch rate 0.20.

### Discussion

Flow visualization, surface pressure topologies, and spanwise normal force loading histories provided diverse information regarding the unsteady flow over the pitching wing-splitter plate configuration. Correlating these data enabled formulation of a cohesive account of vortex kinematics, underlying vorticity dynamics and spanwise normal force loading.

Temporal and spatial fluctuations of considerable magnitude were observed in flow visualization, surface pressure topologies, and spanwise normal force loading histories. In contrast, Fig. 2 showed that the rigid wing-splitter plate combination pitched at constant rate in uninterrupted fashion. Thus, kinematic or geometric anomalies did not contribute to these prominent temporal and spatial variations.

Dye flow visualization revealed a large, energetic leading-edge vortex that persisted during a significant interval of the pitch motion and extended over a large area of the wing planform. Following initiation near the wing leading edge, the vortex convected downstream toward the wing trailing edge while growing in cross section. Vortex growth and convection were accompanied by radical three-dimensional deformation. Visualized vortex structures and locations were corroborated by prominent pressure minima that dominated surface pressure topologies, consistent with observations made by Walker and colleagues<sup>14</sup> for surface pressure distributions on two-dimensional airfoils. Modifications to vortex structure or location were accompanied by corresponding alterations to surface pressure topologies.

Soon after a predominantly two-dimensional initiation, Fig. 3 (frame 1,  $t_{nd} = 5.28$ ) showed that the leading-edge vortex

had experienced limited convection near the splitter plate and wingtip. Here, pressure minima occurred in the surface pressure contours consistent with enhanced vortex-surface interaction due to vorticity straining. The central portion of the vortex had convected downstream, forming a moderate vortex arc lying near the wing surface. This limited three dimensionality was reflected in the Fig. 8 normal force contour plot as a mild disruption to the previously two-dimensional contour lines.

The gradual vortex arc was initially disrupted as visualized in Fig. 4, and confirmed by surface pressure contours in Fig. 5. Initial vortex disruptions moved farther apart, and closer to both splitter plate and wingtip, with higher nondimensional pitch rate. The two delayed leading-edge suction maxima of Fig. 7 also moved apart, shifting the inboard one closer to the splitter plate, and the outboard one closer to the wingtip as nondimensional pitch rate increased. Comparing Table 1 to Fig. 7 showed that leading-edge suction collapse preceded initial vortex disruption by approximately 1.0–2.0 nondimensional time units, and that this intervening period shortened with higher nondimensional pitch rate. Table 1 also showed that the vortex was located closer to the wing leading edge at initial disruption with increasing nondimensional pitch rate.

These correlations indicate that leading-edge suction collapse indicated the demise of pressure gradients responsible for vorticity production. Vorticity production curtailment, in turn, disrupted the vorticity sheet feeding the downstream leading-edge vortex. Acharya and Metwally<sup>16</sup> have shown that disruption of vorticity production in the leading-edge region imposes pronounced modifications upon leading-edge vortex kinematics downstream.

That portion of the vortex between the two initial vortex disruptions subsequently arched over the wing surface as visualized in Fig. 3 (frame 2,  $t_{nd} = 5.88$ ). Vortex arching kinematics in the current investigation were consistent with those visualized by Schreck et al.,<sup>11</sup> Freymuth,<sup>4</sup> and Horner et al.<sup>10</sup> Vortex arching was accompanied by suction collapse on the wing area vacated by the vortex. Here, vortex-surface separation distance increased, reducing vortex-surface interaction and attenuating suction as demonstrated by Panaras.<sup>15</sup>

Following vortex arching, the apex of the arch convected downstream at a significantly higher speed than the remainder of the vortex. Vortex convection velocity was locally accelerated when the arched portion of the vortex encountered stronger freestream influence.<sup>10,20</sup> However, vortex arch height above the wing prevented vortex convection from strongly impacting either surface pressures or normal forces.<sup>15</sup> This was indicated by the sparse and then vertical contours immediately inboard of center span in Fig. 8. Vorticity straining in the remainder of the vortex was augmented by the vortex arch and continued to amplify vortex-surface interaction, both near the splitter plate and the wingtip. This, in turn, prompted corresponding maxima in surface pressure topologies and spanwise normal force loading topologies.

At the two sites where the vortex flexed to accommodate arching, counter-rotating cells appeared at the wing surface, as visualized in Fig. 3 (frame 3,  $t_{nd} = 6.30$ ). Initially, these cells were symmetric in the spanwise direction about a line just inboard of the wing center span. Similar cell pairs have been observed under dynamic conditions by Shih,<sup>9</sup> Schreck,<sup>17</sup> and Horner et al.,<sup>10</sup> and in the static regime by Winkelmann and Barlow.<sup>18</sup> Rotational sense of the cells was consistent with that of the contiguous leading-edge vortex that had arched up over the wing surface. At this time, the leading-edge vortex near the splitter plate began to convect away from the leading edge, locally deforming the vortex. Figure 8 showed approximately equal values of normal force inboard and outboard. However, normal force had peaked and was decreasing inboard near the splitter plate while continuing to increase outboard near the wingtip.

After the symmetric pair of counter-rotating cells appeared, these cells and the associated vortex convected asymmetri-

cally. Figure 3 (frame 4,  $t_{nd} = 6.96$ ) showed that the inboard cell reached the trailing edge well in advance of the outboard one, even though both began at the same chord location. This observation is consistent with observations made by Schreck et al.<sup>11</sup> who observed accelerated vortex convection near the wing-splitter plate juncture. Inboard, vortex convection began shortly after leading-edge suction finally collapsed near the splitter plate, as recorded in Fig. 7. The influence of asymmetric convection was consistent with normal force stall times shown in Fig. 9, which showed that normal force stall occurred inboard significantly earlier than it did at outboard span stations. Asymmetric vortex convection was prompted by a combination of influences. Outboard, near the wingtip, vortex convection was retarded by pinning at the tip region as visualized by Freymuth,<sup>4</sup> and quantitatively corroborated by Robinson and coworkers.<sup>8</sup> Inboard, vortex convection was accelerated by mutual induction acting between the inboard leg of the vortex arch and the vortex image presented by the splitter plate.

Finally, Fig. 3 (frame 5,  $t_{nd} = 7.26$ ) showed the outboard portion of the leading-edge vortex began to convect downstream and away from the leading edge near the wingtip. Soon after this time Fig. 8 showed normal force reaching a maximum near the wingtip and beginning to decline. Experiments by Lorber et al.<sup>19</sup> have recorded similar lift maxima restricted to the wingtip region. Inboard, visualization showed the vortex above and behind the wing surface, but still apparently connected to the wing surface by two vortex segments emanating from the wing surface. By this time, the inboard portion of the wing had stalled and nearly reached minimum normal force.

Figure 7 showed that leading-edge suction collapse, near both the splitter plate and wingtip, was significantly delayed relative to central span locations. Outboard, downwash produced by the prominent wingtip vortex delayed leading-edge suction collapse compared to center span. Similar delays in leading-edge suction collapse inboard suggest a concentration of streamwise vorticity, of opposite sense to that at the wingtip, is also present near the wing-splitter plate juncture.

Surface pressure gradients on the wing-splitter plate configuration gave rise to localized concentrations of streamwise vorticity. Low pressures produced on the wing during pitching would induce secondary flows over the splitter plate toward the wing. Thus, streamwise vorticity would be generated and convected over the splitter plate toward the wing, collecting in the wing-splitter plate juncture. Although no streamwise vortex was observed in the juncture region, a concentration of streamwise vorticity not coalesced into a vortex would also induce downwash and preserve leading-edge suction. Juncture vortices have been visualized by Klinge et al.<sup>12</sup> near the juncture of a pitching wing-splitter plate configuration.

The amount of streamwise vorticity present at either the wingtip or the juncture dictated the influence that it exercised. In Fig. 7, leading-edge suction collapse delays were longer and extended farther inboard from the wingtip than delays near the splitter plate. This asymmetry suggests that larger amounts of streamwise vorticity were present near the wingtip than at the juncture at leading-edge suction collapse. Figure 7 also showed that leading-edge suction collapse delay was displaced closer to the wingtip and juncture with increasing nondimensional pitch rate. This is consistent with the model proposed by Luttgies and Kennedy,<sup>20</sup> wherein higher nondimensional pitch rates reduce total vorticity production and prompt more condensed vorticity distributions.

### Conclusions

A generic wing-splitter plate configuration was pitched at constant rate to angles exceeding the static stall angle. The resulting three-dimensional unsteady flowfield was characterized using dye flow visualization and unsteady surface pressure measurements. Visualized three-dimensional deformations of the leading-edge vortex were corroborated by complex

surface pressure topologies that were similarly three-dimensional in nature. Spanwise variations in normal force loading were consistent with three-dimensional vortex deformations. Mechanisms based upon vorticity dynamics were postulated to account for these observed kinematics.

The initially two-dimensional unsteady vortex rapidly underwent three-dimensional deformation along the entire wing span. Three-dimensional deformation began when vortex convection was arrested near the splitter plate and wingtip, but continued near center span. Soon, disruptions appeared in the vortex upstream boundary, and were quickly followed by vortex arching above the wing surface near center span. Subsequently, vortex convection near the splitter plate outpaced that near the tip, with the inboard portion of the vortex being shed prior to that outboard.

Vortex kinematics were driven by an identifiable set of vorticity dynamics. Streamwise vorticity accumulated near the splitter plate and wingtip. These vorticity accumulations temporarily arrested vortex convection and delayed vortex arching. Mutual induction acting between the vortex arch and the image of it presented by the splitter plate accelerated vortex convection near the splitter plate.

Spanwise normal force loading was consistent with vortex kinematics. Two-dimensional and moderately three-dimensional vortex structure yielded normal force loading that was uniform along the span. Prominently three-dimensional vortex structure prompted correspondingly nonuniform spanwise normal force loading. Normal force stall times varied substantially across the span, and were closely correlated to vortex arching or shedding.

This experiment has examined three-dimensional dynamically separated flow over a generic wing-splitter plate configuration. Many aspects of this flow have been successfully characterized and explained, though only for a limited parameter range. As such, the current investigation provides a basis for further investigations employing configurations of more practical interest and encompassing broader parameter ranges.

### Acknowledgments

The authors would like to express their gratitude to Marvin Luttgies and Michael Robinson, University of Colorado at Boulder, for many helpful discussions and suggestions.

### References

- <sup>1</sup>Adler, J., and Luttgies, M., "Three-Dimensionality in Unsteady Flow About a Wing," AIAA Paper 85-0132, Jan. 1985.
- <sup>2</sup>Ashworth, J., and Luttgies, M., "Comparisons in Three-Dimensionality in the Unsteady Flows Elicited by Straight and Swept Wings," AIAA Paper 86-2280, Aug. 1986.
- <sup>3</sup>Robinson, M., Helin, H., Gilliam, F., Russell, J., and Walker, J., "Visualization of Three-Dimensional Forced Unsteady Separated Flow," AIAA Paper 86-1066, May 1986.
- <sup>4</sup>Freymuth, P., Finaish, F., and Bank, W., "Three-Dimensional Vortex Systems of Finite Wings," *Journal of Aircraft*, Vol. 25, No. 10, 1988, pp. 971, 972.
- <sup>5</sup>Freymuth, P., "Visualizing the Connectivity of Vortex Systems for Pitching Wings," *Journal of Fluids Engineering*, Vol. 111, June 1989, pp. 217-219.
- <sup>6</sup>Gad-el-Hak, M., and Ho, C.-M., "Three-Dimensional Effects on a Pitching Lifting Surface," AIAA Paper 85-0041, Jan. 1985.
- <sup>7</sup>Lorber, P. F., "Tip Vortex, Stall Vortex, and Separation Observations on Pitching Three-Dimensional Wings," AIAA Paper 93-2972, July 1993.
- <sup>8</sup>Robinson, M., Walker, J., and Wissler, J., "Unsteady Surface Pressure Measurements on a Pitching Rectangular Wing," *Proceedings of Workshop II on Unsteady Separated Flow*, U.S. Air Force Academy, Colorado Springs, CO, 1988, pp. 225-237.
- <sup>9</sup>Shih, C., "Unsteady Aerodynamics of a Stationary Airfoil in a Periodically Varying Freestream," Ph.D. Dissertation, Univ. of Southern California, Los Angeles, CA, 1988.

<sup>10</sup>Horner, M., Addington, G., Young, J., and Luttgies, M., "Controlled Three-Dimensionality in Unsteady Separated Flows About a Sinusoidally Oscillating Flat Plate," AIAA Paper 90-0689, Jan. 1990.

<sup>11</sup>Schreck, S., Addington, G., and Luttgies, M., "Flow Field Structure and Development Near the Root of a Straight Wing Pitching at Constant Rate," AIAA Paper 91-1793, June 1991.

<sup>12</sup>Klinge, J., Schreck, S., Robinson, M., and Luttgies, M., "Three-Dimensional Flow Field Kinematics near the Root of an Oscillating Wing," AIAA Paper 91-3264, Sept. 1991.

<sup>13</sup>Schlichting, H., *Boundary Layer Theory*, 7th ed., McGraw-Hill, New York, 1979, p. 383.

<sup>14</sup>Walker, J., Helin, H., and Chou, D., "Unsteady Surface Pressure Measurements on a Pitching Airfoil," AIAA Paper 85-0532, March 1985.

<sup>15</sup>Panaras, A., "Numerical Modeling of the Vortex/Airfoil Interaction," *AIAA Journal*, Vol. 25, No. 1, 1987, pp. 5-11.

<sup>16</sup>Acharya, M., and Metwally, M., "Evolution of the Unsteady Pressure Field and Vorticity Production at the Surface of a Pitching Airfoil," AIAA Paper 90-1472, June 1990.

<sup>17</sup>Schreck, S. J., "Experimental Investigation of the Mechanisms Underlying Vortex Kinematics in Unsteady Separated Flows," Ph.D. Dissertation, Univ. of Colorado, Boulder, CO, 1989.

<sup>18</sup>Winkelmann, H., and Barlow, J., "Flowfield Model for a Rectangular Planform Wing Beyond Stall," *AIAA Journal*, Vol. 18, No. 8, 1980, pp. 1006-1008.

<sup>19</sup>Lorber, P., Covino, A., and Carta, F., "Dynamic Stall Experiments on a Swept Three-Dimensional Wing in Compressible Flow," AIAA Paper 91-1795, June 1991.

<sup>20</sup>Luttgies, M., and Kennedy, D., "Initiation and Use of Three-Dimensional Unsteady Separated Flows," *Proceedings of Workshop II on Unsteady Separated Flow*, U.S. Air Force Academy, Colorado Springs, CO, 1988, pp. 211-222.



**AIAA 94-2259**

**Navier-Stokes Simulation of Wing-Tip  
and Wing-Juncture Interactions for a  
Pitching Wing**

**R. W. Newsome  
Frank J. Seiler Research Laboratory  
USAF Academy, CO**

**25th AIAA Fluid Dynamics  
Conference**

**June 20-23, 1994 / Colorado Springs, CO**

# Navier-Stokes Simulation of Wing-Tip and Wing-Juncture Interactions For a Pitching Wing

Richard W. Newsome\*  
Frank J. Seiler Research Laboratory  
United States Air Force Academy CO 80840-6272

## Abstract

The three-dimensional Navier-Stokes equations were solved for the unsteady flow about a generic wing-wall configuration for constant rate pitching from  $0^\circ$  to  $60^\circ$  angle of attack at non-dimensional pitch rates of 0.2 and 0.1. The configuration consisted of a straight wing with a NACA 0015 cross section bounded on one end by a flat splitter plate orthogonally attached to the wing root and by a free tip on the other. The numerical results compare favorably with experimental flow visualization and surface pressure measurements, particularly at the higher pitch rate. The strong interaction of the wing-tip vortex with the dynamic stall vortex and the resulting amplification of the normal force near the wing tip are predicted in good agreement with the experiment. In contrast, the viscous interaction at the wing-wall juncture is much less significant in altering the overall force distribution on the wing. Spanwise and chordwise vorticity contours and instantaneous limiting streamlines are combined with surface pressure and normal force plots to provide a detailed understanding of the temporal evolution of the massively separated, three-dimensional, unsteady flow structure.

## Introduction

When a wing or other lifting surface is rapidly pitched beyond its static stall angle of attack, the motion is accompanied by intense vorticity generation at the wing surface. Due to a disparity between the rate of production and the rate of transport, the vorticity accumulates on the leeward side of the wing near the leading-edge and the boundary layer remains attached well beyond the point at which separation occurs under static conditions. Eventually, the boundary layer separates in response to an increasingly adverse pressure gradient or the upstream propagation of a trailing-edge separation and the concentrated vorticity rolls up to form a discrete vortex, the dynamic stall vortex, which then detaches and convects downstream over the upper surface of the wing. The accumulated vorticity in the attached boundary layer and, later, the dynamic stall vortex alters the circulation and the resulting pressure distribution on the wing, producing transient forces and moments that are much larger than those realized under static conditions. The entire process, known as dynamic stall, is important in many aerodynamic applications. The dynamic lift overshoot that accompanies the formation of

the dynamic stall vortex potentially can be exploited to greatly enhance the maneuvering performance of combat aircraft. Dynamic stall is also a limiting factor in the performance of helicopter rotors and wind turbines due to vibration and fatigue problems induced by the large transient aerodynamic loads. The development of control methodologies that effectively exploit dynamic stall to enhance aerodynamic performance as well as the modification or avoidance of adverse unsteady effects require a thorough understanding of the physics of unsteady separated flows.

Reference 1 provides a recent overview and assessment of the issues related to dynamic stall and unsteady separated flows. As a result of extensive experimental and computational study, an understanding of many aspects of two-dimensional dynamic stall is relatively mature. A similar understanding of three-dimensional dynamic stall is at a much earlier stage of development. A finite wing, for example, admits a variety of unsteady flow interactions not present in the two-dimensional case including wing-tip effects, wall effects, and spanwise flow. These three-dimensional interactions significantly complicate the two-dimensional dynamic stall model described earlier.

Robinson and Wissler<sup>2</sup> experimentally studied the large-amplitude pitching motion for a straight rectangular wing and found that the interaction of the wing-tip and dynamic stall vortices significantly amplified the sectional lift coefficients near the wing tip. Schreck et al.<sup>3</sup>, Klinge et al.<sup>4</sup>, and Schreck and Helin<sup>5</sup> investigated the unsteady separated flow for a finite wing undergoing sinusoidal and constant rate pitching. Both surface pressure measurements and flow visualization showed significant spanwise variation with respect to leading-edge vortex cross section, convection rate, and normal force coefficient, corresponding to prominent wing-tip and wing-juncture interactions. Lorber<sup>6</sup> examined the wing-tip interaction for a pitching finite wing at higher Mach and Reynolds numbers and noted similar trends in wing-tip force amplification and dynamic stall propagation patterns.

Numerous two-dimensional Navier-Stokes solutions have been presented for an airfoil undergoing either oscillatory or constant rate pitching motions. Representative works include those of Visbal<sup>7-10</sup>, Rumsey and Anderson<sup>11</sup>, Patterson and Lorber<sup>12</sup>, Ghia et al.<sup>13</sup>, and Knight and Choudhuri<sup>14</sup>. Three-dimensional, Navier-Stokes solutions for the unsteady flow generated by the forced motion of a finite wing include the work of Guruswamy<sup>15</sup> for a swept wing in pitching motion,

\*Lt. Col., USAF; Chief, Aerospace Sciences Division  
Associate Fellow, AIAA

This paper is declared a work of the U.S. Government and is not subject to copyright protection in the United States

Chaderjian and Guruswamy<sup>16</sup> and Yang and Przekwas<sup>17,18</sup> for the sinusoidal oscillation of rectangular and forward-swept wings, Visbal<sup>19</sup> and Visbal and Gordnier<sup>20</sup> for a pitching delta wing, and Gordnier<sup>21</sup> for a rolling delta wing.

In Ref. 22, Newsome numerically studied the three-dimensional, unsteady, separated flow in the juncture of a wing-wall configuration corresponding to the experimental model of Schreck et al.<sup>3,5</sup>. The numerical results provided a detailed view of the influence of the wall in inducing a complex spanwise secondary flow on the wing in the juncture region. Because interest was focused on the wing juncture, the wing-tip interaction was not modeled, thus limiting a comparison with the experiment to the juncture region. However, the experimental results of Schreck<sup>3,5</sup> and others<sup>2,6</sup> clearly show that the wing-tip flow is the predominant three-dimensional interaction. The present calculations model both the wing tip and wing juncture but focus on wing tip and the interaction of the wing-tip vortex and the dynamic stall vortex leading to locally amplified sectional force coefficients in the tip region. Two different pitch rates are considered for large amplitude pitching to 60° angle of attack, corresponding to maneuvers representative of those likely to be employed by future combat aircraft.

### Governing Equations

The governing equations are the three-dimensional, compressible, time-dependent, Navier-Stokes equations, written in generalized coordinates and conservation form

$$\frac{\partial(\hat{Q})}{\partial \tau} + \frac{\partial(\hat{F} - \hat{F}_v)}{\partial \xi} + \frac{\partial(\hat{G} - \hat{G}_v)}{\partial \eta} + \frac{\partial(\hat{H} - \hat{H}_v)}{\partial \zeta} = 0 \quad (1)$$

where

$$\hat{Q} = \frac{Q}{J} = \frac{1}{J} \begin{bmatrix} \rho \\ \rho u \\ \rho v \\ \rho w \\ E \end{bmatrix} \quad \hat{F} = \frac{1}{J} \begin{bmatrix} \rho U \\ \rho U u + \xi_x p \\ \rho U v + \xi_y p \\ \rho U w + \xi_z p \\ (E + p)U - \xi_i p \end{bmatrix} \quad (2a)$$

$$\hat{G} = \frac{1}{J} \begin{bmatrix} \rho V \\ \rho V u + \eta_x p \\ \rho V v + \eta_y p \\ \rho V w + \eta_z p \\ (E + p)V - \eta_i p \end{bmatrix} \quad \hat{H} = \frac{1}{J} \begin{bmatrix} \rho W \\ \rho W u + \zeta_x p \\ \rho W v + \zeta_y p \\ \rho W w + \zeta_z p \\ (E + p)W - \zeta_i p \end{bmatrix} \quad (2b)$$

and  $\rho$  is density,  $(u, v, w)$  are Cartesian velocities in the inertial coordinate frame,  $E$  is the total energy per unit volume,  $p$  is pressure

$$p = (\gamma - 1) \left[ E - \frac{1}{2} \rho (u^2 + v^2 + w^2) \right] \quad (3)$$

and contravariant velocities  $(U, V, W)$  are

$$\begin{aligned} U &= \xi_x u + \xi_y v + \xi_z w + \xi_t \\ V &= \eta_x u + \eta_y v + \eta_z w + \eta_t \\ W &= \zeta_x u + \zeta_y v + \zeta_z w + \zeta_t \end{aligned} \quad (4)$$

The generalized coordinates  $(\xi, \eta, \zeta)$  correspond to the directions along the wing span ( $\xi$ ), the wing chord circumferential direction ( $\eta$ ), and the direction normal to the wing surface ( $\zeta$ ). In the thin-layer assumption, only derivatives normal to non-slip wall surfaces are retained, greatly simplifying the viscous terms in Eqn. 1. Consistent with the results of Ref. 22 in which the effects of the viscous cross derivative terms were found to be small and then confined to the juncture boundary layer region, only the thin layer terms in the two viscous directions ( $\xi, \zeta$ ) are retained. Thus  $\partial \hat{G}_v / \partial \eta = 0$  and the viscous term,  $\hat{F}_v$ , may be written as

$$\hat{F}_v = \frac{M_\infty \mu}{Re_\infty J} \begin{bmatrix} 0 \\ |\nabla \xi|^2 u_\xi + \frac{1}{3} \xi_x (\nabla \xi \cdot \bar{u}_\xi) \\ |\nabla \xi|^2 v_\xi + \frac{1}{3} \xi_y (\nabla \xi \cdot \bar{u}_\xi) \\ |\nabla \xi|^2 w_\xi + \frac{1}{3} \xi_z (\nabla \xi \cdot \bar{u}_\xi) \\ |\nabla \xi|^2 \left[ \frac{1}{2} (\bar{u} \cdot \bar{u})_\xi + \frac{(c^2)_\xi}{P_r(\gamma - 1)} \right] \\ + \frac{1}{3} U (\nabla \xi \cdot \bar{u}_\xi) \end{bmatrix} \quad (5)$$

A corresponding expression for  $\hat{H}_v$  is obtained by substituting  $\zeta$  and  $W$  in place of  $\xi$  and  $U$  in Eqn. 5. In the above, the equations are non-dimensionalized in terms of free stream density,  $\rho_\infty$ , and sound speed,  $c_\infty$ .  $M_\infty$  and  $Re_\infty$  are the freestream Mach number and Reynolds number and  $P_r$  is the Prandtl number. Equation 1 is closed by Stoke's hypothesis for bulk viscosity and Sutherland's law for molecular viscosity ( $\mu$ ). All calculations are for laminar flow.

### Computational Method

NASA Langley's computer code, CFL3D<sup>23,24</sup>, was utilized as the flow solver. The code is an upwind-biased, finite-volume, approximate factorization algorithm employing either Van Leer's flux vector splitting or Roe's flux difference splitting. Details of the algorithm are given in Ref. 23. In Ref. 22, several modifications were made to improve the accuracy and efficiency of the code for unsteady applications. The diagonalized algorithm was generalized for unsteady flows with moving grids by in-

cluding the time-dependent transformation derivatives,  $\xi, \eta, \zeta$ , in the definition of the eigenvalues corresponding to the diagonalized operators. To ensure temporal conservation and achieve second order time accuracy, ( $\phi = 1/2$ ), three point backward time differencing and a subiteration capability were added to the baseline algorithm. The resulting algorithm, used in the present calculations, solves directly for the primitive variables  $q = (\rho, u, v, w, p)^T$  as:

$$\left[ \frac{(1+\phi)}{J\Delta t} \mathbf{I} + \delta_\zeta \lambda_\zeta \right] \delta w^* = \mathbf{T}_\zeta^{-1} \left[ \frac{(1+\phi)}{J\Delta t} (Q^{n+1,m} - Q^n) - \frac{\phi}{J\Delta t} \Delta Q^{n-1} + \hat{R}^{n+1,m} \right] \quad (6a)$$

$$\delta q^* = \mathbf{M}^{-1} \mathbf{T}_\zeta \delta w^* \quad \left[ \frac{(1+\phi)}{J\Delta t} \mathbf{I} + \delta_\eta \lambda_\eta \right] \delta w^* = \frac{(1+\phi)}{J\Delta t} \mathbf{T}_\eta^{-1} \mathbf{M} \delta q^* \quad (6b)$$

$$\delta q^* = \mathbf{M}^{-1} \mathbf{T}_\eta \delta w^* \quad \left[ \frac{(1+\phi)}{J\Delta t} \mathbf{I} + \delta_\zeta \lambda_\zeta \right] \delta w^* = \frac{(1+\phi)}{J\Delta t} \mathbf{T}_\zeta^{-1} \mathbf{M} \delta q^* \quad \delta q^{n+1,m} = \mathbf{M}^{-1} \mathbf{T}_\zeta \delta w^* \quad (6c)$$

$$q^{n+1} = q^{n+1,m+1} = q^{n+1,m} + \delta q^{n+1,m}$$

In the above,  $\mathbf{M} = \partial Q / \partial q$ ,  $J$  is the Jacobian of the coordinate transformation,  $R$  is the steady state residual,  $\lambda$  and  $\mathbf{T}$  are the eigenvalues and eigenvectors of the inviscid flux Jacobians, and  $\delta w$  is a temporary variable defined above by context. To obtain second order temporal accuracy, an inner iteration,  $m$ , at the  $n+1$  time level is employed such that Eqns. 6a, 6b, 6c are solved iteratively until the right hand side of Eqn. 6a. (corresponding to the residual of the unsteady equation) is less than a prescribed tolerance, usually two to three orders of magnitude below the steady state residual,  $R$ .

Roe's flux difference splitting was used to evaluate the inviscid terms. A third-order upwind-biased interpolation of the state variables,  $q$ , was used to obtain the required flux values at cell interfaces. Second-order central differencing was used to evaluate the viscous terms.

The grid was rigidly attached to the wing-wall configuration and rotated with the configuration without deformation. The Navier-Stokes equations were solved with respect to inertial coordinates at the coordinate locations determined by the moving grid. On the wing and wall surfaces, no slip boundary conditions were applied for the moving surfaces. An adiabatic wall was assumed and an expression for the normal pressure gradient in terms of the wall surface acceleration provided surface pressure. On the wing root boundary beyond the wall surface, symmetry conditions corresponding to an inviscid slip wall were im-

posed. The far field boundary condition specification was based upon Riemann invariants for one-dimensional flow normal to the far field boundary. For the O-grid wing-tip boundary and the C-grid wake cut, continuation boundary conditions were applied implicitly by reordering the approximately factored matrix equations (Eqn. 6a and Eqn. 6c) so that these boundaries are treated as regular interior points. All other boundary conditions were applied explicitly. Unsteady pitching flow solutions were started from a nominally steady solution at zero degrees angle of attack. Calculations were performed on the Cray C90 computer at the U.S. Army Corps of Engineers Waterways Experiment Station at Vicksburg, Mississippi.

## Experiment

Schreck<sup>3-5</sup> experimentally studied the flow for a straight wing having a NACA 0015 cross-section and a rectangular planform. The wing chord and span were 6 and 12 inches respectively. A circular splitter plate 12 inches in diameter was orthogonally attached to the root of the wing. The wing tip was a square end with no rounding. The model was pitched from 0 to 60° about the  $1/4$  and  $1/3$  chord locations for five non-dimensional pitch rates,  $\dot{\Omega}^+ = \dot{\Omega} C / (M_\infty c_\infty) = 0.01, 0.02, 0.05, 0.10, 0.20$ . In the above,  $\dot{\Omega}$  is the pitch rate in rad/sec,  $C$  is the wing chord and  $M_\infty$  and  $c_\infty$  are the freestream Mach number and speed of sound. The configuration was studied in the wind tunnel and water tunnel facilities of the F. J. Seiler Research Laboratory and the USAF Academy, combining surface pressure measurements and flow visualization to obtain a more complete understanding of the three-dimensional, unsteady vortex dynamics. The wind tunnel model was instrumented to obtain surface pressure at fifteen chordwise locations on both the upper and lower wing surfaces at 11 spanwise locations (0.0, 0.05, 0.1, 0.15, 0.25, 0.375, 0.5, 0.625, 0.7, 0.75, 0.8). All pressure readings were ensemble averaged over 20 different pitch cycles. The test section velocity,  $U_\infty = 30$  ft/sec, produced a Reynolds number based upon chord of about 69,000 and a freestream Mach number,  $M_\infty = 0.026$ . In addition to surface pressure measurements, water tunnel flow visualization was accomplished by injecting dye into the boundary layer at the leading edge along the span of the wing. The corresponding chord Reynolds number was 56,000.

During most of the pitching motion, flow visualization revealed a large, energetic, leading-edge vortex that extended over a broad area of the wing planform. Both surface pressure and flow visualization data show that the leading-edge vortex underwent significant three-dimensional alteration in convection rate and cross-section. These modifications were accompanied by prominent spanwise variations in stall angle and normal force coefficient. Three distinct spanwise regions were identified corresponding to the wing-tip, wing-juncture, and center

span regions. The wing-tip vortex successfully maintained leading-edge suction well beyond regions further inboard. The leading-edge vortex remained anchored to the wing tip until late in the pitching cycle when it detached and convected downstream to produce a broad pressure minimum on the outboard wing planform. Overall normal force stall was associated with the departure of the leading-edge vortex from the wing tip. The flow near the wing-wall juncture was initially more diffuse due to the presence of the wall. Later, however, the pitching motion induced steep transverse pressure gradients in the juncture region. The most prominent feature associated with the center span region was the tendency of the leading-edge vortex, for certain test conditions, to arch up and form a horseshoe-shaped vortex stretching from the "pinned" wing-tip region to the splitter-plate wall. Two counter-rotating cells were observed on the wing surface near the base of the legs of the arched vortex. All of the effects described above were more pronounced at higher non-dimensional pitch rates.

### Numerical Results

Three-dimensional Navier-Stokes solutions were computed for the wing-wall configuration pitching about the quarter chord for non-dimensional pitch rate constants of  $\dot{\Omega}_0^+ = 0.2$  and 0.1. An analytical expression for the non-dimensional pitch rate, similar to that of Visbal<sup>7</sup>, was derived as a best fit to the experimental pitch rate schedule

$$\dot{\Omega}^+ = \dot{\Omega}_0^+ \left( 1 - e^{-4.6t^*/t_1^+} - e^{-4.6(t_1^+ - t^*)/t_2^+} \right) \quad (7)$$

where the nondimensional time,  $t^+ = tc_\infty/C$ , is valid over the range  $0 \leq t^+ \leq t_f^+$ . In the above,  $t_f^+$  is the non-dimensional end time, and  $t_1^+$  and  $t_2^+$  are constants chosen to match the experimental pitch rate time history.

	$t_f^+$	$t_1^+$	$t_2^+$
$\dot{\Omega}_0^+ = 0.2$	33.0	12.6133	18.7648
$\dot{\Omega}_0^+ = 0.1$	53.75	2.94423	3.45023

Table 1 Constants for Pitch Rate Schedule, Eqn. 7

Figure 1 provides a comparison of the resulting pitch angle schedule (obtained by integrating Eqn. 7) with the experimental schedule.

Experimentally, both the wind and water tunnel flow regimes correspond to incompressible flow. Computationally, a higher Mach number ( $M_\infty = 0.2$ ) was specified in order not to degrade the convergence of the compressible flow solver. Even at this low Mach number, compressibility effects are significant for the pitch rates considered and do impact the comparison of experimental

and computational results. Experimentally, no information was available concerning the turbulent state of the flow. As a practical matter, appropriate turbulence models for massively separated, three-dimensional, unsteady flows do not currently exist. Accordingly, the flow was assumed to remain laminar and calculations were made at the lower experimental Reynolds number of 56,000 used in the water tunnel flow visualization studies.

Fig. 2 shows the baseline grid for the wing-wall configuration. The grid topology is a C grid along the chord and a 1/2 O grid along the wing span. Two modifications were made to the configuration to simplify the grid generation process. First, the wing tip was rounded with a circular tip cap corresponding to the local chord thickness. Second, the aft end of the circular splitter plate was changed to a rectangular shape to conform to the C-grid topology. The grid extended 15 chords outward and consisted of 213 circumferential points, 75 radial points, and 61 spanwise points. It was constructed to be nearly orthogonal to the wing and splitter plate surfaces and to conform to the semi-circular outer boundary of the splitter plate. The minimum cell-centered spacing adjacent to the wing and wall surfaces was set at  $\Delta s/C = 0.00005$ , corresponding to roughly 17-18 points in the steady state boundary layer. The wing surface was defined by 152 circumferential grid points.

### Numerical Accuracy

Because of the large resource requirements for three-dimensional unsteady solutions, preliminary temporal and spatial accuracy assessments were accomplished in two dimensions for the equivalent pitching airfoil. Due to the numerous approximations made in the implicit operators, the algorithm represented by Eqn. 6 is not unconditionally stable. For the three-dimensional grid shown in Fig. 2, the global unsteady time step size was limited by the local stability limit of the grid volumes at the trailing edge of the wing tip. However, this stability-limited time step was still less restrictive than that required for temporal accuracy, even for two-dimensional flows. Thus a more accurate scheme employing larger but more expensive time steps may be more efficient than a less accurate scheme requiring more but less expensive time steps. Figures 3a and 3b demonstrate this point for a two-dimensional airfoil pitching about the quarter chord at a non-dimensional pitch rate of  $\dot{\Omega}^+ = 0.2$  according to the pitch rate schedule of Eqn. 7. The grid was identical to the three-dimensional grid at the wing root. Figure 3a compares solutions employing three point backward time differencing and subiteration to achieve second order temporal accuracy. The least expensive option,  $\Delta t^+ = 0.002$ , employing two subiterations, correctly resolved the temporal dynamics of the flow. Figure 3b shows the results of first-order time-accurate solutions without subiteration for the same time step sizes as Fig. 3a and for time step sizes four times

smaller, corresponding to an equivalent computational cost of a single larger time step with three subiterations. There is a significant amount of scatter in the results with the smaller time steps consistently approaching but not equaling the more accurate solutions with subiteration. In this particular case, the second-order solution with two subiterations was more accurate than the first-order solution without subiteration but using a time step eight times smaller. The first-order solution was obtained at a computational cost 2.66 (8/3) times higher. Furthermore, since second-order accuracy was obtained with the diagonal algorithm which is 2.6 times less expensive than the block inversion algorithm, the total improvement in code efficiency, compared to the first-order, time-accurate, block inversion algorithm, was nearly a factor of seven. In all the results presented in Fig. 3, the C-grid wake boundary condition was updated implicitly. As noted in Ref. 22, the rapid convergence of the subiteration force coefficient histories was not achieved unless this boundary condition was updated implicitly.

The effect of grid resolution on the two-dimensional solution is shown in Fig. 4 in which the baseline 213x75 grid was uniformly refined to produce a 425x149 grid. A comparison of normal and tangential force coefficients indicates that the baseline two-dimensional grid accurately follows the overall fine grid prediction but tends to smooth the smaller fluctuations present in the fine grid calculation. Although finer grid resolution is desirable, when extrapolated to three-dimensional unsteady flow, this level of grid refinement greatly increases computer memory and processing requirements for relatively modest accuracy improvements. The three-dimensional grid was constructed to provide equal viscous resolution on the wing and wall surfaces and to provide fine spanwise resolution of the wing-tip region.

### Unsteady Flow - Initial Condition

The pitching wing computations were initiated from a nominally converged steady state solution at  $0^\circ$  angle of attack. In fact, the flow over a NACA 0015 airfoil at the Reynolds numbers considered (56,000-69,000) does not exhibit a steady state solution, but rather is characterized by periodic vortex shedding and a lift coefficient that oscillates around a zero mean value. The computation developed as an attached flow solution, followed by trailing edge boundary layer separation, propagation of the separated region upstream, and eventually, asymmetric separation and periodic vortex shedding. In the experiment, differences in starting conditions were minimized by ensemble averaging data over 20 pitch cycles. In the computation, a phase-neutral starting solution was obtained by terminating the calculation after the forward propagation of the separated region but prior to the development of significant flow asymmetry. Figure 5 shows the limiting streamlines on the upper surface of the wing and the

splitter plate at  $0^\circ$  angle of attack. The primary separation line is evident at a chord location of  $x/C \approx 0.55$ . Near the juncture, the separation line was swept forward to a chord location  $x/C \approx 0.29$ . The distinctive recirculation pattern observed downstream of the separation line near the juncture was produced by a forward unstable node, a trailing stable focus and two nearby saddle points. Additionally, the flow separated on the splitter plate at a position 0.1 chord upstream of the wing leading edge, producing a "horseshoe vortex" that wrapped around the wing and was then convected downstream, introducing longitudinal vorticity into the juncture region. At the wing tip, separation was suppressed by the spanwise flow around the tip and the separation line was displaced almost to the wing trailing edge.

### Unsteady Flow - Pitch Rate of $\dot{\Omega}^+ = 0.2$

For the pitching motion of a three-dimensional wing, the influence of the wing-tip vortex on the dynamic stall vortex is the most interesting and most significant interaction in terms of its effect on the forces and moments imparted on the wing. As noted by Lorber<sup>6</sup>, before stall, the wing-tip vortex lowers the effective angle of attack, reduces lift, and delays the onset of stall. During stall, the interaction of the wing-tip vortex prolongs the residence of the dynamic stall vortex on the wing, and increases the unsteady increments to lift, drag, and pitching moment.

The wing-splitter plate configuration was pitched from  $0^\circ$  to  $60^\circ$  angle of attack according to the pitch rate schedule of Eqn. 7 for  $\dot{\Omega}^+ = 0.2$ , starting from the initial solution shown in Fig. 5. A constant non-dimensional time step of  $\Delta t^+ = 0.002$  with two subiterations per time step was maintained throughout the pitch cycle. Figures 6, 8, and 9 graphically depict the evolution of the unsteady flow field on the lee side of the wing. In Fig 6, contours of constant vorticity magnitude at nine spanwise stations ( $y/C = 0.05, 0.25, 0.50, 0.75, 1.0, 1.25, 1.50, 1.75, 2.0$ ) are plotted by slicing the three-dimensional vorticity field. Fig. 8 focuses on the wing-tip region, displaying vorticity magnitude contours at five chordwise planes ( $x/C = 0.05, 0.25, 0.5, 0.75, 1.0$ ). Fig. 9 displays the much larger surface vorticity magnitudes on the wing and splitter plate. Fig. 6 provides a good view of the global flow features. At  $10^\circ$  angle of attack, the primary separation, originally near mid chord, has propagated further forward and, at  $20^\circ$ , reached the wing leading edge. At  $30^\circ$ , the dynamic stall has formed and extends spanwise from the wing root to a position,  $y/C \approx 1.5$ . At  $40^\circ$ , the dynamic stall vortex appears bowed, with maximum displacement above the wing midspan, curving downward toward the wing root and wing tip. Near the center span, secondary and tertiary vortices, characteristic of the two-dimensional pitching airfoil are evident. At the tip, the dynamic stall vortex formation was suppressed by the wing-tip vortex. At  $50^\circ$  and  $60^\circ$ , the dynamic stall vortex near the wing root that

previously lagged center span propagation has accelerated to a downstream position beyond the center span. As the wing was pitched to 60° angle of attack, the position of the dynamic stall vortex varied uniformly with span from a "pinned" position at the wing tip to a position well downstream at the wing root. Figure 7 presents water tunnel flow visualization results at 40°, 51°, and 59° angles of attack for the same flow conditions (pitch rate, pitch axis, and Reynolds number). The photographs show that the simulation accurately predicted the principal flow features. In particular, the photographs confirm the bowed appearance of the dynamic stall vortex at 40°, the accelerated convection near the wing root at 50° and 60°, and the vortex "pinning" at the wing tip.

As mentioned previously, a rounded tip was used for the computations while a square tip was used in the experiment. The primary motivation for this change was a desire to simplify the grid generation process and to model the computational domain with a single grid in which all interior boundary conditions were updated implicitly. In contrast to the square wing tip, the separation line for the wing-tip vortex was determined by the boundary layer dynamics and not fixed at the sharp wing-tip edge. Lorber<sup>6</sup> experimentally compared rounded and square wing-tip caps and found that, in the immediate vicinity of the wing tip, the square tip cap produced higher unsteady loads presumably because of a more concentrated wing-tip vortex. Globally, the difference in the tip geometry is expected to be small. In any event, the experimental data of Schreck<sup>3,5</sup> did not include surface pressure measurements beyond the  $y/C = 1.6$  span location so there were no measurements to compare with in the immediate tip region. Figure 8 shows the development of the wing-tip vortex and its effect upon the dynamic stall vortex. At 10°, the wing-tip vortex first appeared at the wing trailing edge. With increasing angle of attack, it propagated forward and grew in size. The effect on the dynamic stall vortex is quite evident. At 30° and 40° angle of attack, the flow at the leading edge near the wing tip remained attached with the wing-tip vortex effectively terminating and "pinning" the dynamic stall vortex to the wing tip. The flow did not fully separate at the first chordwise station until the wing reached 60° angle of attack. It is interesting to note that the flow visualization results of Fig. 7 also show the dynamic stall vortex terminated inboard of the wing tip at 40° as predicted by the computation.

Figures 9 and 10 examine the surface vorticity and instantaneous limiting streamlines on the wing surface. Throughout the pitching cycle, the highest levels of vorticity generation occurred at the wing leading edge. For the lower angles of attack, this vorticity was relatively uniform along the wing span. However, at 30° and beyond, the wing-tip vortex forced the leading-edge flow to remain attached near the tip, increasing the intensity of vorticity generation in this region. At 20°, numerous

spanwise vorticity streaks are evident. Comparison with Fig. 10 shows that these streaks were the result of numerous small-scale separations and reattachments in the wing midspan region. At 30°, a strong ridge of concentrated vorticity can be seen along the entire span of the wing from the wing-tip leading edge to the wing root. This ridge is associated with the separation line of the dynamic stall vortex. At 40° and 50°, this ridge weakened near the wing root as the dynamic stall vortex propagated away from the wing. At 20°, 30°, and 40°, there was another strong vorticity region associated with the secondary separation of the wing-tip vortex. At 50°, these two vorticity concentrations apparently merged and, at 60°, disappeared as the flow was completely separated over the entire wing surface.

Instantaneous limiting streamlines provide a final representation of the three-dimensional unsteady flow structure on the wing surface and, through inference, the flow field above the surface. Instantaneous limiting streamlines are obtained by "freezing" the unsteady flow field at a particular time instant and integrating the surface trajectories of massless particles introduced at a limiting distance above the wing surface. The frame of reference adopted here is the body fixed frame that rotates with the wing about the 1/4 chord position. Considerable research<sup>25,26</sup> has been devoted to the identification of critical points and the establishment of topological rules which govern to type and connectivity of critical points as an aid to understanding three-dimensional flow separation. Interest here is restricted to identifying lines of separation (S) upon which other limiting streamlines converge and lines of reattachment (R) from which other limiting streamlines diverge. In Fig. 10, the limiting streamlines are plotted on a flooded surface map of total pressure loss  $\Delta P_t / P_t$ , a property directly related to entropy and, consequently, to vorticity. The limiting streamlines reinforce many of the flow features already identified. In particular, the limiting streamlines clearly show the movement of the primary separation toward the leading edge and the concurrent formation and forward propagation of the wing-tip vortex. At 30° angle of attack, the curved lines of separation and reattachment associated with the "pinning" of the dynamic stall vortex are obvious. The wing-tip vortex and the chordwise vortical structures were separated by a line of reattachment that extended from the wing tip inward toward the trailing edge. Figure 10 clearly shows that the regions of high vorticity production and total pressure loss evident in both Figs. 9 and 10 correspond to separation lines. In addition to these primary features, both the wing-tip vortex and chordwise vortical structures were characterized by very complex patterns of flow separation and reattachment.

A comparison of the computed and experimental pressure coefficients is provided in Fig. 11. The comparison is limited to spanwise locations less than  $y/C = 1.6$ , the last

station at which experimental measurements were taken. The computation correctly predicted all primary flow features including the suction pressure ridge seen at  $30^\circ$  incidence along the span of the wing resulting from the formation of the dynamic stall vortex. At  $40^\circ$ , both the computation and experiment show the downstream propagation of this ridge except at the wing tip where propagation was delayed and the suction pressure minimum intensified due to the interaction of the dynamic-stall and wing-tip vortices. At  $50^\circ$  and beyond, the computation and experiment show the weakening and disappearance of the low suction pressure region from the wing midspan to wing root as the dynamic stall vortex propagated further away from the wing. Figure 12 presents a similar comparison of the computational and experimental normal force coefficients. The two results are in good agreement regarding the location and shape of the broad region in which normal force was amplified due to vortex interaction as well as a much smaller normal force amplification near the wing root from  $35^\circ$  to  $45^\circ$  angle of attack. However, the computation appears to underpredict the strength of the suction pressure minimum and the corresponding normal force amplification. This underprediction is most likely caused by inadequate grid resolution or compressibility effects. A two-dimensional grid resolution study (Fig. 4) showed that further grid enhancement did not significantly change the intensity of the pressure minimum or increase the predicted normal force coefficient. However, it is well known<sup>12,27</sup> that compressibility decreases the peak suction pressure and unsteady force amplification when compared to values for very low Mach number or incompressible flows. For the computed freestream Mach number of 0.2, local Mach numbers in the wing-tip region near the leading edge were well into the compressible range ( $M \geq 0.65$ ), thus supporting the hypothesis that compressibility was the factor most responsible for the underprediction.

Although the normal force amplification near the wing tip is easily traced to the interaction of the wing-tip and dynamic-stall vortices, the source of the smaller normal force local maximum near the wing root is less obvious. To assess viscous wall effects at the wing juncture, a computation was made in which the viscous wall boundary was modeled as an inviscid surface on a grid that did not provide spanwise viscous resolution of the splitter plate wall. The grid was otherwise identical to the baseline grid. In this case, the normal force coefficient showed no evidence of amplification near the wall. Additionally, the dynamic stall vortex was not bowed inward toward the wing surface in the juncture region as in the viscous wall case. Both features appear to be consequences of three-dimensional viscous interaction. Further evidence for this hypothesis is provided in Fig. 13 which examines the velocity field in the wing juncture under the dynamic-stall vortex at a time corresponding to a  $35^\circ$  pitch angle. This particular angle of attack was near the point at which the

wing root suction pressure was a minimum. Both three-dimensional and surface tangent velocities are shown for a chordwise slicing plane. The surface tangent velocities, in particular, show a well developed region of longitudinal vorticity in the juncture. Apparently, this additional vorticity in the juncture region increased the vortex strength and the suction pressure under the vortex in comparison with spanwise stations further outboard. This longitudinal vorticity also pulled the dynamic stall vortex inward toward the wing surface near the juncture. Both effects would act to intensify the local suction pressure minimum and increase the sectional normal force coefficient near the wing root. The same phenomenon was also observed in earlier calculations that modeled the wing juncture but not the wing tip.<sup>22</sup>

Figure 14 compares the overall normal, tangential, and lift force coefficients generated by the two-dimensional airfoil and the three-dimensional wing. As expected, over most of the pitching motion, the finite wing force coefficients were less than those of the airfoil because the tip vortex lowered the effective angle of attack near the wing tip. Above  $50^\circ$ , however, because the wing-tip vortex "pinned" the dynamic stall vortex to the tip, both the lift and normal force coefficients of the finite wing were higher than the airfoil.

#### Unsteady Flow - Pitch Rate of $\dot{\Omega}^+ = 0.1$

A second computation was made for the lower pitch rate of  $\dot{\Omega}^+ = 0.1$ . In general, the lower pitch rates are more difficult to compute.<sup>12</sup> At higher pitch rates, the vigorous forcing motion produces an inertially dominated flow that is less sensitive to secondary effects. In contrast, at lower pitch rates, relatively small inaccuracies in the prediction of critical events, when magnified over the larger time scale, can result in significant differences in the global flow features as well as flow details.

The  $\dot{\Omega}^+ = 0.1$  pitch rate case used the same grid and initial condition as the  $\dot{\Omega}^+ = 0.2$  case. The pitch rate schedule was again governed by Eqn. 7 with the appropriate constants for the lower pitch rate. A larger time step,  $\Delta t^+ = 0.003$  with two subiterations, was used after a comparison with the smaller time step,  $\Delta t^+ = 0.002$ , revealed identical solutions for the equivalent two-dimensional airfoil.

Figure 15 provides vorticity contours for the lower pitch rate at selected cross sectional planes in a format identical to Fig. 6. The same general flow features are observed. The dynamic stall vortex was again pinned to the wing leading edge until very late in the pitch cycle. Near the root, the vortex propagation was first retarded and then accelerated as the pitch cycle progressed. In contrast to the higher pitch rate, the dynamic stall vortex at  $30^\circ$  was larger and had propagated further downstream to the

midchord position. At  $50^\circ$  incidence and above, the original dynamic stall vortex has propagated beyond the field of view in Fig. 15. However, a new vortex is evident at  $50^\circ$  and by the time  $60^\circ$  has been reached, this vortex was a dominant flow feature at midspan. A comparison of the predicted and experimental normal force coefficients is provided in Fig. 16. Overall, the agreement is not as good as in the higher pitch rate case. As before, the magnitude of the normal force coefficient was underpredicted. In addition, the normal force distribution appeared to lead the experiment by a time interval corresponding to about  $5^\circ$  in angle of attack. A two-dimensional grid resolution study, Fig. 17, indicated that additional grid resolution did not significantly change either the magnitude or the timing of the predicted normal force time history. Compressibility is again the most likely source of the discrepancy. The most direct support for this view was provided by Patterson and Lorber<sup>12</sup> who compared a compressible flow solver at  $M_\infty = 0.2$  with an incompressible flow solver for the same two-dimensional airfoil pitching at non-dimensional pitch rate of 0.02. They found that the compressible flow solver predicted the formation of the dynamic stall vortex earlier than did the incompressible code and that it underpredicted the magnitude of the resulting force coefficients. Both observations are in agreement with the present results.

### Conclusions

A numerical study of wing-tip and wing-juncture interactions for a finite wing-splitter plate configuration pitching through extreme angles of attack was conducted and the solutions compared with corresponding experimental wind tunnel and water tunnel data. At the higher of two pitch rates examined, the computations agree well with available experimental data and provide new insight into the massively stalled, three-dimensional, unsteady flow. At the lower pitch rate, the computation again correctly predicted the overall flow features but predicted the formation and propagation of the dynamic stall vortex prematurely. Evidence was presented to suggest that this discrepancy resulted from the difference in the computational and experimental Mach numbers. The computational freestream Mach number selected,  $M_\infty = 0.2$ , corresponds to a generally accepted lower limit for reasonable convergence behavior of a compressible flow solver. Since compressibility effects were significant at this Mach number, it appears that an incompressible flow solver would be required to rigorously match the experimental test conditions.

Conversely, most unsteady flows involving real flight vehicles are compressible. Ultimately, the unsteady flow regime of interest to maneuvering aircraft is further characterized by high Reynolds numbers, turbulent flow, and three dimensionality. All pose significant challenges to experimental and numerical investigations. The present

study has focused on the latter characteristic--three-dimensional, unsteady, separated flows. The computational results provided a detailed description of the three-dimensional interactions at the wing tip and wing-juncture of a generic pitching wing. At the wing tip, the numerical results delineated the interaction of the wing-tip vortex and the dynamic stall vortex, the influence of the wing-tip vortex in "pinning" the dynamic stall vortex to the leading edge, and the resulting amplification of the sectional force coefficients in the leading-edge region. At the wing juncture, the numerical results provided insight into the three-dimensional viscous interaction leading to a smaller local normal force maximum near the wing root.

### References

1. Fant, D. B. and Rockwell, D. Eds., Proceedings, "AFOSR Workshop on Supermaneuverability: Physics of Unsteady Separated Flows at High Angle of Attack," Lehigh University, Apr. 9-10, 1992.
2. Robinson M. R., and Wissler J. B., "Unsteady Surface Pressure Measurements on a Pitching Rectangular Wing," AIAA Paper 88-0328, Jan. 1988.
3. Schreck, S. J., Addington, G. A., and Luttges, M.W., "Flow Field Structure and Development Near the Root of a Straight Wing Pitching at Constant Rate," AIAA Paper No. 91-1793, June 1991.
4. Klinge, J., Schreck, S. Robinson, M., and Luttges, M. W., "Three-Dimensional Flow Field Kinematics near the Root of an Oscillating Wing," AIAA Paper 91-3264, Sept. 1991.
5. Schreck, S. J. and Helin, H. E., "Unsteady Vortex Dynamics and Surface Pressure Topologies on a Pitching Wing," AIAA Paper 93-0435, Jan. 1993.
6. Lorber, P. F., "Tip Vortex, Stall Vortex, and Separation Observations on Pitching Three-Dimensional Wings," AIAA Paper 93-2972, July 1993.
7. Visbal, M. R., "Investigation of the Flow Structure Around a Rapidly Pitching Airfoil," *AIAA Journal*, Vol. 27, No. 8, Aug. 1989, pp. 1044-1051.
8. Visbal, M. R., and Shang, J. S., "Numerical Investigation of the Flow Structure Around A Rapidly Pitching Airfoil," Proceedings from Workshop II on Unsteady Separated Flows, Sept. 1988, FJSRL-TR-88-0004, pp. 91-108.
9. Visbal, M. R., "On Some Physical Aspects of Airfoil Dynamic Stall," ASME Symposium on Non-Steady Fluid Dynamics, June 4-7, 1990, Toronto, Canada.

10. Visbal, M. R., "On the Formation and Control of the Dynamic Stall Vortex on a Pitching Airfoil," AIAA Paper 91-0006, Jan. 1991.
11. Rumsey, C.L. and Anderson, W.K., "Some Numerical and Physical Aspects of Unsteady Computations Over Airfoils Using Dynamic Meshes," AIAA Paper 88-0329, Jan. 1988.
12. Patterson, M. T., and Lorber, P.F., "Computation and Experimental Studies of Compressible Dynamic Stall," *Journal of Fluids and Structures*, Vol. 4, 1990, pp. 259-285.
13. Ghia, K., Yang, J. Osswald, G., Ghia, U., "Study of the Dynamic Stall Mechanism Using Simulation of Two-Dimensional Navier-Stokes Equations," AIAA Paper No. 91-0546, Jan. 1991.
14. Knight, D.D. and Choudhuri, P.G., "2-D Unsteady Leading-Edge Separation on a Pitching Airfoil," AIAA Paper 93-2977, July 1993.
15. Guruswamy, G., "Vortical Flow Computations on Swept Flexible Wings Using Navier-Stokes Equations," *AIAA Journal*, Vol. 28, No. 12, Dec. 1990, pp. 2077-2084.
16. Chaderjian, N.M., and Guruswamy, G.P., "Transonic Navier Stokes Computations for an Oscillating Wing Using Zonal Grids," *Journal of Aircraft*, Vol. 29, No. 3, May-June 1992, pp. 326-335.
17. Yang, H. Q., and Przekwas, A. J., "Dynamic Stall on a Three-Dimensional Rectangular Wing," AIAA Paper 93-0637, Jan. 1993.
18. Yang, H. Q., and Przekwas, A. J., "Three-dimensional Unsteady Separated Flows around an Oscillatory Forward Swept Wing," AIAA Paper 93-2976, July 1993.
19. Visbal, M. R., "Computational Study of Vortex Breakdown over a Pitching Delta Wing," AIAA Paper 93-2974, July 1993.
20. Visbal, M. R., and Gordnier, R. E., "Parametric Effects on Vortex Breakdown Over a Pitching Delta Wing," AIAA 94-0538, Jan. 1993.
21. Gordnier, R. E., "Computation of Delta Wing Roll Maneuvers," AIAA 93-2975, July 1993.
22. Newsome, R. W., "Numerical Simulation of Wing-Wall Juncture Flow for a Pitching Wing," AIAA Paper 93-3401, Aug. 1993.
23. Vatsa, V.N., Thomas, J.L., and Wedan, B.W., "Navier-Stokes Computations of Prolate Spheroids at Angle of Attack," AIAA Paper 87-2627, 1987.
24. Ghaffari, F., Bates, B.L., Luckring, J.M., Thomas, J.L., Biedron, R.T., "Navier-Stokes Solutions About the F/A-18 Wing-LEX-Fuselage Configuration with Multi-Block Structured Grids," AIAA-91-3291-CP, 1991.
25. Perry, A.E. and Chong, M.S., "A Description of Eddy Motions and Flow Patterns Using Critical Point Concepts," *Annual Review of Fluid Mechanics*, Vol. 19, 1987, pp. 125-155.
26. Chapman, G.T., and Yates, L.A., "Topology of Flow of Separation on Three-Dimensional Bodies," *Applied Mechanics Review*, Vol. 44, No 7, July 1991, pp. 329-345.
27. Chandrasekhara, M.S., Carr, L.W., and Wilder, M.C., "Interferometric Investigations of Compressible Dynamic Stall over a Transiently Pitching Airfoil," *AIAA Journal*, Vol. 32, No. 3, March 1994, pp. 586-593.

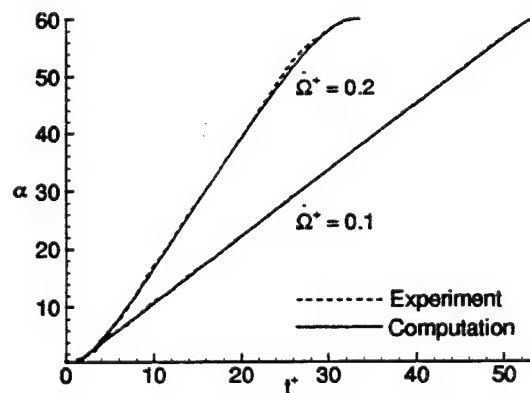


Fig. 1 Angle of attack histories for non-dimensional pitch rates  $\dot{\Omega}^+ = 0.1$ ,  $\dot{\Omega}^+ = 0.2$

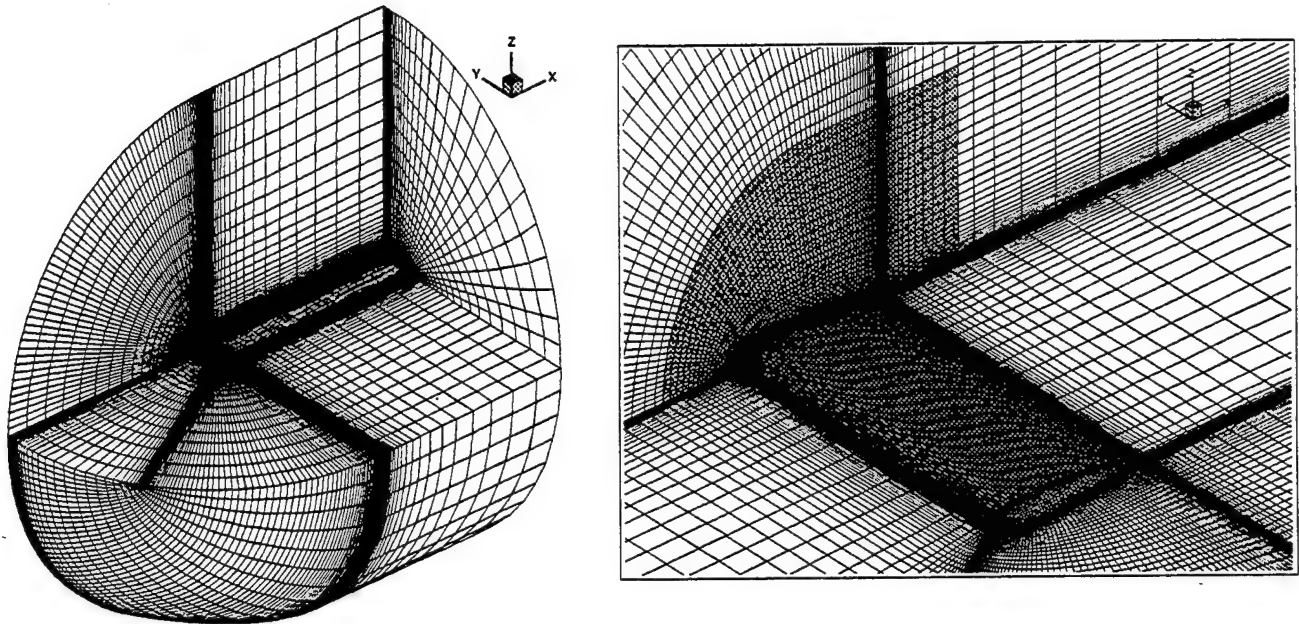


Fig. 2 Grid for wing-splitter plate configuration - 213x75x61

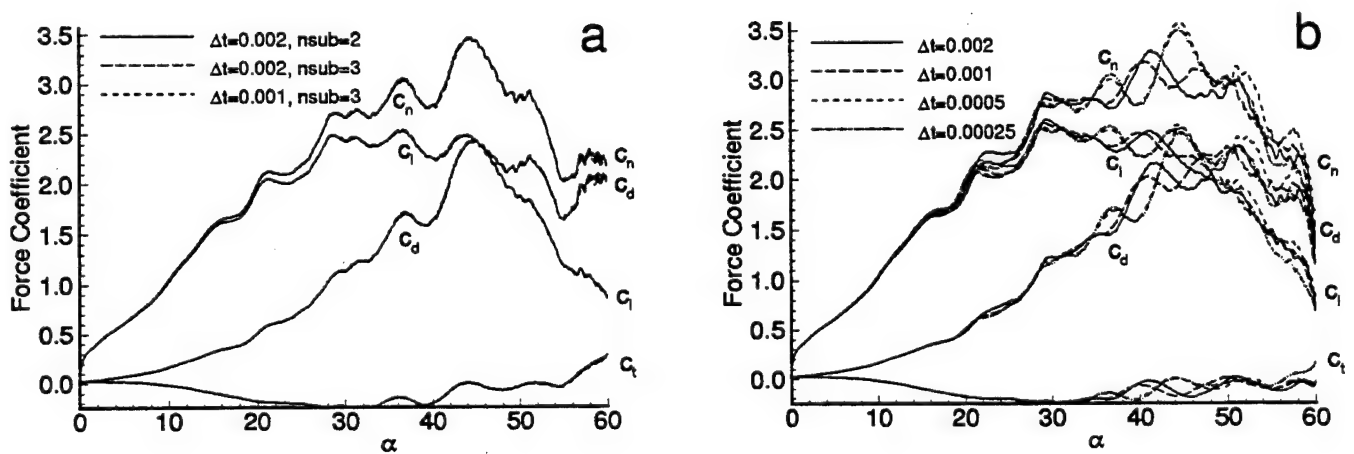


Fig. 3 Temporal Accuracy for equivalent 2D pitching airfoil,  $\Omega^+ = 0.2$ ,  $Re_\infty = 56000$   
a. With subiteration      b. Without subiteration

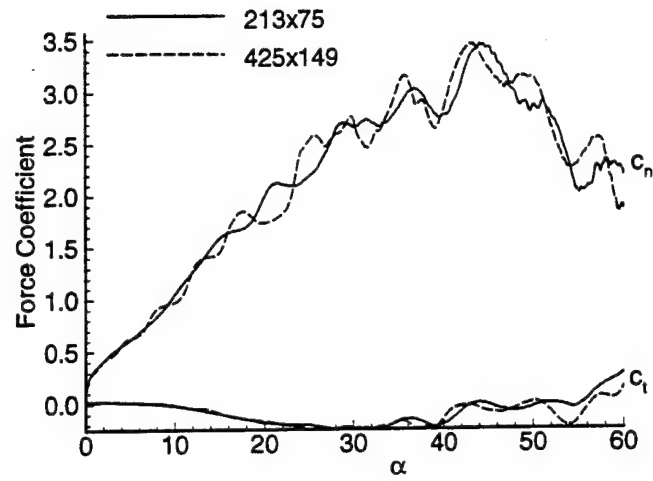


Fig. 4 Spatial accuracy for equivalent 2D airfoil,  $\dot{\Omega}^+ = 0.2$ ,  $Re_\infty = 56000$   
Grid sizes: 213x75 425x149

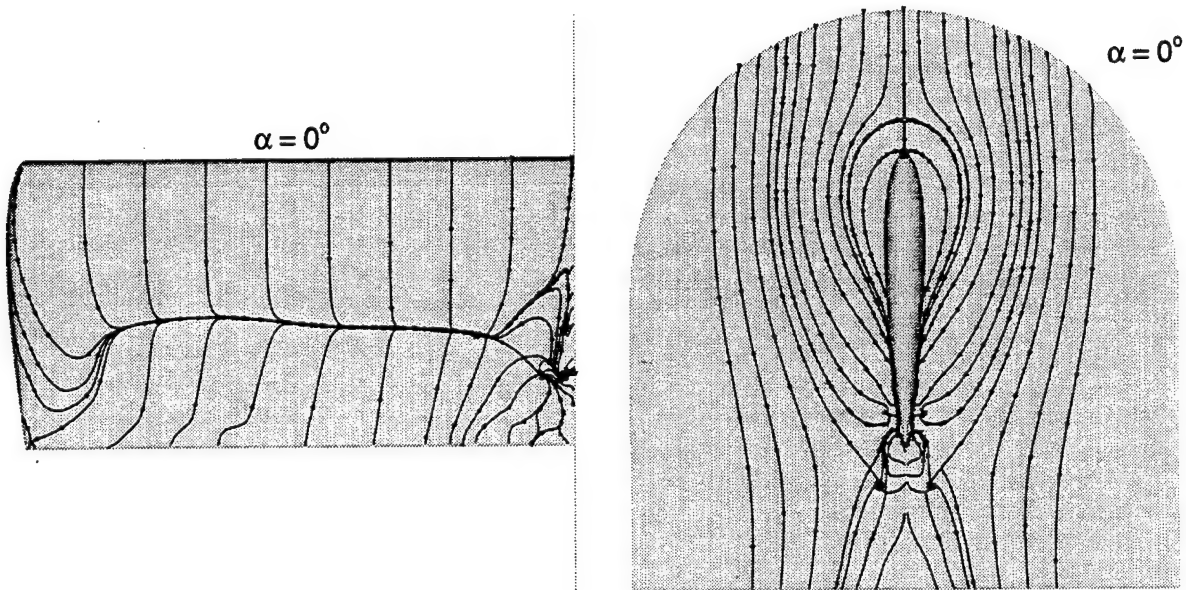


Fig. 5 Limiting streamlines for wing splitter plate configuration, initial condition,  $\alpha = 0^\circ$ ,  $Re_\infty = 56000$

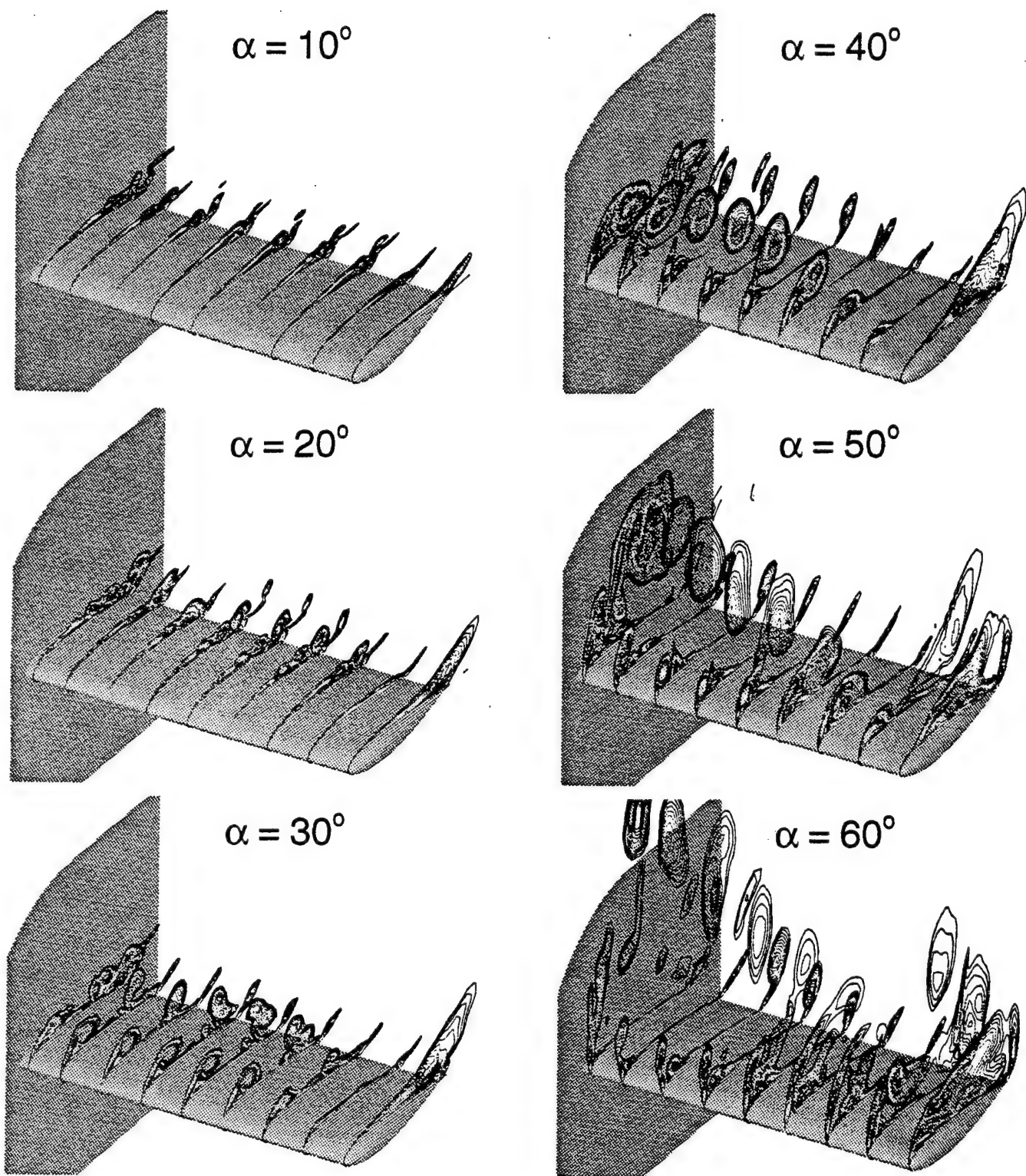


Fig. 6 Vorticity contours at 9 spanwise stations,  $\dot{\Omega}^+ = 0.2$ ,  $Re_\infty = 56000$   
 $y/c = \{0.05, 0.25, 0.5, 0.75, 1.0, 1.25, 1.5, 1.75, 2.0\}$



$$\alpha = 40.1^{\circ}$$



$$\alpha = 50.0^{\circ}$$



$$\alpha = 59.2^{\circ}$$

**Fig. 7 Water tunnel flow visualization,  $\dot{\Omega}^+ = 0.2$ ,  $Re_{\infty} = 56000$   
Dye injection at leading edge**

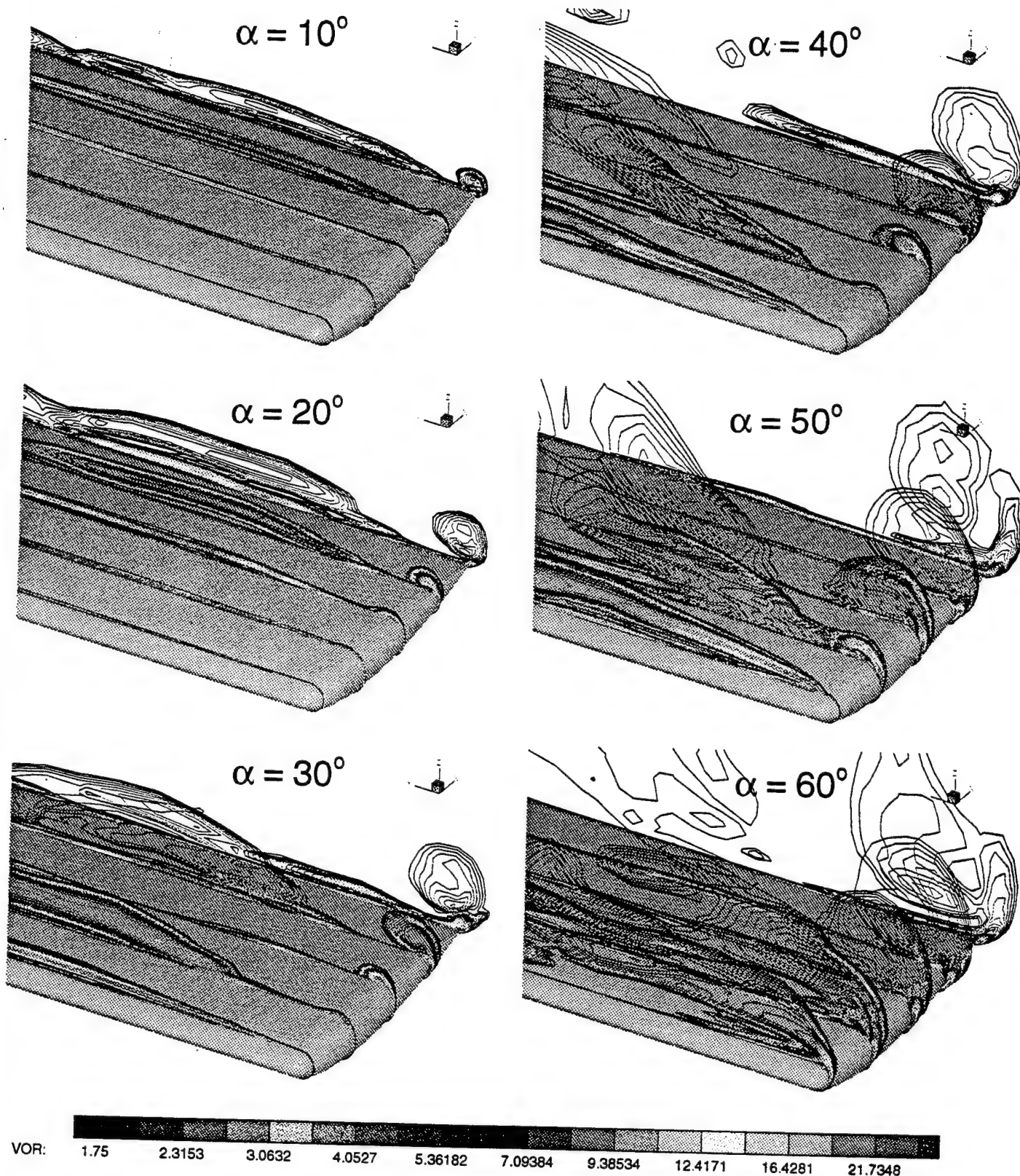


Fig. 8 Vorticity contours at 5 chordwise stations,  $\Omega^+ = 0.2$ ,  $Re_\infty = 56000$   
 $x/c = \{0.05, 0.25, 0.5, 0.75, 1.0\}$

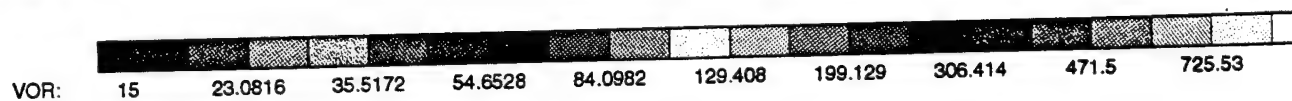
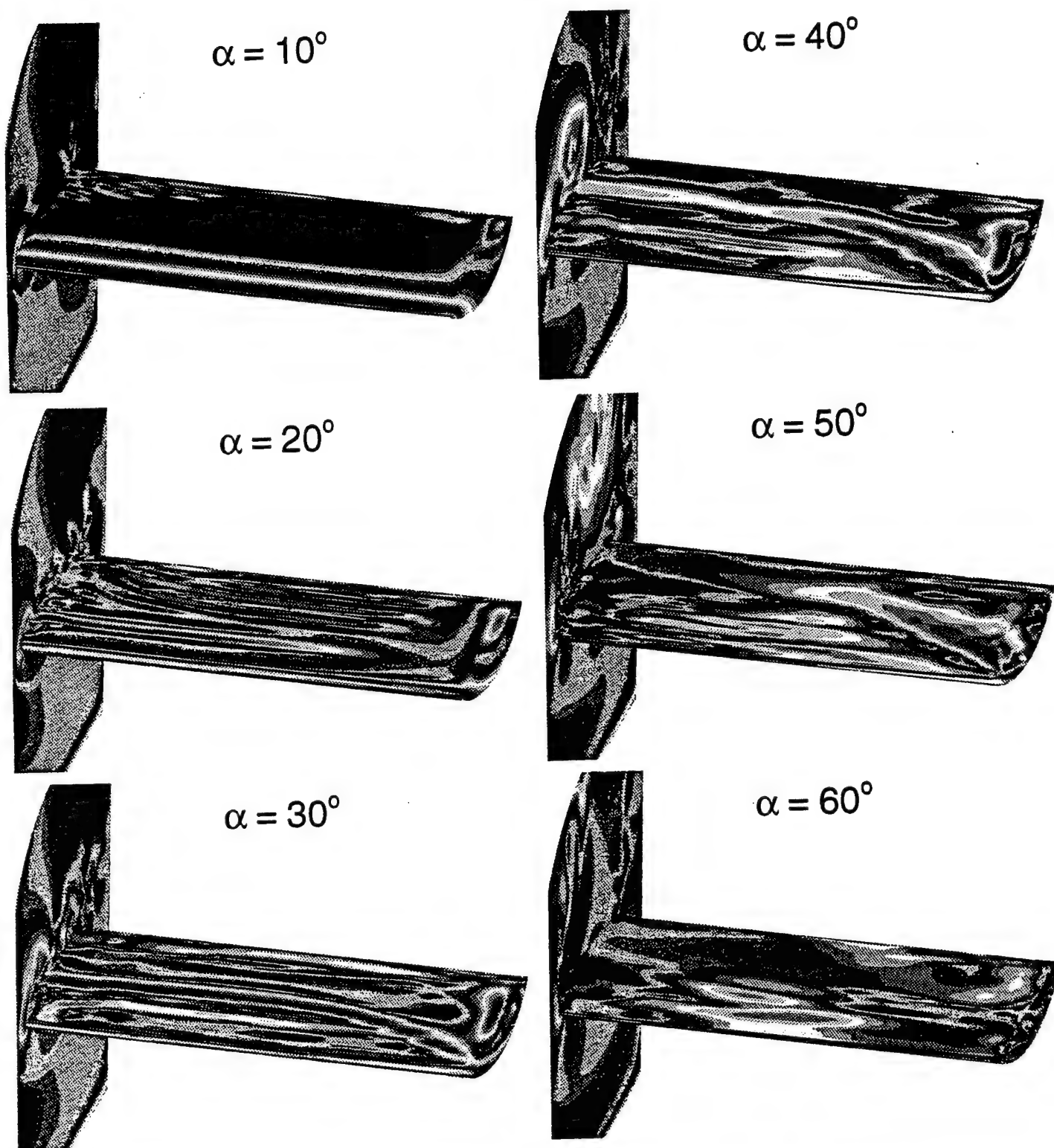


Fig. 9 Surface vorticity flooded contours on wing and splitter plate  
 $\dot{\Omega}^+ = 0.2$ ,  $Re_\infty = 56000$

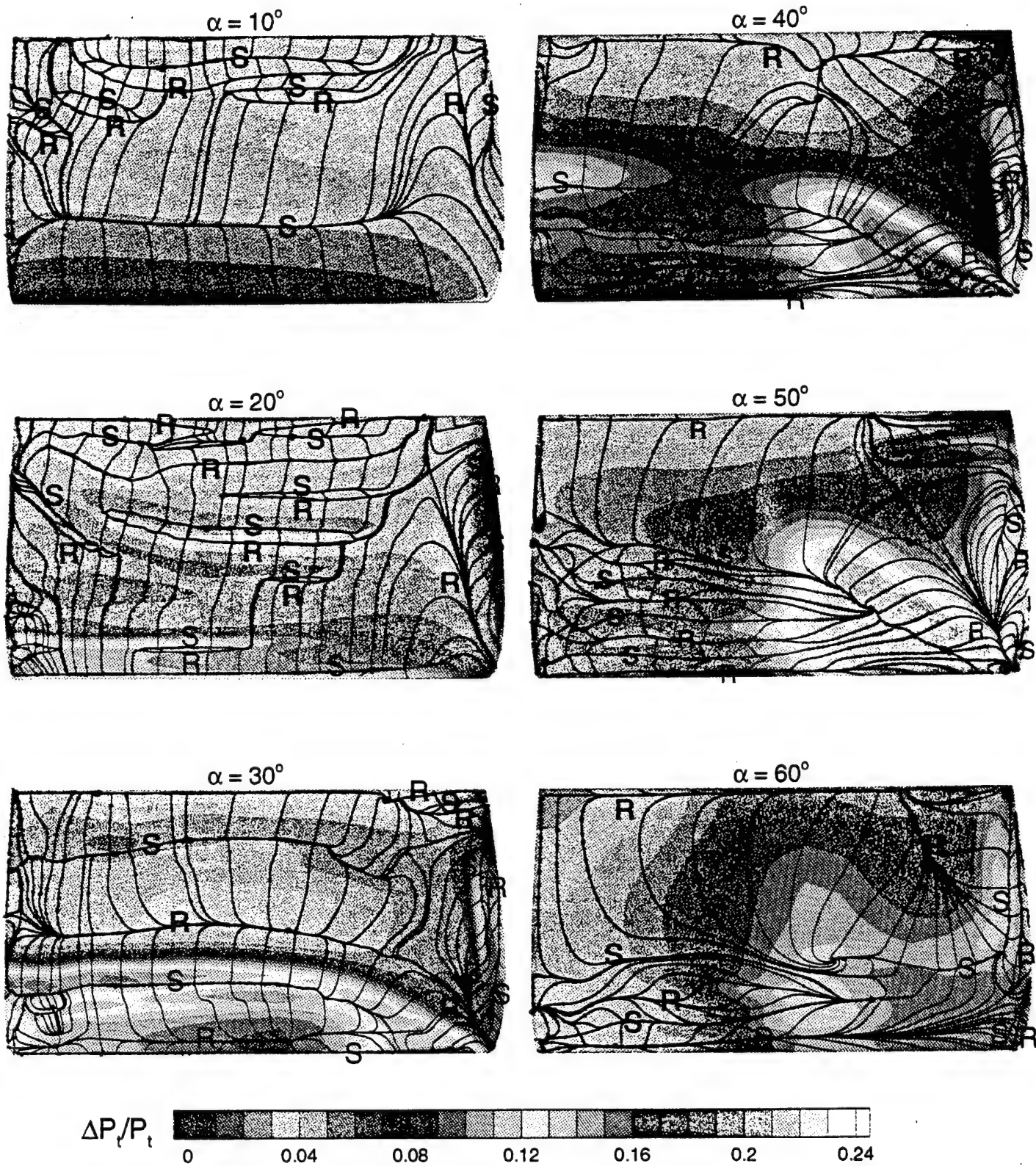


Fig. 10 Instantaneous limiting streamlines,  $\dot{\Omega}^+ = 0.2$ ,  $Re_\infty = 56000$   
 Plotted over normalized total pressure loss flooded contours

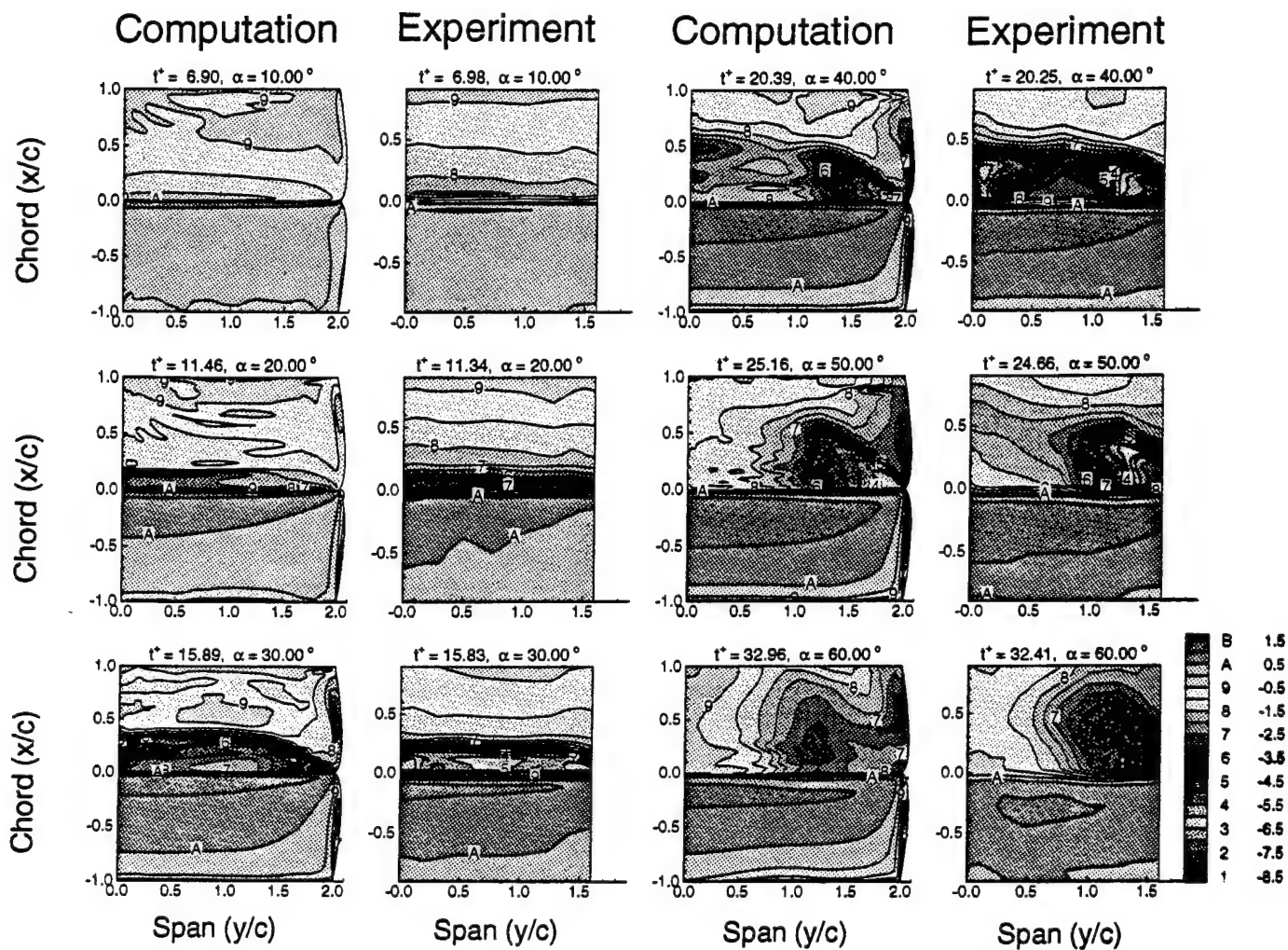


Fig. 11 Comparison of computational and experimental pressure coefficients  
 $\dot{\Omega}^+ = 0.2$ ,  $Re_\infty = 56000$

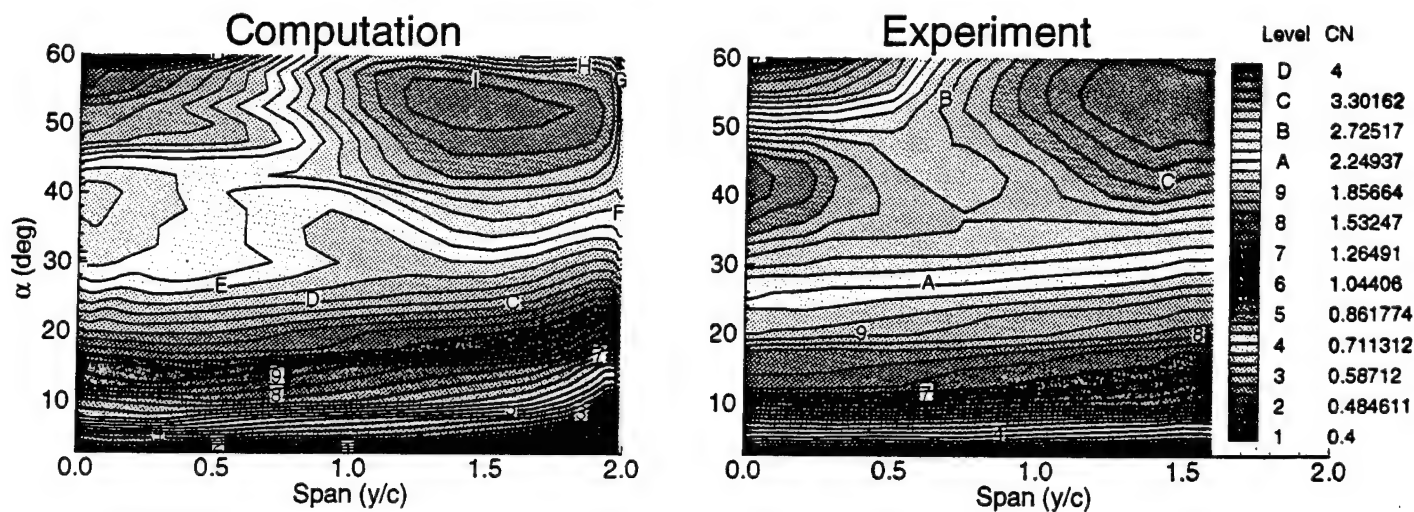


Fig. 12 Comparison of computational and experimental normal force coefficients  
 $\dot{\Omega}^+ = 0.2$ ,  $Re_\infty = 56000$

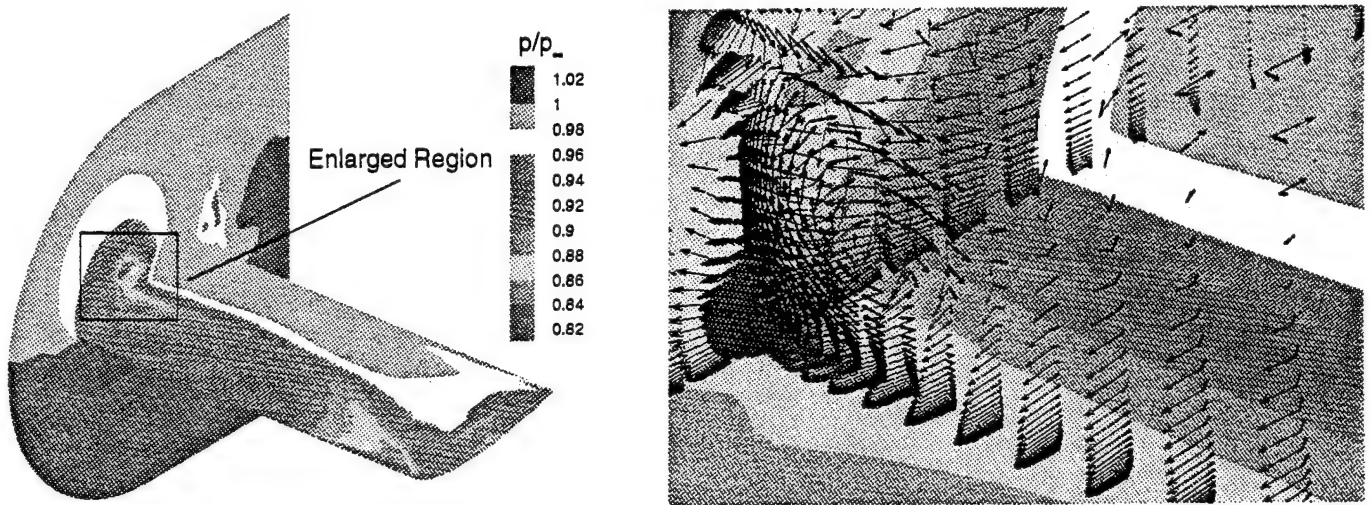


Fig. 13 Velocity vectors near wing root at  $\alpha = 35^\circ$ ,  $\Omega^+ = 0.2$ ,  $Re_\infty = 56000$   
Plotted over surface pressure flooded contours

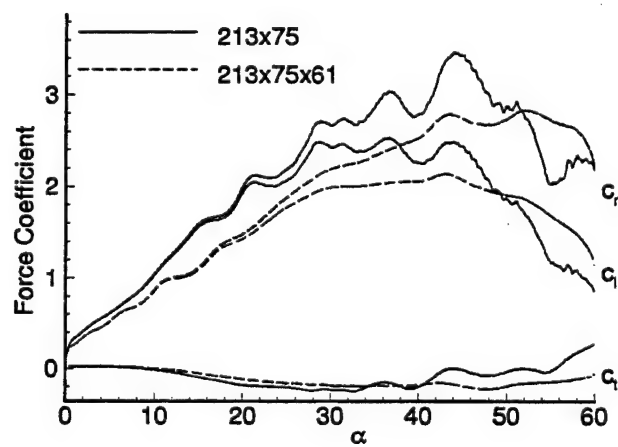


Fig. 14 Comparison of normal and tangential force coefficients for 3D finite wing and equivalent 2D airfoil,  $\Omega^+ = 0.2$ ,  $Re_\infty = 56000$

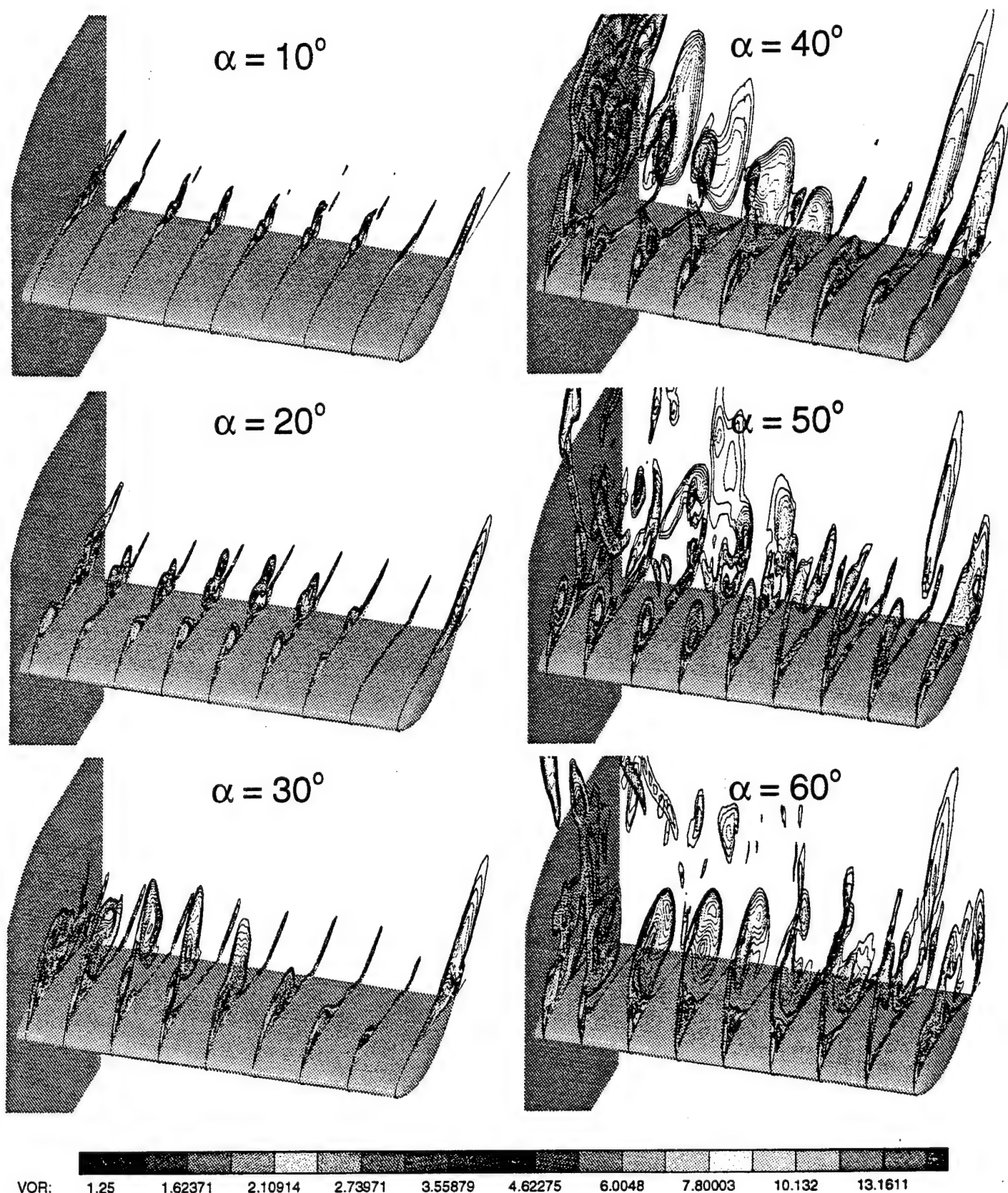


Fig. 15 Vorticity contours at 9 spanwise stations,  $\hat{\Omega}^+ = 0.1$ ,  $Re_\tau = 56000$   
 $y/c = \{0.05, 0.25, 0.5, 0.75, 1.0, 1.25, 1.5, 1.75, 2.0\}$

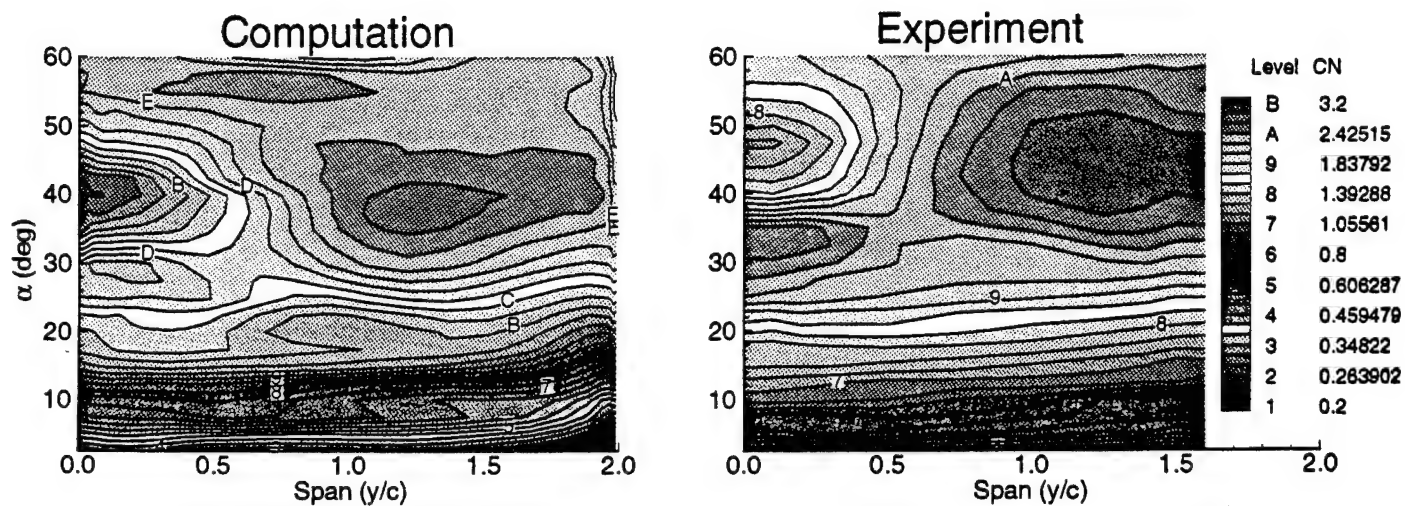


Fig. 16 Comparison of computational and experimental normal force coefficients  
 $\dot{\Omega}^+ = 0.1$ ,  $Re_\infty = 56000$

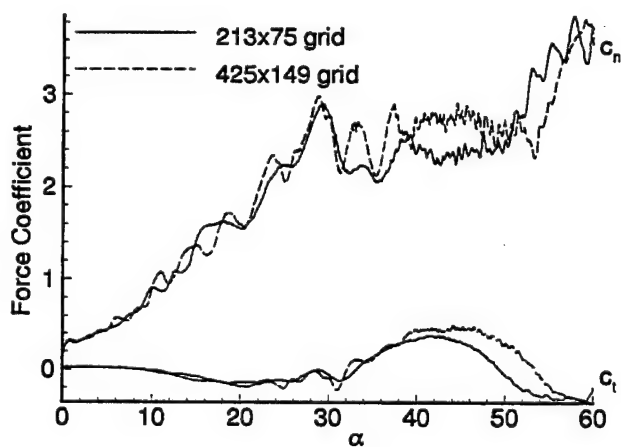


Fig. 17 Spatial accuracy for equivalent 2D airfoil,  $\dot{\Omega}^+ = 0.1$ ,  $Re_\infty = 56000$   
 Grid Sizes: 213x75 425x149

## Analysis of Rolled Delta Wings Flows Using Effective Sweep and Attack Angles

Eric J. Stephen

The Frank J. Seiler Research Laboratory

USAF Academy, Colorado 80840

### Abstract

Flow visualization data over the suction surface of a  $65^\circ$  swept delta wing were recorded at a  $30^\circ$  incidence angle for a range of static roll angles ( $-42^\circ$  to  $42^\circ$ ) and Reynolds number of  $9.0 \times 10^5$ . The data were reduced to provide information on the vortex relative position and the burst point location. The results were compared to previously recorded rolling moment data, to provide an understanding of the relationship between flow behavior and aerodynamic loading. The combination of roll about the body axis and an axis incidence angle with the flow induced a sideslip angle relative to the wing. Combining the sideslip angle with the nominal leading edge sweep of the wing provided an effective leading edge sweep angle. Using the effective sweep angle, along with the previous data for unyawed delta wings, the flow behavior over the either side of the wing was predicted. Extending this analysis suggested the presence of non-zero trim positions in roll, based on wing movement in and out a stalled regime. These trim positions have been recorded in free-to-roll experiments.

### Symbols

s	= local semispan
x	= chordwise position
y	= spanwise position
z	= position normal to the wing surface
$\Lambda$	= sweep angle
$\alpha$	= angle of attack between the wing and the freestream
$\Delta$	= increment
$\sigma$	= incidence angle between the root chord and the wind tunnel floor
$\phi$	= roll angle about the body axis
Subscripts	
bp	= burst point
eff	= effective
0	= nominal

### Introduction

The flow over the delta wing planform has been of interest since the 1950's due to the delta wing design used on high speed aircraft. The delta wing provides a unique type of flow field with the formation of large helical vortices over the upper wing surface. This flow structure allows the delta wing to maintain lift to high angles of attack when compared to the conventional straight wing.

With the current emphasis on improving aircraft maneuverability, the flight envelope is being pushed to higher limits, even into the post stall regime. In these flight regimes the stall characteristics of the wing become important. For the delta wing, a precursor to stall on the delta wing is the movement of the burst point to a position over the wing. Therefore the position of the vortex burst point can be an indicator for wing performance.

To evaluate the fluid dynamics and aerodynamic loading of the delta wing undergoing high angle of attack maneuvers, the Canadian National Research Council (NRC) developed a comprehensive test program for testing a  $65^\circ$  swept delta wing in a wind tunnel. Force balance, surface pressure, and flow visualization data were recorded for the flow over a delta wing, which was held at an incidence angle of  $30^\circ$  and was forced statically and dynamically through a range of roll angles about the body axis.

The force balance results have been discussed previously. In this paper the flow visualization will be discussed with emphasis on the behavior of the burst point and the changing structure of the vortex flow for different geometric orientations. This presentation is limited to the static results. The results were analyzed according to the effective sweep angles on leading edges of the wing. The effective sweep angle was determined by the relative orientation of the leading edge to the freestream. This analysis provides some physical interpretation of the rolling moment results that have been previously published.

## Methods

The delta wing model and the tunnel set up have been documented by Hanff (Fig. 1). The model was 65° swept back flat plate model with a 25° knife edge bevel and a root chord length was 24.48 inches. The root chord axis of the model was held at a 30° incidence angle relative to the floor of the wind tunnel. Roll angles were measured about this axis. Kerosene smoke was injected forward of the apex and was entrained into the two vortices of the suction surface of the wing. A movable set of optics was designed to produce a laser sheet normal to the root chord axis. The laser sheet was moved along the model from the trailing edge to the apex illuminating cross section cuts of the conical vortices.

The flow visualization was reduced using an image analysis program documented by McLaughlin. The image analysis program, first, identified the wing and its roll orientation. Then the position and size of both leading edge vortices, as well as the burst condition, were determined for each analyzed frame of the video data. Vortex size was determined by the area of the smoke illuminated over either side of the wing. The vortex position was initially estimated as the centroid of that illuminated smoke region.

The burst condition of the vortex was determined by the presence or absence of coherent core flow, denoted by a small darkened circle near the center of the illuminated smoke region (Fig. 2, Frame a.). Reasons for the dark appearance of the core flow are discussed in Nelson. If the core was detected, the core center was used to estimate the position of the vortex.

Other researchers have discussed the nature of vortex burst<sup>3,6,7,8</sup>, either as the sudden expansion of the core (bubble breakdown) or as a sudden core trajectory change from a line to a helix (helical breakdown). In either case the breakdown was manifested in the flow visualization as the expansion of the darkened core, followed by its disappearance as the core flow diffuses. Once the general spatial region of core diffusion was determined from the image analysis program, the region was reviewed manually to determine where core expansion initiated. The burst location was recorded as the chordwise position where the darkened core began to expand. A similar burst identification criteria was used previously by Kegelman. Since the burst location is not fixed, this technique determined the most upstream burst location.

## Results

Examples of the flow visualization data (viewed from the front<sup>2</sup>) are shown in Fig. 2 for roll angles from -14° to 42°. These results were recorded for the 60% chord position. Since the vortex remains conical over the surface, the relative spanwise position of the vortex ( $y/s$ ) was nearly constant, so a single position was representative of the vortex flow position over the whole wing. The frames show the smoke, entrained in the vortices on either side of the rolled wing and illuminated by a laser sheet perpendicular to the roll axis. The wing can be seen highly illuminated at the bottom of each frame. The hump in the center of the wing is the housing for the force balance and mounting apparatus.

The images show that flow over the leeward (upper) side produced a more compact vortex with a more aft burst location. The aft burst location was indicated by the presence of a core in the leeward vortex only. At the higher roll angles the core on the leeward side was present, but was washed out by the high intensity of the illuminated smoke. The leeward vortices also exhibited vortical ornamentation, evidenced by the wavy outline of the illuminated smoke. The ornamentation is the discretization of the outer shear layer into a series of vortices similar to that shown by Gad-el-Hak (Fig. 2, 2nd column).

For roll angles greater than 7° the flow on the windward wing no longer exhibited the organized outboard flow along the surface, indicative of a vortex. This flow was appropriately referred to as separated rather than as vortical flow. As the roll angle increased past 14°, the smoke on the windward side did not fill the separated region completely, but remained in the inboard part of the region. The height of the separated region could still be estimated, however. From the estimation the separation height reached a maximum at 21° roll, declining with higher angles.

The trend of having a small, coherent vortex on the leeward side and a burst vortex or separated flow on the windward side was consistent in all the frames. The negative roll angles were included in Fig. 2 to show the symmetry of the tests. The lack of antisymmetry between the flow fields for 14 and -14° suggests that the roll angles may have had a slight offset in the zero roll position, possibly because of support interference<sup>11</sup>.

From the flow visualization data the vortex positions, as well as the vortex burst point locations, were tracked. The relative spanwise positions of the vortex,  $y/s$ , at the 60% chord

position are shown in Fig. 3 for the range of roll angles from  $-42^\circ$  to  $42^\circ$ . As discussed above, these data represent the spanwise core positions when a vortex core was apparent. When a vortex core was not apparent, i. e. the vortex was burst or the flow was separated, the data were the spanwise centroid positions of the illuminated smoke. The spanwise position is shown because the far inboard spanwise position corresponded with separation of the flow. Therefore these data provide a indication of the changing structure of the flow.

The data on the upper half of the graph correspond to the right wing shown in Fig. 2, while the lower half data correspond to the left wing. The general trend of the vortex position was to move inboard as the wing moved into a more windward position. The vortices reached a most inboard position near  $35^\circ$  and  $-35^\circ$  roll for the left and right wings, respectively. A lack of antisymmetry was apparent at  $\phi = 0^\circ$  with the vortex on the left moving slightly further inboard. This may also be a result of support interference<sup>11</sup> as suggested earlier.

Several regions have been labeled on the graph to show the relation between vortex position and burst condition. When the burst point was aft of the trailing edge or over the surface, there is a near linear relationship between the roll angle and vortex position. When the burst point reached the apex, the character of the flow changed from vortex to separated flow. Also the smoke did not reach the outboard separated region, as was described above. Both of these factors contributed to the inboard movement of the position data.

The burst point data for either wing are shown in Fig. 4 with the relative chordwise burst location plotted versus roll angle. Similar to the position data, these data show the inverse behavior of the burst point data from one wing to the other. As the roll angle increased the burst point on the right wing moved aft while the burst point moved forward on the left wing. The intersection of the two curves occurred at a slightly negative roll angle.

The graph shows that the burst point was only over the surface for small portion of the test range. When the burst point was at or aft of the trailing edge, the data show the burst point at the trailing edge. Since the laser sheet did not move past the end of the model, it was not possible to track the burst point aft of the wing. The data show the burst point at the apex for all cases where no vortex core was apparent over the wing.

## Discussion

In order to discuss these results, a conceptual model for delta wing flow is suggested. For the model, it is postulated that the organization of vortices over the delta wing is a function of the sweep back angle, the angle of attack and the influence of the vortex on the opposite side of the wing. The sweep angle and the angle of attack determine the orientation of the leading edge relative to the flow. The orientation should determine the vorticity flux from the leading edge into the delta wing vortex. The sweep angle and the angle of attack also determine the region shadowed from the freestream in which vorticity can accumulate. The sweep angle and angle of attack are important parameters in the determination of vortex organization.

The influence of the opposite vortex, for delta wings with sweep angle less than  $70^\circ$ , would be to impose a downward velocity component on the vortex. At higher sweep angles the vortex-vortex interactions become more complicated. The magnitude of the influence is determined by the strength and the proximity of the two vortices. Roos and Kegelmann<sup>12</sup> have shown that the spanwise position of the vortex core is roughly 60% of the semispan from the root chord, a function of the sweep angle. For a lower swept wing the vortices are farther apart. Nelson<sup>13</sup> has shown that the circulation contained in the vortex is also proportional to the sweep angle. The lower swept wing produces higher circulation values. Since these two effects act counter to one another, as a first approximation for analysis, the influence of the opposite vortex is assumed to be constant. Changes in vortex development are therefore assumed to be only a function of the sweep angle and angle of attack. This appears to be true from the half models results reported by Roos<sup>12</sup> which showed excellent flow similarity to full delta wing models with sweep angles of  $60^\circ$  and  $70^\circ$ .

The implication for a yawed delta wing is that the flow will develop according to the effective sweep of the wing leading edge. The effective sweep would be a combination of the nominal sweep of the wing and the sideslip angle. The flow over the windward wing would develop as if the sweep angle were reduced and vice versa for the leeward wing. The trend for this behavior was seen in previously reported burst point data<sup>3</sup> over yawed delta wings. The burst point on the windward wing moved forward with an increase in yaw, consistent with a decrease in the leading edge sweep angle.

In the current tests, the incorporation of roll onto the delta wing at an angle of attack induced a sideslip angle while reducing the angle of attack. Equations for calculating the reduced angle of attack and the sideslip angle as functions of  $\phi$  and  $\sigma$  are found in Ericsson .

$$\alpha(\phi) = \tan^{-1}(\tan \sigma \cos \phi)$$

$$\Delta\Lambda(\phi) = \tan^{-1}(\tan \sigma \sin \phi)$$

The effective sweep angle of the leading edge would be determined by a combination increment of the sweep angle due to the induced side slip angle and the nominal sweep angle,  $\Lambda$ .

$$\text{windward wing: } \Lambda_{\text{eff}} = \Lambda_0 - \Delta\Lambda$$

$$\text{leeward wing : } \Lambda_{\text{eff}} = \Lambda_0 + \Delta\Lambda$$

Using the calculated effective sweep angle and angle of attack, combined with previously reported burst point data the burst point locations for the rolling delta wing could be predicted.

In order to address the accuracy of this simple estimation technique, burst data were taken from several sources<sup>13,15,16,17</sup> for a range of sweep angles and angles of attack. These data are plotted in Fig. 5. These data were collected over as wide of a range of sweep angles as possible. On the low end, researchers have reported no evidence of a coherent vortex over the surface for a sweep angle of 45° or less, regardless of angle of attack. The upper end is obviously limited to less than 90°. The angle of attack range was determined by the presence of the burst point over the surface. For any model the burst point was over the surface for 10° to 15° angle of attack range. For the 85° delta wing the burst point would reach the apex at about 70° angle of attack.

The different symbols on the graph represent the different sweep angles. The separation of the symbols shows a shift to higher angles of attack with increased sweep angle. The scatter in the data was due to differences in the model shape. Kegelman has shown that this scatter can be reduced by comparing wings with the same leading edge shape.<sup>16</sup> The flagged data points were taken from Wentz . Their test model had a flat surface and a convex surface. Data taken using the convex surface as the upper surface produced a definite change in the burst behavior. Therefore the data from the convex-up tests are flagged. All other data were taken with flat plate models.

Visual inspection of the data indicated that the burst point location had a similar function of the angle of attack, regardless of the sweep angle. Lambourne had previously shown that the burst point location data, under different sweep conditions, collapsed on a single curve when plotted against  $\cos^{-1}(\cos \alpha \sin \Lambda)$ . Plotting the collection data from Fig.

5 against this function did not produce the same level of collapse that Lambourne had reported so another function was developed using curve fitting techniques.

$$x_{bp} = \left( \frac{0.00741\Lambda - 0.287}{\alpha - (0.00866\Lambda - 0.3573)} \right) - 0.25$$

It is stressed that the model is not based on a physics of the flow field. Rather, a function for the burst point location was sought to model sweep and attack angle effects in order to compare the nominal behavior of the flow over delta wings to that under yawed conditions. The results of applying this function to the  $\Lambda$  and  $\alpha$  conditions for Fig. 5 are shown in Fig. 6.

The burst point function was applied to the data taken from McKernan in Fig. 7. The burst point location data were recorded for a 70° swept wing over a range of angles of attack and sideslip angles. The data were presented for the windward side of the wing only. The burst point location was estimated by substituting  $\Lambda_{\text{eff}}$  in the burst point function. The results show excellent agreement between the predicted vortex burst position and the measured values suggesting that, at least in this limited range, the flow field on either side of the delta wing can be determined by the effective sweep angles and angle of attack.

The same function was applied to the current data for a delta wing with a combination of pitch and roll. The comparison between the measured data and that predicted by the function are shown in Fig. 8. For this comparison the data from Fig. 4 were replotted versus the effective sweep angle of each side of the wing. For these cases, the burst point function predicted the experimental data within 20% chord for effective sweep angles below 70°. A 20% chord change in the burst location with different leading edge shapes was not unreasonable, since most of the reference data were collected on models with flat upper surfaces, and the upper surface of this delta wing model was beveled at the edges<sup>19</sup>. Also, it was difficult to determine burst locations forward of 20% chord because the bright illumination of the dense smoke in that region washed out the small, dark core flow. It is noted that the excellent comparison with McKernan's data, for the windward wing only, was also for effective sweep angles less than the 70°.

These results show that a burst point equation based on the nominal wing configurations provided accurate burst point estimates for effective

sweep angles less than  $70^\circ$ . Above  $70^\circ$  the trend was predicted but the error increases. This may be indicative of the scatter in the data on which the predictive equation was based or it may indicate a breakdown in the premise of opposite vortex influence at higher sweep angles.

The first possibility could be resolved with a parametric set of flow visualization tests over delta wings with common leading edge shapes and a wide range of sweep back angles. As for the second possibility, it has been shown that the vortex sheets separating from both sides of the wing come in contact prior to vortex breakdown<sup>16</sup> for sweep angles greater than  $75^\circ$ . For angles of attack above initial vortex sheet contact, the vortex cores can be forcibly displaced off the surface. This is presumably an effect of the interaction between the vortices due to their proximity. This core displacement may explain stall for higher sweep angles prior to the burst point reaching the apex<sup>16</sup>. For the case of the yawed wing, with lower nominal sweep than the effective value, opposite vortices would not have the same proximity and would not interact in the same manner. This may be why this predictive technique becomes less accurate for effective sweep angles greater than  $70^\circ$ .

This flow field dependence on the effective sweep and attack angles was used to estimate the burst point behavior. The roll angle range, within which the burst point was over the surface, was only a small portion of the tested roll angle range. In the remainder of the range this effective sweep angle concept allows for speculation about the static loading behavior. In particular, trends in the rolling moment data could be estimated.

Using the effective angle estimates discussed above, the effective leading edge sweep and attack angles were calculated for a  $65^\circ$  swept wing with a  $30^\circ$  nominal angle of attack and a range of roll angles. The results are plotted as the solid curve in Fig. 9. The upper half of the curve represents the leeward wing and the lower half, the windward wing.

Also included on the graph (open circles) are the stall angles for a range of delta wing sweep angles<sup>1,15,16,20</sup>. These data were taken from the flow over complete delta wing models. The flat plate rectangular wing was assumed to stall at about  $7^\circ$  angle of attack. The dashed line on the graph represents an average stall angle for the different sweep angles and divides the graph into stalled and unstalled regions. The effective sweep angle analysis would predict that movement of the windward wing into the stalled region would cause the flow over that wing to stall, along with a loss of lift.

Finally, a line was included at the  $90^\circ$  effective sweep position and is denoted as wingtip. Erickson<sup>21</sup> has shown, on highly swept wings, imparting a sideslip angle to the wing can cause the vortex to move off of the surface. The  $90^\circ$  position provided a limit for this type of behavior.

The results on Fig. 8 can be related to the rolling moments in the following manner. Earnshaw<sup>22</sup> showed that the lift curve slope for a lower swept wing is higher than for a higher swept wing if neither has stalled. On the figure the windward wing, with the lower effective sweep angle, would produce more lift than the leeward wing at the same angle of attack. If the moment arms about the root chord are assumed to be nearly equal, this loading behavior would provide a stabilizing rolling moment and a trim position at  $0^\circ$  of roll.

Movement of the windward wing into the stalled region would cause the lift produced by the windward wing to decrease. The leeward lift could then dominate and produce an unstable rolling moment. A limit factor to instability could be the movement of the leeward wing past the  $90^\circ$  effective sweep angle, which would cause the vortex to move off the surface, reducing the lift due to the presence of the vortex. The result would be an increase in the correcting moment back to  $0^\circ$  roll. Similarly movement of the windward wing back into the unstalled region at high roll angles should again produce a correcting moment back toward  $0^\circ$ .

For the test data ( $\Lambda = 65^\circ$ ,  $\sigma = 30^\circ$ ) the effective angle curve is in the unstalled region at  $0^\circ$  roll. As described above a statically stable roll point would be expected at  $0^\circ$ . This point was demonstrated in free-to-roll tests reported by Hanff<sup>2</sup>.

The effective angle curve intersects the estimated stall curve at approximately  $10^\circ$  roll. If the effective angle analysis holds, a destabilizing rolling moment would be produced for higher roll angles. When the roll angle was increased to  $50^\circ$ , however, the windward wing returns to the unstalled region and a stabilizing rolling moment would again be produced. A zero rolling moment and non-zero stable roll position must then occur somewhere between  $10^\circ$  and  $50^\circ$  of roll. Rolling moment and free-to-roll data for a  $65^\circ$  delta wing, reported by Hanff<sup>2</sup>, showed this general trend in the moment data with non-zero, static stability (critical) points at  $\pm 21^\circ$ .

Further results, also for the  $65^\circ$  model, were reported by Hanff<sup>2</sup> for attack angles of  $20^\circ$ ,  $25^\circ$ ,  $35^\circ$  and  $40^\circ$ . The corresponding stability points were at  $0^\circ$ ,  $|1.5^\circ|$ ,  $|11^\circ|$ , and  $0^\circ$ , respectively.

Using the current analysis, effective angle diagrams were plotted for these cases in Figs. 11-14.

In Fig. 10 the entire effective angle curve was well out of the stalled region for all cases. Only a stability point at  $0^\circ$  would be expected for this case, consistent with the Hanff's experimental results. The same results would be expected from Fig. 11. Hanff reported a slight deviation from that point.

For an attack angle of  $35^\circ$  (Fig. 12), the  $0^\circ$  roll position on the curve has moved into the stalled region. No rolling moment would be expected under these symmetric conditions, however, a increase in the roll angle moves the leeward wing into the unstalled region producing an destabilizing moment. No zero stability point was expected for this case. This analysis would again suggest the presence of a non-zero stability point. It does not provide the  $11^\circ$  trim point value reported by Hanff and again by Jenkins. This analysis would, at first, might suggest that the stability point would be at a position greater than the  $21^\circ$  value reported for an attack angle of  $30^\circ$  since the return to the unstalled region occurs at a higher roll angle. Other considerations, however, would have to be the roll angle where the leeward wing passes  $90^\circ$  effective sweep and that the wing is stalled for  $0^\circ$  roll. Also the flow behavior on either side of the wing, once one side has stalled, can no longer be considered as independent. These factors make it more impossible predict where the trim point would be located using this simple analysis.

In Fig. 13 ( $\alpha = 40^\circ$ ) the wing is well into the stalled region for  $\phi = 0^\circ$ . In this case the  $0^\circ$  roll position may become neutrally stable. Again it would be difficult to make accurate estimates of any non-zero statically stable roll positions.

Increasing the wing sweep angle could move the effective angle curve up and out of the stalled region. Rolling moment data from free-to-roll tests by Thompson for a  $80^\circ$  sweep wing shows no signs of the non-zero trim points. Increasing the sweep angle, however, moves the models into a regime where wing rock can occur, a dynamic problem which will not be addressed here.

For sweep angles less than  $70^\circ$ , the model predicts three stable point cases; one, two or three stable roll positions. One point can occur at  $0^\circ$  roll when the effective angle curve is outside the stall region. Two statically stable points can occur when the  $0^\circ$  point is slightly in the stalled region. Three points can occur when the  $0^\circ$  roll position is slight outside the stalled region and the effective angle curve passes through the stalled region.

## Conclusions

The results show that the vortex behavior on either side of a delta wing can be related to the effective sweep and the attack angles of the leading edge. Applications of an empirical equation for the burst point based on unyawed data showed good comparisons to yawed data for effective sweep angles below  $70^\circ$ . The differences may be due to the influence of the vortex on the opposite wing. This issue could be addressed in a parametric study comparing the flow over yawed and unyawed wings. Comparison of existing data from several authors is difficult due to the sensitivity of the flow to model leading edge shape.

The empirical equation was not based on physical phenomenon but rather was a curve fit for comparison between yawed and unyawed data. A similar formula based on the fluid dynamic should be developed. Such an equation could then be extended to apply to the dynamic data for which the reported data was a baseline. The importance of the effective sweep and attack angles, shown here, may help to develop this equation.

Finally the non-zero stability points, shown by Hanff, have been discussed from a different point of view. The simple analysis using effective sweep and attack angles provides and explanation for the general trends. An extended study to try to define the sweep and attack angle limitations of this behavior and to predict these points would be valuable.

## Bibliography

- <sup>1</sup>Lee, M., Ho, C-M, "Vortex Dynamics of Delta Wings" *Frontiers in Experimental Fluid Mechanics, Lecture Notes in Engineering*, Vol. 46, Springer-Verlag, Berlin, 1989, pp 365-427.
- <sup>2</sup>Hanff, E. S., Jenkins, S. B., "Large-Amplitude High -Rate Roll Experiments on a Delta and Double Delta Wing," AIAA Paper No. AIAA-90-0224, Jan 1990.
- <sup>3</sup>McLaughlin, T. E., "Aerodynamic Foundation for Use of Unsteady Aerodynamic Effects in Flight Control," Ph.D. Dissertation, Univ. of Colo. at Boulder, Aug 1992, pp 121-132.
- <sup>4</sup>Nelson, R. C., Visser, K. D., "Breaking Down the Delta Wing Vortex: The Role of Vorticity in the Breakdown Process," AGARD CP-494, Oct 1990, pp 21-1 - 21-15.
- <sup>5</sup>Sarpkaya, T., "On Stationary and Travelling Vortex Breakdowns," *Journal of Fluid Mechanics*, Vol. 45, 1971, pp. 545-559.
- <sup>6</sup>Jumper, E. J., Nelson, R. C., Cheung, K., "A Simple Criterion for Vortex Breakdown", AIAA Paper No. AIAA-93-0866, Jan 1993.
- <sup>7</sup>Leibovich, S., "The Structure of Vortex Breakdown," *Ann. Rev. of Fluid Mech.*, Vol. 10, 1978.
- <sup>8</sup>Faler, J. H., Leibovich, S., "Disrupted States of Vortex Flow and Vortex Breakdown," *Phys. of Fluids*, Vol. 20, No. 9, Sep. 1977, pp 1385-1400.
- <sup>9</sup>Kegelman, J., Roos, F., "Effects of Leading-Edge Shape and Vortex Burst on Flowfield of a 70 Degree Sweep Delta-Wing", AIAA Paper No. AIAA-89-0086, Jan 1989.
- <sup>10</sup>Gad-el-Hak, M., Blackwelder, R. F., "The Discrete Vortices from a Delta Wing," *AIAA Journal*, Vol. 23, No. 6, June 1985, pp 961-962.
- <sup>11</sup>Beyers, M. E., Ericsson, L. E., "Ground Facility Interference in Aircraft Configurations with Separated Flow," *J. Aircraft*, Vol 30, No. 5, 1993, pp. 682-688.
- <sup>12</sup>Roos, F. W., Kegelman, J. T., "An Experimental Investigation of Sweep-Angle Influence on Delta-Wing Flows", AIAA Paper No. AIAA-90-0383, Jan 1990.
- <sup>13</sup>McKernan, J. F., Payne, F. M., Nelson, R. C., "Vortex Breakdown Measurements on a 70 Deg Sweepback Delta Wing", *J. Aircraft*, Vol. 25, No. 11, Nov 1988, pp 991-992.
- <sup>14</sup>Ericsson, L. E., "The Fluid Mechanics of Slender Wing Rock", *J. Aircraft*, Vol. 21, No. 5, May 1984, pp 322-328.
- <sup>15</sup>Earnshaw, P. B., Lawford, J. A., "Low-Speed Wind-Tunnel Experiments on a Series of Sharp-Edged Delta Wings", *R&M No. 3424*, Mar 1964.
- <sup>16</sup>Wentz, W. H., Kohlman, D. L., "Vortex Breakdown on Slender Sharp-Edged Wings", *J. Aircraft*, Vol. 8, No. 3, Mar 1971, pp 156-161.
- <sup>17</sup>Payne, F. M., Ng, T. T., Nelson, R. C., "Visualization and Wake Surveys of the Vortical Flow over a Delta Wing", *AIAA Journal*, Vol. 26, No. 2, Feb. 1988, pp 137-143.
- <sup>18</sup>Lambourne, N. C., Bryer, D. W., "The Bursting of Leading-Edge Vortices - Some Observations and Discussion of the Phenomenon," *R & M No. 3282*, April, 1961.
- <sup>19</sup>Ericsson, L. E., King, H. H. C., "Effect of Cross-Sectional Geometry on Slender Wing Unsteady Aerodynamics," *J.Aircraft*, Vol. 30, No. 5, 1993, pp 793-795.
- <sup>20</sup>Huyer, S. A., "Forced Unsteady Separated Flows on a 45 Degree Delta Wing," Ph.D. Dissertation, Univ. of Colo. at Boulder, May 1991, p 73.
- <sup>21</sup>Erickson, G. E., "Water Tunnel Studies of Leading-Edge Vortices," *J. Aircraft*, Vol. 19, No. 6, June 1982, pp 442-448.
- <sup>22</sup>Hanff, E. S., Ericsson, L. E., "Multiple Roll Attractors of a Delta wing at High Incidence," *AGARD Symposium on Vortex Flow Aerodynamics*, AGARD CP 494, Oct 1990.
- <sup>23</sup>Jenkins, J. E., Myatt, J. H., "Body-Axis Rolling Motion Critical States of a 65-Degree Delta Wing," AIAA Paper No. AIAA 93-0621, Jan 1993.

<sup>24</sup>Thompson, S. A., Arena, A. S. Jr., Nelson, R. C., Batill, S. M., "Dynamic Surface Pressure Measurements on a Delta Wing Constrained to a Pitching or Rolling Motion," NASA Conf. Pub. 3149, *Proceedings from High Angle of Attack Technology Conference*, Langley Research Center, Hampton, VI, pp 1003-1023, May 1992

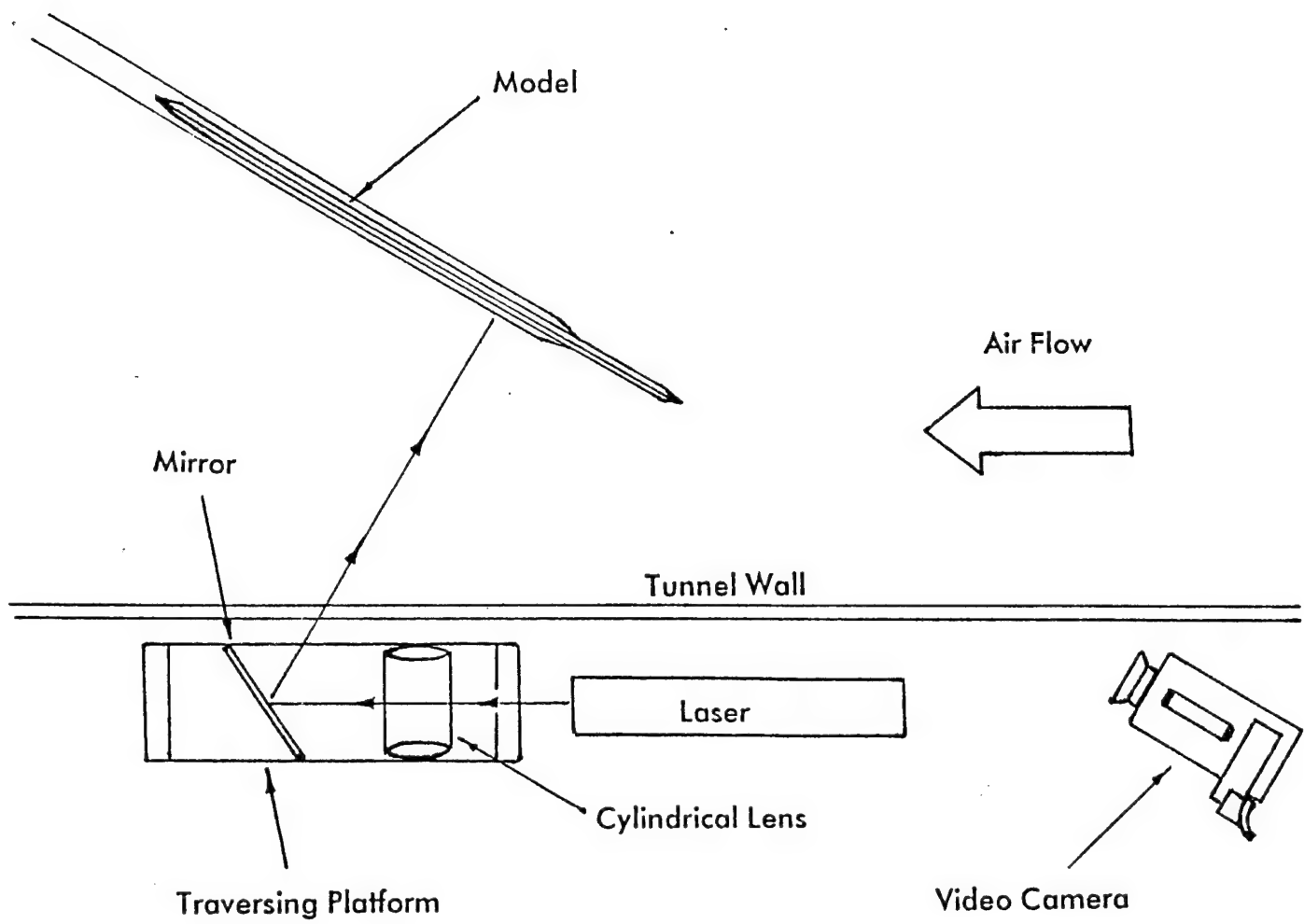


Figure 1. Experimental Set Up

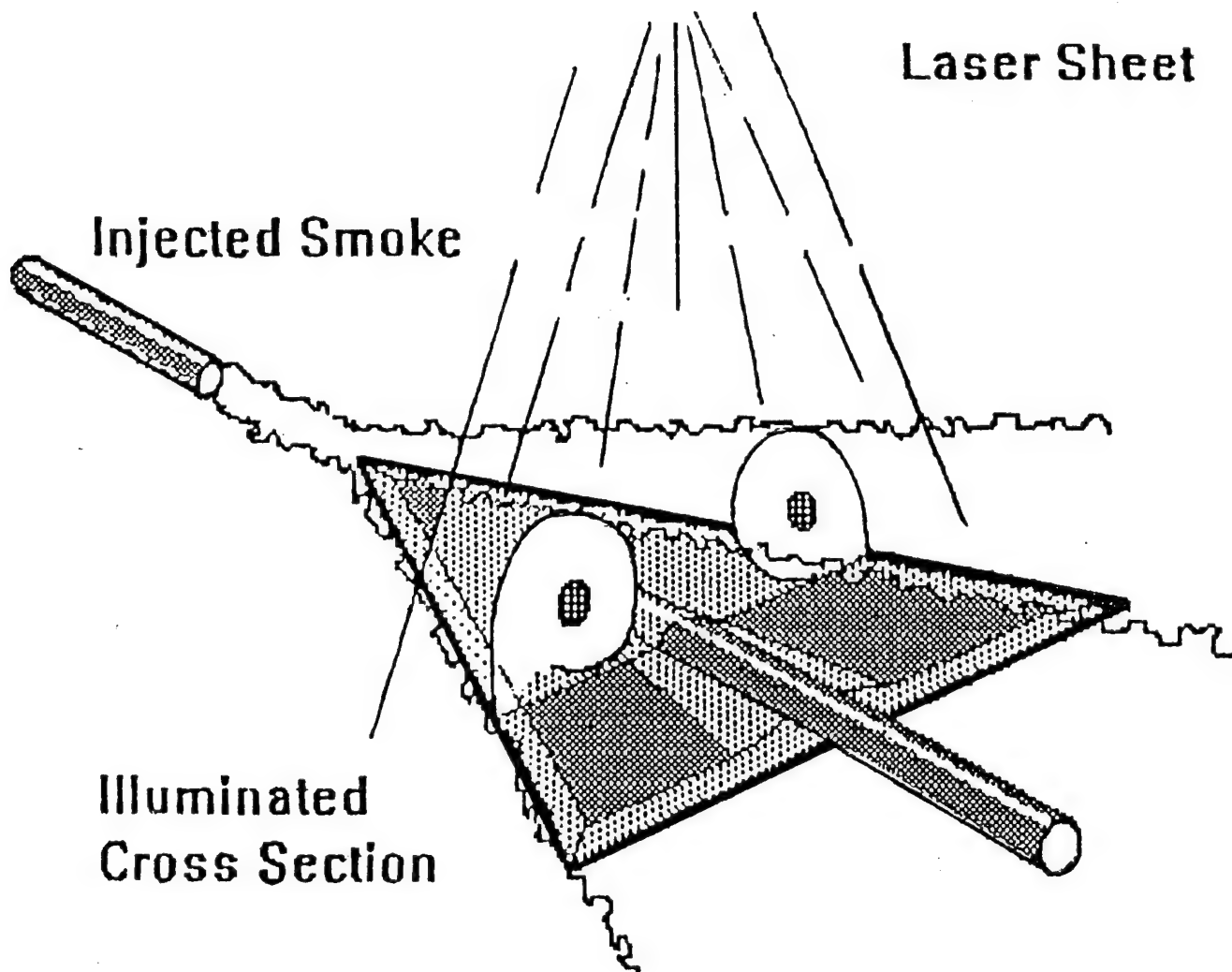


Figure 2. Caricature of the flow visualization results.

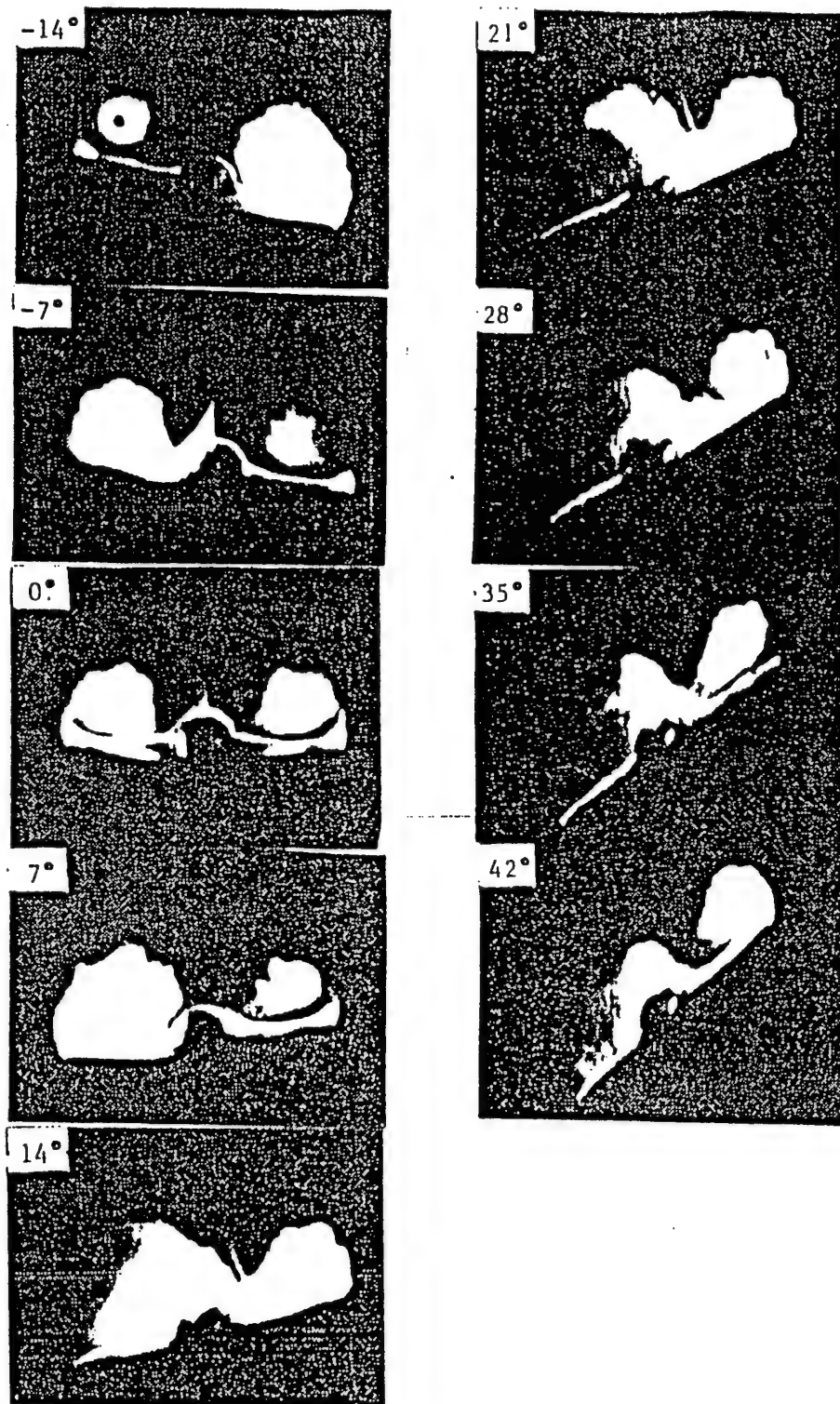


Figure 3. Flow visualization images; recorded at the 60% chord position,  $\sigma = 30^\circ$ ,  $\phi = -14^\circ$  to  $42^\circ$ .

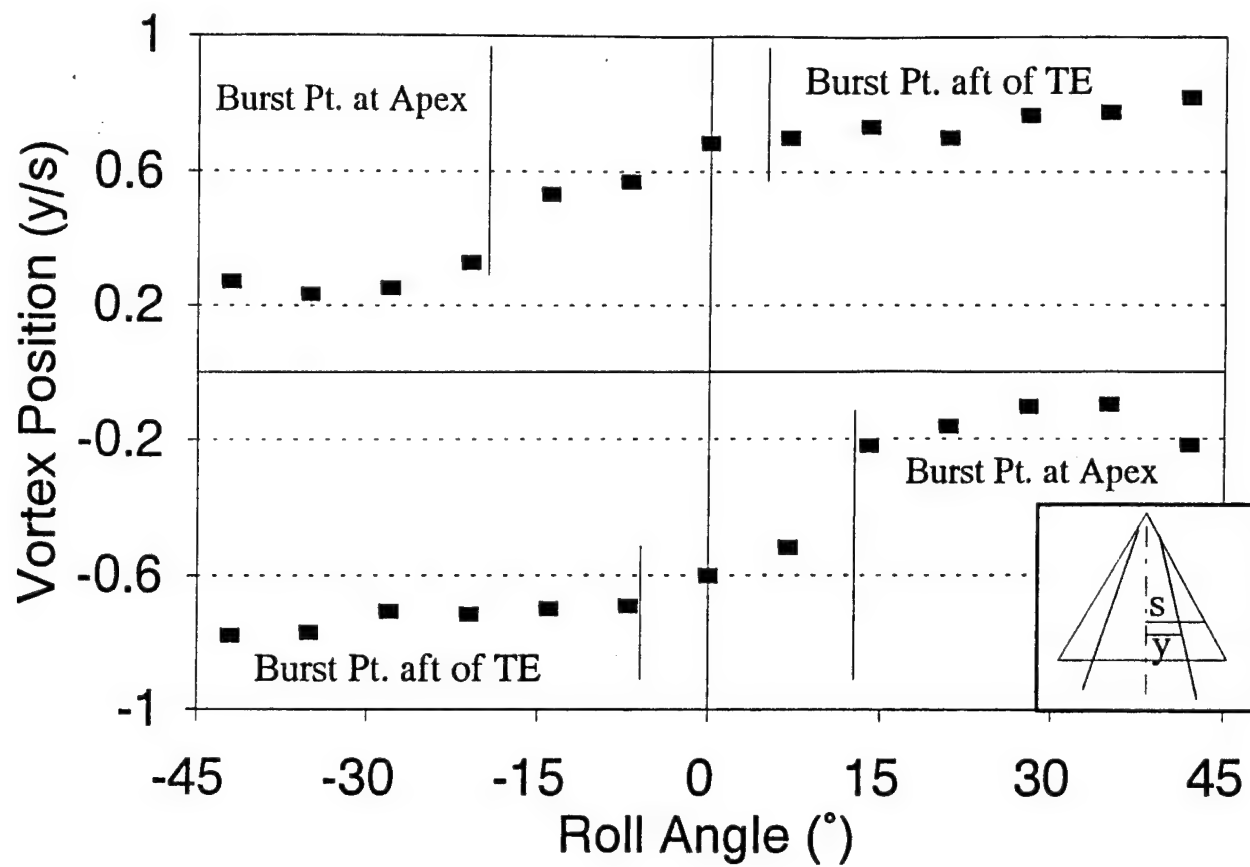


Figure 4. Vortex relative spanwise positions; recorded at the 60% chord position,  $\sigma = 30^\circ$ ,  $\phi = -42^\circ$  to  $42^\circ$ .

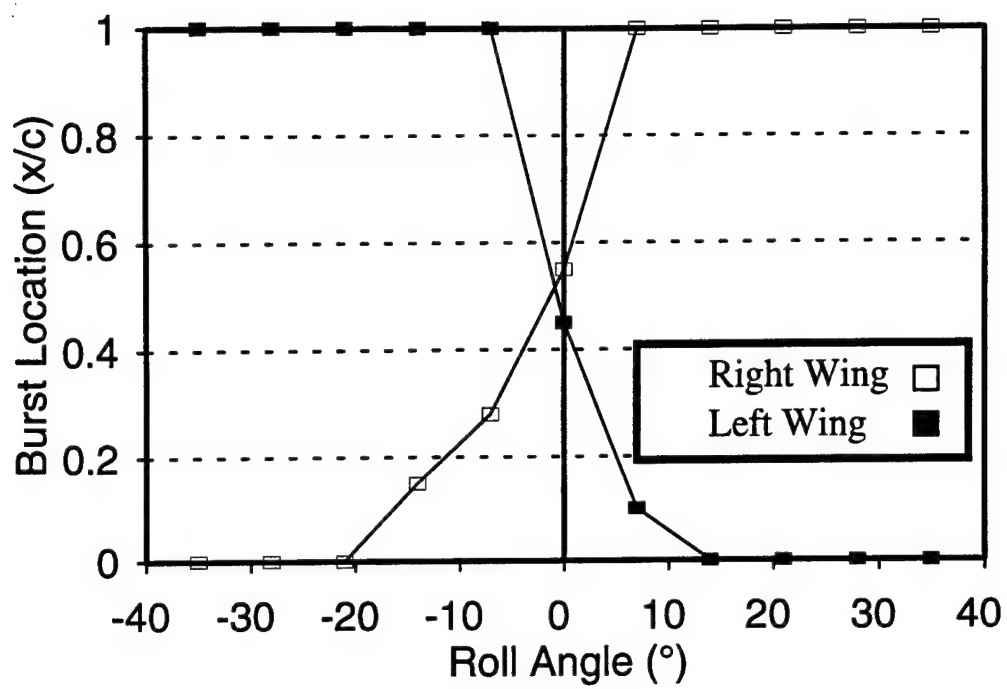


Figure 5. Vortex burst point relative chordwise positions,  $\sigma = 30^\circ$ ,  $\phi = -42^\circ$  to  $42^\circ$ .

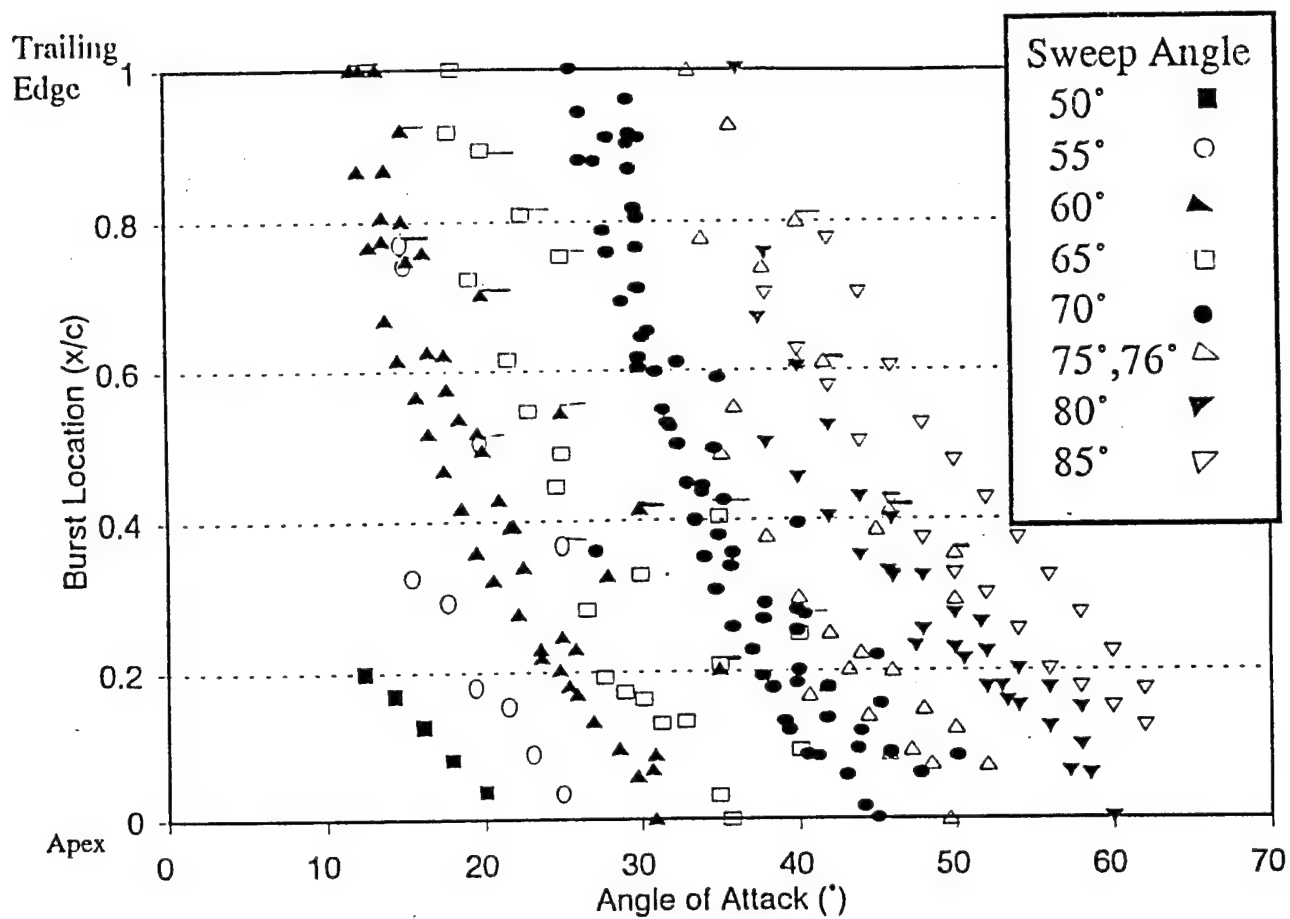


Figure 6. Relative vortex burst positions versus angle of attack for  $\Lambda = 50^\circ$  to  $85^\circ$  (References 10, 13, 14, 15).

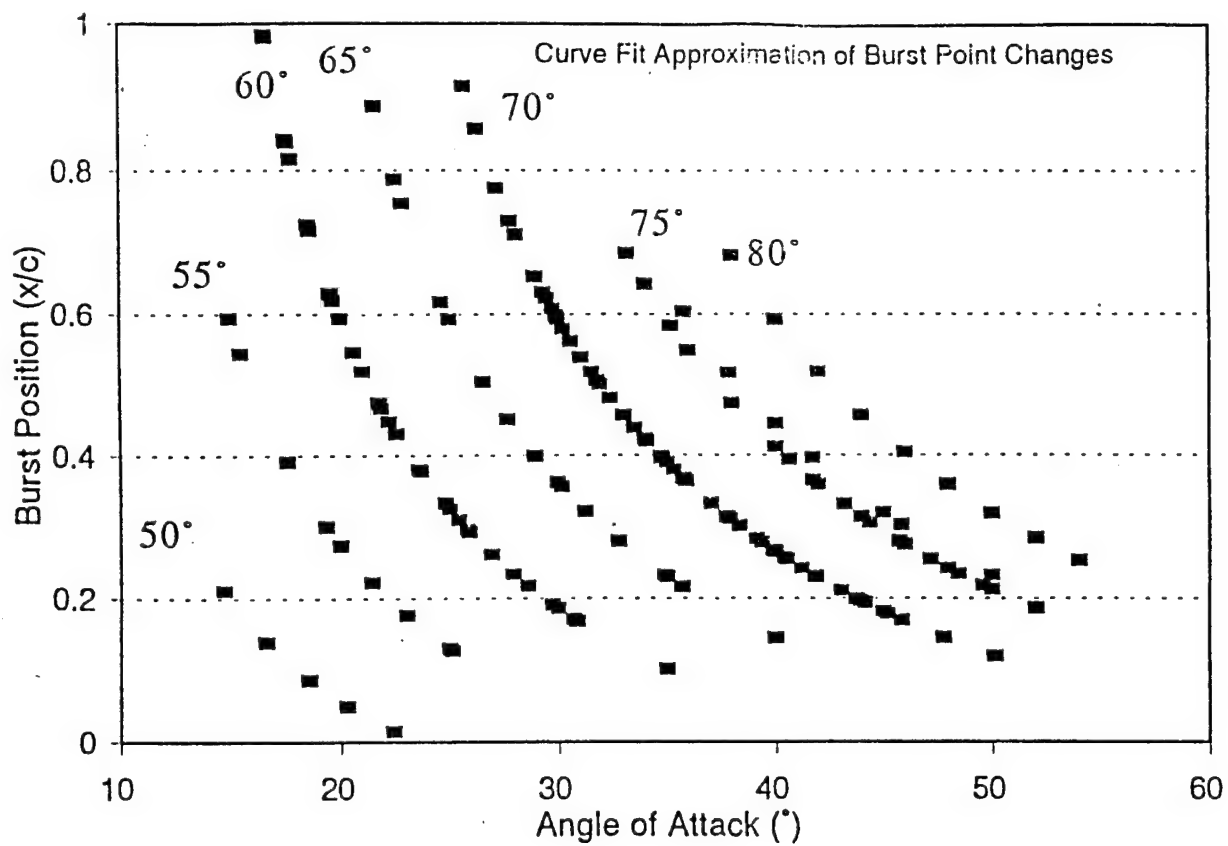


Figure 7. Approximated burst point data based on a curve fit of the data in Fig. 5.

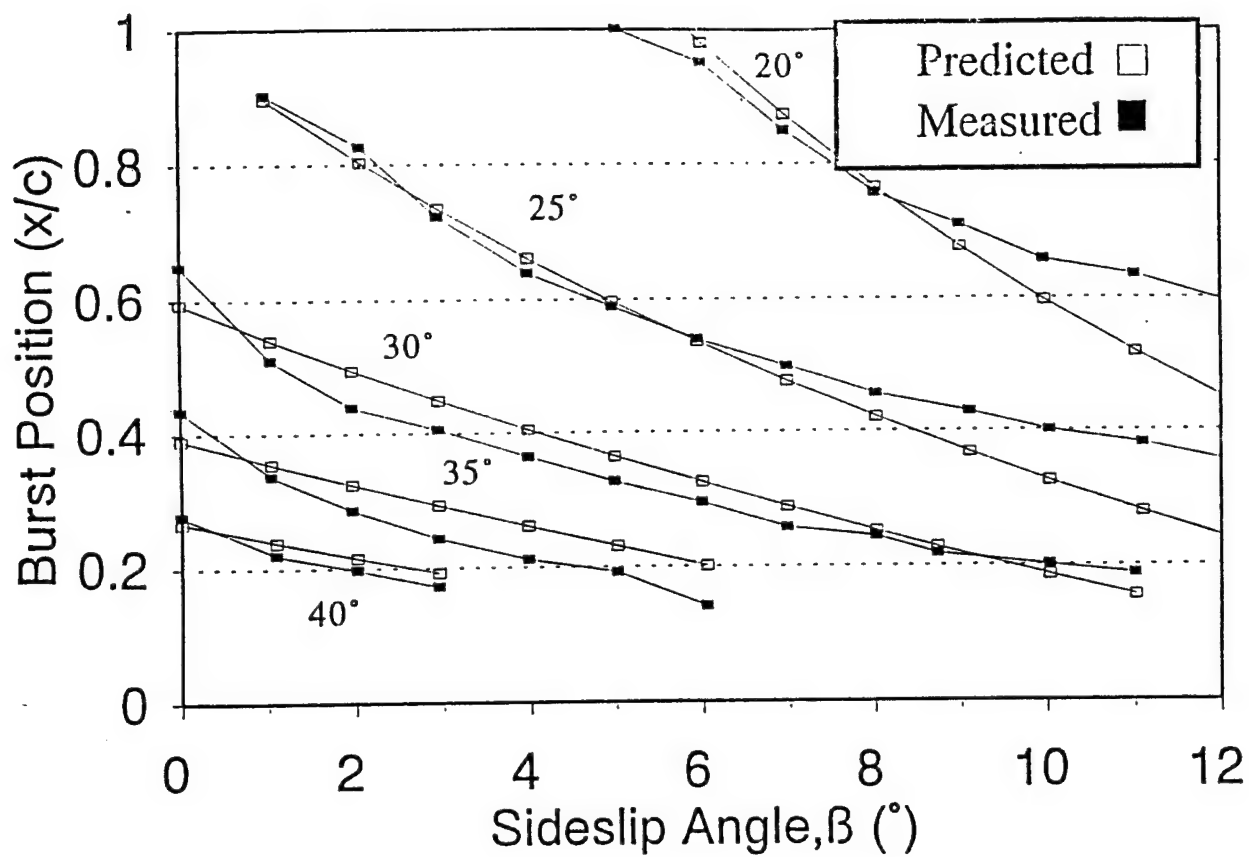


Figure 8. Burst point position data taken on a yawed  $70^\circ$  swept delta wing compared to the curve fit approximation (Reference McKernan<sup>11</sup>).

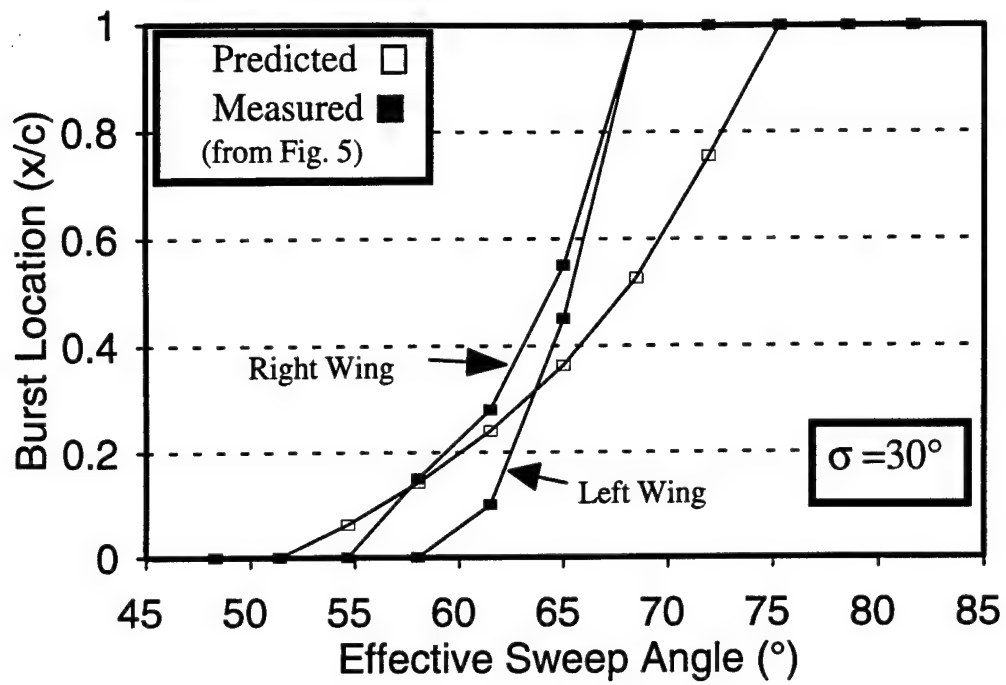


Figure 9. Burst point position from Fig. 5 compared to burst point function approximation.

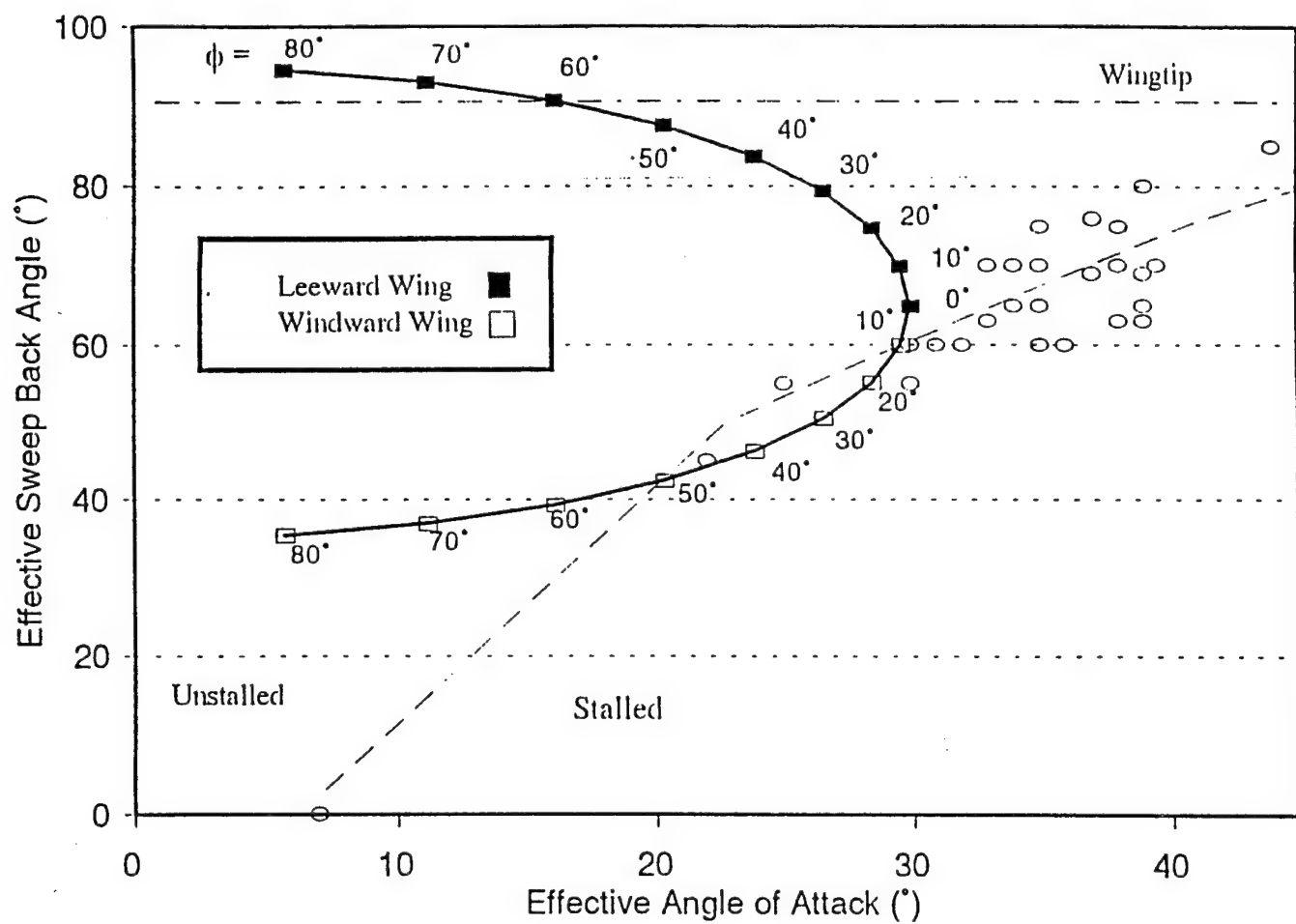


Figure 10. An effective sweep angle and effective angle of attack curve plotted over the effective angle map showing the stalled regime for the delta wing;  $\sigma = 30^\circ$ ,  $\Lambda = 65^\circ$ ,  $\phi = 0^\circ$  to  $80^\circ$ .

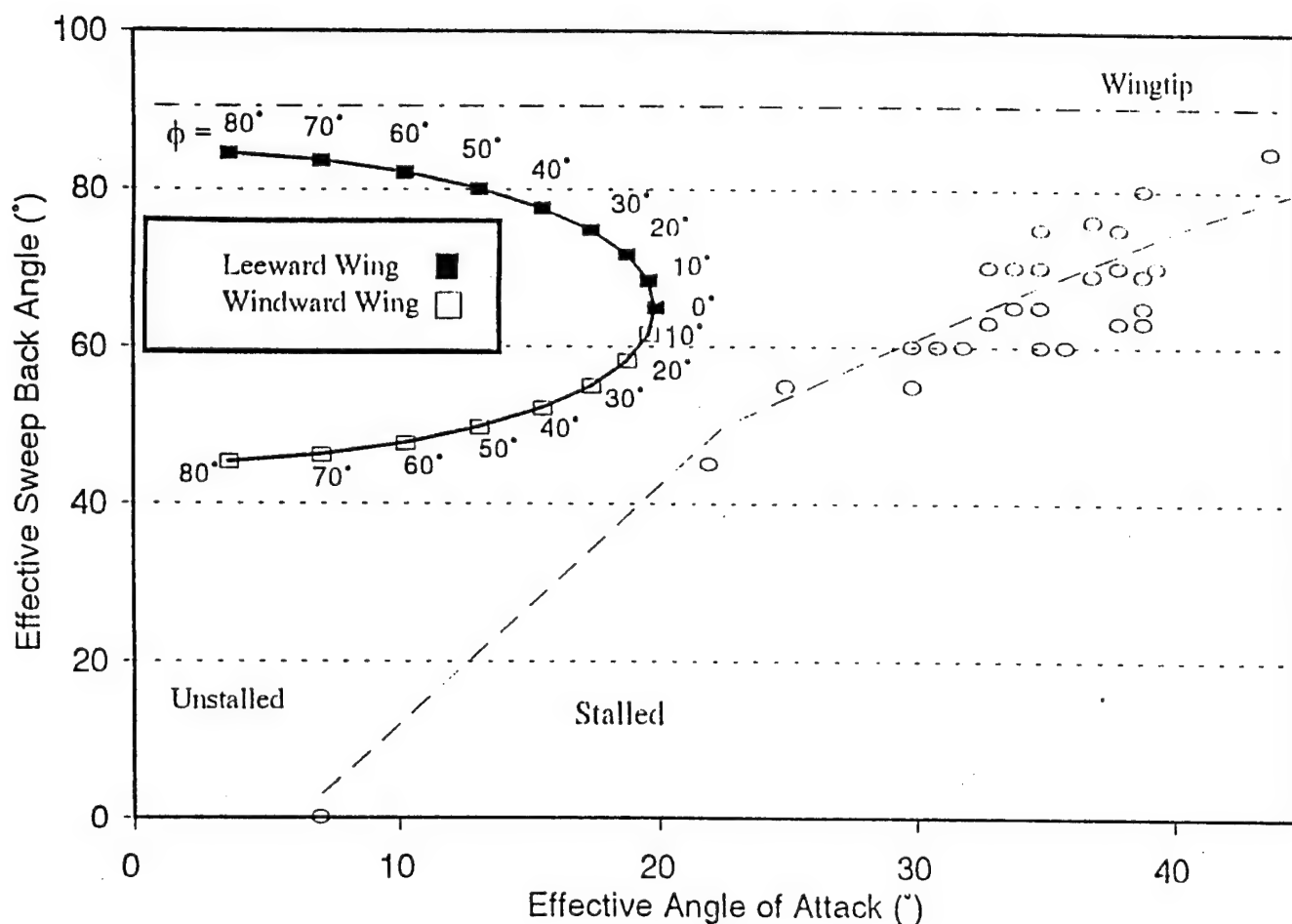


Figure 11. An effective sweep angle and effective angle of attack curve plotted over the effective angle map showing the stalled regime for the delta wing;  $\sigma = 20^\circ$ ,  $\Lambda = 65^\circ$ ,  $\phi = 0^\circ$  to  $80^\circ$ .

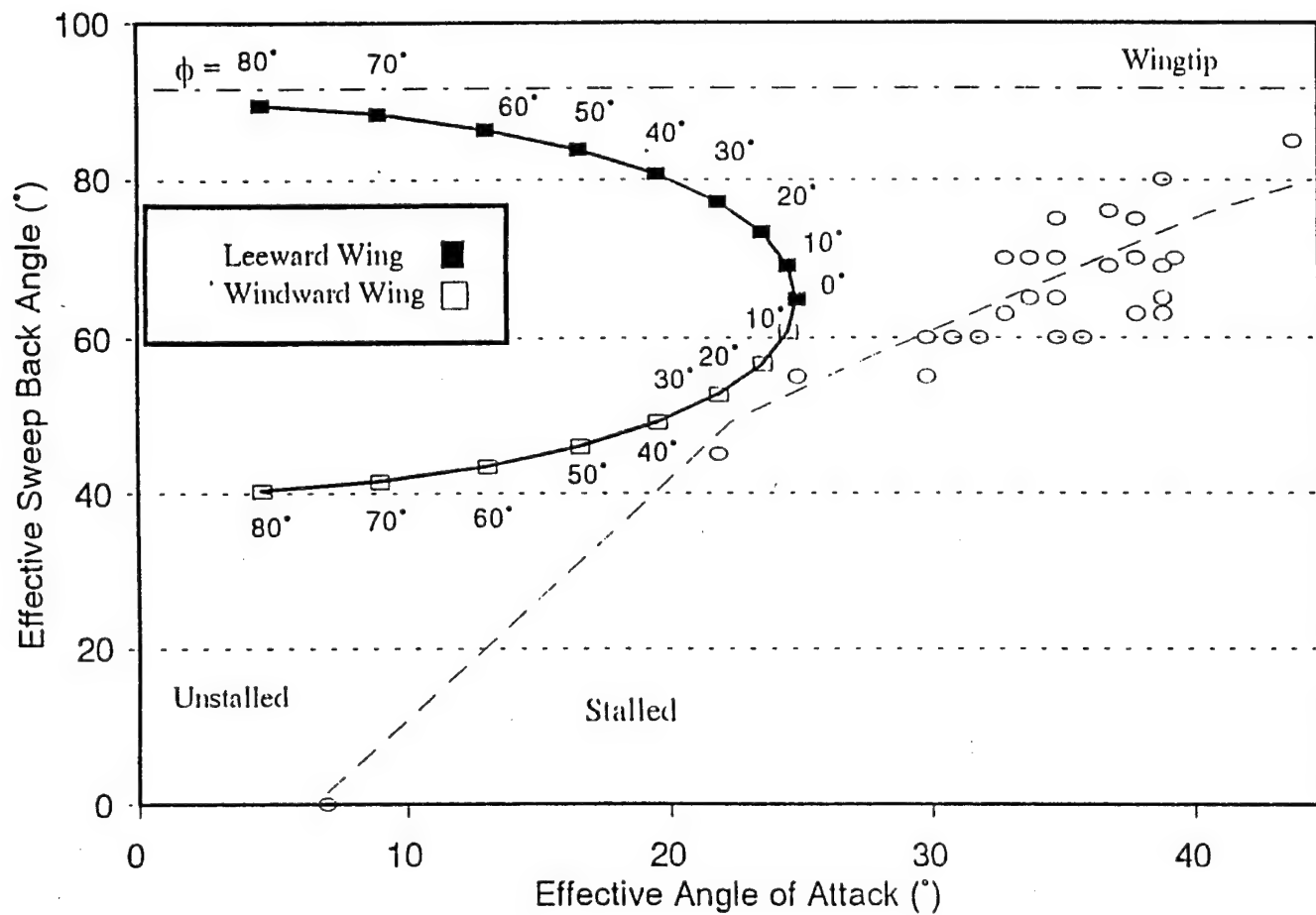


Figure 12. An effective sweep angle and effective angle of attack curve plotted over the effective angle map showing the stalled regime for the delta wing;  $\sigma = 25^\circ$ ,  $\Lambda = 65^\circ$ ,  $\phi = 0^\circ$  to  $80^\circ$ .

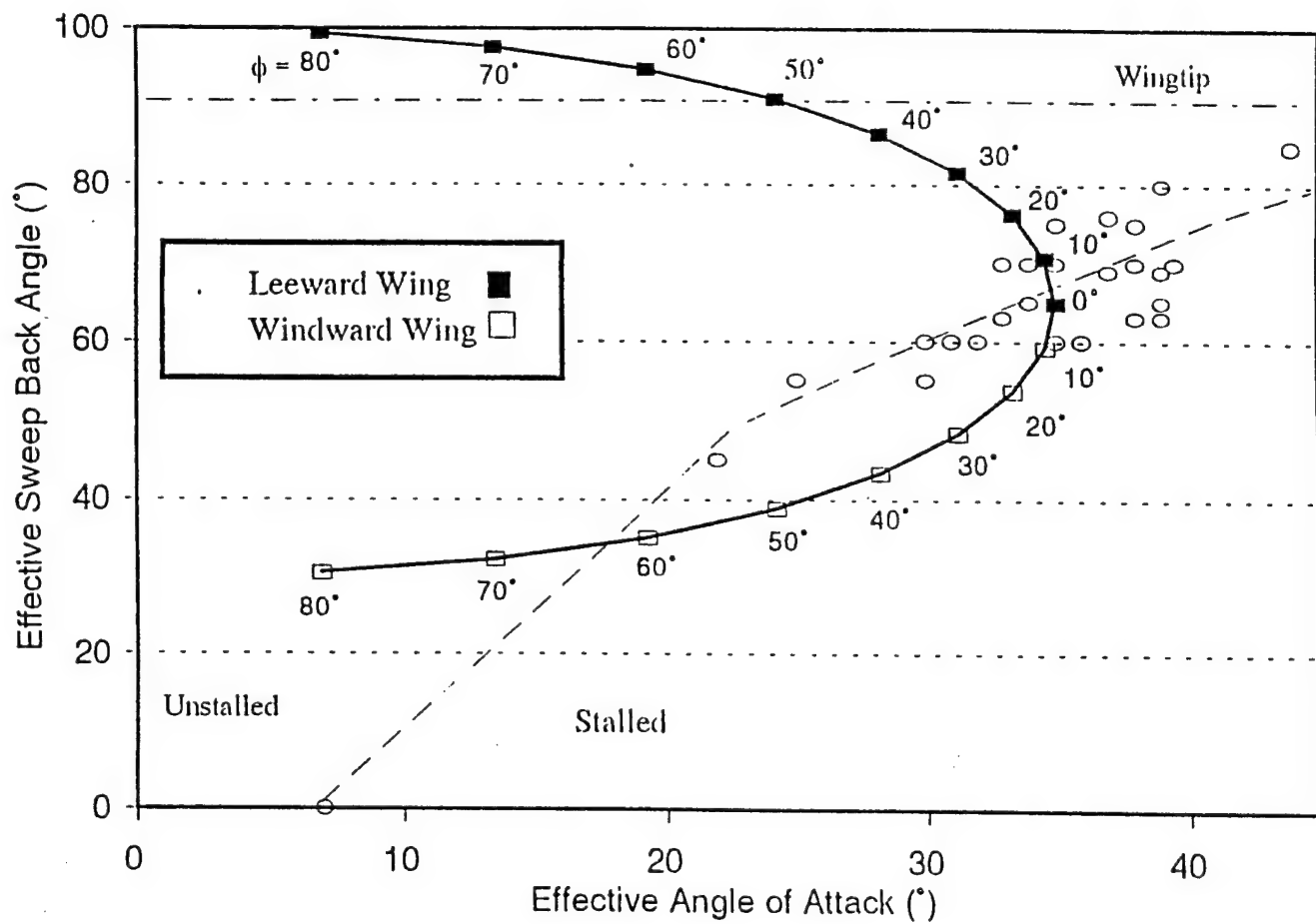


Figure 13. An effective sweep angle and effective angle of attack curve plotted over the effective angle map showing the stalled regime for the delta wing;  $\sigma = 35^\circ$ ,  $\Lambda = 65^\circ$ ,  $\phi = 0^\circ$  to  $80^\circ$ .

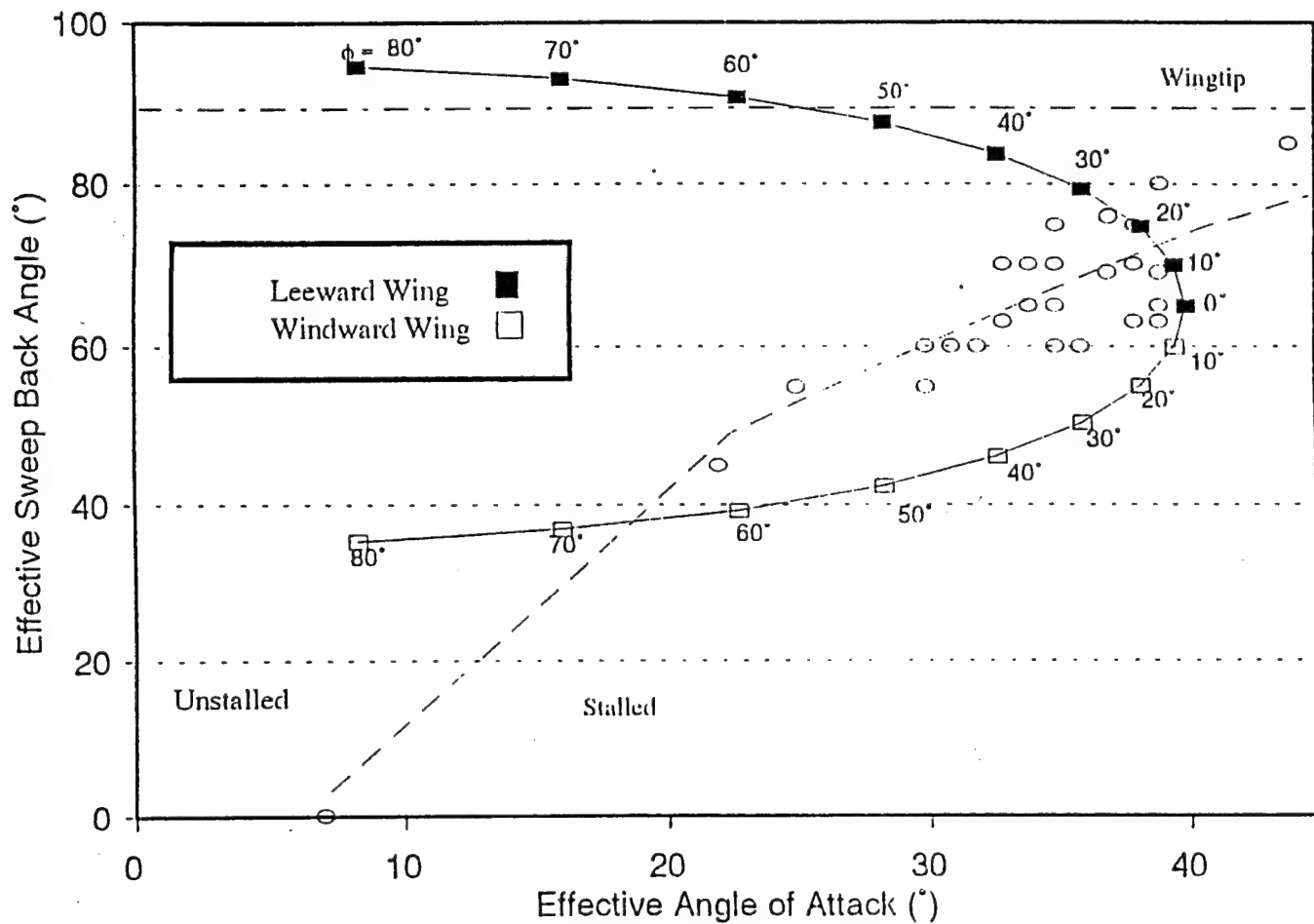


Figure 14. An effective sweep angle and effective angle of attack curve plotted over the effective angle map showing the stalled regime for the delta wing;  $\sigma = 40^\circ$ ,  $\Lambda = 65^\circ$ ,  $\phi = 0^\circ$  to  $80^\circ$ .



**AIAA 94-2284**

**FLOW VISUALIZATION INVESTIGATION OF  
THE WAKE BEHIND AN OGIVE CYLINDER**

**D. Bunker, M. Luttges, M. Robinson**  
University of Colorado  
Boulder, CO

**25th AIAA Fluid Dynamics  
Conference**

**June 20-23, 1994 / Colorado Springs, CO**

# FLOW VISUALIZATION INVESTIGATION OF THE WAKE BEHIND AN OGIVE CYLINDER

D. Bunker\*, M. Luttges\*\* and M. Robinson\*\*\*

Aerospace Engineering Sciences  
University of Colorado, Campus Box 429  
Boulder, CO 80309

## Abstract

The wake development behind an ogive cylinder was investigated using smoke-wire visualization methods. Both steady and unsteady flow structures were examined over a wide range of incidence angles and reduced frequencies. Results show a qualitative similarity between the static and dynamic wake development. At lower reduced frequencies, the dynamic wake development appears to be a phase-shifted variation of static wake development. Finally, an analytic model is proposed to explain the wake development behind a slender body.

## Nomenclature

D	Maximum body diameter
f	Oscillation frequency (Hz)
g	Distance from nose tip to vortex separation location
k	Reduced frequency ( $\pi f l / V_{\infty}$ )
l	Distance from tip to pivot point
L	Overall model length
Re	Reynolds number, $V_{\infty} L / \nu$
w	Wake width
$\alpha_{\omega}$	Oscillation amplitude
$\alpha$	Static or instantaneous angle of attack
$\alpha_m$	Mean pitch angle

## Subscripts

A	Aftbody
N	Nose

## Introduction

Modern fighter designs are characterized by long, slender noses well forward of the aircraft's center of gravity. This configuration complicates aircraft maneuverability through the post-stall flight regime. Vortical flows generated by the extended forebody produce non-linear aerodynamic loading which make predictable control extremely difficult. Missiles launched in a highly dynamic environment or at large incidence angles experience similar problems. Ultimately, in order to utilize both dynamic and high- $\alpha$  environments, comprehensive control paradigms need to be developed based upon an understanding of the vortical flow phenomenology.

The aerodynamics associated with slender bodies of revolution at high angles of attack have been the subject of numerous investigations<sup>1</sup>. At sufficiently high angle of attack, an asymmetric vortex wake develops which produces significant side force loading. Attempts to quantify and control the magnitude and direction of the wake asymmetry have met with varying degrees of success. The reader is referred to reviews by Hunt<sup>2</sup> and Ericsson & Reding<sup>3</sup> for thorough discussions of high angle-of-attack asymmetric flow separation studies.

Since most maneuvers involve rapid attitude changes, it is necessary to both predict and control the resulting wake structures. Smith and Nunn<sup>4</sup> found a slight increase in normal force associated with a slender body pitched from 0° to 90°. They attributed the effect to a motion-induced delay in wake transition. Gad-el-Hak and Ho<sup>5</sup> investigated the wake structure of an ogive-cylinder oscillating in pitch. The model was pitched about the mid-chord while traversed through a towing tank. Flow visualization results were reported for a variety of reduced frequencies at angles of attack ranging from 0° to 30°. They noted a strong hysteresis in vortex position not unlike that seen for pitching delta wings.

\* Graduate Research Assistant, Aerospace Engineering Sciences, Member AIAA

\*\* Professor, Aerospace Engineering Sciences, Member AIAA

\*\*\* Research Associate, Aerospace Engineering Sciences, Member AIAA

Montividas Reisenthal and Nagib<sup>6</sup> conducted smoke wire visualizations of the wake structure generated behind a pitching ogive cylinder. A variety of cylinder lengths and pitch rates were investigated. The dynamic nose vortex separation locations data collapsed when plotted against the pitch rate non-dimensionalized by the distance from the tip to the pitch point rather than body diameter. This definition of non-dimensional pitch rate is adopted in this investigation.

Stanek and Visbal<sup>7</sup> developed a Navier-Stokes based model of the vorticity field development over a 3.5 caliber ogive forebody undergoing a 0° to 20° pitch up maneuver. Strong shear layers and their roll-up into dynamic stall-like vortical structures was observed as the body decelerated. Subsequent vortex/surface interactions produced secondary separation regions, ejection of vorticity from the surface and localized regions of high suction.

The most recent investigations of dynamic slender bodies were completed by Panzer, Rediniotis and Telionis<sup>8</sup> and Hoang, Wetzel and Simpson<sup>9</sup>. Panzer *et al.* mapped the velocity flow field behind a hemisphere-cylinder using laser-Doppler velocimetry and seven-hole probes. Hoang *et al.* measured the surface pressures of a spheroid undergoing a pitch-up maneuver. The delay in wake development was noted in both investigations.

The wake structure behind a slender body at various angles of attack is quite complicated. A number of very different flow characteristics evolve as the pitch angle varies from 0° to 90°. Each change in wake structure reflects a different methodology to shed vorticity generated in the boundary layer. A more complete understanding of these characteristics is necessary in order to develop effective control and prediction strategies related to the underlying physics governing slender body wake characteristics.

This investigation documented the large-scale flow structures generated by an ogive cylinder at angles of attack ranging from 0° to 90°. First, static flow visualization data were collected to quantify the various flow structures. These data provided the metrics for subsequent dynamic tests. Quantitative comparisons were then made between the steady and unsteady test conditions in order to evaluate any change in the characteristics of the wake structures produced.

### Experimental Facilities

The experiments were conducted in the University of Colorado's large subsonic (2'x2') wind tunnel. A variable-speed DC motor coupled to a fixed-pitch fan allows test section velocities from 0 to 65 fps. One entire side wall is constructed of clear cast acrylic to allow unobstructed visualization. A circular polycarbonate window in the test section ceiling is used for top-view visualization. The freestream turbulence level was previously measured at less than 0.05%.

The model used in all tests consisted of an ogive nose attached to a cylindrical aftbody (Figure 1). The overall model dimensions were 13.9" long and 1.65" in diameter. The nose was 8.4" long and the aftbody was 5.5" long providing a length to diameter ratios of  $L_N/D$  of 5.0 and  $L_A/D = 3.4$ , respectively. The nose tip bluntness ratio, defined as the local nose radius divided by the body diameter was 7.5%. The models were tested at freestream velocities of 6.6 fps and 15 fps. The Reynolds numbers based on body diameter were 5,000 and 12,000. Pitch frequencies were varied between 2.2 Hz and 5 Hz. Pitch amplitude and pivot point were held constant at 10° and 10.5" from the tip, respectively.

A double smoke-wire located upstream of the model provided flow visualization. The smoke wires were stretched vertically and offset approximately 1 mm to either side of the model centerline. A mixture of theatrical fog fluid and 20W50 weight motor oil coated on the wires was ohmically heated to produce uniformly dense streaklines with a duration of approximately 2-3 seconds. The smoke wires could be independently heated to permit visualizations of just one side of the model.

The resulting vortical flow structures were photographed with a 35mm camera located outside of the tunnel test section. Camera positions above and to the sides of the test model produced orthogonal perspectives. High-intensity strobes mounted downstream of the test section illuminated the streaklines with 7  $\mu$ sec flash pulses. For the dynamic motion cases, the strobe flash was phase-locked to specific angles. Some photos were also taken with the camera positioned inside the test section at a point directly downstream of the model. In this configuration, strobes were mounted on the top of the test section directly above the base of the model. The flash was constricted to a narrow plane to produce a

light sheet which allowed examination of the wake cross-sectional properties.

A Kodak Ektapro 1000 high-speed video camera was used to capture the time dependent nature of certain flow events. Flow events were videotaped at 500 full-frames per second. The Kodak videotaped images were downloaded to standard VHS format tapes for later analysis.

## Results

### Steady State

Photographs were taken from the side and top of the test section at model pitch angles ranging from  $0^\circ$  to  $90^\circ$ . The Reynolds numbers based on maximum body diameter were 5,000 and 12,000. The smoke wires were heated independently during the side view photographs so that the near and far sides of the wake (looking from the side) could be differentiated and analyzed separately. The right and left sides of the wake structure are more easily distinguishable from above the model, thus, both smoke wires were heated simultaneously for top view photos. This latter approach also produced symmetric thermal heating in the flow about the model thereby reducing asymmetric flow perturbations from being introduced upstream.

The wake asymmetry has been shown to be highly sensitive to model nose roll angle<sup>10</sup>. Fortunately, the wake tends to favor a 'regular' state over wide ranges of nose roll angle<sup>11</sup>. The roll angle sensitivity of the model used in this study was determined and the regular states were identified. The nose roll angle was set at approximately the midpoint of one of these regular states and care was taken throughout testing to ensure that the nose roll angle remained at that angle.

Wake sensitivity to minor variations in freestream direction was also investigated. The pitch angle was varied from  $0^\circ$  to  $90^\circ$  at yaw angles of  $\beta = \pm 2^\circ$ . No noticeable differences in large-scale wake structures compared to the zero sideslip case were evident, thus eliminating minor freestream variations as possible causes of flow asymmetry at the specific roll angle investigated.

Figure 2 is representative of the wake structure development as the model angle of attack is increased from  $0^\circ$  to  $90^\circ$ . The first column contains actual visualizations while the second contains caricatures to clarify and highlight the main flow features. Although

the wake structure developed from a static slender body have been extensively studied, static results are presented here for later comparison with dynamic results.

The photo/caricature pair in the top row is representative of the wake structure at very small incidences. From  $\alpha = 0^\circ$  to  $10^\circ$ , the flow over the model remains attached to the surface. The only large-scale flow disruption is the bluff body wake.

At approximately  $\alpha = 10^\circ$ , a pair of counter-rotating vortices develop over the leeward side of the model (Figure 2, second row). These nose vortices grow larger as the incidence angle is increased. Base shedding is also evident.

Between  $\alpha = 25^\circ$  and  $\alpha = 30^\circ$ , the near side vortex separates from the model surface (Figure 2, third row). Separation of the far side vortex occurs at approximately  $35^\circ$ . Asymmetric nose vortex separation locations have been linked to the onset of significant asymmetric side force loading<sup>2</sup>. The onset of asymmetric separation locations in this investigation is consistent with the previously documented data for this model geometry.

Figure 3 is an enlargement of the shear layer between the separated near side vortex and the model surface. The shear layer clearly exhibits a pronounced and well-behaved instability. The nature of this instability is unknown, however, the frequency corresponds to periodic variations in the density of the freestream smokelines. To the authors' knowledge, this instability has not been previously visualized. However, Degani and Ziliac<sup>12</sup> noted fluctuations in surface pressure measurements in the region of the nose vortex separation point which they attributed to a shear layer instability.

The last photograph and caricature of Figure 2 contain all the events present in the wake from  $\alpha = 45^\circ$  to  $70^\circ$ . Downstream of the nose vortex separation locations, aftbody vortices develop which grow larger with angle of attack. These aftbody vortices exist over about  $10^\circ$  angle of attack range before transforming into periodic aftbody shedding. The nose vortex streaklines remain stable and coherent up to  $\alpha = 55^\circ$ . From  $\alpha = 55^\circ$  to  $\alpha = 70^\circ$ , the nose vortices are still distinctly separate from the aftbody shedding, however, they also appear to shed structures in a discrete, periodic fashion.

Beginning at  $\alpha = 70^\circ$ , the nose vortices alternate between two shedding methods: at some times the nose vortices are distinctly separate from the lower wake, but at other times they merge with the lower wake. This transition from one type of shedding to the other occurs randomly. The vortex transition region extends up to  $\alpha = 80^\circ$ , at which point the wake sheds periodically from one side to the other, much like Karman vortex shedding.

### Dynamic

The ogive-cylinder was pitched about the center of gravity of the model and support system to minimize inertia effects. The distance from the tip to the center of gravity was 11". All photographs were taken with the shutter open while the five strobe flash events, phase locked to pitch motion, were collected. The mean angle of attack was varied from  $\alpha_m = 10^\circ$  to  $\alpha_m = 70^\circ$ , however, the pitch amplitude cases was held constant at  $10^\circ$ . Testing was conducted at freestream velocities of 6.5 ft/sec and 15 ft/sec and at pitch frequencies of 2 Hz and 5 Hz to produce reduced frequencies of  $k = 0.4, 0.8$  and  $2.0$ . The non-dimensionalizing length was the distance from the tip to the pivot point.

Figure 4 depicts the typical sequence of events in the near side flow structure development behind the ogive-cylinder for the three non-zero reduced frequencies considered. Static results are presented for comparison. The unsteady results were photographed a mean pitch angle,  $\alpha_m$ , of  $30^\circ$ .

At the minimum angle of attack,  $\alpha = 20^\circ$  (top row), the dominant feature at both  $k = 0.4$  and  $k = 0.8$  is the nose vortex which separates from the surface approximately halfway between the tip and the base. The wake appears similar at  $k = 0.4$  and  $0.8$ , although at the higher pitch rate, the nose vortex appears more turbulent. The flow development at very high pitch rates is shown in the fourth column. Clearly, the wake development methodology is different than at the lower pitch rates. The shape of the wake above the model appears similar to that of the nose vortices at the lower reduced frequencies, however, the smokelines have been highly diffused, indicating a greater degree of turbulence relative to the other cases. Also, this vortex appears to originate at a point downstream from the tip, unlike the other cases, where the nose vortex appears to originate at or very near the tip. Upstream of the separation location, the flow appears to be completely attached to the model surface as if the nose vortex originates at the separation location. For

convenience, this structure will be referred to as the separated nose vortex. In the steady state case, the nose vortex is still completely attached at this angle.

By  $\alpha = 30^\circ$  during the upstroke (Figure 4, second row), the nose vortices have reattached along the entire length of the model and remain so during the remainder of the upstroke at  $k = 0.4$  and  $0.8$ . Note that at in the steady state case, the nose vortex has separated at  $\alpha = 30^\circ$ . At  $k = 2.0$ , the separated nose vortex convects downstream while the attached flow region continues to grow.

The third row of photographs in Figure 4 depicts the wake structure at the maximum angle of attack,  $\alpha = 40^\circ$ . In the steady state case, the nose vortex separation location has moved closer to the nose while an aftbody vortex is evident downstream of the separation location. At  $k = 0.4$ , the wake appears very similar to the steady state case. However, the nose vortex remains completely attached in the  $k = 0.8$  case. The nose vortex does not separate at this higher pitch rate until  $\alpha = 35^\circ$  during the downstroke (not shown). At  $k = 2.0$ , the separated nose vortex has completely detached itself from the model surface. The flow over the model is now attached along the entire surface with the exception of a small disturbance near the model base.

At  $\alpha = 30^\circ$  during the downstroke (Figure 4), the nose vortex separation location at  $k = 0.4$  and  $0.8$  is closer to the nose than in the steady state case. At  $k = 0.8$ , the nose vortex appears to have separated from the middle portion of the body first, rather from the base of the model as was the situation at  $k = 0$  and  $0.4$ . The distance from the model surface to the vortex core at  $k = 0.8$  indicates a greater lag in the development of vortex separation, relative to the static case, than at  $k = 0.4$ . At  $k = 2.0$ , a vortex develops along the entire length of the model which will be labeled a cylindrical vortex as it is roughly cylindrical in shape. As the model approaches the minimum angle of attack, the cylindrical vortex begins to convect downstream, thus giving rise to the separated nose vortex present during the upstroke.

The effect of mean pitch angle can be seen in Figure 5. The reduced frequencies in these photos are again  $k = 0, 0.4, 0.8$  and  $2.0$ , however, the mean angle of attack is now  $50^\circ$ . During the upstroke, the nose vortex separation location moves farther from the tip as the reduced frequency increases. Aftbody vortices and aftbody shedding are evident downstream of the

separation location in all cases. However, the aftbody wake at  $k = 0.8$  appears to be as large as that at  $k = 0.4$ . This is probably due to the fact that the pitch point is located forward of the model base. Therefore, a portion of the aftbody actually encounters an increased effective velocity during the upstroke.

During the downstroke, the nose vortex separation location at  $k = 0.4$  and  $0.8$  is close to the nose than the static case. The aftbody wake in both cases appears larger than in the static case. At  $k = 2.0$ , the wake appears to have evolved into a cylindrical vortex just as it did at  $\alpha_m = 30^\circ$ . Near the tip, a small disruption in the smokelines is evident. This disruption later develops into the nose vortex during the upstroke. The detached nose vortex present during the preceding upstroke can be seen just downstream of the model mid chord.

Figure 6 shows the near and far side wake visualization for the model at an instantaneous angle of attack of  $50^\circ$  and at  $k = 0.0, 0.4$  and  $2.0$ . Clearly, the separation locations of the nose vortices are different in all three cases, indicating the presence of a non-zero side force. Further evidence of wake asymmetry is presented in rear view, cross-sectional photographs of the cross-sectional wake geometry at  $\alpha = 25^\circ$  shown in Figure 7. The top photo depicts the static wake, while the bottom photo is at  $k = 0.8$ ,  $\alpha_m = 30^\circ$  during the downstroke. This data show that, at least for strictly planar motions, motion induced effects do not overpower the origins of asymmetry and that asymmetric side force alleviation will require attention in the unsteady environment as well as the steady environment.

#### Steady Vs. Dynamic

The detailed flow visualization conducted for this investigation allows for the identification of all large-scale structures shed into the wake of a static and pitching slender body. These structures can now be categorized into different regimes and plotted as a function of angle of attack as shown in Figure 8. The static regimes, indicated by the shaded boxes, are an elaboration of previously defined wake regimes behind a static slender body<sup>13</sup>.

At  $k = 0.4$  (Figure 8a), the regimes occur at roughly the same angles of attack as the static regimes, however, the motion induced effects are manifested as a shifting of the regime boundaries. This phase-shifting is to higher angles of attack during the upstroke and to lower angles during the downstroke.

Note that no new regimes have developed at this reduced frequency and that, with the exception of the shear layer instability, all regimes developed by a static slender body are also generated by the pitching slender body. The shear layer instability also occurs in the dynamic instance, however, its presence was only captured very briefly and so was not noted on the regime map. The regime map for  $k = 0.8$  is similar in nature, although the phase shifts are vary slightly.

However, at  $k = 2.0$  (Figure 8b), two dynamic regimes emerge: the detached vortex phenomena and the development of a cylindrical vortex during the downstroke. Neither of these phenomena are present in the static case, nor are they evident at the lower pitch rates. The existence of these two regimes at very high pitch rates demonstrates the truly dynamic effects of model motion on the wake development.

Nose vortex width obtained from the light sheet photos is plotted in Figure 9 for  $k = 0$ . The total width, defined as the near side vortex width plus the far side vortex width, increases in a fairly linear fashion up to  $\alpha = 25^\circ$ . As the angle of attack increases, the far side vortex width increases dramatically to a value equal to about one and a half times the model diameter. The near side vortex width increases at approximately the same rate, reaching a maximum of three-quarters of the body diameter at  $\alpha = 35^\circ$ . An interesting feature of this data is that the near side vortex separates from the surface when the total vortex width approaches the body diameter. Unfortunately, the synchronization of the strobe flash to model motion prevented the use of high flash rates necessary to provide sufficient illumination for the dynamic cases.

Nose vortex separation location provides an easily measurable index of vortex strength<sup>14</sup>. Static and dynamic separation locations of the near side nose vortex are plotted in Figure 10. The data are plotted as a function of the non-dimensionalized pitch cycle with the minimum angle of attack considered to be the beginning of the cycle while the maximum angle of attack occurs at the mid-point of the cycle. During the upstroke, the separation location is located further from the tip than the corresponding static location for all pitch rates considered. At the maximum angle of attack, the separation location quickly moves upstream towards the model nose at  $k = 0.4$  and  $0.8$ . As mentioned previously, at  $k = 2.0$ , the nose vortex detaches from the model at the maximum angle of attack. During the downstroke, the dynamic nose

vortex separation location is located nearer to the nose than the corresponding static location.

The nose vortex is presumably the principal method of convection for vorticity generated upstream of the separation point. Downstream of the separation location, the vorticity generated must be removed from the model surface by some other means. For this particular geometry, the aftbody vortices emerge over a relatively small angle of attack range before developing into aftbody shedding. For convenience, the aftbody vortices and aftbody shedding will be grouped together and referred to as the aftbody wake. The length of the aftbody wake measured parallel to the model axis along a line one body diameter downstream of the model surface is plotted in Figure 11 as a function of the pitch cycle. As expected, the aftbody length is inversely proportional to the nose vortex separation location; as the separation location moves away from the tip, the aftbody wake length decreases and vice versa.

#### Discussion

The flow visualization and kinematic analysis serve to characterize the wake development behind a slender ogive-cylinder. In general, an increase in angle of attack, either statically or dynamically, allows for the formation of nose vortices which separate from the surface at a well-defined and highly repeatable angle of attack. Aftbody vortices and aftbody shedding become significant structures at higher angles. Dynamically forced model motion phase-shifted the boundaries between the various regimes, with the amount of phase shifting dependent upon the pitch rate. At very high pitch rates, the truly dynamic effects of motion history are sufficiently exaggerated to allow for direct visualization. Based on the data presented, general observations can be made concerning the mechanics of wake development behind a pitching slender body.

First, except for very high reduced frequencies, all the data indicate that the wake development behind a dynamically forced pitching slender body is very similar in nature to the wake development behind a static slender body. The regime maps demonstrate the similarities as well as the phase shifting which arises from model motion. The fact that dynamic motion elicits no new shed structures suggests that the static vorticity convection mechanisms are able to modify themselves to accommodate the motion induced change in vorticity generation.

The kinematic behavior of the nose vortex separation location hysteresis loops is further evidence

of the static/dynamic wake similarities. The separation location plotted against the cycle show that the nose vortices experience a "catch-up/overshoot" cycle. At either extremum of the pitch cycle, the nose vortex separation locations lag the steady state values. As the model begins to pitch up or down, the separation location catches up to and then surpasses the static location. The process repeats as the model reaches the other extremum of the cycle. The static separation location seems to act as an anchor for the dynamically forced separation locations. The length of the aftbody wake follows an opposite, but otherwise similar trend.

The hysteresis loops formed by the separation location as a function of instantaneous angle of attack clearly depict the dependence of the dynamic separation location on the static value. At all mean angles considered, the hysteresis loops are centered around the static curve. Similar trends were reported by Gad-el-Hak & Ho<sup>5</sup> for pitching ogive cylinder and by Montividas *et al*<sup>6</sup> for an ogive cylinder undergoing a single pitch up or pitch down motion.

A second observation concerns the nature of the wake development at the highest reduced frequency considered. Any rapid changes in model incidence will most likely elicit rapid changes in wake circulation strength. In accordance with the laws of Helmholtz, these circulation changes must be accompanied by a new vortex system. Figure 12 indicates this type of contiguous vortex system. Although smoke was introduced on just the near side, smoke entrained to the far side illuminated the entire vortex ring. This vortex system was formed during the latter portion of model pitch down with the vorticity contained within the structure generated during the down stroke. This is the same vortex system which detached from the model near the maximum angle of attack.

Since the vortex ring develops during the pitch down and detaches at the end of the upstroke, it appears that the pitch down tends to increase wake circulation. In contrast, pitch up leads to a decrease in wake circulation.

Finally, the discrete, or 'quantized' behavior of the wake structure (the nose vortex in particular) suggests that the discrete, attached vortex/wake structures can sustain only a certain level of vorticity. Beyond some threshold value, the wake is unable to support additional vorticity and the wake structure is altered accordingly. One re-structure method allows the vortex to separate from the body. Additional vorticity generated downstream of the separation point is then

convected through a newly developed structure, in this case the aftbody wake.

For the conditions where vortex separation does not occur (low static angles or during pitch up at low mean angles) additional vorticity is accommodated by an increase in vortex size. The static cross-sectional visualization indicate that the maximum vortex size is bounded by the diameter of the body. As vorticity increases with increasing angle of attack, the threshold limit is again exceeded. This effect is demonstrated by the near side nose vortex separation when the total wake width approached the body diameter. Convection of additional vorticity was accomplished by near side vortex separation, and the production of an additional vortex system which permitted both vortex structures to grow.

The vortex ring discussed earlier is also indicative of the quantized nature of the wake development. As the model pitches down, the vorticity level in the attached wake increases. At some point, the attached wake can no longer support additional vorticity. The wake casts off the vortex ring, pinned at the nose, so that the downstream wake can accommodate additional vorticity.

The concept of a critical vorticity concentration level above which the vortex system must transition is not new. Visser and Nelson<sup>15</sup> carefully measured the flow field properties of a delta wing vortex prior to breakdown. Their results led them to postulate that the circulation concentration gives rise to vortex breakdown. Also, Ng<sup>16</sup> considered the possibility of critical threshold vorticity concentration in his development of a model for control of delta wing leading edge vortices.

### Summary

Additional work is necessary to support an analytic model for threshold vorticity driving wake structure. Dynamic force balance measurements currently underway at the University of Colorado will provide more definitive measurements of the effect of model motion history on the wake development. Also, hot-wire investigations are scheduled which will yield nose vortex strength measurements. These quantitative measures should provide further insight into the unsteady development of wake structure from pitching slender body geometries.

### References

1. Chambers, J., "High Angle of Attack Aerodynamics: Lessons Learned," AIAA Paper 86-1774, Jun 1986.
2. Hunt, B.L., "Asymmetric Vortex Forces and Wakes on Slender Bodies," AIAA Paper 82-1336, Aug 1982.
3. Ericsson, L. and Redding, J.P., "Asymmetric Flow Separation and Vortex Shedding on Bodies of Revolution," Tactical Missile Aerodynamics: General Topics, ed. by Mendenhall, M., Progress in Astronautics and Aeronautics, Vol. 141, AIAA, Washington, D.C., 1992.
4. Smith, L.H., and Nunn, R.H., "Aerodynamic Characteristics of an Axisymmetric Body Undergoing a Uniform Pitching Motion," *Journal of Spacecraft*, Vol. 13, No. 1, Jan 1976, pp. 8-14.
5. Gad-el-Hak, M. and Ho, C-H, "Unsteady Flow Around an Ogive Cylinder," *Journal of Aircraft*, Vol. 23, No. 6, Jun 1986, pp. 520-528.
6. Montividas, R., Reisenhal, P. and Nagib, H., "The Scaling and Control of Vortex Geometry Behind Pitching Cylinders," AIAA Paper 89-1003, Mar 1989.
7. Stanek, M.J. and Visbal, M.R., "Investigation of Vortex Development on a Pitching Slender Body of Revolution," AIAA Paper 91-3273
8. Panzer, E.C., Rediniotis, O.K. and Telionis, D.P., "The Hemisphere-Cylinder in Dynamic Pitch-Up Motions," AIAA Paper 93-2963, July 1993.
9. Hoang, N.T., Wetzcl, T.G. and Simpson, R.L., "Unsteady Measurements Over a 6:1 Prolate Spheroid Undergoing a Pitch-Up Maneuver," AIAA Paper 94-0197, January 1994.
10. Moskovitz, C.A., Hall, R.M. and DeJarnette, F.R., "Effects of Nose Bluntness, Roughness and Surface Perturbations on the Asymmetric Flow Past Slender Bodies at Large Angles of Attack," AIAA Paper 89-2236, Sep 1989.
11. Zilliac, G., Degani, D. and Tobak, M., "Asymmetric Vortices on a Slender Body of Revolution," AIAA Paper 90-0388, Jan 1990.
12. Detain, D. and Zilliac, G.G., "Experimental Study of Nonsteady Asymmetric Flow Around an Ogive-

Cylinder at Incidence," *AIAA Journal*, Vol. 28, No. 4, 1990, pp. 642-649.

13. Nelson, R.C. and Malcolm, G.N., "Visualization of Flow Phenomena", *Tactical Missile Aerodynamics: General Topics*, Vol. 141, Progress in Astronautics and Aeronautics, ed. by M. J. Hemsch, AIAA, Washington, 1992.

14. Thomson, K. D. and Morrison, D. F., "The Spacing, Position and Strength of Vortices in the Wake of Slender Cylindrical Bodies at Large Incidence," *Journal of Fluid Mechanics*, Vol. 50, part 4, pp. 751-783, 1971.

15. Visser, K. D. and Nelson, R. C., "Measurements of Circulation and Vorticity in the Leading-Edge Vortex of a Delta Wing," *AIAA Journal*, Vol. 31, No. 1, pp. 104-111, 1993.

16. Ng, T. T., "On Leading Edge Vortex and Its Control," AIAA Paper 89-3340.

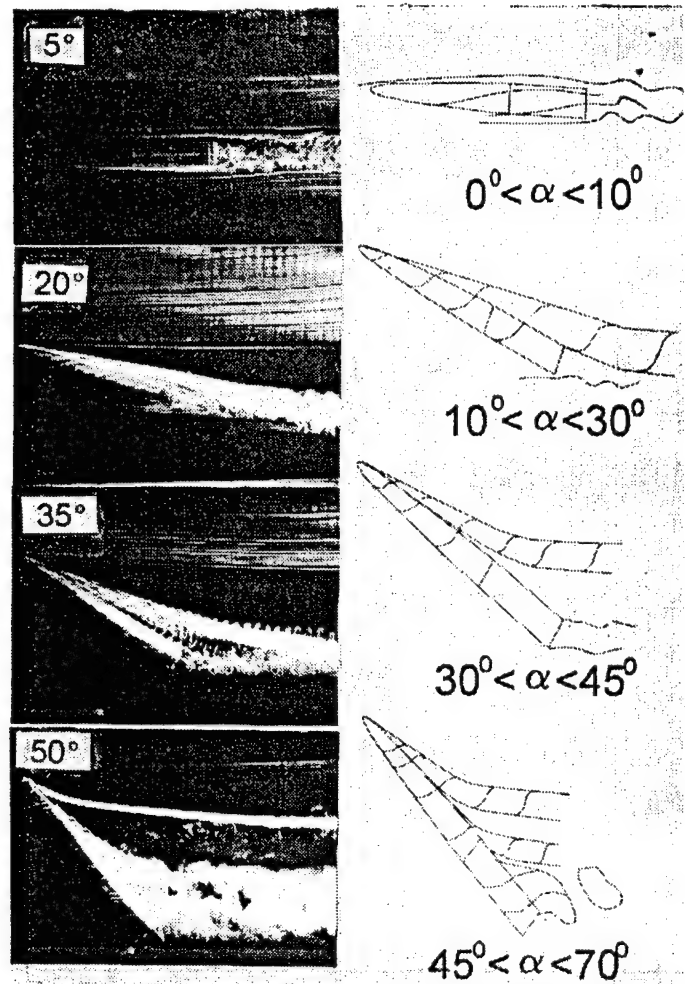


Figure 2: Typical static wake development with increasing angle of attack.

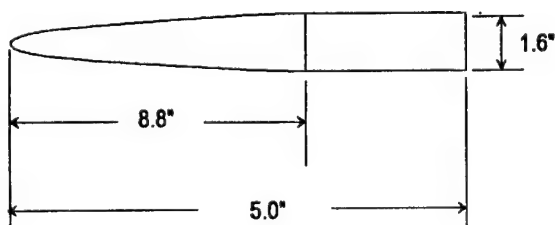


Figure 1: Schematic of model dimensions

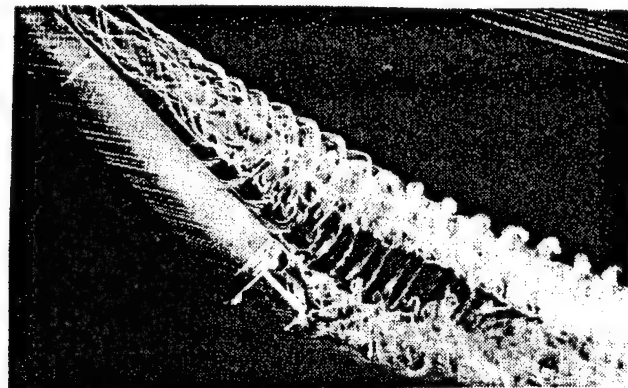


Figure 3: Enlargement of shear layer instability.

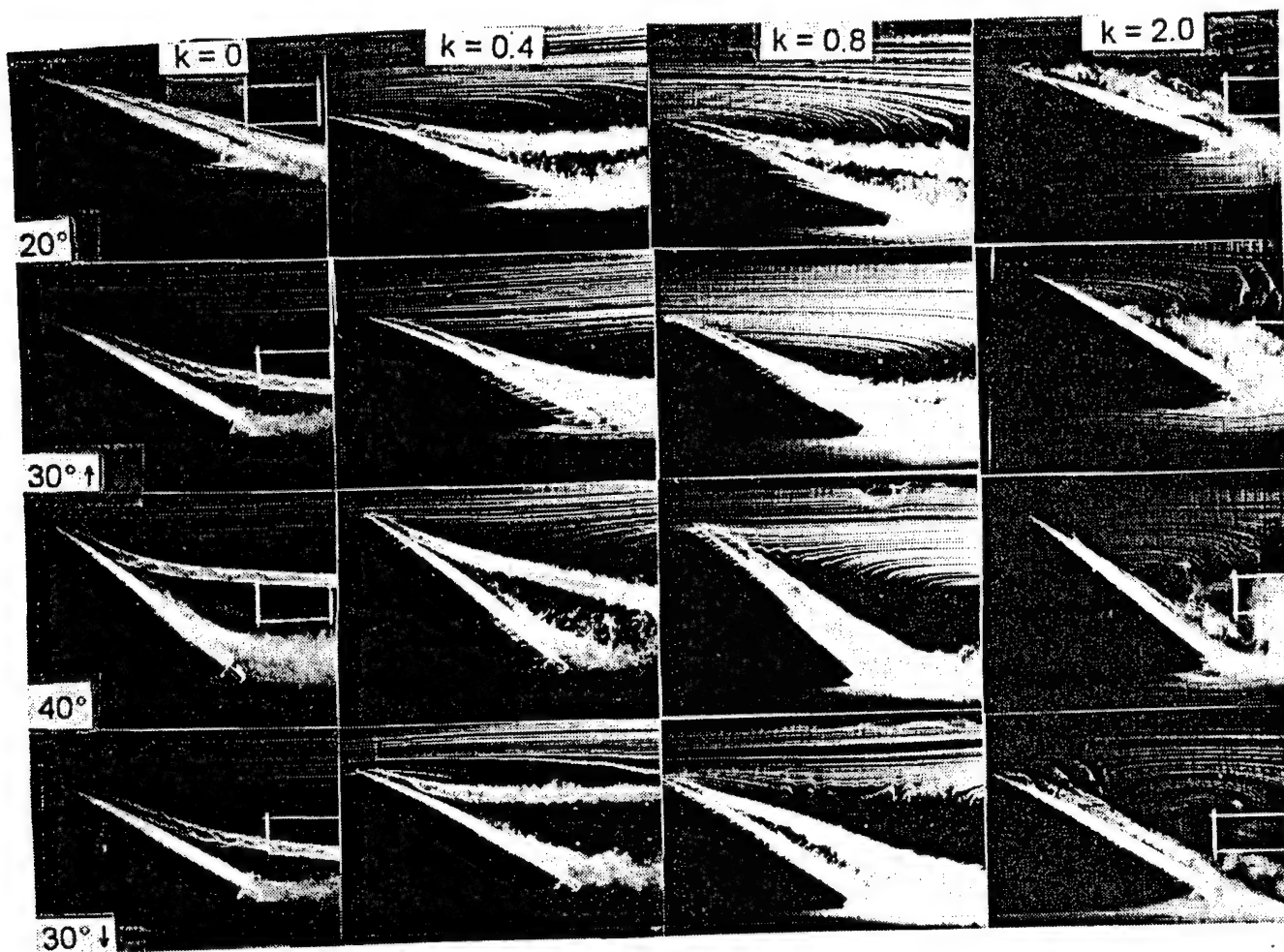


Figure 4: Comparison of wake development for  $k = 0, 0.4, 0.8$  and  $2.0$ . Dynamic photos at  $\alpha = 30 + 10\sin\omega t$ .

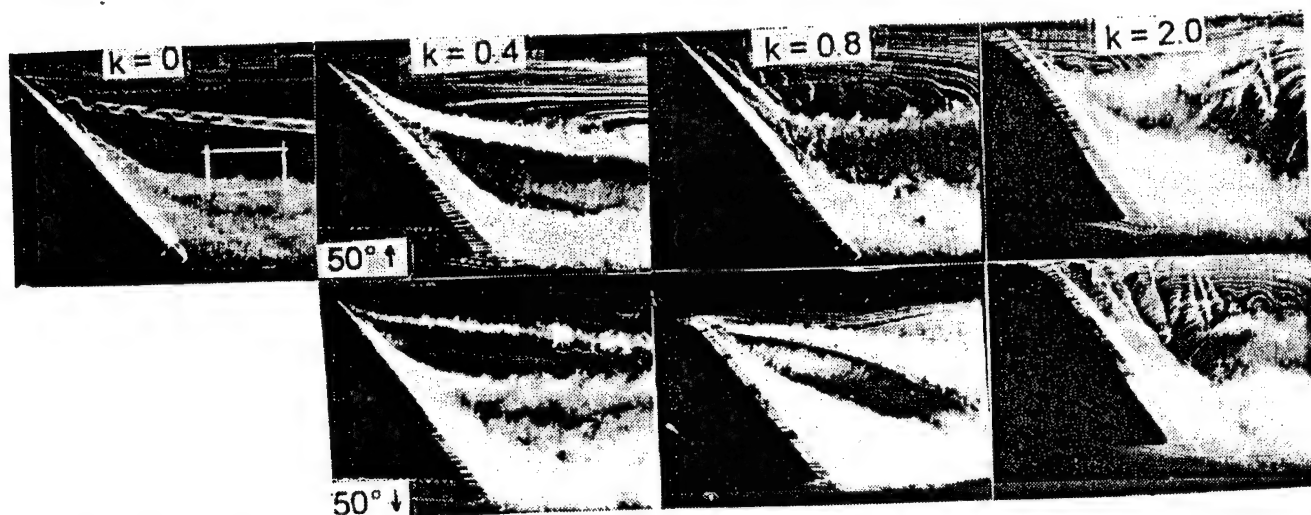


Figure 5: Wake development during pitch-up and pitch-down at  $k = 0, 0.4, 0.8$  and  $2.0$ . Dynamic photos are at  $\alpha = 50 + 10\sin\omega t$ .

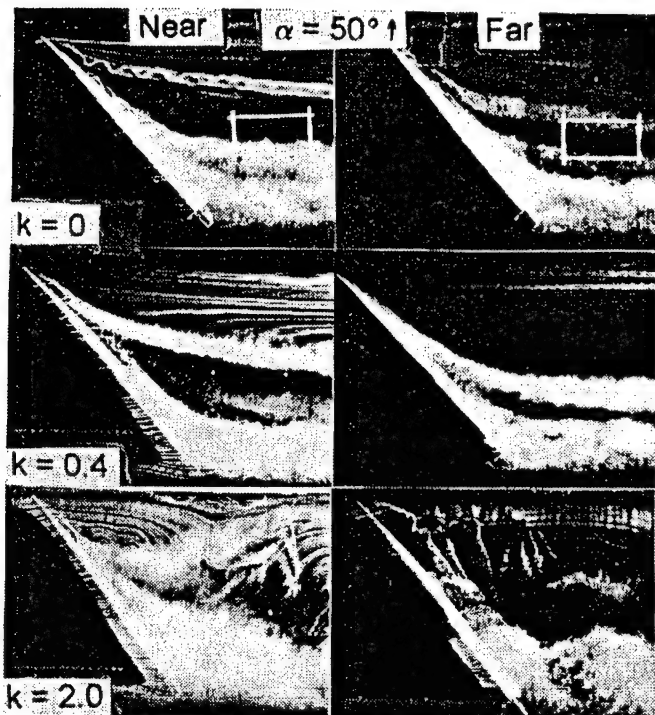


Figure 6: Near and far side wake visualization at  $\alpha = 50^\circ$ ,  $k = 0$  (top), 0.4 (middle) and 2.0 (bottom).

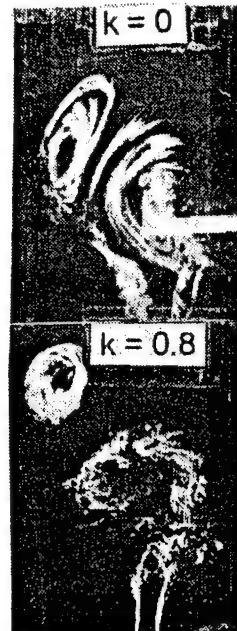


Figure 7: Light sheet visualization of wake cross-section at  $\alpha = 30^\circ$ ,  $k = 0$  (top) and 0.8 (bottom).

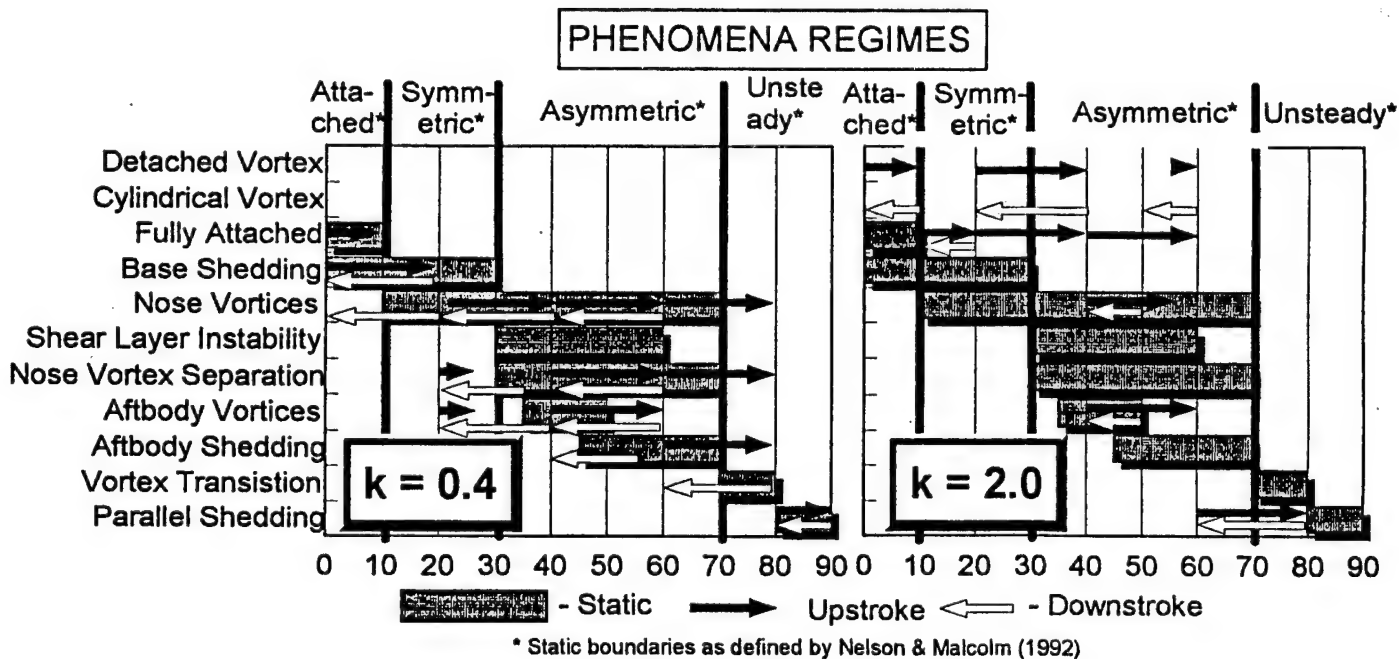


Figure 8: Static and Dynamic (top,  $k = 0.4$ ; bottom,  $k = 2.0$ ) wake regimes as a function of angle of attack.

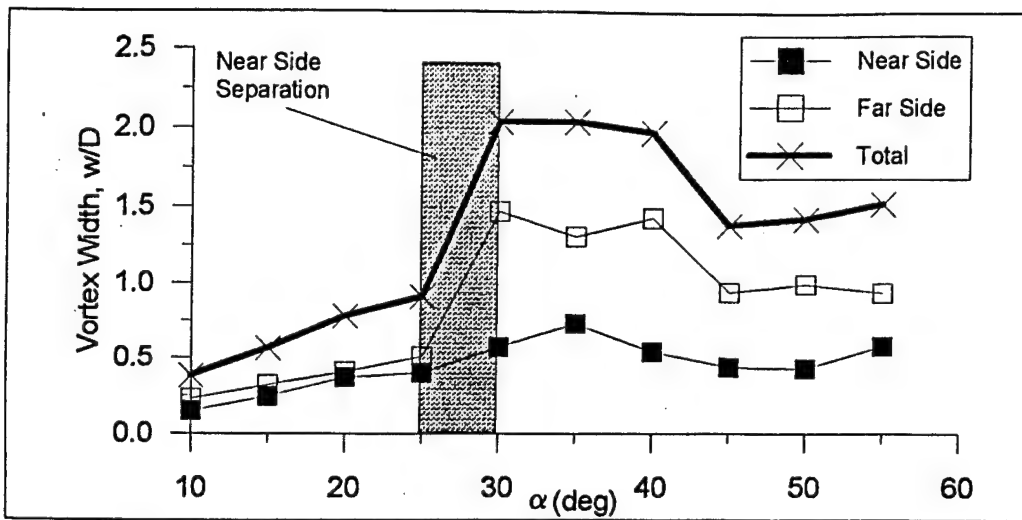


Figure 9: Nose vortex width.

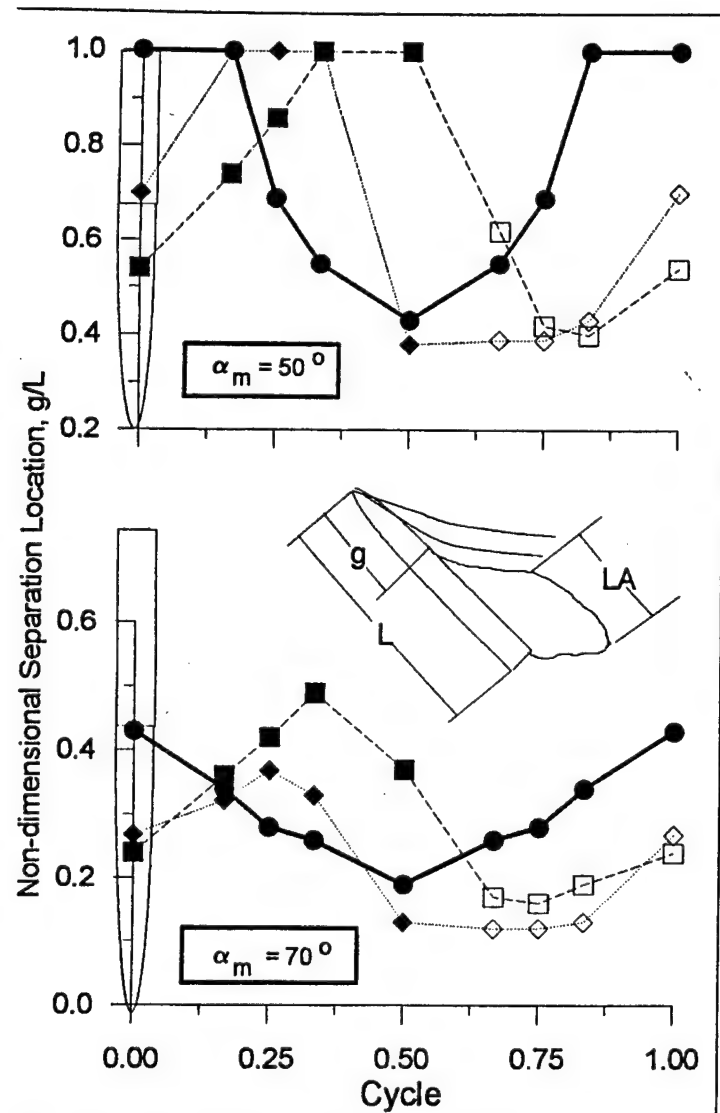


Figure 10: Nose vortex separation location. Closed symbols - upstroke, open symbols - downstroke.

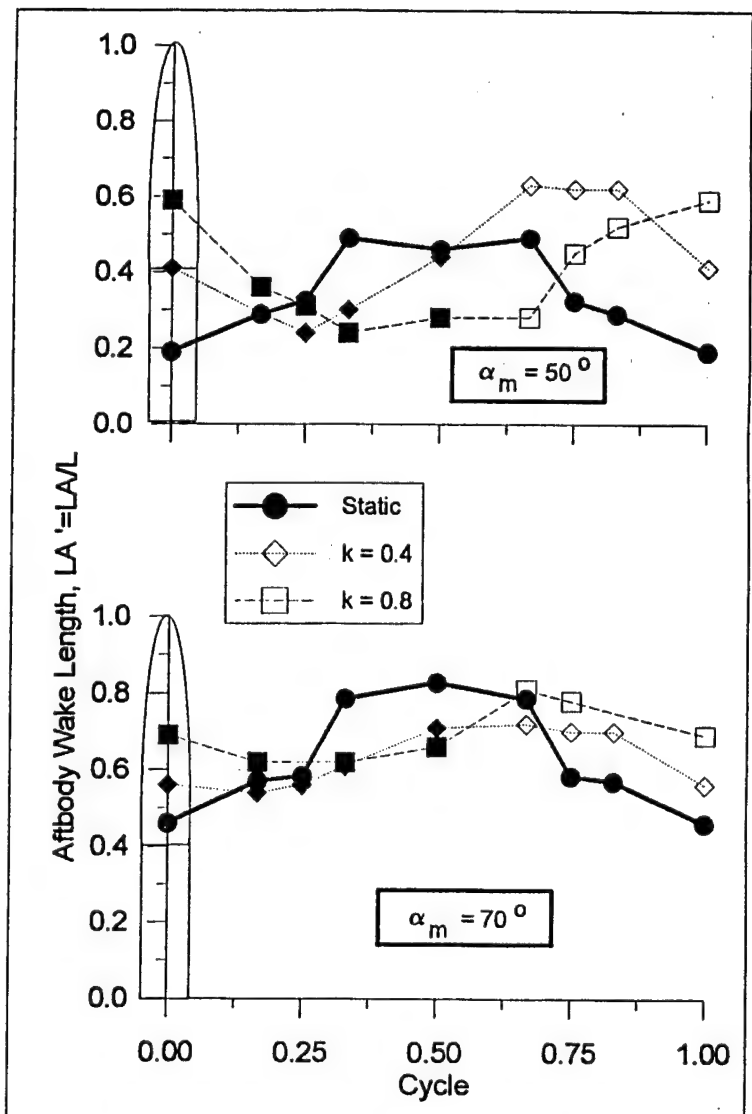


Figure 11: Aftbody structure length. Closed symbols - upstroke, open symbols - downstroke.

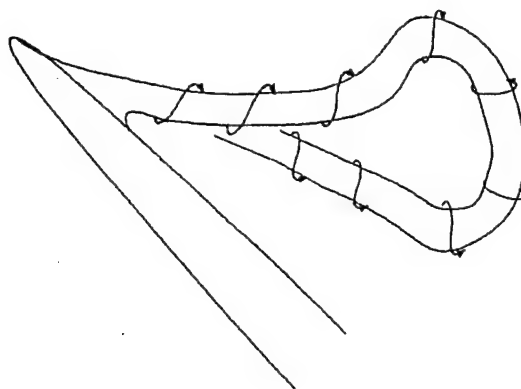
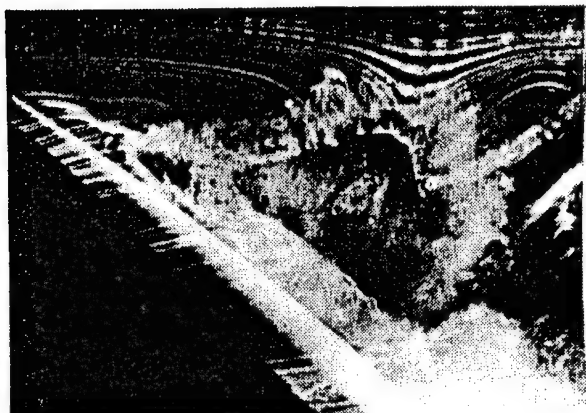


Figure 12: Photograph and caricature illustrating vortex ring.



**AIAA 94 - 0070**

**Experimental Investigation of the  
Vortex - Vertical Tail Interaction on an F-15**

S. P. LeMay  
Department of Aeronautics  
USAF Academy, CO

J. A. Lovato  
Frank J. Seiler Research Laboratory  
USAF Academy, CO

**32nd Aerospace Sciences  
Meeting & Exhibit  
January 10-13, 1994 / Reno, NV**

# EXPERIMENTAL INVESTIGATION OF THE VORTEX-VERTICAL TAIL INTERACTION ON AN F-15

Scott P. LeMay<sup>†</sup>

Department of Aeronautics  
USAF Academy, CO 80840

Julie A. Lovato<sup>††</sup>

Frank J. Seiler Research Laboratory  
USAF Academy, CO 80840

## ABSTRACT

An experimental investigation of vortex development and interaction with downstream vertical surfaces is presented. A 1/48 scale model of an F-15C is evaluated using both colored dye and fluorescent dye laser-light-sheet flow visualization in conjunction with hot-film anemometry. A combination of side view, plan view, and cross-cut views equated with cross-cut velocity and turbulence data gives a detailed accounting of the events leading up to vertical tail buffet. Specifically, it was determined that the primary vortex progresses from one originating only from the flow over the wing to that emanating from the forebody and the wing flowfields. The vortex tracks downstream, encompassing the vertical tails with a highly turbulent flow. The maximum turbulence intensity in the vicinity of the vertical tails occurs between 20° and 25° angle of attack. This corresponds to regions where the local velocity magnitudes are near freestream values.

## INTRODUCTION

It is only recently that fighter aircraft have extended their operational realm to prolonged periods spent at high angles of attack. Coexistent with this expansion of the viable flight regime is a necessitated increase in aircraft control versatility and an expanded interest in the vertical stabilizer buffet problem which has plagued fighter aircraft in the past. Previous

research has studied the interaction between upstream generated longitudinal vortices and downstream twin tails.<sup>1</sup> On the F/A-18, the source of the vortices is due primarily to bursting of vortices shed off the leading edge extension.<sup>2</sup> On the F-15, the source is principally due to shedding off the wing leading edge.<sup>3</sup> Forebody vortices are not a primary contributor to the tail buffet since the maximum buffeting occurs in the angle of attack range from 18° - 30° in both cases.<sup>4</sup>

Mechanisms designed to control the flow interacting with the vertical fins have been explored recently. Hebbar and Platzer<sup>5</sup> found that addition of LEX fences successfully redistributed turbulence in the vicinity of the tails on a YF-17 to higher frequencies. By drawing the dominant frequencies away from the critical low frequencies of the vertical tails and spreading them over a wider band, the buffet effect was reduced. The fences were also successful in diminishing the magnitude of the unsteady surface pressures interacting with the tails. Bean and Wood<sup>6</sup> used tangential leading edge blowing of the leading edge of a delta wing to modify the flowfield influencing downstream twin tails. The blowing shifted both the buffet frequencies to higher values and extended the angle of attack corresponding to peak buffet intensity. Increasing the blowing level essentially compressed the vortex cores, re-establishing flow on the delta wing from an initially stalled condition.

A basic understanding of how vortex development is interrelated to downstream tail buffeting is a necessary precursor to development of a comprehensive control strategy. Perhaps the most extensive study evaluating the flow physics involved with vortex-tail interaction was done by Washburn, Jenkins, and Ferman<sup>7</sup>. In their investigation of the effect of tail location on flow parameters, they determined that the buffet load could be reduced by moving the tails toward the vortex core trajectory. They also mapped out vortex trajectories, magnitude of

<sup>†</sup>Instructor, Department of Aeronautics, Member AIAA

<sup>††</sup>Research Aerospace Engineer, Member, AIAA

This paper is a work of the US Government and is not subject to copyright protection in the United States.

aerodynamic force coefficients, and tail surface pressures as a function of tail location.

To date, there has not been a comprehensive study designed to track and evaluate the vortex from its inception point to its interaction with the downstream vertical tails on an F-15. By thoroughly understanding the flow physics which lead to the twin tail buffet problem on an F-15, the possibility of developing a successful control methodology is significantly enhanced. This study investigates correlation between multi-aspect flow visualization and hot-film anemometry measurements obtained in planes perpendicular to the freestream velocity. Detailed velocity and turbulence values are analyzed in conjunction with both vortex characteristics and trajectories to gain a thorough grasp of the specific physical mechanisms governing the twin tail buffet phenomena on an F-15.

## EXPERIMENTAL METHODS

### Facilities

A qualitative and quantitative understanding of the flow physics governing flow over the F-15 was obtained using two experimental methods, flow visualization and hot-film anemometry. Flow visualization was conducted in the 0.38 m x 0.50 m test section of the Aeronautics Laboratory's water tunnel at a velocity of 7.6 cm/s, or a chord Reynolds number of 11,000. The hot-film anemometry experiments were conducted in the Aeronautics Laboratory's open return, low speed wind tunnel at the U. S. Air Force Academy. The 0.91 m x 0.91 m test section is designed for use with flow sensor measurements, and has freestream turbulence intensity levels below 0.5%. All measurements were taken at a freestream velocity of 15.2 m/s, or a chord Reynolds number of 166,000.

### Model Configuration

The models used for the experiments were 1/48 scale models of the F-15C. The water tunnel model contained four dye ports on the forebody and one on each wing glove located below the apex. These were used for both colored and fluorescent dye flow visualization. All control surfaces were fixed in the neutral position, and the aircraft was "clean", with no armament. The model was sting mounted through the starboard engine nozzle. The model engine inlets were open so that entering mass flow could exit through the port nozzle. The wind tunnel model was similar to the water tunnel model with the exception of the engine

inlets and the sting mount. The wind tunnel model had a solid fuselage core for added rigidity and therefore the inlets were closed. The wind tunnel model was sting mounted along the centerline.

### Flow Visualization

Visualization pictures were taken at 5°, 10°, 15°, 20°, and 25° angles of attack. Both colored and fluorescent dyes were used for flow visualization in the water tunnel, with dye supplied to the model from a containment reservoir using compressed air. The rate of dye bleed was controlled by regulating the air pressure through a needle valve. Dye was supplied to two regions on the model: 1) two pair of dye ports on the forebody, with one pair on the upper surface and one pair on the lower surface, and 2) the engine inlet/wing glove area, where the dye ports were located on the outer side of the inlet and just below the apex of the wing glove. An example of the water tunnel model mounted in the test facility is given in Figure 1.

An SLR 35mm camera was used in combination with a 50mm lens to record the data. In the colored dye cases, two 1000 Watt flood lamps were used to illuminate the dye. A sheet of multimode laser light produced by a 12 watt Argon-Ion laser was used to fluoresce the dye in the fluorescent experiments. The dye used was a mixture of 100 mg rhodamine 6G per one liter of methanol, which fluoresced bright yellow when excited by the laser light sheet. The laser light sheet, generated by an Aerometrics LVS 170 fiber optic package, made it possible to obtain cross-cuts of the vortex flowfield, providing an excellent means for examining the vortex structure in detail. The configurations for the fiber optics and the laser light sheet are shown in Figures 2 and 3. Perpendicular cross-cuts relative to the freestream flowfield were obtained for 15°, 20°, and 25° angles of attack at locations of  $x/l = 0.62, 0.78, \text{ and } 0.93$ , where ( $x$ ) is the distance along the fuselage centerline and ( $l$ ) is the overall model length. The locations coincided physically to the engine nacelle-fuselage juncture, just upstream and just downstream of the vertical control surfaces. The measurement stations are shown in Figure 4. The laser light was filtered out of the photographic data using a short pass filter, leaving only the fluorescent light for the photographic exposure.

### Hot-Film Anemometry

All hot-film measurements were taken at a freestream velocity of 15.2 m/s. Data was taken at points corresponding to the same non-dimensional

fuselage locations as the flow visualization. The 21 by 21 point grids were set up perpendicular to the tunnel floor, coincident with the flow visualization photographs, with data points taken at 5 mm intervals. This resulted in 441 data points for each plane. The sampling frequency for the data was 128 samples per second. The upper surface velocity field was surveyed using a hot-film probe, set at a 30% overheat ratio, in conjunction with a TSI IFA 100 Intelligent Flow Analyzer. All data acquisition utilized a Keithley 500A measurement and control system. The hot-film probe was moved at specific increments using a computer operated traverse coupled with the data acquisition system. Turbulence intensity calculations were made for the tunnel axis u-component of velocity only, represented by:

$$\text{Turbulence Intensity} = \frac{\sqrt{(u')^2}}{\bar{u}}$$

## RESULTS

### Colored Dye Flow Visualization

Colored dye flow visualization data were acquired at angles of attack of 5°, 10°, 15°, 20°, and 25°, at zero degrees sideslip. Both side view and plan view photographs were obtained. In the data presented, blue dye was used to visualize the vortices forming at the apex of the wing glove and green dye was used to visualize the forebody flowfield.

Figure 5 shows the flowfield about the F-15 at 5° angle of attack. At this angle of attack the majority of the blue wing glove dye tracks below the wing. The dye which tracks across the top surface of the wing shows that the flow remains attached to the top surface of the wing and no discernible vortex is generated at the wing glove. The flow originating from the forebody at 5° angle of attack separates from the fuselage just aft of the canopy and then tracks downstream along the centerline of the aircraft. The forebody flow remains close to the top surface of the aircraft and does not interact with the vertical tails.

At 10° angle of attack, shown in Figure 6, two vortical structures are present at the engine inlet/wing glove locations on both sides of the model (Figure 6b). This is evidenced by the two distinct regions of dye parallel to the fuselage centerline. The dominant vortex is formed outboard of the engine inlet at the apex of the wing glove, tracks downstream along the wing-fuselage juncture, and is then split by the vertical tail. This

vortex remains close to the fuselage, as seen from the side view, and breaks down, or spreads out, approximately at the 40% root chord location. The second vortical structure forms on the inboard side of the engine inlet, tracks downstream along the forebody, and then coalesces with the primary wing-glove vortex. Approximately 40% of the vertical tail span is encompassed by the vortex wake at this angle of attack. The flow begins to separate from the wing leading edge, forming a vortex which flows spanwise. The forebody flowfield remains laminar and attached until the wing apex and then transitions to turbulent flow. As the forebody flow moves downstream the majority of the fluid appears to enter the inboard vortex, which subsequently breaks down. The remainder of the flow which originated at the forebody enters into the outer wing glove vortex, as seen in Figure 6d.

As the angle of attack is increased to 15°, shown in Figure 7, the vortices which form about the wing glove quickly breakdown into a large scale turbulent vortex wake structure. The flowfield no longer tracks directly downstream, as in the 10° case, but rather flows spanwise toward the wing tips. Low pressure areas atop the engine inlets and main wing contribute to the breakdown of the vortex structure by causing it to spread spanwise. The large vortical turbulent wake grows in height slightly in comparison to the 10° angle of attack case and impinges on the vertical tails, immersing approximately 75 percent of the vertical tail span in the wake. The majority of the flowfield produced by the forebody disassociates quickly and is entrained into the large turbulent vortex structure resident above the main wing. However, as evident in Figure 7d, a segment of the forebody flow does pass between the vertical tails.

More fluid from the forebody and wing glove regions is entrained into the low pressure areas above the wing and engine inlet at 20° angle of attack, shown in Figure 8. The vortex wake becomes larger, encompassing most of the wing planform as the vortex tracks downstream. At this angle of attack very little of the fluid originating from the forebody passes between the vertical tails. The forebody flow is drawn instead towards the fuselage surface just aft of the canopy and flows spanwise. The large turbulent vortical structure resident over the wing begins to separate from the aft fuselage region, turning towards the favorable pressure gradient of the freestream flowfield, as seen in Figure 8c. This results in the entire span of the vertical tails being immersed in the turbulent vortex flowfield (Figures 8a and 8c).

At an angle of attack of 25° the vortex is very similar to that of the 20° case, except the vortex wake

expansion occurs further upstream. The turbulent vortical structure in the vicinity of the vertical tails continues to expand, as seen in Figures 9, and more fluid from the turbulent vortex wake is now present between the twin vertical tails.

### Fluorescent Dye Flow Visualization

Fluorescent dye flow visualization data were acquired at 15°, 20° and 25° angle of attack. Laser light sheet cross-cuts of the flowfield were obtained at each angle of attack for the three fuselage locations. The light sheet was perpendicular to the tunnel axis and intercepted the top of the fuselage at  $x/l$  positions of 0.62 (position 1), 0.78 (position 2), and 0.93 (position 3). Corresponding data is presented in Figures 10 through 12. The photographs were taken from the aft end of the model looking upstream along the tunnel centerline. Fluorescent dye was introduced into the flowfield at the wing glove/inlet location as in the blue colored dye cases.

The 15° angle of attack case is shown in Figure 10. At position 1 (Figure 10a), the laser light sheet cross-cut reveals a vortex in the vicinity of the wing/fuselage juncture and a separated turbulent flowfield in the region above the main wing, forming off the wing leading edge. At position 2, the vortical wake over the wing has widened to envelop the entire wing span, and has increased in height. The turbulent vortex wake continues to widen in the spanwise direction as it separates from the wing trailing edge, as seen in Figure 10c where the laser light sheet crosses the tail plane. The wake remains outboard of the vertical tails and remains below the tip of the tail. This figure coincides with the colored dye visualization in Figure 7.

Laser light sheet cross-cuts are presented at 20° angle of attack in Figure 11. At position 1 the flowfield resembles the flowfield observed at 15° angle of attack, with the exception that a more clearly defined vortical flow is observed above the inboard section of the wing. The flow separates from the wing leading edge and enters the large vortical wake above the wing. At position 2 (Figure 11b) the size of turbulent vortex wake has increased with respect to the 15° case, and at position 3 it is clear that the region of turbulence envelopes the entire span of the vertical tails. Some of the vortex wake at position 3 is now observed inboard of the vertical tails. From visual real time observations during flow visualization, it was evident that the complex structure observed at position 3 is vortical in nature, and remains so as the angle of attack is increased to 25°.

The turbulent wake continues to grow in size at all three positions for the 25° angle of attack case, as seen in Figure 12. At position 1 the vortex which was observed over the wing/fuselage juncture at 20° angle of attack is now less structured and continues to be fed from the fluid separating from the wing leading edge. At position 2, near the wing trailing edge, more of the vortical wake moves inboard toward the centerline of the model. This confirms previous observations from the colored dye visualization in Figure 9. In the tail plane, position 3, the vortical wake has substantially increased in size with the increased angle of attack, and has moved to a higher position. This again compares well with the colored dye flow visualization case at 25° angle of attack, in which the wake in the vicinity of the empennage separates from the wing trailing edge and bends toward the direction of the freestream flowfield.

### Flowfield Measurements

Contour plots of turbulence intensities above 5 percent and non-dimensional velocities were obtained at angles of attack of 15°, 20° and 25° in the same cross sectional planes as those presented in the fluorescent dye photographs. Consequently, the flow visualization photographs described in the previous section can be used to aid in the understanding of the quantitative data obtained.

It is important to point out that in this preliminary investigation of the vortex flowfield about an F-15, only the x-component of velocity in the stability axis was measured with the hot-film probe. In Figures 13, 14 and 15, the contour plots of turbulence intensity and non-dimensional velocity are shown for angles of attack of 15°, 20° and 25° respectively.

In Figure 13, it is readily apparent that the region of turbulence intensity increases in both width and height as the flowfield propagates downstream. At position 1, approximately mid-wing, a maximum turbulence of 25% to 30% occurs near the surface of fuselage along the model centerline. These high turbulence intensity pockets occur in regions of decreasing velocity, where the local velocity decreases to 60% of the freestream value. The non-dimensional velocity contours show the flow accelerating above the wing, which is expected due to the low pressure area which exists in that region. At position 2, near the wing trailing edge, the regions of maximum turbulence intensity occur at 60% - 75% of the half-span, most likely due to the flowfield separating from the wing trailing edge. Again, a decrease in local velocity occurs in the same region where maximum turbulence

intensity is observed. In Figures 13e and 13f a line drawing of the vertical tail is added to the contour plot because the tail intersects this cross-sectional plane. A turbulence intensity of 5% is measured at approximately the 60% span location of the vertical tail and increases to 25% at the vertical tail base. The local velocities in these regions vary between 100% and 60% of the freestream velocity. Comparing these plots with the flow visualization in Figures 5 and 10, it is apparent that the 40% turbulence intensity measured outboard near the 70% half-span location is due to the vortical wake being shed off of the wing trailing edge.

Contour plots of turbulence intensity and non-dimensional velocity are presented in Figure 14 for the 20° angle of attack case. In comparison to the 15° cases, the regions of high turbulence intensity have grown at the respective positions, and again increase in size as the measurement location progresses downstream. This finding is well substantiated by reviewing the fluorescent dye photographs at 20° angle of attack in Figure 11, where the growth of the vortical regions with downstream distance is clearly visible. At position 1, the maximum turbulent intensity has increased to 45% and occurs approximately at the mid-span of the wing. This coincides with reduced velocities and indicates possible flow separation on the wing. Above this region of turbulence, the flowfield is accelerated due to entrainment of the potential flowfield above the wing.

Closer to the model centerline, the characteristics of the flowfield have not changed significantly from the 15° angle of attack case. At position 2, the maximum turbulence intensity is 55% and occurs at 40% wing half-span, at a location 10% of the half-span above the wing. This appears to be the center of the turbulent vortex wake from examination of Figure 14b. The local velocities in this region range from 30% to 60% of the freestream value. As the turbulent wake flows downstream, the region of turbulence intensity grows in size according to Figure 14e. At this location, the minimum turbulence intensity level plotted (5%) now extends to the tip of the tail but increases to 25% at the base of the tail. The region of maximum intensity is much closer to the vertical tail at position 3 than in the 15° angle of attack case and reaches a level of 55% at its peak. These observations were confirmed by the flow visualization results in Figure 11. At this location, the non-dimensional velocities range from 100% where the turbulence intensity is 15% to half of that level where the turbulence intensities are 45% to 55%.

In Figure 15, turbulence intensity contours and non-dimensional velocity contours are presented for an

angle of attack of 25°. At position 1, the low turbulence intensity boundary of 5% is similar to that observed in the 20° angle of attack case, but the location of maximum turbulence intensity is located further inboard than at the lower angle of attack. The maximum turbulence intensity measured is 45%, which is the same maximum as in the 20° case, but occurs at a half-span location of approximately 20% as opposed to 40% at the lower attack angle. The point of maximum turbulence has also moved from just above the surface to 15% of the half-span above the wing's surface. The local velocity corresponding to this region was approximately 95% of the freestream velocity. Examining Figure 15b, there is a region of accelerated flow (110% of freestream) that seems to correspond to the vortex feeding sheet shedding off the wing leading edge. The local accelerations and deceleration are difficult to explain, but could be caused by discrete vortices in the shear layer propagating downstream.<sup>8</sup>

As the large rotating turbulent wake reaches position 2, the region of measured turbulence intensity has grown significantly, which corresponds well with the laser light sheet photographs presented in Figure 12. The value of maximum turbulence intensity of 45% to 55% remains similar to that observed in the 20° angle of attack case, but the location has shifted upward and inward as it did at position 1. The plot of non-dimensional velocity indicates that the local velocities in this region of maximum turbulence intensity range from 40% to 100% of the freestream. In addition, a large region of reduced velocity occurs just above the wing trailing edge. At position 3, in the vertical tail plane, the contours of measured turbulence intensity now extend well above the tip of the tail, and a large region of 45%+ turbulence intensity is observed along the outboard section of the tail and near the tip. The local velocities in this region range from 40% to 60% of the freestream velocity. On the inboard section of the tail turbulence intensities of 35% were measured with corresponding local velocities of 60% to 70% of the freestream. From this data it appears that the vortex wake "spills over" the tail. This is confirmed by the flow visualization results in Figure 12c.

## DISCUSSION

A good understanding of the flowfield development about an F-15 is obtained through combined analyses of the colored dye flow visualization photographs, laser light sheet fluorescent dye cross-cut photographs, flowfield measurements of non-dimensional velocities, and turbulence intensity calculations. Plots of non-dimensional velocity used in

conjunction with the plots of turbulence intensity and flow visualization allow for a more complete analysis of the flowfield. For example, regions of high velocity and high turbulence intensity are going to impart a greater momentum change than those of high turbulence and low velocity or low turbulence and high velocity. It is this momentum change in the fluid which leads to the forces causing tail buffeting.

As the aircraft's angle of attack is increased, a complex vortical flowfield develops between 5° and 10° angle of attack. At 10° angle of attack, flow visualization data indicate that the vortical flows originate from the engine inlet and wing glove areas. There are two distinct vortices observed at 10° angle of attack; a dominate vortex structure which forms about the wing glove, and a secondary vortex which seems to originate from the inboard corner of the engine inlet. As these vortices track downstream they breakdown and combine into a single turbulent vortex wake and impinge on the vertical tails. The flow originating from the forebody becomes turbulent aft of the canopy and tracks downstream between the vertical tails with some of the fluid entering the turbulent wake.

At 15° angle of attack the vortex flowfield changes considerably. The vortices which originate from the wing glove/inlet area quickly breakdown and are drawn spanwise over the wing. In addition, flow separates from the wing leading edge, forming a large vortex feeding sheet. The fluid moving spanwise from the wing glove area enters this feeding sheet. A classical delta wing vortex flowfield is established which is relatively large due to the low sweep angle of the wing. The flowfield is more comparable to a broken down vortical wake structure than a tightly wound longitudinal vortex. This vortical structure separates from the trailing edge of the wing and flows just outside of the vertical tails. Comparisons between the laser light sheet photographs and velocity measurements show the flowfield is highly turbulent and large velocity fluctuations exist in the vicinity of the vertical tails. These conditions coincide with the immersion of the tail in the vortical flow. This explains at least one source for the vertical tail buffeting.

As the angle of attack is increased to 20° the flowfield structure remains analogous to the 15° angle of attack case, but changes in scale. The fluid originating from the forebody becomes entrained into the separated flowfield above the wing. The vortical structure grows in height due to influence from the potential freestream flow above the model. The vortex wake in the vicinity of the vertical tails now extends to the tip of the tail, and the turbulence intensity data shows that the regions of maximum turbulence have

moved closer to the surface of the tail. This presumably results in higher dynamic loading on the vertical tails at this angle of attack, and collaborates well with findings from other researchers.

At 25° angle of attack the vortical structure continues to expand, and moves upward in relationship to the model as the vortex wake propagates downstream. The fluid originating from the forebody enters into the vortex in much the same way as in the 20° angle of attack case. Now the regions of maximum turbulence in the tail plane are much closer to the tail surface and measured intensities of at least 5% extend well above the tail tip. However, the local velocities in the vicinity of the tail are not as high as in the 20° case.

Although tail loadings cannot be obtained from this data, some conclusions can be hypothesized. The flow measurement data indicates that at 20° angle of attack the local velocities are higher in the vicinity of the tail than in the 25° case, but the levels of turbulence are lower. This could lead one to conclude that the angle of attack at which maximum momentum fluctuations are occurring, and hence buffeting, would be between 20° and 25° angle of attack. Komerath, et al,<sup>4</sup> found that the level of maximum buffeting occurred at 22° angle of attack. The flow visualization data and quantitative data presented in this paper reinforce those findings.

## SUMMARY AND CONCLUSIONS

Analysis of the vortical flowfield about an F-15 and its interaction with the twin vertical tails was accomplished through qualitative flow visualization data and quantitative hot-film data. The combination of the wind tunnel and water tunnel data provided an excellent means for analyzing the complex flowfield existing about the F-15 at moderate to high angles of attack. The major findings from these experimental investigations follow:

- 1) At 10° angle of attack a vortex forms at the apex of the wing glove outboard of the engine inlet. This vortex tracks downstream, parallel to the fuselage centerline and impinges on the vertical tail of the F-15, encompassing approximately 40% of the vertical tail span. The flowfield above the wing separates from the wing leading edge, forming a vortex which flowed spanwise toward the wing tip.

- 2) At 15° angle of attack the vortex originating from the wing glove area and a portion of the forebody fluid is now drawn into a large vortical structure resident

above the wing. This vortex results from separation at the wing leading edge, and causes turbulence intensities of up to 55% near the wing leading edge. As this turbulent wake flows downstream it passes outboard of the vertical tails, resulting in turbulence intensities of 20% near the base of the tail.

3) At 20° and 25° angle of attack the basic structure of the vortex flowfield remains similar to that of the 15° angle of attack case. The significant difference in these cases are that the vortical flowfield above the wing has increased in size in both the spanwise and vertical directions and more fluid originating at the forebody is now drawn spanwise into the vortex. The vortical wake surrounds the entire span of the vertical tail at 20° angle of attack, and extends above the tip of the tail at 25° angle of attack. Turbulence intensities near the base of the tail increase from 25% to 35% as the attack angle is increased. In addition, the region of maximum turbulence intensity has moved much closer to the vertical tail surface. For the 25° angle of attack case, the maximum turbulence region is at the surface of the tail. The local velocities in the tail vicinity were slightly higher in the 20° case than in the 25° case. Based upon these results it could be hypothesized that the maximum momentum changes, and hence dynamic loadings on the tail, occur between 20° and 25° angle of attack.

The combination of the flow visualization data and the numerical data provided a means of studying the vortical flowfield about F-15 in great detail. It was determined that at 10° angle of attack, the vortex flow originates at the wing glove. At angles of attack of 15° and above, the primary vortex progresses from one fed only from the flow over the wing to that fed from the forebody and the wing flowfields. The vortex tracks downstream, encompassing the vertical tails with a highly turbulent flow. Through the continuation of this study, to include a more detailed survey of the vortical wake, the ability of controlling the vortex flowfield to alleviate buffeting can be realized.

#### ACKNOWLEDGEMENTS

The authors would like to thank CIC's Fritzinger, Keeton, Bradley, and Forest for their help in this project. The assistance of Mr. Jim Philp in model preparation and TSgt Rick Durmon in the data acquisition is also greatly appreciated. Special thanks are due to 2Lt Bill Bryant for all of his support.

#### REFERENCES

- 1 Lee, B. H. K., et al "Flowfield in the Vicinity of an F/A-18 Vertical Fin at High Angles of Attack," J. Aircraft, Vol. 30, No. 1, Jan-Feb 1993, pp. 69-74.
- 2 Meyn, L. E., Lanser, W. R., and James, K.D., "Full-Scale High Angle-of-Attack Tests of an F/A-18," AIAA Paper No. 92-2676, 10th Applied Aero., June 1992, Palo Alto, CA.
- 3 Triplett, W. E. "Pressure Measurements on Twin Vertical Tails in Buffeting Flow," J. Aircraft, Vol. 20, No. 11, Nov 1983, pp. 920-925.
- 4 Komerath, N. M., et al, "Flow over a Twin-Tailed Aircraft at Angle of Attack Part I: Spatial Characteristics," J. Aircraft, Vol. 29, No. 3, May-June 1992, pp. 413-420.
- 5 Hebbbar, S., Platzter, M., and Frink, W., "Vortex Wake Investigations of a Twin-Tail Fighter Aircraft Model at High Angles of Attack With and Without LEX Fences," AIAA Paper No. 93-0868, Jan 1993, Reno, NV.
- 6 Bean, D. E. and Wood, N. J. "An Experimental Investigation of Twin Fin Buffeting and Suppression," AIAA Paper No. 93-0054, Jan 1993, Reno NV.
- 7 Washburn, A. E., Jenkins, L. N., and Ferman, M. A., "Experimental Investigation of Vortex-Fin Interaction," AIAA Paper No. 93-0050, Jan 1993, Reno, NV.
- 8 Gad-el-Hak, M. and Blackwelder, R., "The Discrete Vortices from a Delta Wing," AIAA Journal, Vol. 23, No. 6, June 1985, p. 961.

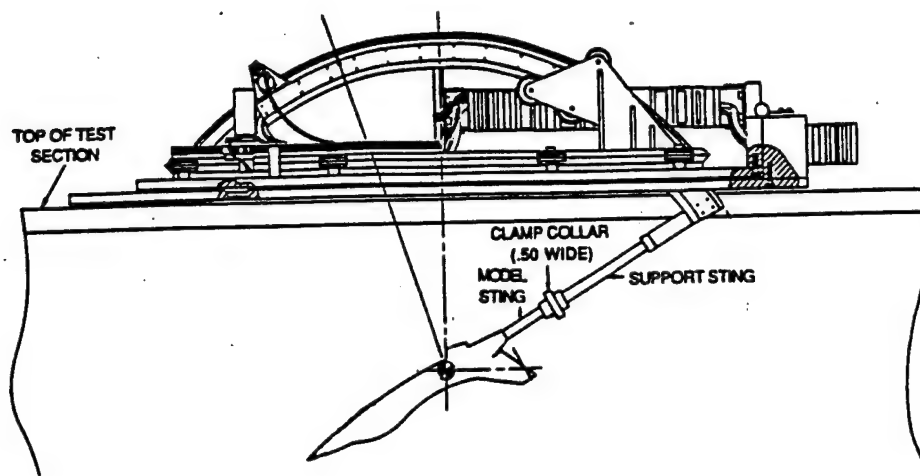


**Figure 1. Water Tunnel Test Configuration**

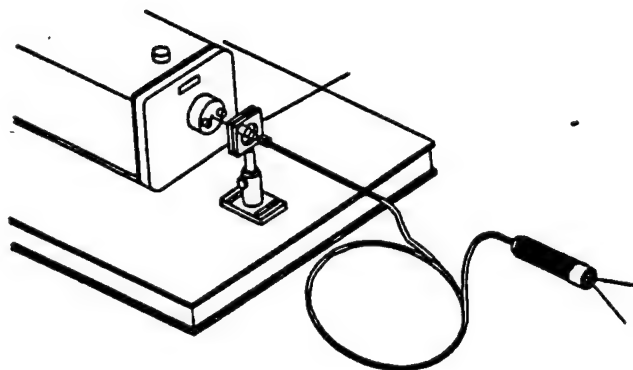


**Figure 2. Laser Light Sheet Fiber Optics**

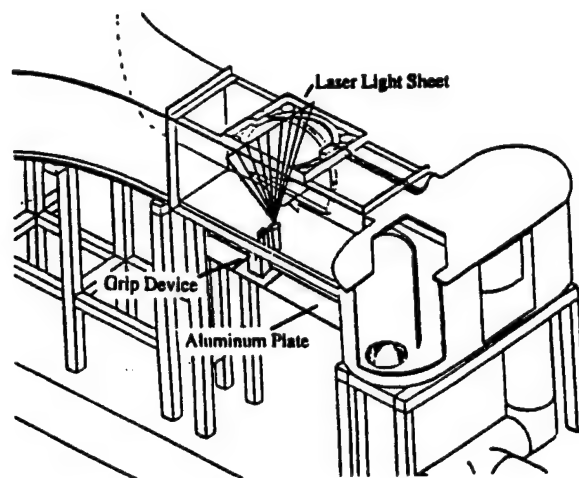


**Figure 3. Laser Light Sheet Configuration**

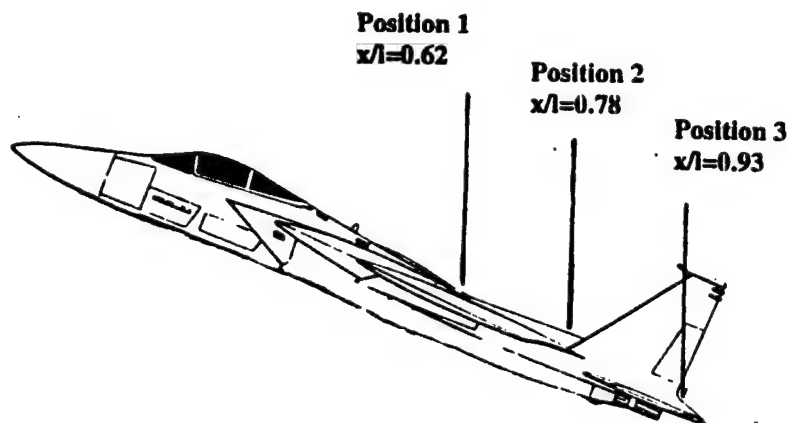
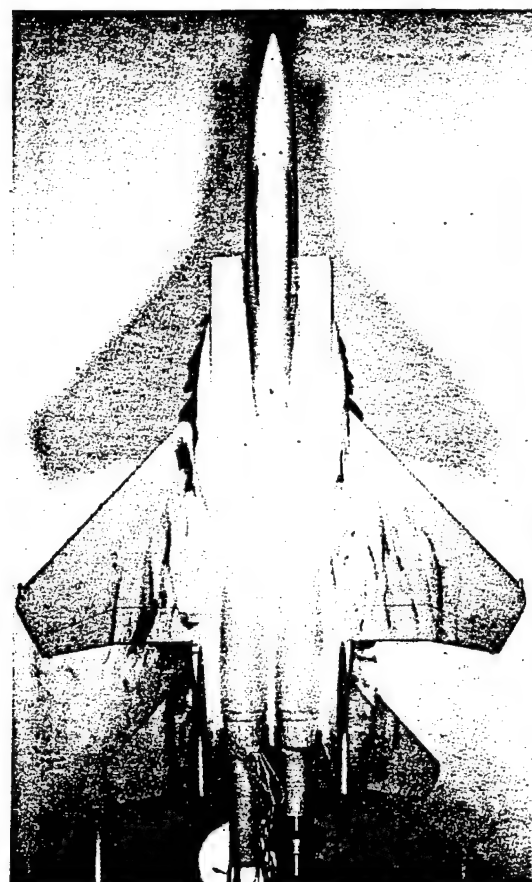


**Figure 4. Flow Visualization and Hot-Film Measurement Locations**



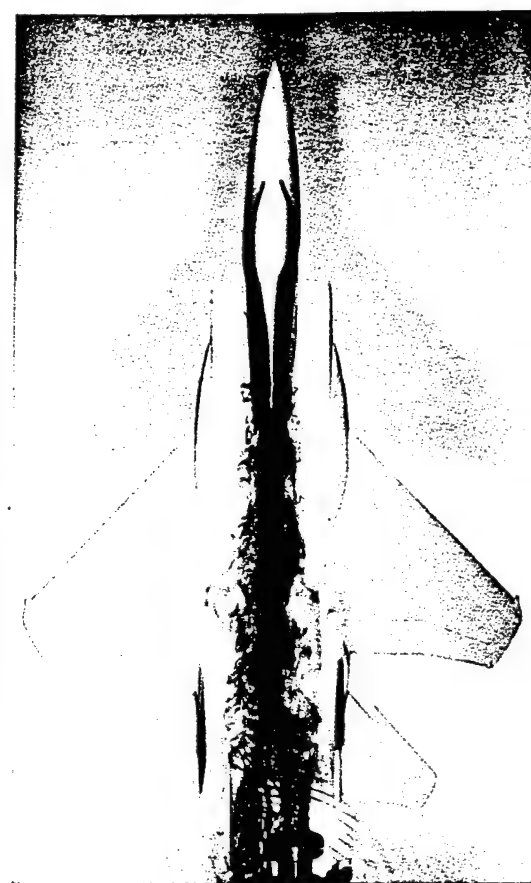
a) wing glove/inlet flow visualization - side view



b) wing glove/inlet flow visualization - top view



c) forebody flow visualization - side view

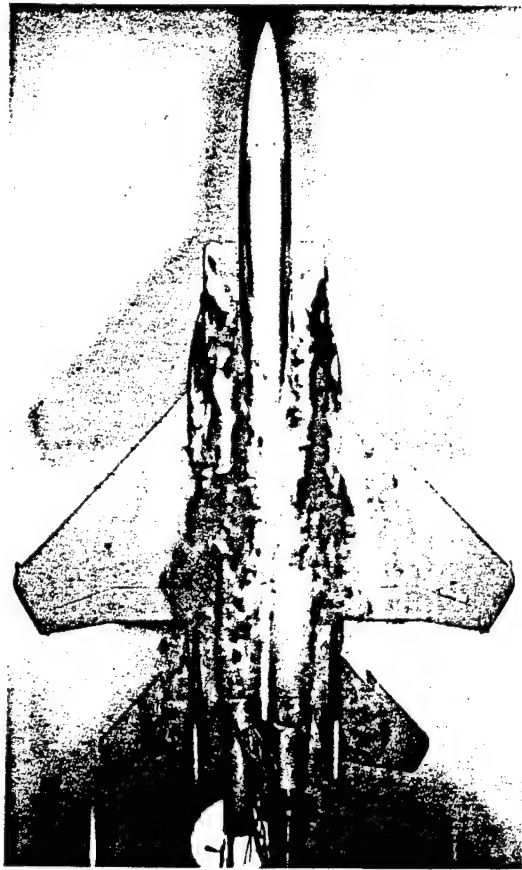


d) forebody flow visualization - top view

Figure 5: Colored Dye Flow Visualization at  $\alpha = 5^\circ$ .



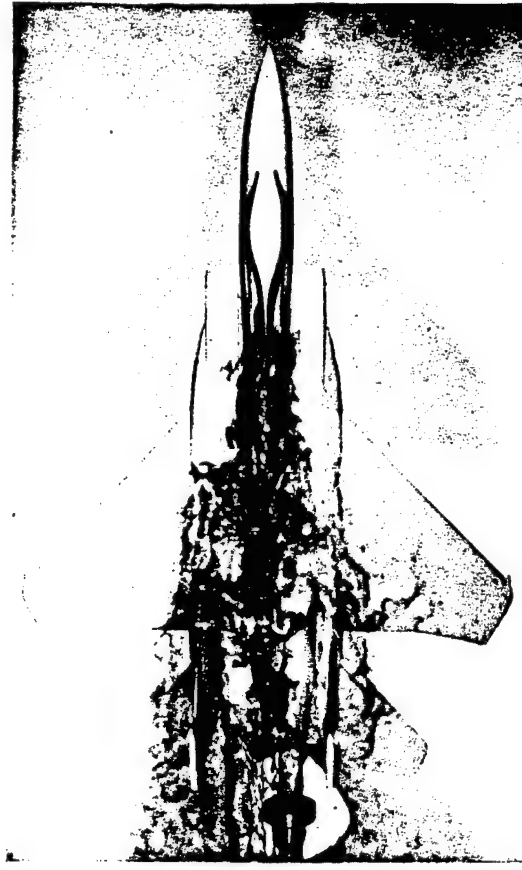
a) wing glove/inlet flow visualization - side view



b) wing glove/inlet flow visualization - top view



c) forebody flow visualization - side view

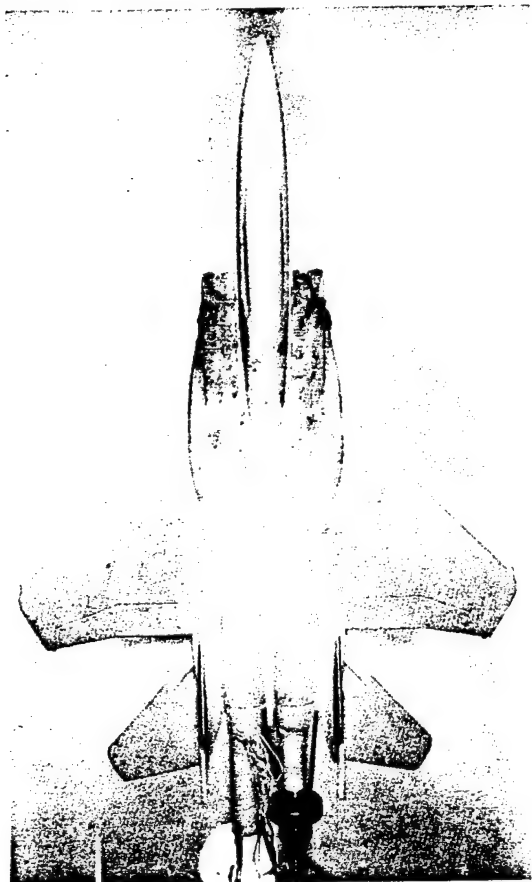


d) forebody flow visualization - top view

Figure 6: Colored Dye Flow Visualization at  $\alpha = 10^\circ$ .



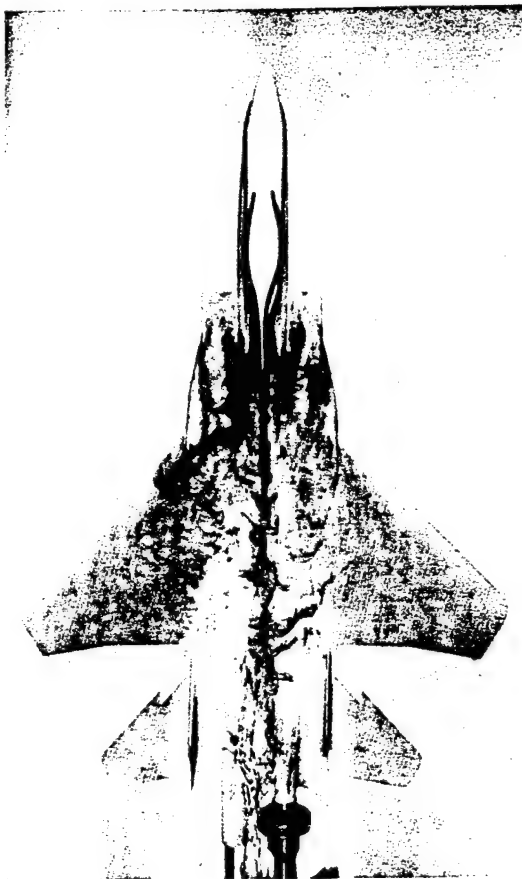
a) wing glove/inlet flow visualization - side view



b) wing glove/inlet flow visualization - top view



c) forebody flow visualization - side view

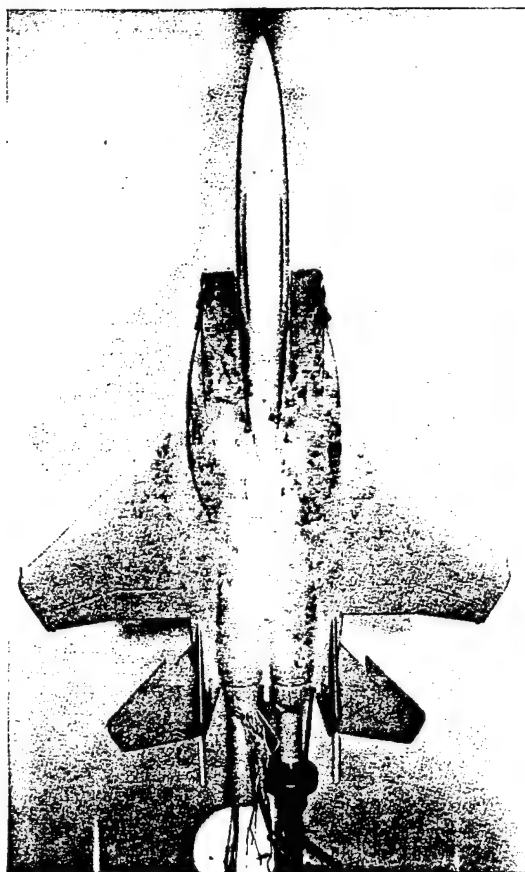


d) forebody flow visualization - top view

Figure 7: Colored Dye Flow Visualization at  $\alpha = 15^\circ$ .



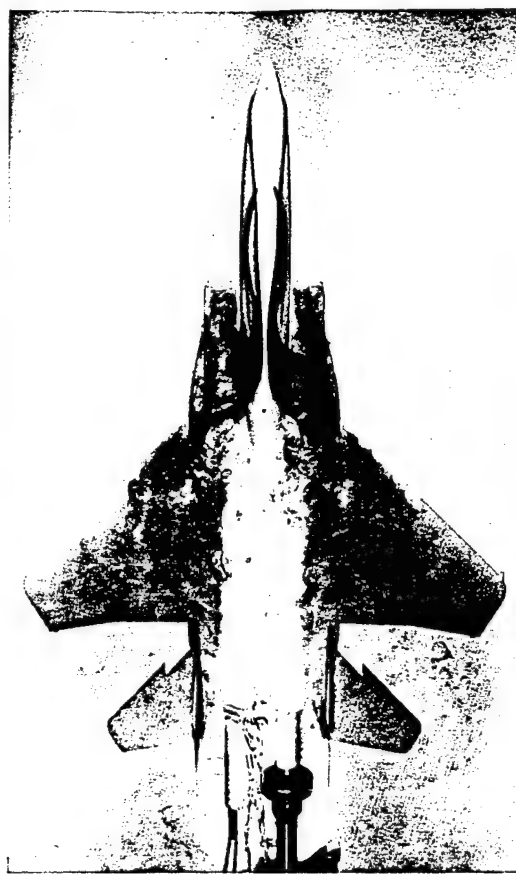
a) wing glove/inlet flow visualization - side view



b) wing glove/inlet flow visualization - top view



c) forebody flow visualization - side view

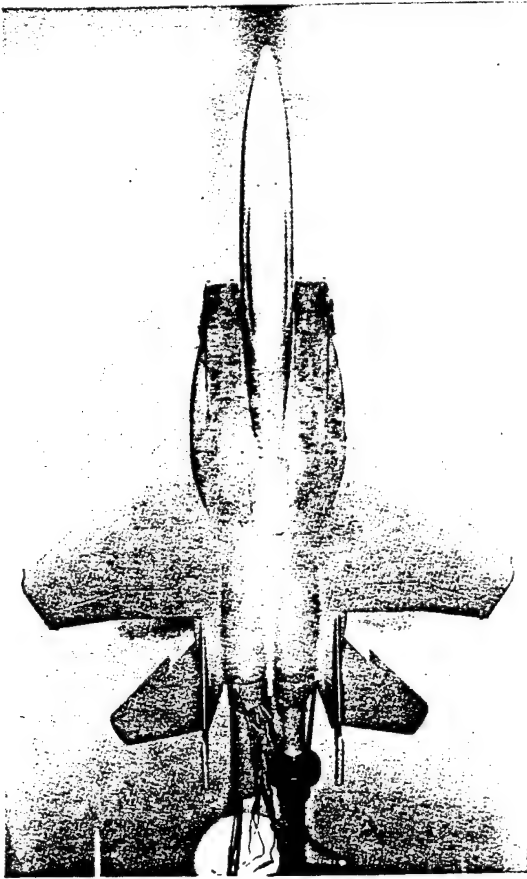


d) forebody flow visualization - top view

Figure 8: Colored Dye Flow Visualization at  $\alpha = 20^\circ$ .



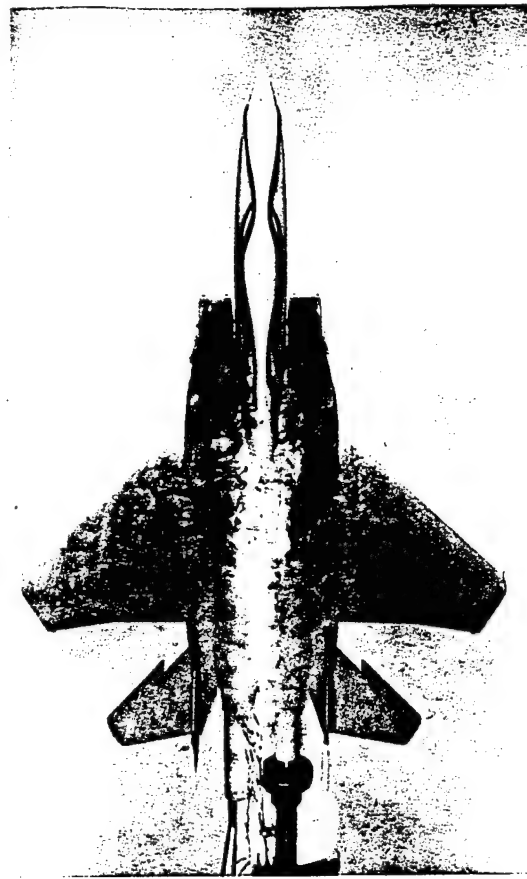
a) wing glove/inlet flow visualization - side view



b) wing glove/inlet flow visualization - top view



c) forebody flow visualization - side view

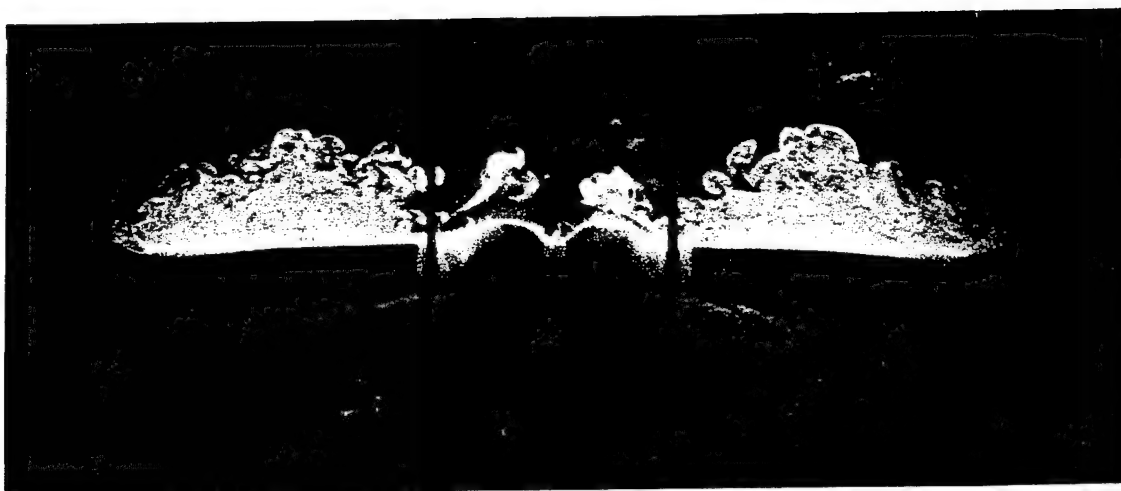


d) forebody flow visualization - top view

Figure 9: Colored Dye Flow Visualization at  $\alpha = 25^\circ$ .



a) position 1,  $x/l = 0.62$

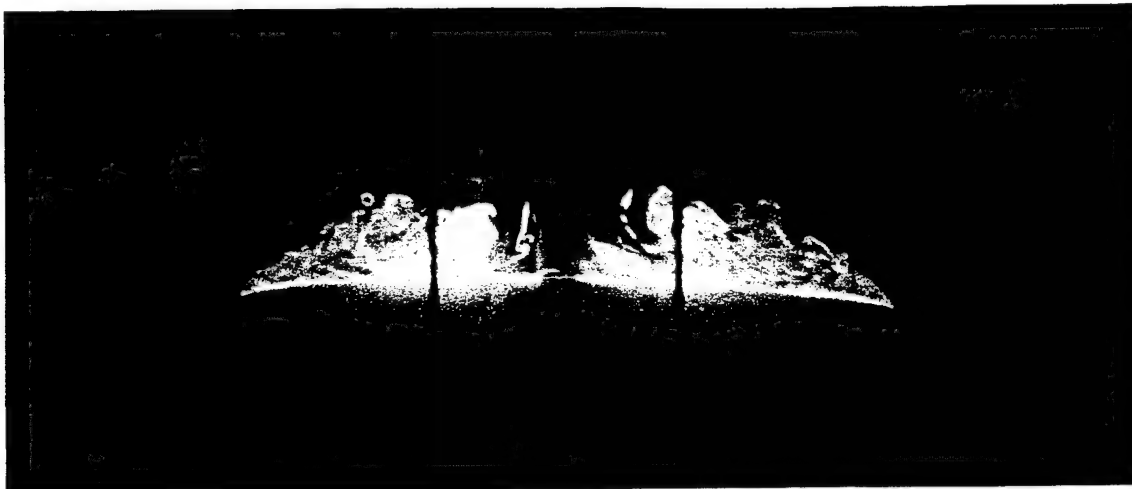


b) position 2,  $x/l = 0.78$



c) position 3,  $x/l = 0.93$

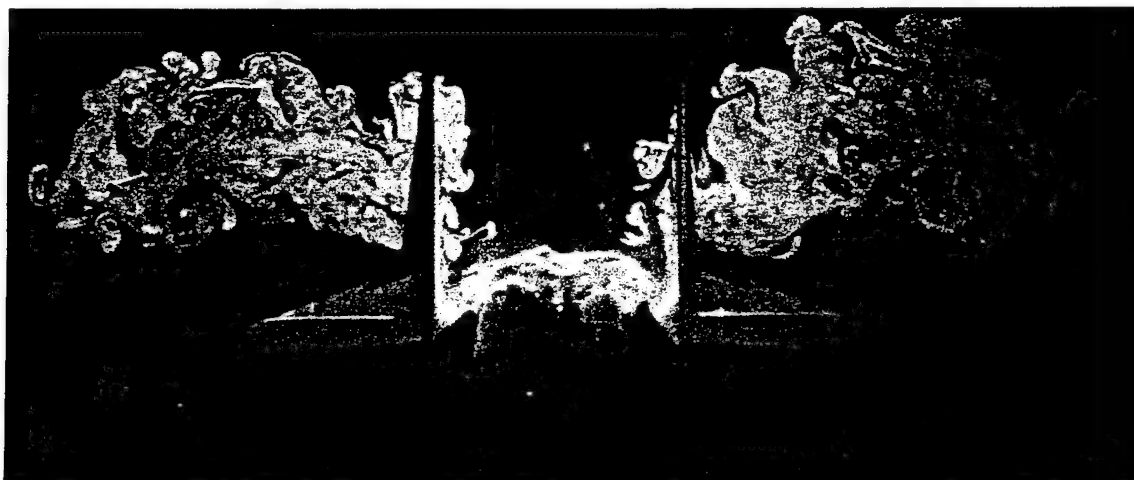
**Figure 10: Laser Light Sheet Fluorescent Dye Flow Visualization  
at  $\alpha = 15^\circ$ ,  $x/l = 0.62, 0.78, 0.93$ .**



a) position 1,  $x/l = 0.62$

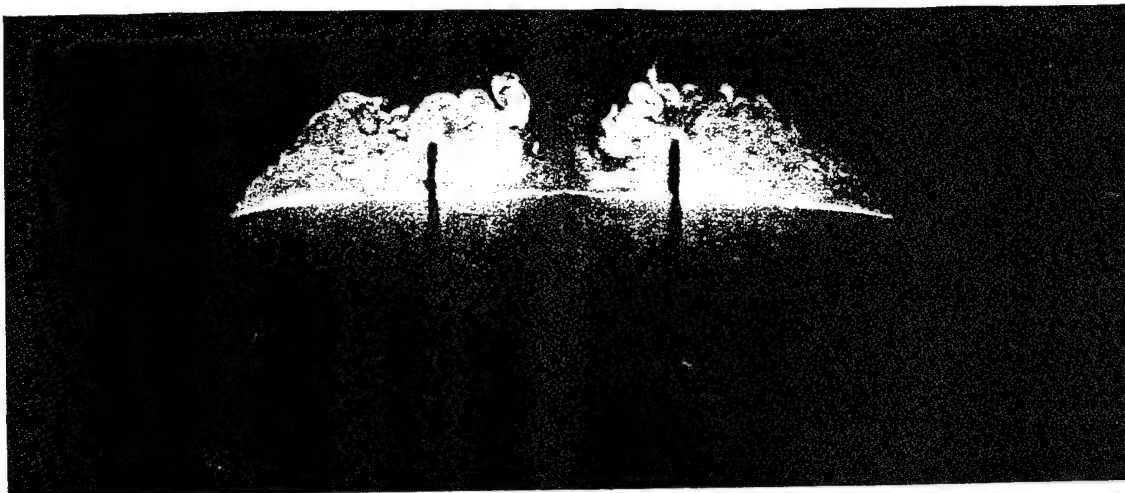


b) position 2,  $x/l = 0.78$

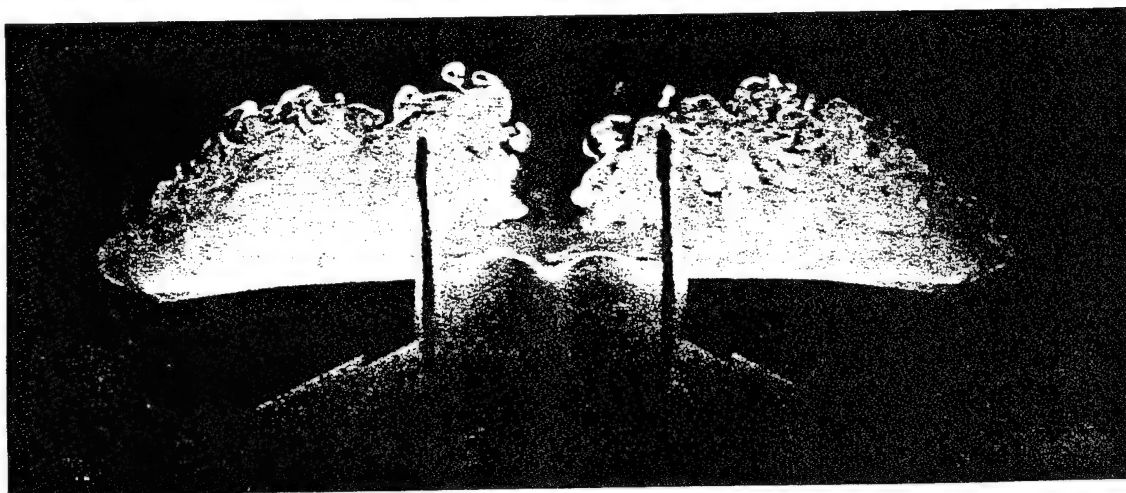


c) position 3,  $x/l = 0.93$

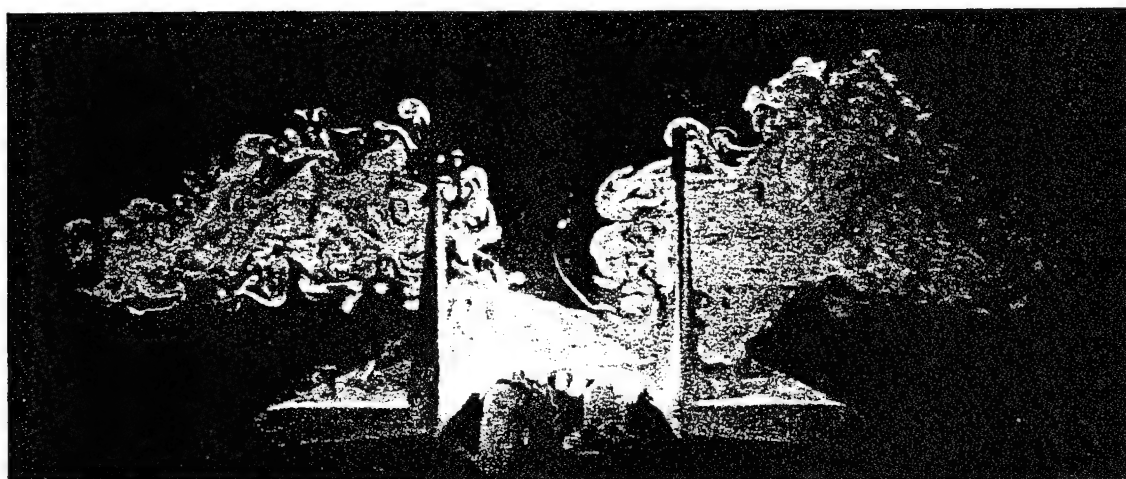
**Figure 11: Laser Light Sheet Fluorescent Dye Flow Visualization  
at  $\alpha = 20^\circ$ ,  $x/l = 0.62, 0.78, 0.93$ .**



a) position 1,  $x/l = 0.62$



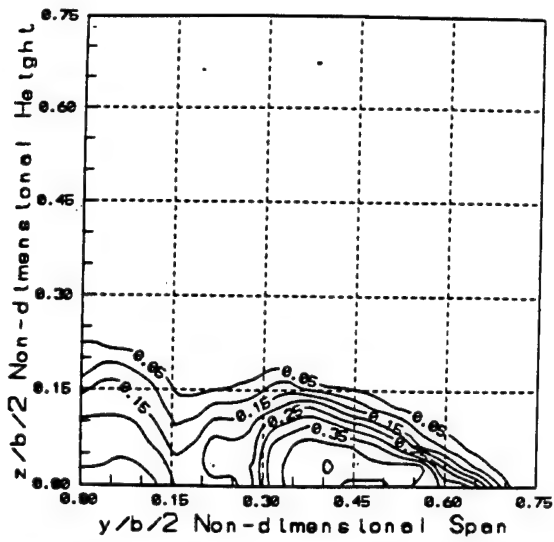
b) position 2,  $x/l = 0.78$



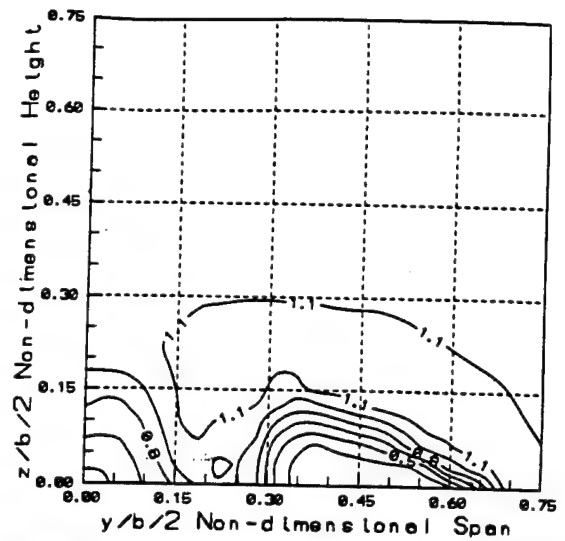
c) position 3,  $x/l = 0.93$

**Figure 12: Laser Light Sheet Fluorescent Dye Flow Visualization**  
at  $\alpha = 25^\circ$ ,  $x/l = 0.62, 0.78, 0.93$ .

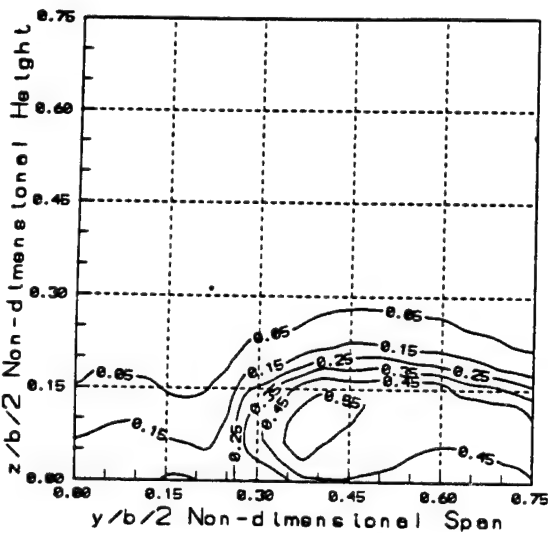




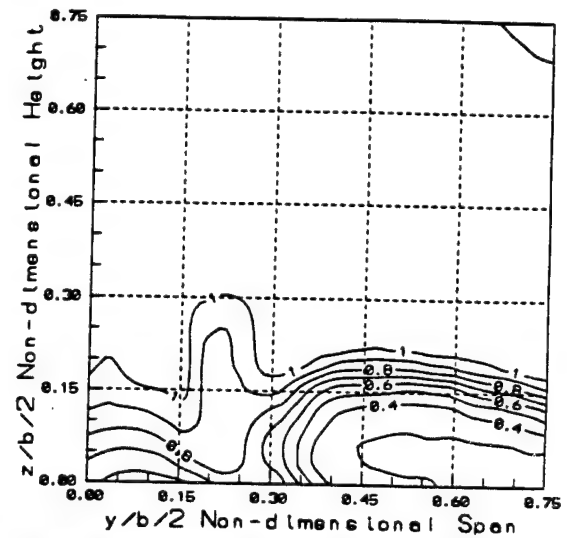
a) turbulence intensity, position 1,  $x/l = 0.62$



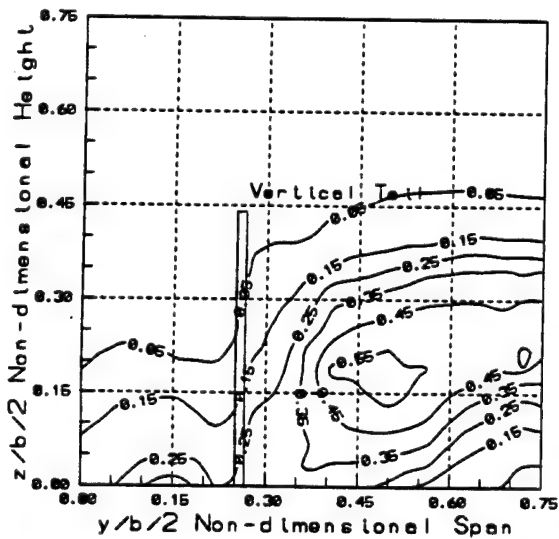
b) non-dimensional velocity, position 1,  $x/l = 0.62$



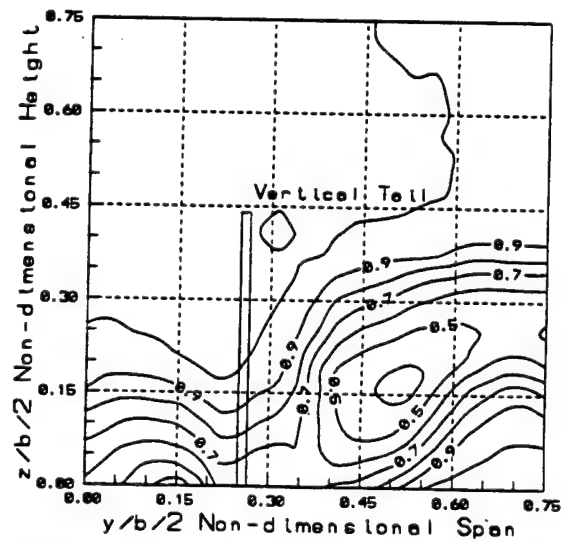
c) turbulence intensity, position 2,  $x/l = 0.78$



d) non-dimensional velocity, position 2,  $x/l = 0.78$

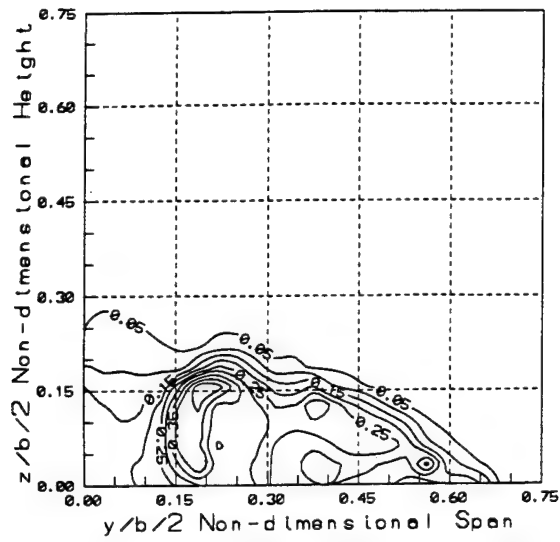


e) turbulence intensity, position 3,  $x/l = 0.93$

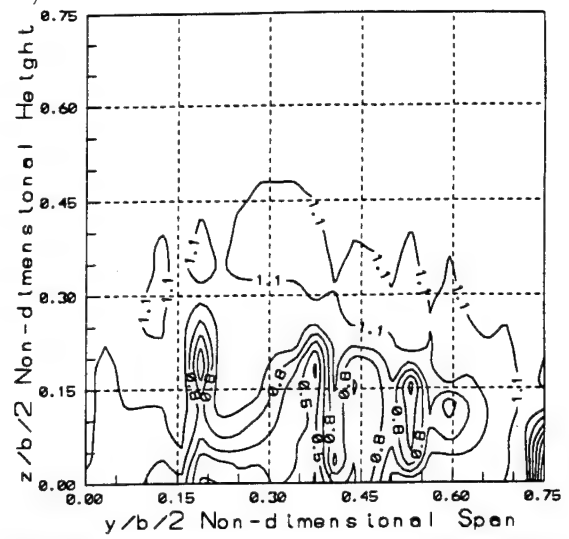


f) non-dimensional velocity, position 3,  $x/l = 0.93$

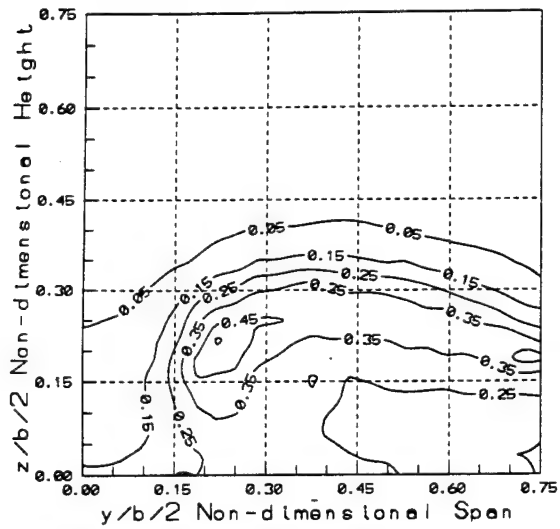
**Figure 14: Turbulence Intensity and Non-dimensional Velocity Contours  
at  $\alpha = 20^\circ$ ,  $x/l = 0.62, 0.78, 0.93$ .**



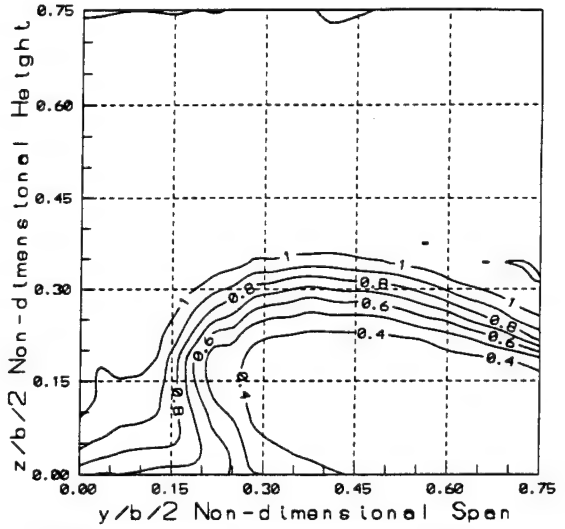
a) turbulence intensity, position 1,  $x/l = 0.62$



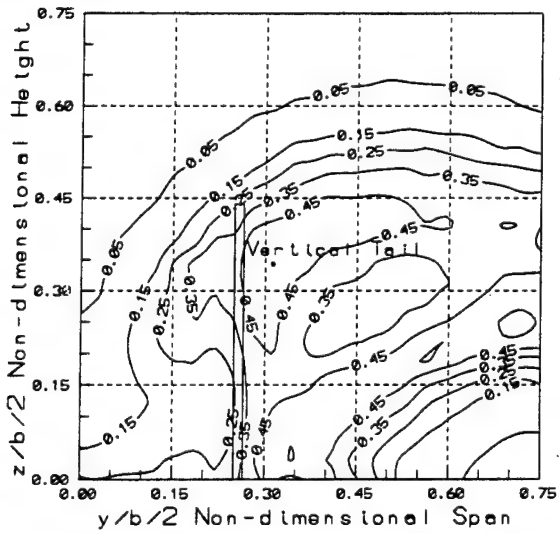
b) non-dimensional velocity, position 1,  $x/l = 0.62$



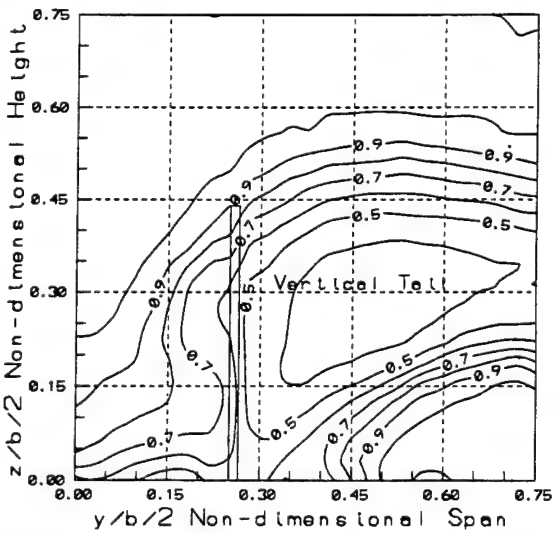
c) turbulence intensity, position 2,  $x/l = 0.78$



d) non-dimensional velocity, position 2,  $x/l = 0.78$



e) turbulence intensity, position 3,  $x/l = 0.93$



f) non-dimensional velocity, position 3,  $x/l = 0.93$

**Figure 15: Turbulence Intensity and Non-dimensional Velocity Contours  
at  $\alpha = 25^\circ$ ,  $x/l = 0.62, 0.78, 0.93$ .**



# **AIAA 95-0675**

## **Feedback Control of the Flow over a Two-Dimensional Airfoil**

**Julie A. Lovato**  
**Craig A. Baer**

**Frank J. Seiler Research Laboratory**  
**United States Air Force Academy, CO**

**33rd Aerospace Sciences  
Meeting and Exhibit**  
**January 9-12, 1995 / Reno, NV**

# FEEDBACK CONTROL OF THE FLOW OVER A TWO-DIMENSIONAL AIRFOIL

Julie A. Lovato\*

&

Craig A. Baer<sup>+</sup>

Frank J. Seiler Research Laboratory  
U.S. Air Force Academy, CO 80840

## Abstract

The development and implementation of a feedback control system for static airfoil performance enhancement is discussed. A two-dimensional NACA-0015 airfoil is evaluated under active control supplied by a spanwise slot at the leading edge. A feedback control loop couples the frequency at which air is tangentially pulsed through the slot to surface pressure coefficients measured near the airfoil leading edge. By optimizing the frequency of the control, lift enhancements of over 25% ( $\pm 4.1\%$ ) and static pressure stall delays of  $4^\circ$  in angle of attack are achieved. Frequencies determined by the feedback control system correspond to Strouhal Number of 0.2 near the angle of attack region of stall. Post stall evaluations show that only very low frequency (5 Hz,  $St_c \approx .04$ ) control inputs are successful in enhancing lift.

## Nomenclature List

$c$	Airfoil Chord
$C_L$	$L/1/2\rho U_\infty^2$ (one unit span)
$St_c$	Strouhal Number based on $csin\alpha$
$\alpha$	Angle of Attack in Degrees
$f$	Control Frequency

\*Research Director, Unsteady Aerodynamics.  
Member AIAA

<sup>+</sup>Research Associate, Unsteady Aerodynamics

This paper is declared a work of the U.S.  
Government and is not subject to copyright  
protection in the United States.

## Introduction

The importance of both understanding and efficiently using active control techniques to enhance the aerodynamic performance of aircraft is presently well accepted. A great deal of research has been conducted to evaluate the effectiveness of various active control methods for static airfoil flow. The reader is directed to Gad el Hak and Bushnell<sup>1</sup> for a summary of these techniques.

The research discussed in this paper is based on previous successful attempts to alter the separation characteristics of a two-dimensional, static airfoil. Active pulse-air injection, with the frequencies of the pulse being coupled to the natural characteristics of the flow, is effective in either delaying separation or reattaching a separating boundary layer and extending the stall angle of attack.<sup>2,3</sup> The benefits of this type of control lie in the low amounts of mass required to effect the performance enhancements of the airfoil. By taking advantage of the natural Kelvin-Helmholtz instabilities in the separating boundary layer, or shear layer, researchers have been able to apply techniques previously developed for mixing layers with beneficial results.<sup>4</sup> By forcing the large scale structures present in the static separating boundary layer to pair, the shear layer growth rate increases, causing it to interact with the airfoil surface and effectively reattach to the airfoil.

Although a thorough physical understanding of the flow has been accomplished, a clear understanding of the parametric response of the flow to the active control needs to be established. In addition, a model must be developed to extend this technique to a practical application. The experimental analysis detailed in

this paper attempts to accomplish both of these goals. A feedback control law which can be implemented as either a state (modern) or classic system has been designed to allow both quick analysis of various parameter combinations as well as determination of the optimum control configuration has been developed. The system uses an integrated control and analysis capability to adjust active air input depending on the status of surface pressure values on the upper airfoil surface. This allows optimization of the surface pressure magnitudes to effect the greatest aerodynamic performance on the airfoil.

### Experimental Methods

Experiments were conducted in the Frank J. Seiler Research Laboratory's Low Speed Wind Tunnel located at the U. S. Air Force Academy. The tunnel has a 0.91m x 0.91m test section, with a freestream turbulence level below 0.5%. The majority of tests were conducted at a freestream velocity of 9.1 m/s, corresponding to a chord Reynolds number of 80,400. A NACA-0015 model with a 60cm span and a 15.2cm chord was evaluated under various static angles of attack. Circular splitter plates 30cm in diameter were fixed to both ends of the airfoil to ensure two-dimensionality. Pressure measurements were obtained along the upper surface of the airfoil using close-coupled Endevco 8502 miniature pressure transducers. The transducers were installed inside the airfoil to minimize any possible lag-time errors in the surface pressure readings. For each case, 200 data points were taken over a 20° angle of range along the center span. The error in lift calculations for all data was 4.1%. After manipulating the control parameters using the controller, detailed pressure measurements were made using a Concurrent Data Acquisition System.

Active control of the flow was accomplished by injecting air through a spanwise slot located at the airfoil leading edge. The system was designed to inject air through the slot in a tangential manner, either using a constant stream or pulsing the air at frequencies specified by the controller. During frequency comparisons, the blowing momentum coefficient,

$C\mu = (U_{slot}^2 / U_\infty^2) (\text{slot width}/c) (\text{percent-on time})$  was kept constant at 0.004. The air injection system employed two solenoid valves supplying air to both ends of the slot. A control circuit was driven by the controller to pulse the valves anywhere from 0-45 Hz. The total mass injection was kept constant. Details of the air injection system can be found reference five<sup>5</sup> and are also shown in Figure 1.

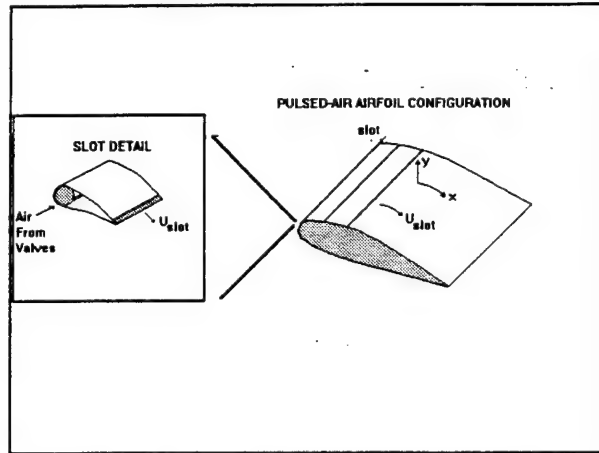


**Figure 1. Detail of the active air injection process**

The feedback control system employed an Integrated Systems, Inc. AC-100 controller, allowing for eight input channels and 16 analog outputs. The configuration used in this experiment is shown in Figure 2. The AC-100, manipulated by a graphical user interface utility called MATRIXx, set the type of active control input (constant or pulsed air blowing) as specified by the operator. The air was then injected into the airfoil flow, and the responses of the surface pressure values recorded and displayed. Adjustments in the active control input were then adjusted accordingly and the process repeated. The controller allowed for real-time adjustments in air pulse width and injection amplitude, keeping the total amount of mass injected per second constant. When the desired levels were reached, data acquisition was accomplished using the Concurrent system, and lift values were calculated. This allowed a clear determination of

the control system's efficiency in enhancing airfoil aerodynamic performance.

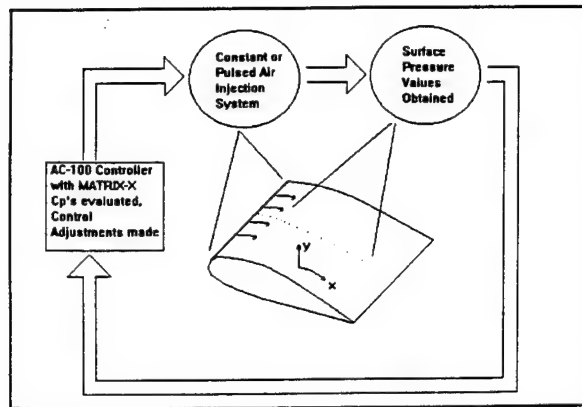


**Figure 2. Configuration of the feedback control system using the AC-100**

### Results and Discussion

The response of the flow was analyzed under various settings of pulsed air injection. For the first part of the study, the feedback control system was configured to allow real-time user interface. Frequency values corresponding to the previously determined vortex passage frequency and its subharmonics were evaluated. Figure 3 shows the lift coefficient values for three frequencies which were tested, compared to the unforced case. Quasi-steady surface pressure measurements were taken up to an angle of attack of  $20^\circ$ . The airfoil was pitched slowly at a pitch rate of  $0.4 \text{ deg/sec}$ , which corresponded to a change of  $0.1 \text{ deg}$  per data point. The results closely resemble data taken previously by statically moving the airfoil, and are therefore considered to be quasi-steady.<sup>6</sup>

The lift values for all four curves are close prior to the near-stall region after  $10^\circ$  angle of attack. The 5Hz injection case is slightly higher at some points along the curve. As the airfoil nears stall and the flow starts to separate, effects of the active air injection become greater. This is to be expected, since the mechanism by which this pulsed air control works is by interaction with natural instabilities in the flow. These instabilities are not present in the flow until the flow begins to separate. Around  $8^\circ$  angle of attack, the 5 Hz controlled case shows a marked

increase of about 7% over the natural case. This increase exceeds the  $\pm 4.1\%$  error for these measurements. This lift enhancement continues until approximately  $15^\circ$ , where the 20 Hz control case becomes the case with the greatest lift coefficients. The 20 Hz control case continues to dominate until about  $17^\circ$  angle of attack, with increases in lift coefficients in the range of 14-16%, where it "exchanges places" with the 5 Hz control case.

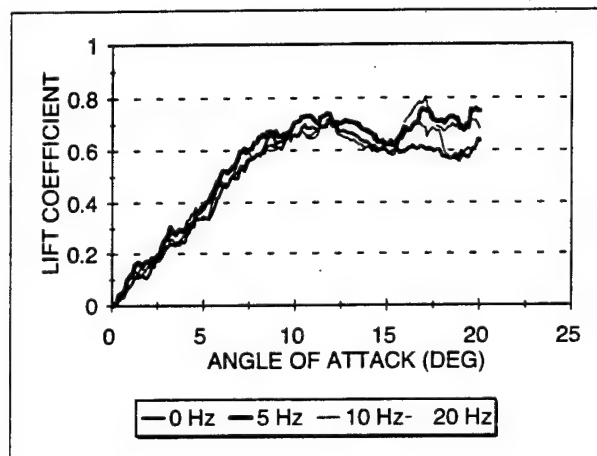


**Figure 3. Lift Coefficient vs Angle of Attack, natural and actively controlled cases.**

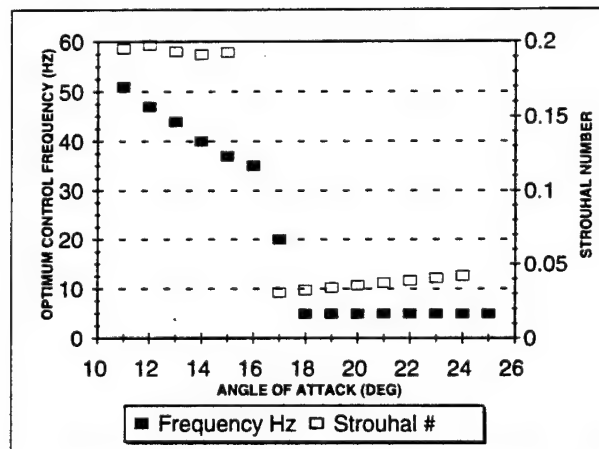


**Figure 4. Value for optimum control frequency based on leading five pressure transducer values for various angles of attack.**

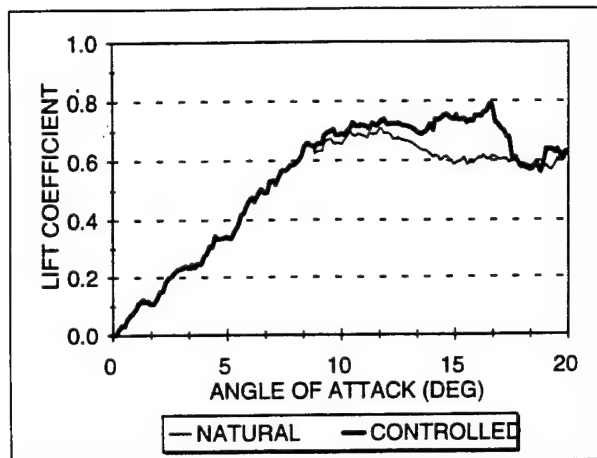


**Figure 5. Lift Coefficient vs Angle of Attack, natural and optimally controlled case.**

Forcing the flow at 5 Hz imparts the greatest lift increases after 17° angle of attack, with increases in lift exceeding 21%. The results clearly show that the most effective forcing frequency changes with angle of attack. This is to be expected, since past work has shown that the characteristic flow frequencies are dependent on both angle of attack and freestream velocity. The benefit of a feedback control system lies in this dependency. While it is feasible to develop a control model in the wind tunnel for simple airfoil or wing configurations, it becomes more difficult in a practical application. The feedback control system can continuously adjust to changing flow parameters to maintaining top aerodynamic performance.

The next step in the analysis was to employ a simple algorithm designed to continuously evaluate the leading three pressure transducers on the airfoil, determine whether they were becoming more or less negative, adjust the pulsed air frequency input, and re-evaluate the surface pressure conditions. The control input was adjusted so that the mass of air injected over a period of time was constant while the frequency was changed. The end result was that the pulse width decreased proportionately with increasing frequency.

The results of this examination are shown in Figure 4. The optimal control frequency, given in Hz, decreases with increasing angle of attack until 18°, where it reaches a constant of 5 Hz.

When these frequencies are converted to Strouhal numbers using chord times the sine of the angle of attack as the characteristic height, the values near stall equate to  $St_c = 0.2$ . This value is within the range determined previously to instill the greatest forcing response to a downstream facing step.<sup>7</sup> A static airfoil positioned at a positive angle of attack imparts a blockage in the flow similar to a downstream facing step.

As determined by Crow and Champagne<sup>8</sup> and Kibens<sup>9</sup>, when forcing is tuned to the fundamental frequency or the corresponding subharmonics, the flow "locks-on" to the control frequency. This transmits more efficient flow control by enhancing vortex pairing. Employing the relation described by Katz<sup>10</sup>,  $St_c = fc(\sin\alpha)/U_\infty$ , where  $St_c$  was found equal to 0.18 - 0.19 for a NACA-0012 airfoil wake. When Lovato and Troutt compared these results to their characterization of the static separating boundary layer, they found that the lock-on fundamental frequency at the leading edge of a stall airfoil corresponded to a  $St_c$  of 0.8.<sup>6</sup> It is reasonable to assume that the structures present in the separating boundary layer undergo pairings prior to reaching the trailing edge of the airfoil, and thus one would expect the lock-on frequency to be less at the trailing edge than at the leading edge. This information indicates that during stall the most effective control frequency is the second subharmonic. Based on past mixing layer research, this would force every four vortices to pair, thus reattaching the separating boundary layer to the airfoil. In the post stall region, a much lower frequency is needed to control the flow, possibly a much lower subharmonic.

The last part of this study investigated the effect of pulsing amplitude on the flow response to active control. While the previous results clearly showed that the optimum aerodynamic performance enhancements were closely tied to the natural frequencies present in the flow, the dependence on amount of mass injected also needs to be determined.

This relationship was investigated by maintaining a constant injection frequency and varying the mass injection magnitude by adjusting the "percent-on" time of the pulse. Figure 6 shows the results for a pulse frequency of 5 Hz at

three different injection magnitudes. The variance in magnitude is indicated by the percentage time the air was being injected per second. Even an injection level as low as 1%, corresponding to a  $C_\mu$  of 0.0004, imparts some lift enhancement. The maximum lift increase of 17% occurs at about  $17^\circ$  angle of attack. Performance enhancements decrease in effectiveness soon thereafter. The control inputs at 3% ( $C_\mu = 0.0012$ ) and 10% ( $C_\mu = 0.004$ ) are virtually identical, resulting in lift increases of over 25% near the  $16^\circ$  angle of attack point. There is also significant stall delays at these levels.

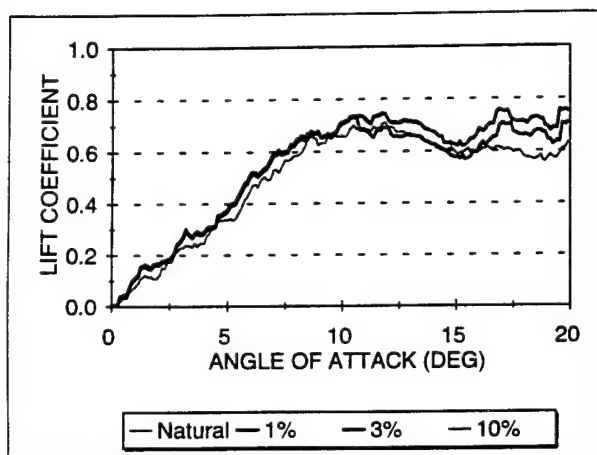


**Figure 6. Variance of Lift Coefficient with control magnitude. Forcing frequency is 5 Hz.**

### Conclusions

The experimental analysis here has demonstrated the plausibility of a feedback control system designed to optimize aerodynamic performance on a static, two-dimensional NACA-0015 airfoil. The control system has been successfully proven to impart active, pulsed-air control on the upper surface flow field of the airfoil to enhance the lift characteristics as much as 25% ( $\pm 4.1\%$ ) in some cases. Current results show that the control efficiency is dependent on forcing frequency and angle of attack, so by altering the control parameters as the flow configuration changes, the maximum

aerodynamic performance enhancement can be obtained.

Specific conclusions can be drawn from the experimental analysis:

- The most effective Strouhal number to enhance aerodynamic performance is near 0.2 in the stall to post-stall region.
- Controlling the flow using continuous, feedback adjustments to frequency input results in lift enhancements over 25% ( $\pm 4.1\%$ ).
- Injecting pulsed air at blowing momentum coefficients as low as  $C_\mu = 0.0004$  can impart significant aerodynamic enhancements to the flow, even delaying the angle of attack of stall.

### Acknowledgments

The authors would like to extend their thanks to 2Lt's John Meiter and Brian Kobashigawa, and Mr. David Emmerson for their assistance in constructing the experimental control system. Special consideration is also due to Mr. Bobby Hatfield and Mr. Jim Philp for design suggestions and fabrication of the model.

### References

- <sup>1</sup> Gad-el-Hak, M. and Bushnell, D. M. "Separation Control: Review," J. Fluids Engr., Vol. 113, March 1991, pp. 5-30.
- <sup>2</sup> Lovato, J. A. and Troutt, T. R. "Active Control of the Shear Layer on a Static Airfoil," AIAA Paper No. 93-0442.
- <sup>3</sup> Seifert, A. et al, "Oscillatory Blowing: A Tool to Delay Boundary-Layer Separation," AIAA J., Vol. 31, No. 11, Nov 1993, pp. 2052-2060.
- <sup>4</sup> Oster, D. and Wygnanski, I. "The Forced Mixing Layer Between Parallel Streams," J. Fluid Mech., Vol. 123, pp 91-130.
- <sup>5</sup> Davis, W., Lovato, J., and Pezeshki, C, "Nonlinear Spectral Characterization of Frequency-Modulated Control Applied to a Static Airfoil Shear Layer," AIAA

---

Paper No. 94-2217, 25th AIAA Fluid Dynamics Conference, Colorado Springs, CO, June 1994.

<sup>6</sup> Lovato, J. A. and Troutt, T. R. "Active Control of the Shear Layer on a Static Airfoil," AIAA Paper No. 93-0442.

<sup>7</sup> Bhattacharjee, S., Scheelke, B., and Troutt, T. "Modification of Vortex Interactions in a Reattaching Separated Flow," AIAA J., Vol. 24, No. 4, 1986, pp. 623-629.

<sup>8</sup> Crow, S. C and Champagne, F. H. (1971) "Orderly Structure in Jet Turbulence," J. Fluid Mech., Vol. 48, Part 3, pp 547-591.

<sup>9</sup> Kibens, V. (1979) Mechanics of Sound Generation by Flows, Ed. E.-A. Muller, p 174. Springer.

<sup>10</sup> Katz, J. "A Discrete Vortex Method for the Non-Steady Separated Flow Over an Airfoil," J. Fluid Mech., Vol. 102, pp. 315-328.

# **Effects of Trailing-Edge Jet Entrainment on Delta Wing Vortices**

H. E. Helin and C. W. Watry

Reprinted from

## **AIAA Journal**

Volume 32, Number 4, Pages 802-804



*A publication of the*  
American Institute of Aeronautics and Astronautics, Inc.  
370 L'Enfant Promenade, SW

# Effects of Trailing-Edge Jet Entrainment on Delta Wing Vortices

H. E. Helin\*

U.S. Air Force Academy, Colorado Springs, Colorado 80840

and

C. W. Watry†

George Washington University, Hampton, Virginia 23681

This paper examines the effects of trailing-edge jet entrainment on the streamwise vortices over a delta wing. Although studies have examined the effects of leading-edge suction and blowing on the burst location of delta wing vortices, very little research has focused on the effects of trailing-edge jet exhaust on the burst location. Using a 60-deg delta wing model in a water tunnel with dye to mark the vortex core, it was possible to visualize how the location of the vortex breakdown changes with trailing-edge jet velocity. This research has determined that at moderate angles of attack it is possible to delay the burst location up to 18% of the chord by increasing the flow velocity from the exhaust ports. In addition, at higher angles of attack, the trailing-edge jets stabilized the asymmetric separated vortices by reattaching the flow and moving the burst location aft on the wing.

## Nomenclature

$V_r$  = trailing-edge jet velocity ratio,  $V_{jet}/V_\infty$   
 $V_\infty$  = freestream velocity  
 $V_{jet}$  = jet exit velocity

## Introduction

**D**ELTA wing vortex dynamics and the effects on aircraft performance have become an important research topic in recent years. The most significant aerodynamic aspect of delta wings at moderate and high angles of attack is the formation of leading-edge vortices. These streamwise vortices are formed as the flow separates at the leading edge and rolls over the upper surface. At high angles of attack, approximately half of the lift generated on a delta wing is a result of these vortices. There are several variables that influence delta wing vortex dynamics. Some of these variables include angle of attack, leading-edge geometry, wing thickness, sweep angle, and freestream conditions. The most significant feature that can be influenced by these variables is the bursting process of the vortices.

Several theories governing vortex bursting have been proposed.<sup>1-4</sup> As the flow separates, it curls over the leading edge to form a well-defined vortex. The flow in core of the vortex accelerates as it travels downstream and can reach values as high as three times the freestream velocity.<sup>3</sup> At some point downstream, the core velocity will stagnate, and the vortex will burst. If the angle of attack is increased sufficiently, the vortex burst location will move upstream over the wing with a highly turbulent, wakelike flow replacing the organized flow of the vortex and its core.

In the study by Sarpkaya,<sup>3</sup> he identifies three types of vortex breakdown. The most common form of vortex breakdown is the spiral breakdown. After some distance, the flow along the vortex core rapidly decelerates until it reaches a stagnation point. At this bursting location, the core will deviate from its centerline and form a helixlike structure with a diameter much larger than the original core. The spiral structure will usually complete three rotations be-

fore it breaks down into the wakelike flow.<sup>4</sup> The flow in the center of the spiral will be in an upstream direction between the stagnation point and the wake region. A second and third type of breakdown identified by Sarpkaya are the bubble and the double helix. These types of breakdown are not as prevalent as the spiral breakdown.

It should be noted that at low angles of attack the burst location may be well behind the trailing edge of the wing. As angle of attack is increased and the burst location moves forward of the trailing edge, the lift generated by the vortices will decrease. In addition, at very high angles of attack or with high wing sweep angles, the shedding of the vortices may not always be symmetrical and/or may be separated. As a result of this asymmetry, the forces on either side of the wing will not be equal. The oscillation of the vortices from one side of the wing to the other can induce the phenomenon of wing rock.

To control delta wing aerodynamics, several studies have looked at the effects of suction and blowing on the leading-edge vortices. The study done by Visser et al.<sup>5</sup> examined the effects of blowing near the leading edge and back to 30% chord. They found that the blowing was most effective when located nearest the leading edge. Another study was conducted by Magness et al.<sup>6</sup> that examined the influence of suction as well as blowing. The suction was applied from a tube located at a distance of 0.95 chord, measured along the centerline, and placed out near the leading edge under the burst vortex core. The blowing was introduced to the flow from a port on the surface of the wing typically near the apex. It should be noted that most of the previous studies involved small amounts of mass flow out of the ports, primarily directed at boundary-layer control. A study by Roos and Kegelman<sup>7</sup> examined the effects of a suction wand downstream of the trailing edge. They found the vortex burst location could be changed, but for the specific cases evaluated, only small changes in the integrated forces on the delta wing were measured.

The work presented in this paper examines a different aspect of delta wing vortex control. Whereas previous studies have primarily used boundary-layer blowing/suction, this study concentrates on the effects of large amounts of mass injection through trailing edge jets. It is proposed that the entrainment from jets, or engines, at the trailing-edge of the wing can be used to control the leading-edge vortices. Thus, the influence of the trailing-edge jets on vortex bursting and asymmetry was examined for a delta wing at various angles of attack.

## Experimental Setup

The model for these experiments was a 60-deg swept delta wing (Fig. 1). The leading edges of the wing were sharp with a 60-deg

Received June 21, 1993; revision received Oct. 11, 1993; accepted for publication Oct. 21, 1993; presented as Paper 94-0072 at the AIAA 31st Aerospace Sciences Meeting, Reno, NV, Jan. 10-13, 1994. This paper is declared a work of the U.S. Government and is not subjected to copyright protection in the United States.

\*Deputy Director, Aeronautics Laboratory, and Assistant Professor, Department of Aeronautics; on sabbatical to F. J. Seiler Research Laboratory, FJSRL/NA, USAFA, CO 80840. Senior Member AIAA.

†Graduate Student, Joint Institute for Advancement of Flight Sciences, NASA Langley Research Center, MS 269, Hampton, VA 23665. Student

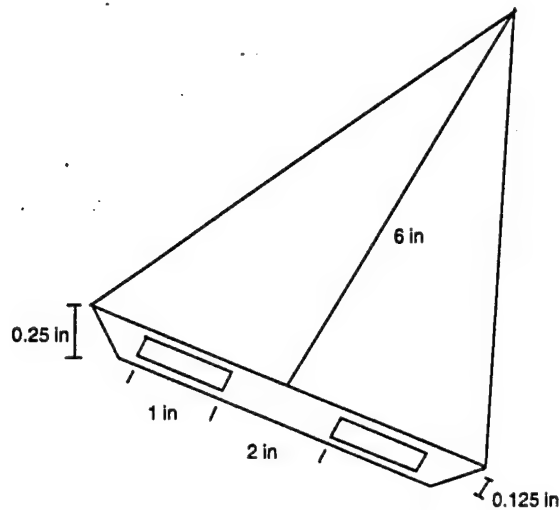


Fig. 1 Delta wing model with 60-deg sweep, 60-deg underside leading-edge bevels, and high-aspect-ratio rectangular trailing-edge jets.

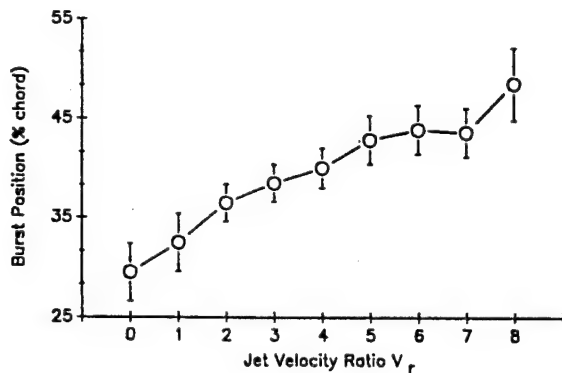


Fig. 2 Plot of burst location vs  $V_r$  for 20-deg angle of attack. Each point is an average of four data measurements with error bars for the standard deviation.

underside bevel. The jet exhaust ports were high aspect ratio (8:1) rectangular jets along the trailing edge of the model. This configuration was chosen due to geometrical similarity to the F-117 stealth fighter and because the 60-deg planform has been used in previous studies. An Eidetics 0.46 × 0.46 m water tunnel located in the United States Air Force Academy Aeronautics Laboratory was used for these studies. The water-tunnel velocity was set at  $7.62 \pm 0.3$  cm/s. This provided a Reynolds number per unit foot of  $2.07 \times 10^4$ . To alleviate wake perturbations the model was sting mounted from the underside and an internal cavity, also ported from the underside of the wing, was used to supply the mass flow for the jets. To insure the flow would exit from the model parallel to the freestream, several thin-walled tubes were inserted into the exhaust ports. At this freestream velocity, trailing-edge jet to freestream velocity ratios  $V_r$  were varied from 0 to 8, in increments of 1.0. The chosen velocity ratios and trailing-edge jet exit areas are representative of actual aircraft parameters.

Flow visualization of the delta wing vortices was accomplished by staining the core of the vortex with dye. The dye was injected into the flow 1.6 mm from the apex on the underside of the leading edges. The dye streaklines were illuminated from the side and photographed with a 35-mm camera.

A transit was used to insure that the model was set up in the tunnel at 0 deg yaw, pitch, and roll. After the initial conditions were set, the model could be pitched by using a crescent traverse with an error of  $\pm 0.05$  deg in angle of attack. The angles of attack used for

this study were 0, 10, 20, and 30 deg. For most combinations of  $V_r$  and angle of attack, the experiment was repeated so that two sets of data could be compared for repeatability. From these sets of data, measurements were made for the burst location, core position with respect to the centerline, and the spreading angle of the burst vortex.

## Results

### Vortex Burst Location

With the model at 0-deg angle of attack, the dye bled over the leading edge and spread into the upper surface boundary layer of the wing. There were no leading-edge vortices, and, in addition, no noticeable flow disturbances due to the dye injection were seen. The flow appeared to be relatively symmetric about the centerline. As  $V_r$  was varied from 0 to 8, no changes were observed.

At 10-deg angle of attack and  $V_r$  equal to 0.0, prominent leading-edge vortices were present. The burst location of these vortices was aft of the trailing edge, and again the flow appeared to be relatively symmetric. The bursting process followed that of the spiral mode, as discussed earlier. As  $V_r$  was increased to 8.0, no discernible changes in burst location were seen. It should be noted at this point that the burst location aft of the trailing-edge is probably dominated by the blunt finite trailing-edge thickness of the model, as it significantly affects the adverse pressure gradient in that region.

When the model was placed at 20-deg angle of attack, dramatic differences were seen in the bursting of the vortices. The burst location vs  $V_r$  is plotted in Fig. 2. Each data point shows the averaged measurements for the left and right burst locations in both sets of data. At  $V_r = 0.0$ , the burst location had an average value of 29% chord. As  $V_r$  was incremented, the burst location moved to 47% chord. Details of this process can be seen in Figs. 3a and 3b, which show the leading-edge vortex system at  $V_r = 0.0$  and 8.0, respectively. In addition to the burst location movement, these photographs show relative symmetry between the left and right vortices and clearly depict the spiral breakdown mode.

As the angle of attack was increased to 30 deg and with  $V_r = 0.0$ , the vortex burst location moved to the apex of the wing. In addition, the completely burst vortices oscillated from one side of the wing to the other. This can be seen in Figs. 3c and 3d, which were taken at different times. The period of this oscillation was about 20 s. Although similar oscillations of burst vortices at the apex have been observed by co-workers, no documentation of this phenomenon could be found in the literature. At this time little insight can be given on the physical mechanism behind this process, although it could be speculated that small instabilities in the test facility, model imperfections, or model positioning could be responsible. As  $V_r$  was increased to 2.0 and 3.0, it appeared that the period of oscillation was increased and the burst vortices began to stabilize. By  $V_r = 5.0$ , small vortex cores were noticed on both sides of the wing (Fig. 3e). Also, these vortices were stabilized without any oscillation. The bursting location was extended to 17% of the chord and remained symmetric when  $V_r$  was increased to 8.0 (Fig. 3f).

### Vortex Core Position

In addition to measuring the change of burst location as  $V_r$  was increased, two other variables were measured to determine how the vortex dynamics were affected by the trailing-edge blowing. The vortex core position was measured by the angle between the centerline of the wing and the vortex core. At both 10- and 20-deg angle of attack, where a vortex core could be seen, the angle was  $17 \pm 1$  deg. There was no positive correlation between small changes in the vortex core position and  $V_r$ . At 30-deg angle of attack and with  $V_r$  greater than 5.0, the vortex core angle was again measured to be approximately 17 deg.

### Spreading Angle

The spreading angle is a measurement of the divergence of the burst vortex once it transitioned to a turbulent state. With spiral

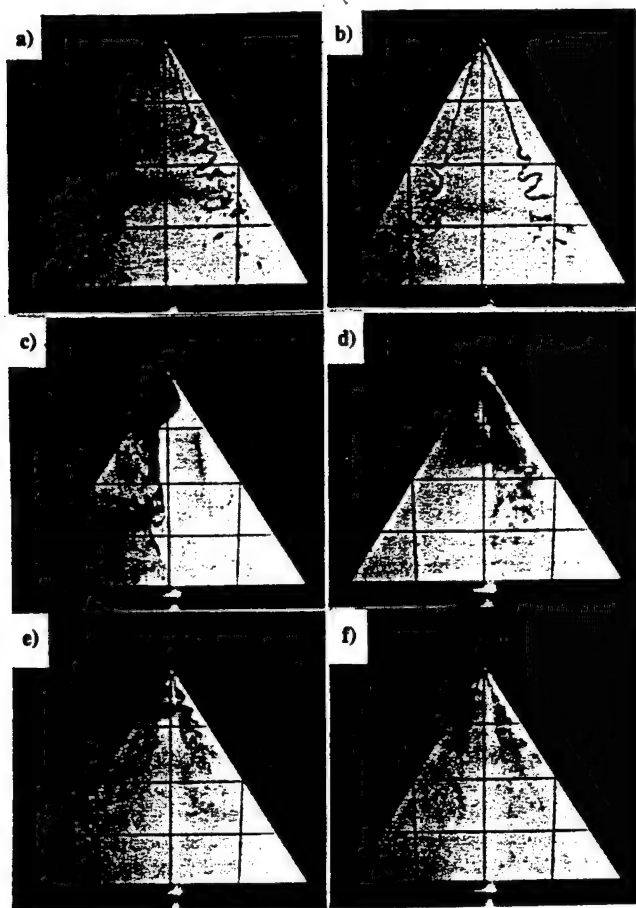


Fig. 3 Photographs of delta wing vortices where a) and b) show burst delay at 20 deg with increased  $V_r$ , c) and d) show oscillation of burst vortices at 30 deg, and e) and f) show stabilization and delay of burst as  $V_r$  increases: a)  $\alpha = 20$  deg,  $V_r = 0.0$ ; b)  $\alpha = 20$  deg,  $V_r = 8.0$ ; c)  $\alpha = 30$  deg,  $V_r = 0.0$ , time 1; d)  $\alpha = 30$  deg,  $V_r = 0.0$ , time 2; e)  $\alpha = 30$  deg,  $V_r = 5.0$ ; and f)  $\alpha = 30$  deg,  $V_r = 8.0$ .

vortex breakdown, the angle could be measured using the burst location and the edges of the spirals. These data were only measured at 20 deg angle of attack, since it was not clearly defined at 10 deg where the burst location was aft of the trailing edge, or at 30 deg where the burst location was close to the apex. The values of the spreading angle varied from 24 to 32 deg, but again there was no positive correlation between these values and  $V_r$ .

### Discussion

The results of trailing-edge jet entrainment on delta wing vortex kinematics demonstrate that it is possible to control vortex bursting and asymmetry. By increasing  $V_r$  to 8.0, the burst location of the leading-edge vortices was delayed by up to 18% of the chord. By delaying the burst location, a more cohesive vortex remains closer to the wing surface and thus should result in an increase in the lift. However, the total amount of vorticity generated at the leading edge does not change; it is simply redistributed from a cohesive vortex to a burst vortex that is spread over a broader extent. The distribution and rate of dissipation of the vorticity in the burst vortex would become factors in determining the amount of lift generated. In an aircraft environment at higher Reynolds numbers, the leading-edge vortices would exist in a fully turbulent fashion. Again, the bursting process will redistribute the vorticity over a much broader region, and the ability to change the burst location

could affect aircraft performance and controllability. Without detailed measurements of the vorticity field, it is difficult to speculate at this time as to the actual effect on integrated lift or lateral stability.

Perhaps a more important result of jet entrainment on the leading-edge vortices is the ability to control the asymmetric nature of flow at high angles of attack. This was clearly demonstrated at 30-deg angle of attack where the flow was initially completely burst, separated, and asymmetric. Not only were the burst vortices reattached and extended over the wing, they were stabilized and became symmetric. This suggests a potential flow control methodology for the undesirable condition of wing rock. Although the current study did not show any appreciable change in the vortex core location or spreading angle due to jet entrainment, it may be possible to vary these characteristics by using asymmetric blowing or by changing the jet location and/or using differential and vectored thrust.

Modern delta wing aircraft fly in a dynamic environment that includes rapid changes in angle of attack and coupled rolling motions, which have been shown to affect vortex dynamics. The potential to control the resulting vortex-dominated flows with specifically programmed thrust/engine settings alludes to performance enhancement with little or no penalty.

### Conclusion

This study examined the effects of trailing-edge jet entrainment on the flow over delta wings. Using a 60-deg delta wing model with high-aspect-ratio trailing-edge jets and  $V_j/V_\infty$  ratios of 0.0–8.0, significant events were observed.

It has been shown that trailing-edge mass injection can be used to move the burst location of the leading-edge vortices back by up to 18% of the chord. Also, in addition to delaying the burst location, trailing-edge mass injection can be used to reduce the asymmetry, commonly found in the leading-edge vortices over delta wings at high angles of attack. By reducing the asymmetry, trailing-edge jet entrainment may provide a technique to prevent undesirable conditions like wing rock. The delayed burst location provided by the trailing-edge blowing could possibly result in higher values of lift. However, to determine the actual effects on lift, experiments employing force balances and/or surface pressure measurements need to be conducted.

### Acknowledgments

The authors would like to acknowledge discussions concerning this study with A. Krothapalli at Florida State University and the technical assistance of J. Philp and R. Durmon at the United States Air Force Academy.

### References

- <sup>1</sup>Atta, R., and Rockwell, D., "Hysteresis of Vortex Development and Breakdown on an Oscillating Delta Wing," *AIAA Journal*, Vol. 25, No. 11, 1987, pp. 1512, 1513.
- <sup>2</sup>Thompson, S. A., "Unsteady Aerodynamics of a Delta Wing Undergoing Large Amplitude Pitching Motion," Ph.D. Dissertation, Dept. of Aerospace and Mechanical Engineering, Univ. of Notre Dame, Notre Dame, IN, April 1992.
- <sup>3</sup>Sarpkaya, T., "On Stationary and Travelling Vortex Breakdowns," *Journal of Fluid Mechanics*, Vol. 45, Pt. 3, Feb. 1971, pp. 545–559.
- <sup>4</sup>Jumper, E. J., Nelson, R. C., and Cheung, K., "A Simple Criterion for Vortex Breakdown," AIAA Paper 93-0866, Jan. 1993.
- <sup>5</sup>Visser, K., Iwanski, K., Nelson, R., and Ng, T., "Control of Leading Edge Vortex Breakdown by Blowing," AIAA Paper 88-0504, Jan. 1988.
- <sup>6</sup>Magness, C., Robinson, O., and Rockwell, D., "Control of Leading Edge Vortices on a Delta Wing," AIAA Paper 89-0999, March 1989.
- <sup>7</sup>Roos, F. W., and Kegelman, J. T., "Recent Explorations of Leading Edge Vortex Flowfields," NASA CP 3149, Vol. 1, Pt. 1, Oct. 1990, pp. 157–172.

## REAL-TIME PREDICTION OF THREE-DIMENSIONAL UNSTEADY SEPARATED FLOW FIELDS USING NEURAL NETWORKS

Capt. Scott J. Schreck and Dr. William E. Faller

Frank J. Seiler Research Laboratory  
2354 Vandenberg Drive, Suite 6H79  
USAF Academy, CO 80840-6272  
Phone: (719) 472-2812

### INTRODUCTION

Control of unsteady separated flow fields would dramatically enhance aircraft agility. To enable control, real-time prediction of these flow fields over a broad parameter range must be realized. However, unsteady separated flows exhibit complex spatial and temporal dependencies which have impeded accurate, real-time flow field prediction. The present work demonstrates that neural network models can perform real-time predictions of three-dimensional unsteady separated flow fields and aerodynamic coefficients. These predictions are accurate over broad parameter ranges for novel conditions and diverse pitch motions.

### METHODS

#### Unsteady Surface Pressure Measurements

Unsteady surface pressure measurements were performed in the Frank J. Seiler low speed wind tunnel using a rectangular wing bounded at the root by a circular splitter plate. The wing had a NACA 0015 cross-section, 0.5 ft chord length and semi-aspect ratio 2.0. Starting at 0 degrees, the wing/splitter plate configuration was pitched at constant rate about the quarter chord to a final angle of 60 degrees. Seven nondimensional pitch rates of 0.01, 0.02, 0.05, 0.075, 0.10, 0.15 and 0.20 were investigated. Sinusoidal pitching was also examined for nondimensional frequency 0.25. Test section velocity was held constant at 9.14 meters per second, corresponding to a chord Reynolds number of 69,000. Fifteen Endevco 8507-2 pressure transducers were close-coupled to 15 pressure ports distributed along the chord line between 0.0 and 0.90 chord. After amplification and anti-alias filtering, these 15 signals and a pitch angle reference signal were sampled and digitized by a Masscomp 5500 data acquisition system. A more detailed description of these methods has been previously given (Schreck and Helin, 1993a).

For all nondimensional pitch rates, prominent temporal variations in vortex structure and surface pressure topology were apparent. In addition, the surface pressure topologies exhibited distinct spatial variations over the span. Dye flow visualization confirmed that, following vortex initiation near the wing leading edge, vortex growth and convection were accompanied by radical three-dimensional deformation of the unsteady separated flow field (Schreck and Helin, 1993a). These spatially and temporally complex three-dimensional unsteady separated flow fields formed the experimental basis for the neural network models developed herein.

#### Neural Network Architecture and Training

The digitized unsteady surface pressure records and pitch angle histories were used to define a neural network model of the three-dimensional unsteady separated flow field. To model the unsteady flow fields, a time-series paradigm based on the backpropagation algorithm was utilized. A standard sigmoidal activation function,  $1/(1+e^{-x})$ , was used and the input to the network was the pitch angle ( $\alpha$ ), the angular velocity ( $d\alpha/dt$ ) and the initial 15 recorded pressure coefficients ( $C_{p1}$ - $C_{p15}$ ) at time ( $t_0$ ). Both hidden layers were comprised of 32 units and the output layer was comprised of 15 units. The targeted outputs were the 15 pressure coefficients at time ( $t+\Delta t$ ), as well as coefficients of lift, drag, normal force, tangential force and moment about the quarter chord. Subsequently, the time ( $t+\Delta t$ ) network predictions, for each of the 15  $C_p$  values, were fed back as the input to the network throughout the pitch history. The training set was comprised of 5 nondimensional pitch rates, 0.01, 0.02, 0.05, 0.10 and 0.20, recorded at 37.5% span outboard of the splitter plate.

During training the 5 data sets were presented randomly with the stipulation that each data set be presented an equal number of times. The initial weights were set randomly and training was performed

until the sum-squared error was less than 0.01 for each of the 5 training sets. Thus, post-training, the network should predict the entire surface pressure distribution record and aerodynamic coefficient records given only the pitch angle history and the 15 pressure coefficients at time ( $t_0$ ). This type of network architecture has previously been described in detail for predictions constrained to small time intervals, ( $\Delta t$ ), for which a linear equation system could be derived from the weight matrices of the neural network (Faller et al., 1993a; Schreck et al., 1993b).

## RESULTS

To evaluate the performance of the neural network, the predicted surface pressure coefficients were compared directly to the measured data, and the predicted aerodynamic coefficients were compared to those calculated from measured surface pressures. Network inputs were the pitch angle ( $\alpha$ ), the angular velocity ( $d\alpha/dt$ ) and the initial 15 recorded pressure coefficients ( $C_{p1}$ - $C_{p15}$ ) at time ( $t_0$ ). Time ( $t+\Delta t$ ) network predictions, for each of the 15  $C_p$  values, were fed back as the input to the network throughout the pitch history. Model performance was evaluated graphically by co-plotting the measured pressure profiles and the predicted data. Thus, post-training, it was possible to determine not only how well the models predicted the training data, but how well the models could extrapolate (generalize) to both other nondimensional pitch rates and to other types of motion histories.

### Unsteady Surface Pressure Predictions

The graphical analyses for predicting both the training data as well as for data sets corresponding to novel pitch rates and motions are shown in Figs. 1 through 4. In all 4 figures, time-varying surface pressure at port 1, the leading edge, is at the bottom of the figure. Time-varying surface pressure at port 15, 90% chord near the trailing edge of the airfoil, is at the top. The ordinate is the pressure coefficient ( $C_p$ ) and the abscissa is nondimensional time. The measured surface pressure data are shown as a solid line and the surface pressures predicted via the neural network as a dashed line. The magnitudes of the pressure coefficients are accurate, but the plots have been offset to ease viewing.

The analysis for nondimensional pitch rate 0.02, 1 of the 5 training sets, is shown in Fig. 1. Prior to suction peak occurrence, the network accurately predicts surface pressure decreases at port locations 1 through 5. However, farther aft, at port locations 5 through 15, the network failed to predict small surface pressure fluctuations. The network successfully predicted the time of suction peak occurrence over the entire wing chord. However, suction peak magnitudes were slightly underpredicted for most pressure port locations. Network predictions of constant pressures after suction peak occurrence were highly accurate.

The analysis for predicting nondimensional pitch rate 0.2, also 1 of the 5 training sets, is shown in Fig. 2. Before suction peak occurrence, network predictions were highly accurate for all pressure port locations. Again, the network failed to predict small surface pressure fluctuations both before and after suction peak occurrence. The network accurately predicted both the time and magnitude of suction peak occurrence for all pressure ports. And, following suction peak occurrence, the network accurately predicted surface pressure magnitudes.

Figure 3 shows a similar plot for nondimensional pitch rate 0.15. This record was not used during training. The neural network accurately predicts the initial surface pressure decline for the first 2 port locations. The initial surface pressure decline is moderately underpredicted at the remaining port locations. For the leading 5 port locations, peak magnitudes are slightly underpredicted, and predicted occurrence times lag measured times by approximately 0.5 nondimensional time units. For port locations 6 through 15, suction peak time of occurrence is accurately predicted and peak magnitude is moderately underpredicted.

Figure 4 shows network predictions for sinusoidal pitch motion of nondimensional frequency 0.25. The wing was pitched sinusoidally  $\pm 10$  degrees around a mean pitch angle of 10 degrees. Nondimensional time 0.0 corresponds to the maximum instantaneous pitch angle of 20 degrees. Since the network was trained only on constant rate pitch motions, this record represents network performance on a distinct class of pitch motions. The results indicated that initial surface pressure increases, during the pitch-down phase of the motion, are underpredicted by the network. During this phase of the motion the predicted times of occurrence tend to lag near the leading edge and lead near the trailing edge. As the wing reaches 0 degrees, at nondimensional time 7.0, the network predictions tend to collapse to the

measured values. During the sinusoidal pitch up, nondimensional time 7.0 to 12.0, the pressure values at ports 1 to 3 are underpredicted but the time of occurrence is accurately predicted. The predicted values for ports 4 through 15 are both underpredicted and tend to lead the measured data.

#### Unsteady Aerodynamic Coefficient Predictions

The graphical analyses for one of the constant rate training sets and the sinusoidal pitch motion are shown in Figs. 5 and 6, respectively. In both figures, the abscissa is nondimensional time and the ordinate corresponds to the aerodynamic coefficients. The measured data is shown as a solid line and the aerodynamic coefficients predicted by the neural network as a dashed line. Again, the magnitudes of the aerodynamic coefficients are accurate, but the plots have been offset to ease viewing. Starting at the bottom of the figure and proceeding to the top, the aerodynamic coefficients shown are lift ( $C_l$ ), drag ( $C_d$ ), normal force ( $C_n$ ), tangential force ( $C_t$ ) and the pitching moment about quarter chord ( $C_m$ ).

Aerodynamic coefficient predictions for a nondimensional pitch rate of 0.02, 1 of the 5 training sets, is shown in Fig. 5. The neural network accurately predicts these force and moment coefficients both before and after attainment of maximum magnitude. For  $C_l$ ,  $C_d$ ,  $C_n$  and  $C_m$ , though, maximum magnitude is slightly underpredicted, and predicted time of occurrence leads measured occurrence time by approximately 0.5 nondimensional time units. Aerodynamic coefficient predictions for the sinusoidal pitch motion are shown in Fig. 6. For this set of conditions, lift and normal force are both overpredicted and lag the measured data. The magnitude of  $C_d$ ,  $C_t$  and  $C_m$  are closely predicted, but tend to lead the measured data.

### CONCLUSIONS

Three-dimensional unsteady separated surface pressure fields were characterized in detail over a wing undergoing constant rate pitching and sinusoidal pitch oscillation. For each data record, surface pressures exhibited prominent temporal and spatial fluctuations. Further, data record features varied in response to changes in nondimensional pitch rate as well as pitch motion. Using a subset of the existing experimental data base, a neural network model was constructed to predict measured and novel unsteady surface pressure fields. Network inputs were tightly constrained, consisting only of instantaneous pitch angle, pitch rate and initial surface pressure distribution. In spite of pronounced disparities in surface pressures and highly constrained network inputs, neural network model predictions were highly accurate.

Overall, as measured by an average deviation over time, the results indicated that the network accurately predicted the unsteady surface pressures and aerodynamic coefficients to within 5% of the experimental data. This was verified graphically by co-plotting the measured and predicted quantities. Consistent results were obtained for the training sets as well as for extrapolation (generalization) to novel constant pitch rates and sinusoidal pitch motions. These results clearly indicate that the neural network model can predict the three-dimensional unsteady surface pressure distributions based solely on the pitch angle information. These results also clearly demonstrate that highly accurate real-time models of unsteady separated flow fields can be developed using neural networks.

### REFERENCES

- (1) Schreck, S.J. and Helin, H.E. (1993a, Submitted) Unsteady Vortex Dynamics and Surface Pressure Topologies on a Pitching Wing, AIAA Journal of Aircraft.
- (2) Schreck, S.J., Faller, W.E. and Luttgies, M.W. (1993b, In press) Neural Network Prediction of Three-Dimensional Unsteady Separated Flow Fields, AIAA 11th Applied Aerodynamics Conference, 9-11 August 1993, Monterey, California.
- (3) Faller, W.E., Schreck, S.J. and Luttgies, M.W. (1993a, Submitted) Modeling Three-Dimensional Unsteady Aerodynamics with Neural Networks, IEEE Transactions on Neural Networks.
- (4) Faller, W.E., Schreck, S.J. and Luttgies, M.W. (1993b, Submitted) Prediction of Three-Dimensional Unsteady Separated Flow Fields and Aerodynamic Coefficients Using Neural Networks, 32nd Aerospace Sciences Meeting, Reno, Nevada.
- (5) Faller, W.E., Schreck, S.J. and Luttgies, M.W. (1993c, In Preparation) Real-Time Prediction of Unsteady Aerodynamics: Application for Aircraft Control and Maneuverability Enhancement, IEEE Transactions on Neural Networks.

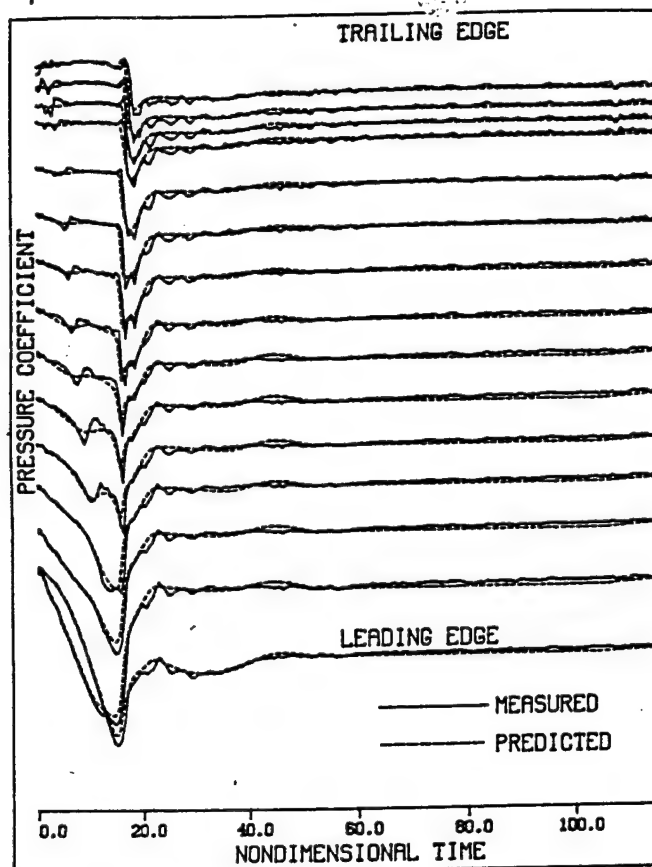


Fig. 1. Unsteady surface pressures for constant rate pitching, nondimensional pitch rate 0.02.

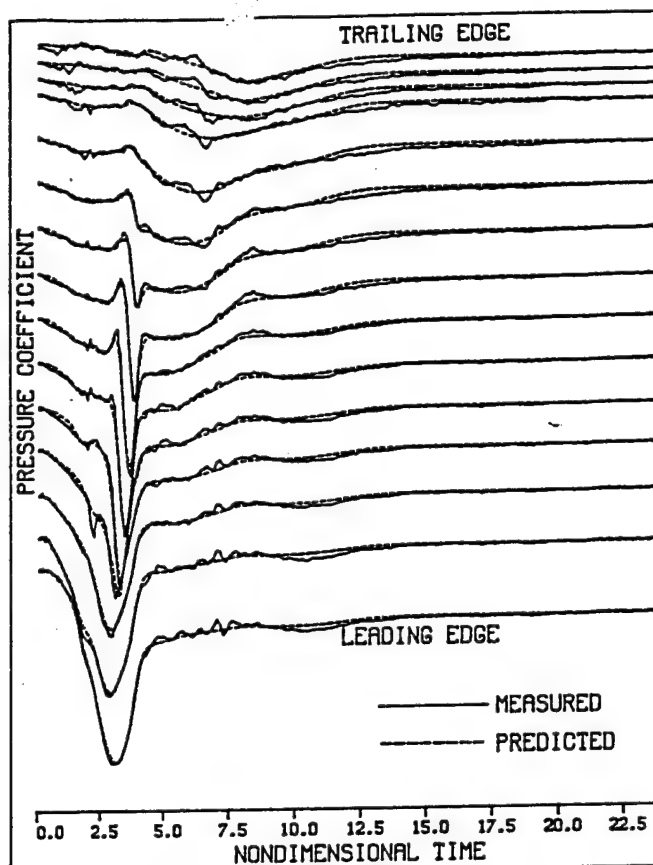


Fig. 2. Unsteady surface pressures for constant rate pitching, nondimensional pitch rate 0.20.

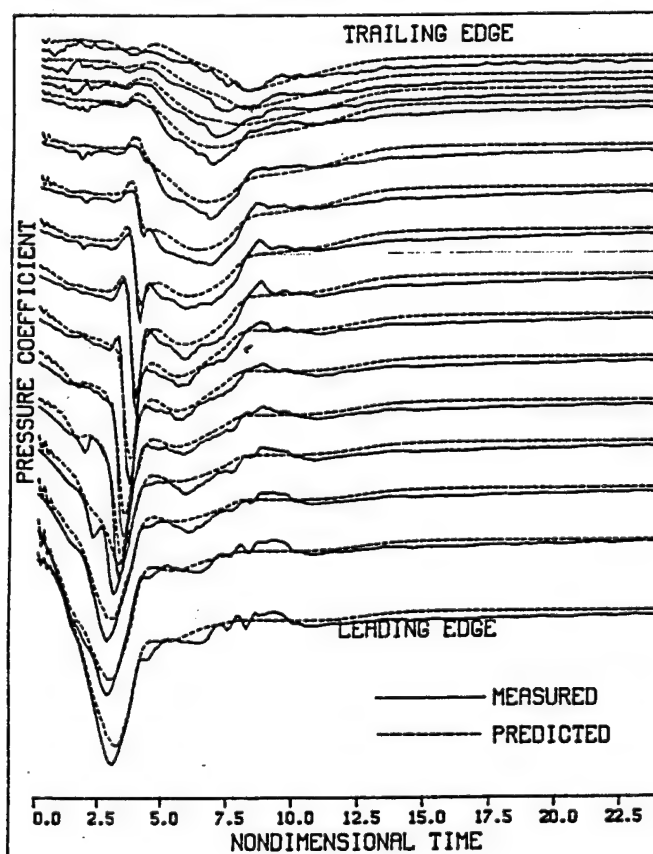


Fig. 3. Unsteady surface pressures for constant rate pitching, nondimensional pitch rate 0.15.

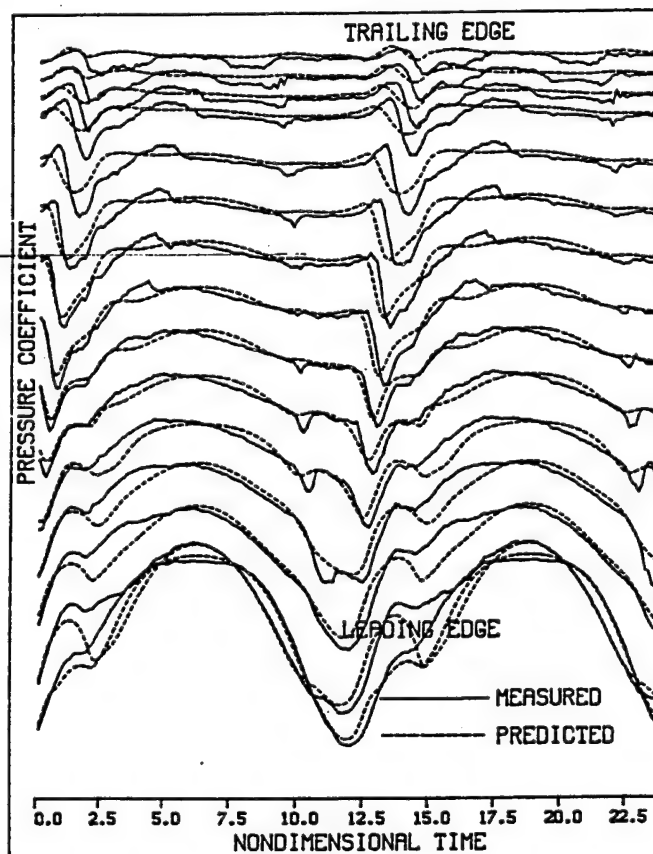


Fig. 4. Unsteady surface pressures for sinusoidal pitching, nondimensional frequency 0.25.

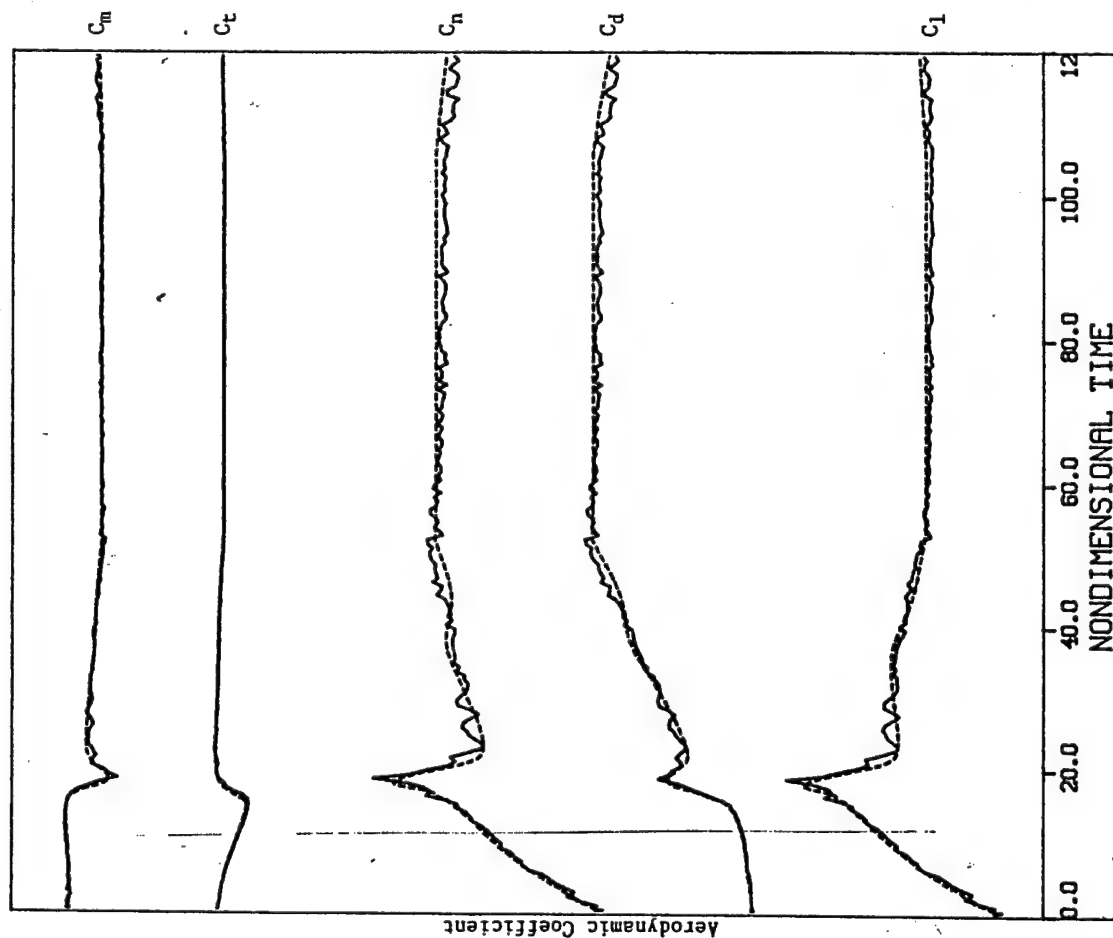


Fig. 5. Unsteady aerodynamic coefficients for constant rate pitching, nondimensional pitch rate 0.02. Coefficients are (from bottom) lift, drag, normal force, tangential force and moment about the quarter chord.

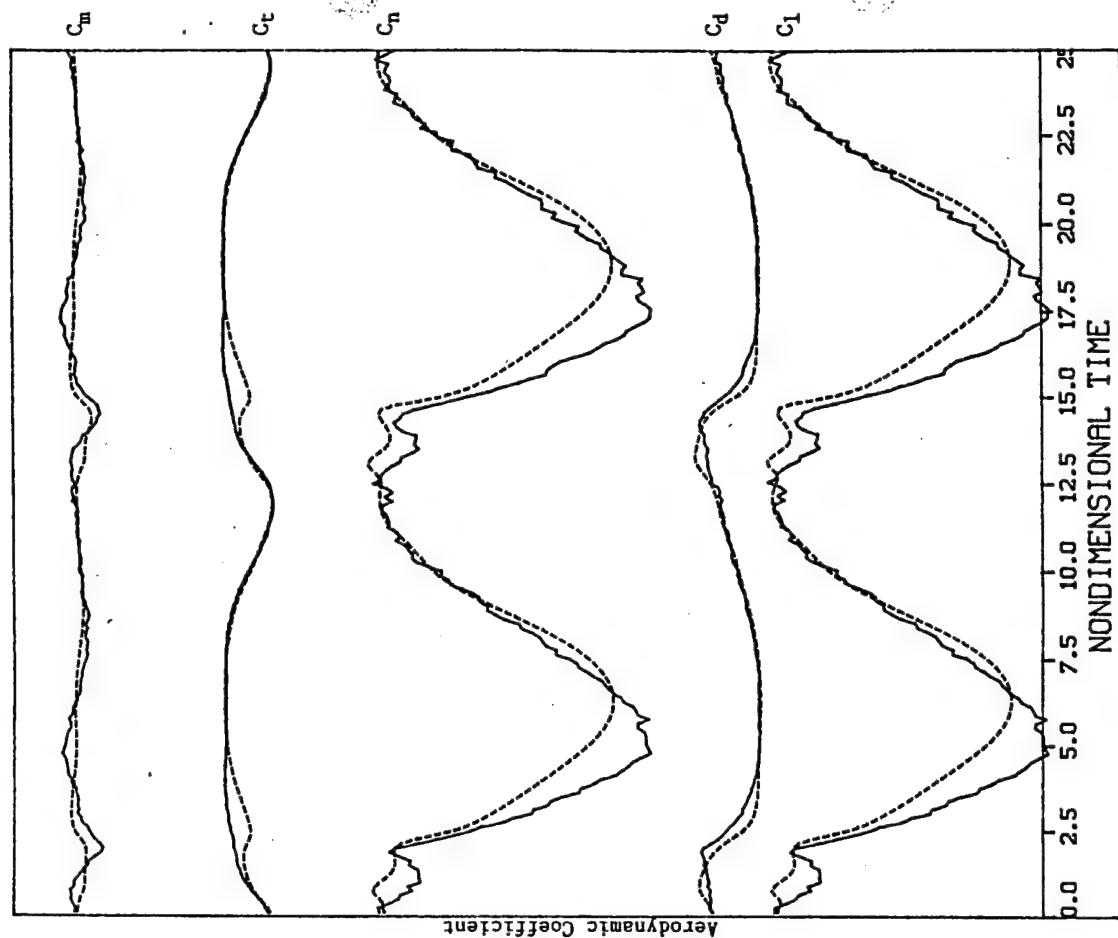


Fig. 6. Unsteady aerodynamic coefficients for sinusoidal pitching, nondimensional frequency 0.25. Coefficients are (from bottom) lift, drag, normal force, tangential force and moment about the quarter chord.

UNSTEADY AERODYNAMICS  
2300/FF/07  
PUBLICATION/PRESENTATION LIST  
1 OCT 91 - 30 SEP 95  
2300-FF-07

Downwash Measurements on a Pitching Canard-Wind Configuration, by John E. Burkhalter. FJSRL-TR-91-0001, Sep 91. Also *Journal of Aircraft*, Vol. 30, No. 6, pp 1005-1008, Nov-Dec 93.

Active Separation Control on a Two-Dimensional Airfoil, by Julie A. Lovato and Timothy R. Troutt (WSU). 44th Meeting of the AIAA Division of Fluid Dynamics, American Physical Society, Scottsdale AZ, 24-16 Nov 91.

Active Control of the Separation Region on a Two-Dimensional Airfoil, by J.A. Lovato. FJSRL-TR-92-0001, Mar 92. (PhD Dissertation)

Development and Application of a Scanning LDV Vorticity Measurement System, by B. Terry Beck. Final URRP report.

Flow Field Development about a Porous Suction Surface Wing Under Static and Dynamic Conditions, by Gregory A. Addington (WL), Marvin W. Luttges (CU), and Scott J. Schreck. The 10th AIAA Applied Aerodynamics Conference, Palo Alto CA, 22-24 Jun 92.

Active Control of Vortex Structures in a Separating Flow Over an Airfoil, by J.A. Lovato and T.R. Troutt (WSU). AIAA 10th Applied Aerodynamics Conference, Palo Alto CA, 22-24 Jun 92.

The Effect of Free Shear Layer Structures on Airfoil Surface Pressure Fields, by J.A. Lovato and Timothy R. Troutt (WSU). 45th Meeting of the AIAA Division of Fluid Dynamics-American Physical Society, Tallahassee FL, 22-24 Nov 92.

Active Control of the Shear Layer on a Static Airfoil, by J.A. Lovato and T.R. Troutt (WSU). The 31st AIAA Aerospace Meeting, Reno NV, 11-14 Jan 93. AIAA Paper No. 93-0442. Submitted to AIAA Journal, Aug 93. Accepted. Projected to be published May/June 95.

Unsteady Vortex Dynamics and Surface Pressure Topologies on a Pitching Wing, by Scott J. Schreck and Hank E. Helin (DFAN). The 31st AIAA Aerospace Sciences Meeting, Reno NV, 11-14 Jan 93. AIAA Paper No. 93-0435. *Journal of Aircraft*, Vol. 31, No. 4, pp 899-907, Jul/Aug 94.

Quasi-Linear Neural Networks: Application to the Prediction and Control of Unsteady Aerodynamics, by William E. Faller (CU), Scott J. Schreck, and Marvin W. Luttges (CU). SPIE Applications of Neural Networks IV and SPIE Science of Artificial Neural Networks II,

Orlando FL, 12-16 Apr 93. SPIE Applications of Neural Networks IV Proceedings, Vol. 1965, pp 543-554.

A Neural Network Model of the Unsteady Aerodynamics on a Pitching Wing, by William E. Faller (CU). Final GSRP report, Sep 92.

Aerodynamic Foundations for Use of Unsteady Aerodynamic Effects in Flight Control, by Captain Tom McLaughlin (DFAN), Dr Mike Robinson, and Dr Marv Luttgies (CU). 31st AIAA Aerospace Sciences Meeting, Reno NV, 11-14 Jan 93.

Neural Network Prediction of Three-Dimensional Unsteady Separated Flow Fields, by Scott J. Schreck, Dr William E. Faller (CU), and Professor Marvin W. Luttgies (CU). AIAA 11th Applied Aerodynamics Conference, Monterey CA, 9-11 Aug 93. AIAA Paper No. 93-3426-CP. AIAA Applied Aerodynamics Proceedings, Part I of CP935, pp 227-240. *Journal of Aircraft*, Vol. 32, No. 1, pp 178-185, Jan/Feb 95.

Numerical Simulation of Wing-Wall Juncture Flow for a Pitching Wing, by Lt Col Richard W. Newsome, Jr. AIAA 11th Applied Aerodynamics Conference, Monterey CA, 9-11 Aug 93. AIAA Paper No. 93-3401-CP. AIAA Applied Aerodynamics Proceedings, Part I of CP935, pp 10-23.

Similarity in Separated Flow Fields Producing Large Scale Vortices, by Eric J. Stephen. FJSRL-TM-92-0005, December 1992 - PhD Dissertation.

Temporal Coding in Neural Networks, by William E. Faller, Scott J. Schreck, and Marvin W. Luttgies (CU). The SPIE Applications of Neural Networks IV and SPIE Science of Artificial Neural Networks II, Orlando FL, 12-16 Apr 93. SPIE Science of Artificial Neural Networks II Proceedings, Vol. 1966, pp 311-321.

Effects of Trailing Edge Jet Entrainment on Delta Wing Vortices, by C1C Craig Watry (DFAN cadet under the guidance of Captain Henry E. Helin (DFAN Sabbatical Officer)). AIAA 5th Region Student Conference, Ft Collins CO, 21-24 Apr 93. *AIAA Journal*, Vol. 32, No. 4, pp 802-804, Apr 94.

Effects of Freestream Turbulence on Dynamic Stall, by C1C Donald V. Bohny and C1C Vincent M. Durant (DFAN cadets under the guidance of Captain Henry E. Helin (DFAN Sabbatical Officer)). AIAA 5th Region Student Conference, Ft Collins CO, 21-24 Apr 93.

Lifting Effects of Oscillating Vortex Generators on a Diamond Wing Planform, C1C Paul D. Copioli (DFAN cadet under the guidance of Captain Scott J. Schreck). AIAA 5th Region Student Conference, Ft Collins CO, 21-24 Apr 93.

Investigation of Buffet and Flow Separation for Sharp and Conventional Airfoils, by C1C Stephen P.H. Frank and C1C David C. Peeling (DFAN cadets under the guidance of Captain Scott J. Schreck). AIAA 5th Region Student Conference, Ft Collins CO, 21-24 Apr 93.

Analysis of Wing Tip Vortices on a Three Dimensional Static Wing, by C1C Edward Hospodar, C1C Brandon Hileman, and C1C Eric Chapital (DFAN cadets under the guidance of Dr Julie A. Lovato). AIAA 5th Region Student Conference, Ft Collins CO, 21-24 Apr 93.

Acoustic Forcing of Three Dimensional Flow About a Wingtip, by C1C Alexis Mezynski and C1C William D. Bryant (DFAN cadets under the guidance of Dr Julie A. Lovato). AIAA 5th Region Student Conference, Ft Collins CO, 21-24 Apr 93.

Experimental Investigation of the Vortex-Vertical Tail Interaction on an F-15, by Captain Scott P. LeMay (DFAN) and Julie A. Lovato. AIAA 32nd Aerospace Sciences Meeting and Exhibit, Reno NV, 10-13 Jan 94.

Real-Time Prediction and Control of Three-Dimensional Unsteady Separated Flow Fields Using Neural Networks. 32nd Aerospace Sciences Meeting, Reno NV, 10-13 Jan 94. AIAA Paper No. 94-0532. Also submitted to AIAA Journal of Aircraft, Jan 94. Accepted Feb 95.

Real-Time Prediction of Unsteady Aerodynamics: Application for Aircraft Control and Maneuverability Enhancement, by William E. Faller, Scott J. Schreck, and Marvin W. Luttgies (CU). Submitted to IEEE Transactions on Neural Networks, Jul 93. Accepted Feb 95.

Real-Time Prediction of Three-Dimensional Unsteady Separated Flow Fields Using Neural Networks, by Captain Scott J. Schreck and Dr William E. Faller. Invited talk at the AFOSR Contractor's Meeting, Flagstaff AZ, 24-27 Aug 93. AFOSR Proceedings, pp 10.4-1 -10.4-5.

Parametric Study of the flow Over a Yawed Delta Wing, by Eric J. Stephen. APS 1993 Meeting of the Division of Fluid Dynamics, Albuquerque NM, 21-23 Nov 93.

Bispectral Characterization of a Static Airfoil Separating Boundary Layer, by Julie a. Lovato, Charles Pezeshki (SFRP), and Wyatt Davis (GSRP)(WSU). APS 1993 Meeting of the Division of Fluid Dynamics, Albuquerque NM, 21-23 Nov 93.

Real-Time Prediction of Three-Dimensional Dynamic Reattachment Using Neural Networks, by William E. Faller, Scott J. Schreck, Henry E. Helin (DFAN). AIAA 25th Fluid Dynamics Conference, Colorado Springs CO, 20-23 Jun 94.

Navier-Stokes Simulation of Wing-Tip and Wing-Juncture Interactions for a Pitching Wing, by Richard W. Newsome, Jr. AIAA 25th Fluid Dynamics Conference, Colorado Springs CO, 20-23 Jun 94.

Quantitative Effects of Yaw on Vortex Burst Behavior, by Eric J. Stephen and Bret Donegan (DFAN). AIAA 25th Fluid Dynamics Conference, Colorado Springs CO, 20-23 Jun 94.

Application of the Volterra Functional Series Approach for Understanding Dynamic Flow Separation, by Julie A. Lovato, Charles Pezeshki and Wyatt Davis (WSU). AIAA 12th Applied Aerodynamics Conference, Colorado Springs CO, 20-23 Jun 94.

Nonlinear Spectral Characterization of Frequency-Modulated Control Applied to a Static Airfoil Shear Layer, by Wyatt Davis (WSU), Julia A. Lovato, and Charles Pezeshki (WSU). AIAA 25th Fluid Dynamics Conference, Colorado Springs CO, 20-23 Jun 94.

The Use of Ground Based Testing in the Aeronautical Engineering Curriculum at the United States Air Force Academy, by Scott P. LeMay, Steven A. Brandt, John K. Harvell (DFAN), and Julie A. Lovato. AIAA 18th AIAA Aerospace Ground Testing Conference, Colorado Springs CO, 20-23 Jun 94.

Pitch Rate and Reynold's Number Effects on Unsteady Boundary Layer Transition and Separation, by Scott J. Schreck, William E. Faller, and Henry E. Helin (DFAN). AIAA 25th Fluid Dynamics Conference, Colorado Springs CO, 20-23 Jun 94.

Dynamic Reattachment on a Downward Pitching Finite Wing, by Scott J. Schreck, William E. Faller, and Marvin W. Luttges (CU). AIAA 12th Applied Aerodynamics Conference, Colorado Springs CO, 20-23 Jun 94.

Application of Neural Networks to Unsteady Aerodynamic Control, by William E. Faller, Scott Schreck, and Marvin Luttges (CU). Workshop on Decade of Neural Network Advances and Applications, Pasadena CA, 10-13 May 94.

The Effects of Leading Edge Sweep Angle on Non-Zero Trimmed Roll, by Eric J. Stephen and C1C Drew A. Sopirak. AIAA 12th Applied Aerodynamics Conference, Colorado Springs CO 20-23 Jun 94.

Freestream Turbulance Effects on Dynamic Separation, by Cadet Sean C. McLay and Cadet Jackkrit Thammavichai (DFAN cadets working under the guidance of Major Scott J. Schreck). AIAA Region V Student Conference, University of Minnesota, Minneapolis MN, 20-22 Apr 94.

Critical Roll Positions of High Angle of Attack Delta Wings, by Cadet Drew Sopirak (DFAN cadet working under the guidance of Major Eric J. Stephen). AIAA Region V Student Conference, University of Minnesota, Minneapolis MN, 20-22 Apr 94.

Differential and Vectored Trailing Edge Jet Control of Delta Wing Vortices, by Cadet D.A. Nawrocki (DFAN cadet working under the guidance of Captain Hank Helin). AIAA Region V Student Conference, University of Minnesota, Minneapolis MN, 20-22 Apr 94. (1st place winner)

Pulsed Air Injection Control of Dynamic Airfoil Stall, by C1C Arturo Alvarado and C1C John Meiter (DFAN cadets working under the guidance of Dr Julie A. Lovato). AIAA Region V

Student Conference, University of Minnesota, Minneapolis MN, 20-22 Apr 94. (2nd place winner)

Analysis of Rolled Delta Wing Flows Using Effective Sweep and Attack Angles, by Eric J. Stephen. Submitted to Journal of Aircraft, Apr 94. Accepted. Projected publication Sep/Oct 95.

Feedback Control of the Flow Over a Two-Dimensional Airfoil, by Julie A. Lovato and Lt Col Craig A. Baer. AIAA 95-0675, AIAA 33rd Aerospace Sciences Meeting and Exhibit, Reno NV, 9-12 Jan 95. Presented.

Encoding of Three-Dimensional Unsteady Separated Flow Field Dynamics in Neural Network Architectures, by Scott J. Schreck and William E. Faller. AIAA 33rd Aerospace Sciences Meeting, Reno NV, 9-12 Jan 95. Presented.

Unsteady Fluid Mechanics Applications of Neural Networks, by William E. Faller and Scott J. Schreck. AIAA 33rd Aerospace Sciences Meeting, Reno NV, 9-12 Jan 95. Presented.

Control of Delta Wing Vortex Impingement on Twin Vertical Tails, by John S. Meiter, Brian K. Kobashigawa, and Julie A. Lovato. 47th Annual Meeting of the American Physical Society, Division of Fluid Dynamics, Atlanta GA, 20-22 Nov 94. Accepted Sep 94. Presented Nov 94.

Dynamic Reattachment on a Downward Pitching Finite Wing, by Scott J. Schreck, William E. Faller, and Marvin Luttges (CU). 12th AIAA Applied Aerodynamics Conference, Colorado Springs CO, 20 Jun 94.

An Experimental Investigation of the Flow Field Behind an Oscillating Slender Body, by David J. Bunker. FJSRL-TM-94-0004, PhD Thesis, Nov 94.

Unsteady Flow Fields Over a Rotating Circular Cylinder, by Eric J. Stephen, Thomas E. McLaughlin (DFAN), and Michael C. Robinson (CU). Submitted to Journal of Fluid Mechanics, 3 April 1995.

Numerical Simulation of Jet Entrainment Effects on Delta Wing Vortices, by Richard W. Newsome, Jr. Submitted to 34th Aerospace Sciences Meeting and Exhibit, Reno NV, 15-18 Jan 96.

Unsteady Aerodynamics - Final Report. FJSRL-TR-95-0004, September 1995, USAF Academy CO.